TECHNISCHE UNIVERSITÄT MÜNCHEN
Lehrstuhl für Ernährung und Immunologie

Mitochondrial impairment drives intestinal stem cell transition towards dysfunctional Paneth cells predicting Crohn's disease recurrence

Sevana Khaloian-Sarnaghi

Vollständiger Abdruck der von der TUM School of Life Sciences der Technischen Universität München zur Erlangung des akademischen Grades eines

Doktors der Naturwissenschaften (Dr. rer. nat.)

genehmigten Dissertation.

Vorsitzende:	Prof. Dr. Martin Klingenspor
Prüfer der Dissertation:	1. Prof. Dr. Dirk Haller
	2. Prof. Dr. Nina Henriette Uhlenhaut

Die Dissertation wurde am 25.11.2020 bei der Technischen Universität München eingereicht und durch die TUM School of Life Sciences am 22.03.2021 angenommen.

Abstract

Inflammatory bowel diseases (IBD) are chronic intestinal disorders with two main pathologies, Crohn's disease (CD) and Ulcerative colitis (UC). Intestinal epithelial cells (IECs) constitute a barrier between the microbiota and the immune system. Crypt base columnar (CBC) intestinal stem cells (ISCs) are the origin for the differentiated IEC-types and are responsible for epithelial renewal and healing. Mitochondrial function has been shown to regulate intestinal epithelial stemness and proliferation. Paneth cells (PCs) secret antimicrobial peptides (AMPs). Moreover, they provide metabolites and growth factors for CBC ISCs, supporting their maintenance. Ileal CD is associated with reduced (PC) numbers and impaired PC function. Furthermore, perturbed mitochondrial function and mitochondrial stress in CD have been associated with PC dysfunction. The aim of this study was to characterize the impact of mitochondrial dysfunction on the ISC niche, including PCs, under inflammatory conditions.

Investigating the impact of intestinal inflammation on PC function and on the stem compartment, we used inflamed margins from CD patients and tissue samples from $TNF^{\Delta ARE}$ mice, a mouse model for CD-like ileitis. Correlation analyses confirmed the link between inflammation and the dysfunctional PC phenotype and indicated an association between inflammation and reduced stemness. Reduced ISC niche function and aberrant PC and ISC phenotypes predicted endoscopic recurrence in non-inflamed margins of CD patients 6-12 months after surgery. The activation of mitochondrial unfolded protein responses (mt-UPR) has been observed under inflammatory conditions. Similarly, the crypt epithelium of $TNF^{\Delta ARE}$ mice showed signs of activated mitochondrial unfolded protein responses. Characterizing the connection between mitochondrial dysfunction and ISC niche function, we investigated an ISC-specific Hsp60 deficient ($Hsp60^{\Delta/\Delta ISC}$) mouse model, where mitochondrial dysfunction could be induced upon loss of mitochondrial chaperone Hsp60. Mitochondrial dysfunction was associated with a transient reduction of stemness, and associated with increased numbers of dysfunctional PCs. Further characterization of the ISC niche confirmed differentiation of ISCs into dysfunctional PCs upon mitochondrial impairment. To depict molecular mechanisms, small intestinal organoid culture was used. Inhibiting mitochondrial respiration through inhibition of the ATP synthase resulted in a disruption of the ISC niche function. Consistent with the reduced stemness *in vivo*, inflamed $TNF^{\Delta ARE}$ mouse-derived intestinal crypts could not generate organoids *ex vivo*. However, a pharmacologically-induced shift towards mitochondrial oxidative phosphorylation rescued inflammation-mediated growth defects in $TNF^{\Delta ARE}$ organoids and restored stemness.

In conclusion, we hypothesize that inflammation-mediated mitochondrial dysfunction might cause a metabolic imbalance between glycolysis and mitochondrial respiration, leading to reduced stemness and PC dysfunction. Reinforcing mitochondrial respiration might be a therapeutic approach to target ISC niche dysfunction in CD patients.

Table of contents

1. Introduction

Inflammatory Bowel Diseases (IBD) are associated with changes in intestinal epithelial cell (IEC) homeostasis. *Lgr5*$^{+}$ stem cells reside in the crypt base, supporting epithelial turnover and epithelial renewal. Paneth cells (PCs) are a sub-type of IECs, producing and secreting antimicrobial peptides. Additionally, PCs contribute to the stem cell niche by providing growth factors and metabolites, supporting *Lgr5*$^{+}$ stem cell maintenance. Reduced numbers of PCs have been observed in intestinal inflammation. On the other hand, mitochondria regulate IEC differentiation and intestinal epithelial stemness. Altered mitochondrial function and activated mitochondrial unfolded protein responses (UPR) have been observed in IBD. In this thesis, the association between mitochondrial dysfunction in stem cell niche and chronic intestinal inflammation was characterized in patients and mouse models.

1.1 Anatomy and function of the digestive tract

The intestinal tract in humans consists of the small and large intestine. The small intestine is structured into the duodenum, jejunum and ileum, ending in the ileocecal valve. Following the small intestine, the large intestine starts from the cecum and consists of three compartments of the proximal, transverse and distal colon [1-3]. The intestinal epithelium together with the lamina propria forms the crypts and the scaffolding of the villi in the small intestine [1]. The epithelial structure of each part of the intestine is organized in a specific pattern to meet its physiological requirements. Differences in the crypt-villus structure and villus length are important for the absorption of nutrients and the nutrient exchange between the host and the lumen throughout the small intestine. The villus length decreases along the length of the small intestine reaching a flat surface with no villi in colon. This is the area where water reabsorption takes place [4] (**Figure 1**). Around 10^{14} microorganisms and more than 500 species inhabit the intestine, comprising the intestinal microbiota [5]. The intestinal bacterial population increases along the intestinal tract, reaching the highest numbers in the terminal ileum and colon [6]. Age [7], diet [8-10], genetics [8] and environmental factors, including antibiotic treatment [11, 12] impact the intestinal microbiota. The intestinal microbiota is important for regulation of host energy metabolism [13], mucosal homeostasis and development of immune responses [14]. Moreover, it has a considerable impact on the number of immune cells in the lamina propria, where in addition to intestinal epithelial cells, the majority of immunological processes take place. Microbial dysbiosis disrupts mucosal homeostasis and is associated with disease. Separation of the bacteria from the epithelium is facilitated by the mucus barrier, which consists of an inner and an outer mucus layer and covers the intestinal epithelium [1, 15]. The thickness of the mucus barrier increases from the small intestine to the colon and correlates with the increase in bacterial load along the intestinal tract [16] (**Figure 1**).

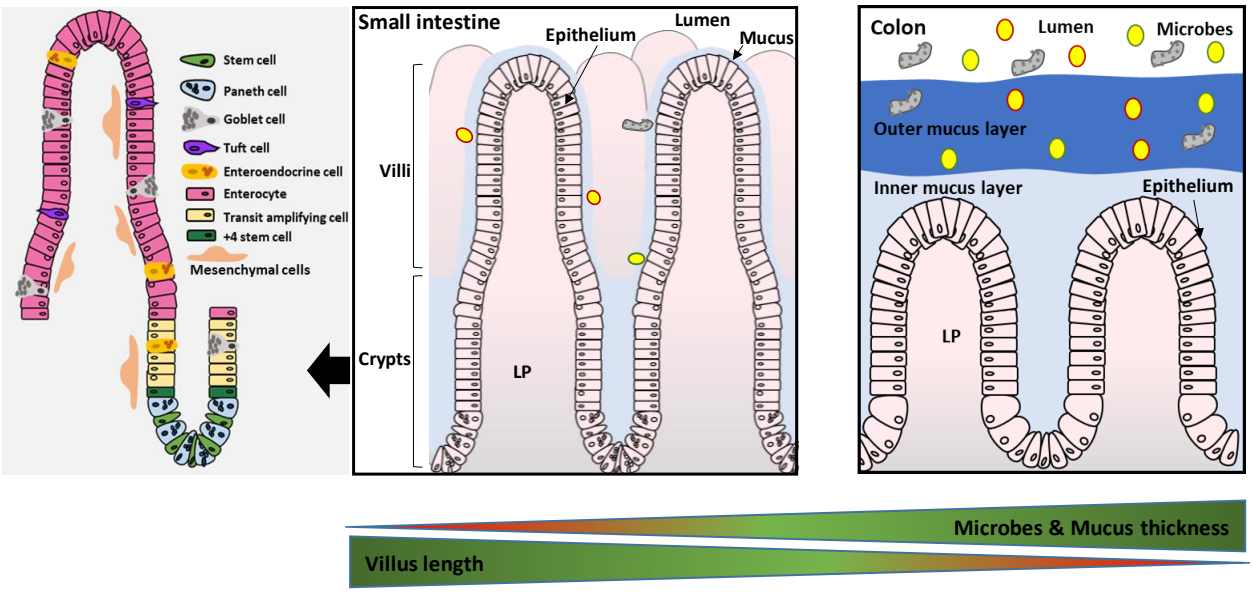

Figure 1 Structure of the small intestine and colon

The intestinal epithelium separates the gut lumen from the lamina-propria. The crypt-villus structure of the small intestine is important for nutrient absorption. The colonic epithelium lacks villus structure. The number of microbes increases from the small intestine to the colon. Moreover, colon contains a thick mucus layer that protects the epithelium from penetration of microbes. Different small intestinal epithelial sub-populations are presented in the left side.

1.2 The intestinal epithelium and its specialized cell-populations

The intestinal epithelium is a monolayer consisting of different cell types that are important for proper intestinal function. Intestinal stem cells (ISCs), PCs, goblet cells, enteroendocrine cells, tuft cells and enterocytes are specialized sub-types of the intestinal epithelium. Absorptive enterocytes constitute the majority (up to 80%) of intestinal epithelial cells (IECs), absorbing nutrients from the gut lumen and transporting them to the host. PCs, goblet cells, enteroendocrine cells and tuft cells have secretory functions. Secretory factors from these cells regulate the immune and metabolic processes [4, 17] (**Figure 1**).

Stem cells are the origin of all IEC sub-populations and are responsible for the intestinal epithelial self-renewal and quick turnover. Intestinal epithelial renewal including cell migration to the villus tip and shedding into the gut lumen takes place every 3-5 days [4, 18]. Crypt base columnar (CBC) cells and quiescent stem cells (reserve cells) are two types of stem cells that reside in small intestinal crypts. CBCs are localized in the crypt base and are identified by Leucine-rich repeat-containing G-protein coupled receptor 5 (*Lgr5*). Besides *Lgr5*$^{+}$ CBCs, an additional sub-set of stem cells resides in the crypt base expressing Olfactomedin 4 (Olfm4). Olfm4^{+} cells are present in large numbers in the small intestine. Unlike in humans, these cells are not present in mouse colonic tissue [19]. *Lgr5*$^{+}$ ISCs, Olfm4^{+} ISCs and cells with overlapping expression of both markers are rapidly cycling, self-renewing and they are sensitive towards genotoxic stress. Therefore, these cells are important for the intestinal epithelial

turnover and homeostasis (**Figure 2**) [4, 20]. In contrast to actively proliferating CBCs, quiescent stem cells are cycling infrequently and remain at the +4 position above the crypt base. Reserve stem cells, including label-retaining cells, express homeodomain-only protein (Hopx), B Lymphoma Mo-MLV Insertion Region 1 Homolog (Bmi1), murine Telomerase Reverse Transcriptase (mTert), Olfm4 and Leucine Rich Repeats and Immunoglobulin-Like Domains 1 (Lrig1) and repopulate the epithelium upon *Lgr5*$^{+}$ ISC loss (**Figure 2**). Quiescent stem cells are less affected by genotoxic stress. However, they get activated by epithelial injury and promote tissue regeneration. [20-23].

Actively cycling *Lgr5*$^{+}$ ISCs give rise to highly proliferative progenitor cells called transit-amplifying (TA) cells. These cells reside in upper crypts up to the crypt-villus junctions, constituting the transit-amplifying zone. The markers Musashi 1 (Msi1) and Prominin 1 (Prom1) label these progenitor cells. TA cells differentiate into absorptive and secretory cell-types, including PCs (**Figure 2**). [18].

PCs are specialized cells of the small intestine and their abundance decreases from the small intestine to the colon. These cells are not present under normal conditions in murine colon [24]. After differentiation, mature PCs relocate to the crypt base, where they reside for 3-6 weeks [24]. The presence of growth factors are essential for the flow of PCs to the crypt base [24] (**Figure 2**). PCs have a diverse range of functions, on one hand, they support *Lgr5*$^{+}$ ISC maintenance and on the other hand, PCs produce and secrete antimicrobial peptides (AMPs). PC-derived AMPs are essential for immunological defense against microbes. Secretory granules of PCs contain wide range of AMPs such as lysozyme, Angiogenin 4 (Ang4) and defensins in mice. PCs in humans also secrete defensins and the most abundant α-defensins are Human defensin 5 and human defensin 6. In the intestine, secreted α-defensins are inactive and they should be activated to promote their antimicrobial function. In this context, matrix metalloproteinases (MMPs) are enzymes that facilitate the activation of PC-derived inactive α-defensins [25-28].

Besides PCs, goblet cells and enteroendocrine cells are additional secretory cell-types of the intestinal epithelium, specialized for mucus and hormone production, respectively [4] (**Figure 2**). Goblet cells are present in the small intestine and predominantly (~20% of the total IECs) in the colon [29]. These cells produce and secrete mucins. Mucin 2 (MUC2) is a gel-forming glycoprotein and is the major component of the intestinal mucus [29, 30]. The presence of bacteria and the mucus secretion of goblet cells influence the function of the inner mucus layer [31]. Disturbed mucus production by goblet cells is associated with reduced thickness of the mucus layer and enhanced bacterial penetration into the epithelium [32]. Enhanced bacterial contact with the epithelium was shown to cause inflammation and induce tumor formation in mice [32, 33]. In contrast to goblet cells, enteroendocrine cells constitute only 1% of the IEC population [34]. All sub-types of enteroendocrine cells are characterized by chromogranin A (ChgA). Enteroendocrine cells are scattered throughout the intestine, secreting more than 20 peptide hormones and regulating digestive processes and metabolism [34, 35]. Similar to enteroendocrine cells, tuft cells constitute a small proportion of IECs (~ 0.5%) (**Figure 2**). These cells activate immune

responses by secreting cytokines. Tuft cells are labeled by doublecortin-like kinase 1 (Dclk1) and are found with a high prevalence in the distal small intestine [36].

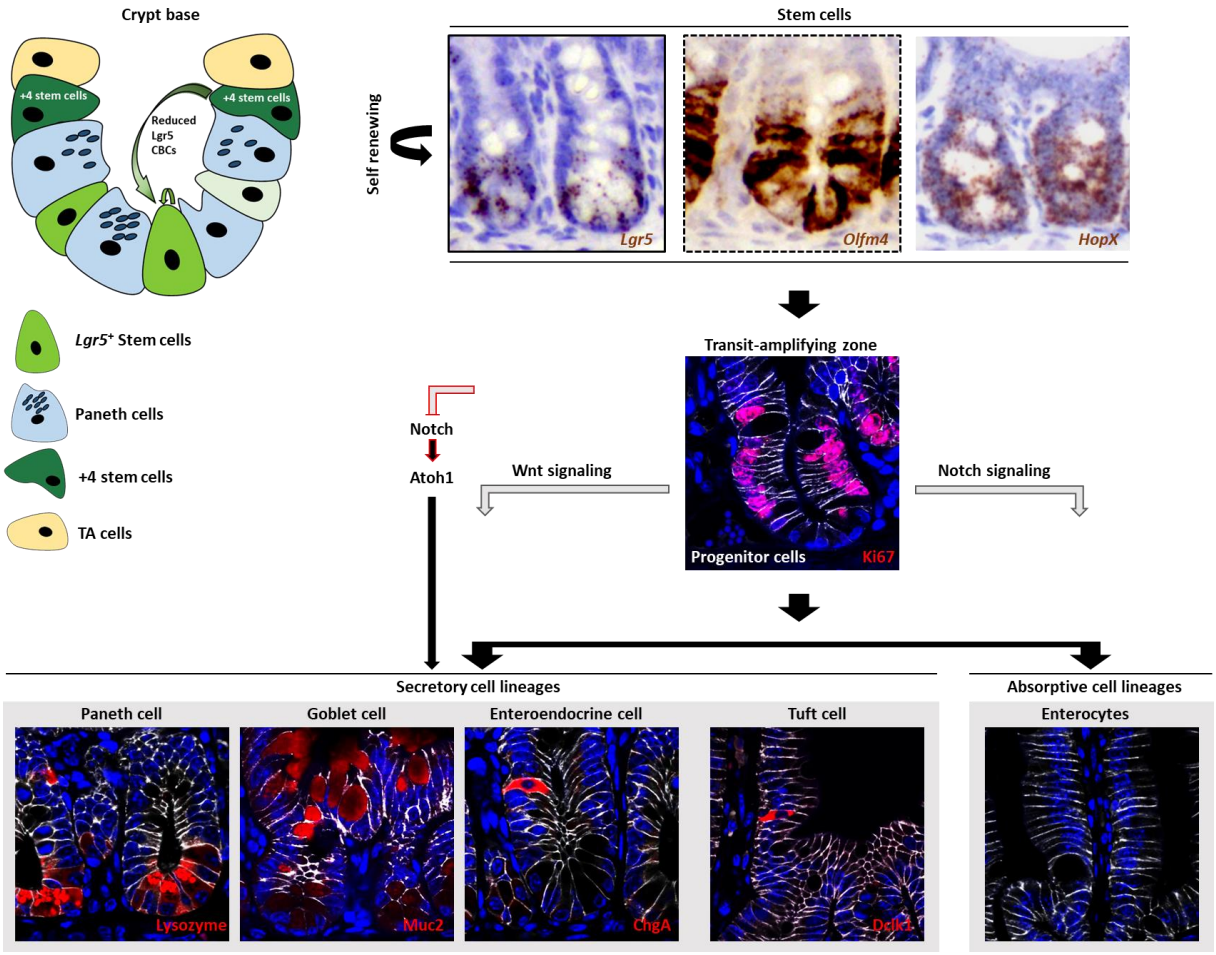

Figure 2 The small intestinal epithelial sub-populations

The small intestinal epithelium is a mono-layer consisting of different epithelial cell-types. Stem cells and Paneth cells constitute the small intestinal crypt-base compartment. Stem cells give rise to transit-amplifying cells, which differentiate into all intestinal epithelial secretory and absorptive cell-types. Quiescent stem cells (+4 position) are reserve stem cells that can compensate for the loss of *Lgr5*$^{+}$ stem cells. Wnt and Notch signaling pathways are important for intestinal epithelial homeostasis by regulation of *Lgr5*$^{+}$ stem cells. Activation of the Notch signaling pathway shifts epithelial differentiation towards absorptive cell-types.

1.3 Signaling pathways important for stemness

Different signaling pathways are involved in PC maturation, stem cells niche maintenance and the regulation of stem cells. The first signaling pathway is the canonical Wingless-related MMTV integration site (Wnt)/β-catenin signaling. Binding of Wnt proteins to their representative cell-surface receptors leads to the activation of the Wnt/β-catenin pathway. Upon activation of this pathway, cytosolic β-catenin translocates into the nucleus, interacts with the transcription factor T-cell factor (Tcf) and activates target genes. In the absence of Wnt proteins, cytosolic β-catenin is phosphorylated by a protein complex, which is composed of adenomatous polyposis coli (APC), glycogen synthase kinase-

3β (GSK-3β), casein kinase 1 (CK1) and Axin. This leads to the proteasomal degradation of β-catenin. Alterations in the Wnt signaling pathway, including but not limited to APC mutations, have been observed in 90% of colorectal cancer cases [37, 38]. The Apc (min/+) mice, which were generated by random Apc mutations to induce multiple intestinal neoplasia (Min), develop small intestinal tumors [39]. Since the Wnt/β-catenin signaling pathway is important for the maintenance of stem cell niche, mice with Tcf4 deficiency show a failure in the maintenance of the stem compartment during embryonic development. Reduced proliferation and decreased small intestinal PC-marker gene expression were further observed in Tcf4 deficient mice [40, 41]. In addition to altered ISC maintenance, the disruption of Wnt target genes and receptors is linked to the mis-localization of PCs [37].

The second signaling pathway is the Notch signaling pathway. This pathway transmits signals between adjacent cells. Activation of Notch requires the presence of transmembrane ligands (delta-like (DLL) 1,3,4 and Jagged (JAG) 1,2) that integrate signals through the cell-surface receptors (NOTCH 1-4) [42]. Notch signaling is not only important for stem cell maintenance, but also for the differentiation of progenitors into absorptive enterocytes. Previous studies showed an association between inhibition of Notch signaling and reduced CBC ISC numbers. Additionally, Notch inhibition was associated with the differentiation of intestinal crypts towards secretory cell-types [43-45] (**Figure 2**). Protein atonal homolog1 (Atoh1/ also called Math1) is a target gene of the Notch signaling pathway [46] and is important for secretory cell-lineage differentiation [43]. In addition to controlling stemness, irradiation-induced Notch activation was shown to enhance de-differentiation of PCs by causing them to gain stem-like properties [47].

Interaction between Wnt and Notch signals is essential for the control of proliferation in crypts [40]. Both signals play crucial roles in intestinal epithelial cell homeostasis. Yet, Notch signaling was also identified to have oncogenic potential in colorectal tumorigenesis. Therefore, the interaction between Wnt and Notch pathways can provide an environment that is favorable for formation of intestinal adenomas [40]. Additional examples for pathways involved in stem cell regulation and epithelial homeostasis upon epithelial injury include Hedgehog signaling, Bone Morphogenic Protein (BMP) signaling and Hippo signaling [48]. BMP signaling promotes cell differentiation in crypts via BMP ligands [48]. Transgenic inhibition of the BMP inhibitor noggin was shown to induce the formation of numerous crypts in the crypt-villus junction [49]. Additionally, a mutation in the BMP receptor *Bmpr1a* activated Wnt/β-catenin signaling and expanded the stem compartment, indicating that activation of BMP signaling limits stemness by repressing Wnt/β-catenin signaling [50].

1.4 Epithelial injury and factors impacting intestinal stemness

The intestinal epithelial renewal is facilitated by stem cells and their progeny that undergo proliferation and differentiation. Inflammation and irradiation are examples of injuries to the epithelium that affect the stem cell self-renewing capacity, leading to tissue damage [48]. In response to injury-mediated ablation of *Lgr5*$^+$ ISCs, quiescent stem cells including label-retaining cells, get involved in tissue regeneration [51]. A high dose of irradiation was shown to cause loss of *Lgr5*$^+$ ISCs. Following this loss, cells arising from certain reserve stem cells expressing Bmi1 reconstituted the intestinal epithelium [52]. Similar to irradiation, chemical wounding, which was induced by dextran sulfate sodium (DSS), and subsequent inflammation led to *Lgr5*$^+$ ISC loss. In this model, increased numbers of reserve stem cells, including Hopx$^+$ cells, promoted tissue reconstitution in the recovery phase [53, 54]. In addition to reserve stem cells, PCs were shown to gain stem-like features, de-differentiate into *Lgr5*$^+$ ISCs and get involved in tissue regeneration upon chemical injury [47, 54]. Moreover, PCs provide Wnt factors including Wnt3, epidermal growth factor (EGF) and delta-like ligands (DLLs), which regulate epithelial stemness [55]. A recent study showed an association between Wnt inhibition in aged PCs and a defect in both stem cells and the stem cell-niche function, resulting in a reduced intestinal regenerative capacity. An elevated mTOR complex I (mTORC1) activity in aged PCs was correlated with increased Notum production, which is an extracellular Wnt inhibitor [56]. On the other hand, caloric restriction was shown to inhibit mTORC1 signaling in PCs. This resulted in an increase in stem cell self-renewal and reduced differentiation, causing reduced numbers of enterocytes and shortening of villi [57]. Apart from growth factors, secretory Phospholipases A2 (sPLA2s) [58] and metabolic signaling molecules, including lactate and cyclic ADP ribose (cADPR), were also identified as stem cell niche factors generated by PCs [57, 59].

Similarly, mesenchymal cells have a key role in supporting the ISC niche. Wnt and growth factors as well as BMP signals arising from stromal cells regulate intestinal epithelial cell proliferation and participate in crypt regeneration [60, 61]. In addition to growth factors supporting the epithelial proliferation and ISC niche, we previously suggested that mitochondrial function and mitochondria-related unfolded protein responses (UPR) regulate intestinal epithelial proliferation and stemness [62].

1.5 Unfolded protein response (UPR): The regulator of cellular proteostasis

Mitochondria and the endoplasmic reticulum (ER) are two cellular organelles in eukaryotic cells. Mitochondria are central regulators of cellular energy generation of the host [63]. Mitochondrial intermembrane space and matrix are two different compartments of mitochondria. The mitochondrial outer membrane separates the mitochondrial intermembrane space from the cytosol and enables the exchange of metabolites, ions and small molecules between mitochondria and the cell. The transfer of larger proteins into mitochondria is facilitated by specific translocases. The mitochondrial inner membrane separates the protein-dense matrix from the intermembrane space [64]. The mitochondrial

matrix contains proteins that are encoded by either the mitochondrial genome (mt-DNA) or the nuclear genome (n-DNA). The majority of proteins are encoded by the n-DNA and have to be imported into mitochondria [65, 66]. After transcription and translation, proteins should be folded and quality controlled. Protein folding in cellular organelles is tightly regulated by several quality control mechanisms. The accumulation of unfolded proteins in organelles is due to different genetic and environmental stressors that disturbs protein folding capacity and induces organelle stress. Unfolded protein responses (UPR) are highly conserved signaling pathways that sense insufficient protein folding capacity and aim to restore protein homeostasis, called proteostasis. Proteostasis is regulated by multiple cellular processes, including protein synthesis, protein folding and degradation, that work in synergy to govern protein quality of each organelle [63, 67].

Organelle-specific molecular chaperones facilitate protein folding and prevent protein aggregation. Mitochondrial unfolded protein response (mt-UPR) is a signaling pathway that senses mitochondrial stress and gets activated in response to mitochondrial dysfunction caused by disturbed protein homeostasis. The mt-UPR signaling pathway regulates the communication between mitochondria and the nucleus [68]. Heat shock protein (Hsp) 60 and Hsp70 are mitochondrial chaperones, localized in the mitochondrial matrix, that assist the import of proteins into the mitochondria and facilitate appropriate folding. Together with chaperones, mitochondrial matrix-localized proteases build a mitochondrial protein quality control machinery and maintain mitochondrial proteostasis by degrading proteins [63, 65].

1.5.1 Different branches of mt-UPR

Different branches of the mt-UPR signaling have been identified in mammalian cells (**Figure 3**) [69]. Accumulation of unfolded proteins in the mitochondrial intermembrane space leads to the production of reactive oxygen species (ROS). Following ROS generation, protein kinase B (Akt) is getting activated, which in turn phosphorylates estrogen receptor-α (ER-α) and activates mitochondrial regulator nuclear respiratory factor 1 (Nrf1) as well as the intermembrane-localized protease HtrA2. The activation of HtrA2 leads to the degradation of misfolded proteins in the mitochondrial intermembrane space [63]. Hsp60 is a mitochondrial matrix-localized chaperone that together with its co-chaperonin Hsp10 supports the mitochondrial protein folding capacity [70]. Unfolded proteins in the matrix activate NAD-dependent protein deacetylase sirtuin 3 (Sirt3). Sirt3-mediated deacetylation of forkhead box transcription factor 3 (Foxo3) leads to the accumulation of Foxo3 in the nucleus. Consequently, this accumulation induces the transcription of superoxide dismutase 2 (Sod2), enhancing ROS detoxification, and increases the expression of mitophagy-related genes [63].

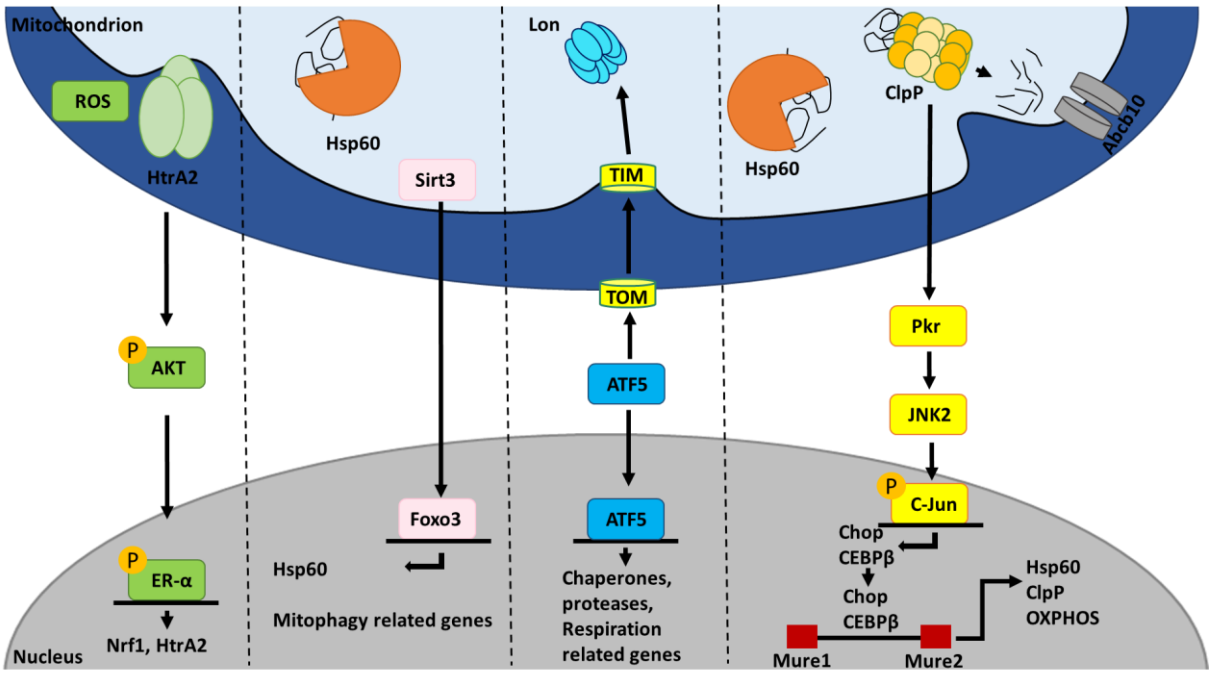

Figure 3 The mitochondrial UPR signaling

Mammalian mt-UPR signaling. The figure illustrates the mitochondrial proteases and chaperones with their function in protein degradation and folding, respectively. Accumulation of mis-/ unfolded- proteins in different mitochondrial compartments activates mt-UPR to maintain mitochondrial proteostasis (adapted from [63]).

Activating transcription factor 5 (ATF5) is an additional regulator of mt-UPR signaling. ATF5 is a mammalian homologue of activating transcription factor associating with stress (ATFS-1) in *Caenorhabditis elegans*. It is hypothesized that in the absence of mitochondrial stress, similar to ATFS-1, ATF5 is imported to mitochondria via translocase of the mitochondrial outer membrane (TOM) and translocase of the mitochondrial inner membrane (TIM). In the mitochondria matrix, ATF5 is then degraded by mitochondrial proteases. However, in the presence of mitochondrial stress, ATF5 translocates to the nucleus and activates mt-UPR target genes, including mitochondrial chaperones, proteases and respiration-related genes [63, 69, 71]. Mitochondrial ATP-dependent matrix- or inner membrane-localized proteases, including caseinolytic peptidase subunit P (ClpP), Lon and mAAA (Afg3l2) degrade proteins upon misfolding [72]. In the case of un-/mis-folding of proteins by Hsp60 or ClpP, respectively, the accumulated proteins activate double-stranded RNA (dsRNA)-dependent protein kinase (Pkr) and c-Jun N-terminal kinase 2 (JNK2). Subsequent activation of the transcription factor activator protein 1 (AP1) via phosphorylation of Jun induces the transcription of CEBP homologous protein (CHOP) and CCAAT/ enhancer binding protein-β (CEBPβ) [73, 74]. Further binding of the dimer of CHOP and CEBPβ to genes containing mt-UPR elements 1 and 2 (Mure1, Mure2) upstream and downstream of the CHOP binding element [75] results in the activation of mitochondrial chaperones and proteases, improving mitochondrial proteostasis, and regulates mitochondrial respiration [63] (**Figure 3**).

1.5.2 Role of Hsp60 in intestinal epithelial function and differentiation

The cell-specific deletion of mt-UPR targets and the induction of mt-UPR signaling can impact the epithelial self-renewal capacity as well as differentiation and show homeostatic responses to the cellular stress [62]. Mice with a *Hsp60* deletion in IECs ($Hsp60^{\Delta/\Delta IEC}$) serve as a model for mitochondrial dysfunction. We previously suggested that mitochondrial function regulates the function of the intestinal epithelium and stemness, and it determines the differentiation processes [62]. Activated mt-UPR, reduced ATP levels and induced anti-oxidative stress-associated transcription factors in $Hsp60^{\Delta/\Delta IEC}$ mice were pointing to the fact that *Hsp60* deletion in IECs causes mitochondrial dysfunction. The mitochondrial chaperone Hsp60 is also regulating the intestinal epithelial stemness and proliferation [62]. In response to altered mitochondrial function PC-derived Wnt signals arising from knockout crypts support stem cells. This indicates that the stem cell niche maintains the stem compartment [62]. In addition to the ER-UPR activation that is important for epithelial stem cell differentiation [76], mitochondrial activity and metabolism were identified critical for stem cell function as well as cellular fate decisions [77, 78]. Upon mitochondrial dysfunction in $Hsp60^{\Delta/\Delta IEC}$ mice, numbers of highly functional and mucus-filled goblet cells were reduced in knock out crypts of the small intestine and the colon. This was suggesting that mitochondrial function might be required for goblet cell maintenance (unpublished observation). Additionally, the formation of hyperproliferative nodules, expressing Hsp60 in the small intestine of $Hsp60^{\Delta/\Delta IEC}$ mice [62] were indicative of an altered cellular differentiation upon mitochondrial dysfunction and the activation of regenerative responses [62].

1.5.3 The Caseinolytic peptidase subunit P (ClpP)

The maintenance of mitochondrial proteostasis is crucial for cell viability. Mitochondria contain at least 45 proteases that are classified in different groups and degrade damaged or unfolded proteins [79]. The first group comprises intrinsic-proteases that are localized in different mitochondrial compartments. The second group are pseudo-proteases that are unable to perform catalysis but control the activity of other proteases. The third group includes transient-proteases that shuttle between mitochondria and the cytosol for additional proteolytic activities [79].

ClpP is an ATP-dependent matrix-localized protease from the intrinsic group that forms the ClpXP complex with the ATP-dependent Clp protease ATP-binding subunit X (ClpX) chaperone. ClpP is part of the mt-UPR stress-signaling pathway with its major function in the degrading of unfolded proteins and protein quality control [79]. The ATP-binding cassette subfamily B member 10 (ABCB10) is an inner membrane-localized transporter in mammalian cells, which is a putative ortholog to HAF-1 transporter in *C. elegans*. Upon mitochondrial stress, ABCB10 might play a role in the mt-UPR signaling pathway and export peptides that are degraded by proteases including ClpP in the mitochondrial matrix to the cytosol [80] (**Figure 3**).

Impaired ClpP function causes abnormalities in both humans and mice [81, 82]. Homozygous CLPP mutations were shown to cause hearing loss and ovarian failure in human Perrault syndrome. Similarly,

male and female ClpP null mice show complete infertility, impaired hearing and growth retardation [82]. Defects in the maturation of oocytes in ClpP deficient female mice were paralleled by reduced size of mitochondria, decreased mitochondrial fusion as well as reduced mitochondrial function, which was identified by decreased mitochondrial chaperone expression and induced ROS production. Therefore, appropriate mitochondrial function and the presence of ClpP is necessary for female reproduction [83]. ClpP deficiency in the liver and muscle of these mice resulted in a mild respiratory dysfunction in cellular level [82, 83].

1.6 Mitochondrial metabolic pathways

Mitochondria perform multiple functions, including cellular respiration. The mitochondrial matrix contains enzymes that are essential for metabolic processes such as the tricarboxylic acid cycle (TCA), oxidative decarboxylation of pyruvate, fatty acid ß-oxidation and iron-sulfur cluster formation [84] (**Figure 4**). Additionally, the urea cycle, in which the degradation of amino acids results in the excretion of nitrogen as urea, takes place partly in the mitochondrial matrix. Glutamine that is generated upon food digestion and synthesized in liver cells, is degraded in the small intestine, where it is converted to ornithine. Besides glutamine and ornithine, citrulline is one of the major metabolites that is produced in the urea cycle. Citrulline in mammals is synthesized from glutamine and converts to arginine. The synthesis of citrulline from ornithine is facilitated by ornithine transcarbamylase (OTC) in the small intestine (**Figure 4**). Finally, argininosuccinate synthase converts citrulline to arginine in kidneys [85, 86].

The second metabolic process that occurs in mitochondria is the fatty acid ß-oxidation. Carnitine is an essential metabolite that transfers long chain fatty acids into the mitochondria for subsequent ß-oxidation. The transfer of carnitine into mitochondria in humans is facilitated by the organic cation/ carnitine transporter 2 (OCTN2). A previous study linked OCTN2 deficiency in intestinal tissues of mice, which results in an altered mitochondrial function, with the development of intestinal inflammation, ulceration and atrophy [87]. Therefore, carnitine supplementation and the enhancement of mitochondrial function by re-boosting fatty acid oxidation might be a beneficial therapeutic approach in patients with intestinal inflammation [87].

Aerobic glycolysis and oxidative phosphorylation (OXPHOS) are additional metabolic processes happening in mitochondria. Glycolysis is a process that starts in the cell cytoplasm. Pyruvate, generated through glycolysis, is translocated into mitochondria by mitochondrial pyruvate carriers (MPC1 and MPC2). Subsequently, the pyruvate dehydrogenase (PDH) complex functions as a gatekeeper for glycolysis by transferring pyruvate into the TCA cycle. Nicotinamide adenine dinucleotide (NADH), produced in the TCA cycle is transferred into the respiratory chain complex I for initiation of mitochondrial OXPHOS [88, 89] (**Figure 4**).

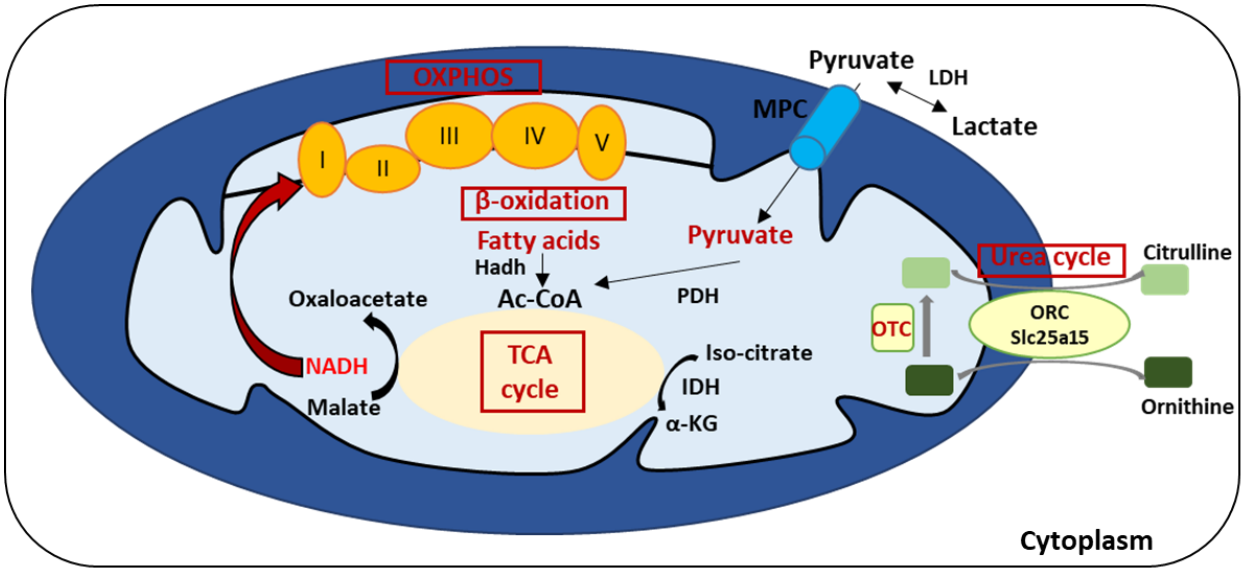

Figure 4 Metabolic pathways in mitochondria

The tricarboxylic acid cycle (TCA), Oxidative phosphorylation (OXPHOS), β-oxidation and the urea cycle are metabolic pathways that are taking place in mitochondria. OTC: Ornithine transcarbamylase; ORC: Ornithine-citrulline carrier; Slc25a15: Mitochondrial ornithine transporter 1; IDH: Isocitrate dehydrogenase; α-KG: alpha-ketoglutarate; LDH: Lactate dehydrogenase; PDH: Pyruvate dehydrogenase; Hadh: Hydroxyacyl-CoA dehydrogenase.

The OXPHOS takes place in the mitochondrial inner membrane. The electron transport chain contains four complexes of the respiratory chain (shown in **Figure 5**). Complex I uses NADH, which is produced in the TCA cycle, as an electron source and transfers the electrons to complex III and subsequently complex IV for further processing. In contrast to complex I, the pathway through complex II uses succinate as substrate. The electron flow through the electron transport chain generates a proton gradient across the mitochondrial inner membrane, which is used by complex V (ATP synthase) for ATP synthesis [64] (**Figure 5**). The maintenance of mitochondrial respiratory function is important for the maintenance of a healthy gut. Impaired function of mitochondrial respiratory complexes and defects in mitochondrial OXPHOS, leading to reduced energy production, were observed in response to intestinal epithelial injury, including inflammation [90-92] and tumorigenesis [93]. Inhibition of the activity of respiratory chain complexes reduces adenosine diphosphate (ADP) phosphorylation, resulting in low ATP generation and induces mitochondrial toxicity by disturbing cellular energy metabolism [94]. Rotenone and Oligomycin are complex I and complex V inhibitors [95], respectively, that induce mitochondrial ROS production, impact ATP synthesis and trigger apoptosis [96, 97]. Partial inhibition of Complex V in inflammatory conditions triggers anti-inflammatory responses in intestinal tissues [97]. In this context, inhibition of OXPHOS and induced mitochondrial ROS shifts energy synthesis towards glycolysis and stimulates innate immunity. This emphasizes the role of ATP synthase as a therapeutic target in inflammation-related gut diseases [97].

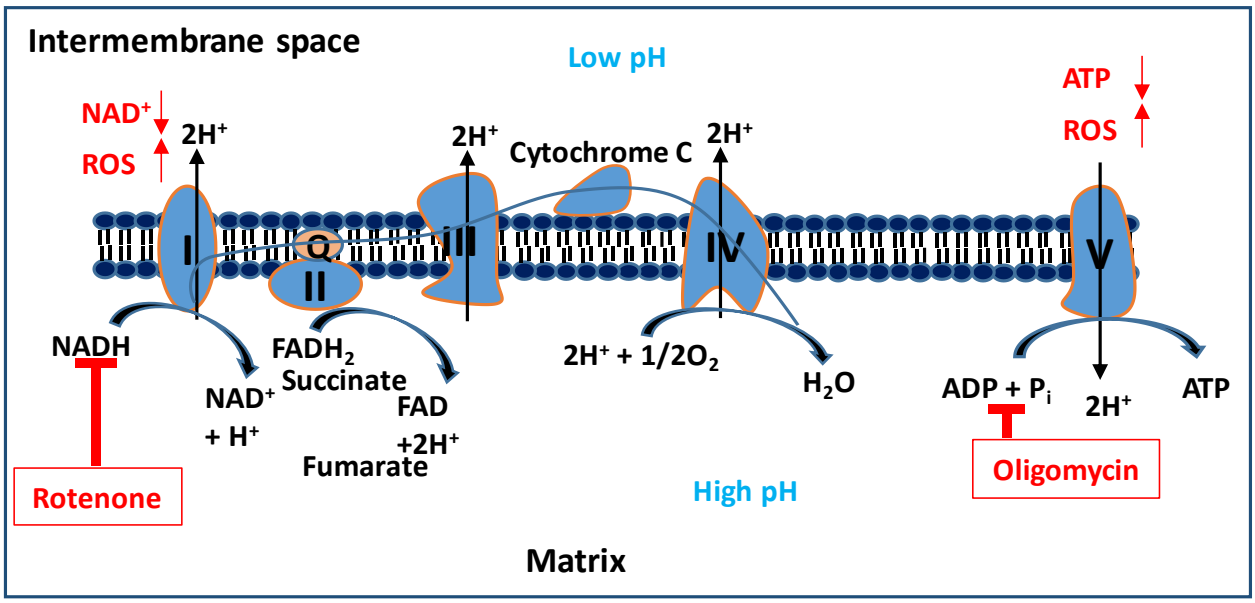

Figure 5 Mitochondrial respiratory chain

Mitochondrial oxidative phosphorylation (OXPHOS) for ATP generation and the complexes involved in this process. Complexes I, II, III IV and cytochrome C build up the electron transport chain. Rotenone and Oligomycin are complex I and V inhibitors respectively.

1.6.1 Glycolysis and OXPHOS in intestinal epithelial cells

Different cell types rely on different energy sources for ATP synthesis. ATP can be generated through glycolysis (2 ATP molecules) or OXPHOS (36 ATP molecules) [88]. Cancer cells rely on glycolysis as a source of energy generation. This phenomenon is due to Warbung effect, a defect in mitochondrial respiration or hypoxia [98].

Cancer cells and pluripotent stem cells have a similar cellular metabolism [99]. The cellular metabolism plays a key role in controlling self-renewal and differentiation of stem cells. While glycolytic processes are the main source of energy generation in undifferentiated pluripotent stem cells, these cells require mitochondrial OXPHOS for differentiation [100]. In the intestinal epithelium, proliferative cells in the crypts have a glycolytic metabolic phenotype. However, enterocytes and differentiated cells along the villi use OXPHOS as their main source for energy generation [101]. Cell-types that are dependent on OXPHOS as their energy source have higher numbers of mitochondria compared to cells that have a glycolytic phenotype. In the crypt compartment, *Lgr5*$^{+}$ stem cells show a higher mitochondrial activity and more dependency on OXPHOS compared to PCs [59, 63]. The lactate that is produced by glycolysis in PCs might support the maintenance of *Lgr5*$^{+}$ stem cells [59].

1.7 UPR activation in disease

Cellular stress, activated UPR and impaired mitochondrial function including an elevated ROS production and dysregulated Calcium homeostasis have been observed in multiple diseases, such as neurodegenerative diseases and autoimmunity [102-104]. Activated ER- or mt-UPR has also been observed in patients with intestinal disorders, including inflammatory bowel diseases (IBD) and colorectal cancer (CRC). In CRC patients, ER-UPR activation was associated with shorter disease-free survival time [32]. Elevated expression of the ER chaperone glucose regulated protein 78 (*Grp78*) and *CHOP* in active IBD patients were signs of organelle stress and UPR activation in response to inflammation [105]. In addition to the ER-stress, IBD patients showed increased HSP60 expression in IECs, indicating an activated mt-UPR in response to chronic intestinal inflammation [66].

Many ER- or mt-UPR-related genes in IECs were shown to alter the balance between epithelial homeostasis and intestinal inflammation, contributing to disease pathogenesis [106, 107]. *X-box-binding protein 1* (*XBP1*) is a transcription factor related to the ER transmembrane inositol-requiring enzyme 1α and β (IRE1α and β) arm. The activation of *Xbp1* induces UPR related target genes [107, 108]. Hypomorphic XBP1 variants were observed in patients with IBD [107]. Similarly, *Xbp1* deletion in IECs of mice was associated with an induced ER-stress, UPR activation and subsequent intestinal inflammation [107, 108]. Therefore, failure in mitochondrial or the ER functionality in intestinal epithelium can lead to chronic intestinal inflammation.

1.8 Inflammatory Bowel Diseases (IBD): Role of IECs

1.8.1 Etiology of IBD

IBD is an immune-mediated chronic disorder that affects the gastrointestinal (GI)-tract. Crohn's disease (CD) and Ulcerative Colitis (UC) are the two main pathologies of IBD with unknown etiology. Different factors including genetics and environmental factors as well as microbes and immunological factors influence IBD pathogenesis [109]. Inflammation in UC mainly occurs in the colonic mucosa and submucosa. In contrast to UC, CD is a patchy disease characterized by transmural inflammation occurring in different parts of the GI tract [6, 109]. In the majority of CD cases, inflammation occurs in the terminal ileum and ileocaecal junction [110]. IBD affects 6.8 million individuals worldwide. The prevalence of IBD has increased from 79.5/100000 to 84.3/100000 population in the time period from 1990-2017 [111].

IBD is characterized by repetitive periods of relapse and remission. Although some patients experience a mild disease course, the majority has continuous alternations between disease remissions and relapses [112]. Disease relapse in the disease course is caused by unknown triggers. The complexity of the disease and the unavailability of specific predictors for disease relapse make it more complicated to handle the disease [112]. Different diagnostic tools are used to assess disease activity and the response to therapy. Colonoscopy is currently considered as the gold standard for the diagnosis of IBD [110].

Since IBD is not curable, the therapeutic goal of IBD is to induce and maintain remission. Corticosteroids, antibiotics, immunomodulators and biologics are used for CD management [110]. In cases of poor response to a single therapy, combination therapies can be a more effective approach in reducing the disease burden. A combination of immunomodulators and anti-Tumor necrosis factor (anti-TNF) biologics were shown to be beneficial in patients with complicated disease course [113]. Interleukin 12 (IL12)/ IL23 inhibitors, small molecule drugs, stem cell therapies using both hematopoietic and mesenchymal stem cells and fecal microbiota transplantation are alternative therapeutic approaches for patients with refractory and severe disease courses [114]. Despite the improvement of techniques and medications for IBD treatment, two-thirds of CD patients require surgery and intestinal resection. Even with resection surgery, patients may experience postoperative recurrence. In a prospective study, male patients, patients with earlier intestinal resections and patients that were classified as smokers at the time of surgery had an increased risk of post-resection endoscopic recurrence [115]. In this context, anti-TNF therapy was identified as an approach to reduce the risk of recurrence after surgery [116]. Patients who received anti-TNF substances after their initial surgery had a lower probability of postoperative endoscopic recurrence [116]. Further research is necessary to understand the mechanisms that may influence CD-relapse. It is also necessary to identify potential predictors for CD recurrence, which will enable us to manage the disease more effectively.

1.8.2 IBD risk factors and their influence on PC phenotype

IBD is a complex disease, in which the combination of susceptibility alleles and environmental factors influence the gut microbiota and IECs, impacting disease pathogenesis [28, 117]. Environmental risk factors that have been identified for IBD include smoking, diet, stress, appendectomy and antibiotic treatments. Smoking is associated with increased risk of disease development, relapse and postoperative endoscopic recurrence in CD patients [116, 118].

In recent years, genetic studies have identified more than 240 genetic variants [119] related to IBD, including some with unknown functions [120]. CD-associated risk alleles are involved in central mechanisms such as oxidative stress, endoplasmic reticulum (ER) stress and autophagy as well as in innate and adaptive immunity [117, 119]. One-third of CD patients show loss of function mutations in the Nucleotide-binding oligomerization domain 2 (NOD2) receptor, which turns NOD2 into one of the most important risk factors in CD. NOD2 is expressed intracellularly in monocytes as well as epithelial cells, including PCs, and is known to play a role in innate immunity [121, 122]. Besides immune cells, PCs are an additional source of defensin production [123]. Mutations in *NOD2* are linked to reduced α-defensin production, which may induce mucosal inflammation and increase the risk of CD-associated ileal involvement [121, 122]. In CD patients, mutations in *NOD2* were shown to induce abnormalities in PC granules. PC abnormalities were defined as reduced numbers of granules as well as aberrant and disorganized granules in PCs. Higher proportion of abnormal PCs were detectable in CD patients with two *NOD2* risk alleles [28, 124]. NOD2 has a bacterial sensing activity and triggers autophagy as

bacteria enter the cell [121]. Autophagy is a homeostatic process that leads to the lysosomal degradation of cytoplasmic material and is fundamental for cellular development and function [125]. *ATG16L1* is an autophagy-related gene and has been identified as an additional important CD susceptible gene [28]. Defects in autophagy have been observed in the pathogenesis of many inflammatory diseases, including CD [125]. ATG16L1 has a protective function by inducing the secretion of PC-derived antimicrobial peptides (AMPs) and reducing the pro-inflammatory cytokine production as well as in the clearance of enteric pathogens. Similar to *NOD2, ATG16L1* mutations are associated with defects in PC function as well as in sensing and presenting bacterial antigens to adaptive immune cells [28, 125]. Mice with a hypomorphic expression of Atg16l1 showed reduced AMP production and secretion [28]. Concomitant with diminished numbers of PCs with normal appearance, *Atg16l1* mutations in mice were associated with elevated numbers of PCs with diminished numbers of granules (≤10 granules), as well as increased numbers of PCs with cytoplasmic lysozyme expression. Similar to mouse models, CD patients homozygous for the CD risk allele ATG16L1 (T300A) showed PC abnormalities and signs of ER-stress. Therefore, XBP1 was characterized as a CD-associated risk allele [107, 124]. *Xbp1* deletion, an induced ER-stress and the development of spontaneous inflammation in the intestinal epithelium of mice were associated with complete loss of PCs and impaired PC function. This indicated that cell-specific organelle stress and activated UPR in IECs contribute to the intestinal inflammation [107, 124, 126].

1.8.3 TNF$^{\Delta ARE}$ mice: A model for CD-like ileitis

Several chemically induced and genetically driven animal models have been established to study the involvement of genetics and/or environmental factors on the development of intestinal inflammation. These models help us to understand the pathogenic mechanisms that cause disease. Besides studying disease etiology, animal models enable us to investigate the consequences of inflammation on the intestinal epithelium [127]. Interleukin 10 (IL10) deficient mice display a colonic phenotype, serving as a genetically driven experimental model for colitis [128]. In addition to mouse models of colitis, several genetically altered mouse models develop inflammation in the ileum (ileitis) by influencing the epithelial homeostasis. XIAP$^{-/-}$ [129], Caspase8$^{\Delta IEC}$ [130], Atg16l1$^{\Delta IEC}$, Xbp1$^{\Delta IEC}$ and Atg16l1; Xbp1$^{\Delta IEC}$ [131] mice are examples of models that develop inflammatory lesions in terminal ileum. Samp1/Yit mice [132] and TNF$^{\Delta ARE}$ mice [12] are additional examples of mouse models representing CD-like ileitis. The spontaneous inflammation in Samp/Yit mice occurs without any genetic, chemical or immunological modification [132], yet TNF$^{\Delta ARE}$ mice are genetically manipulated to systemically overexpress *Tnf* [133].

Tumor necrosis factor (*Tnf*) is a pro-inflammatory cytokine, playing a role in cell survival and cell death by activating nuclear factor kappa-light-chain-enhancer of activated B cells (NFκB) signaling and apoptotic (caspase-dependent) as well as necroptotic (caspase-independent) pathways. Additionally, TNF signaling controls inflammatory processes and cell proliferation, playing a critical role in the pathogenesis of IBD. In this context, transmural inflammation in CD patients is associated with

increased expression of pro-inflammatory cytokines, including *TNF* [134]. Binding of *Tnf* to its receptors (TNFR1, TNFR2) guide the following process into cell survival, inflammatory/non-inflammatory cell death or apoptosis [135].

The deletion of Adenosine-Uracil (AU)-rich regulatory elements (ARE) from TNF mRNA transcripts causes an increased mRNA stability, which leads to an induced translation and a TnfR1-dependent spontaneous phenotype [136]. A dysregulated *Tnf* expression in $TNF^{\Delta ARE}$ mice activates mesenchymal cells before immune effector cell recruitment [137]. This process is sufficient to induce an ileal pathology that represents characteristics of human CD [137]. In line with intestinal bacterial dysbiosis, $TNF^{\Delta ARE}$ mice develop different grades of inflammation. Additionally, intestinal inflammation in $TNF^{\Delta ARE}$ mice leads to loss of lysozyme positive PCs [12]. Perturbed PCs were additionally observed upon deletion of X-ligand inhibitor of apoptosis protein (XIAP) in mice [129]. Therefore, mouse models for CD-like ileitis can be helpful in studying the impact of inflammation on stem cell niche.

2. Study Objective

Reduced PC numbers and impaired PC function are characteristics of CD. PCs secrete antimicrobial peptides involved in the mucosal defense and support the maintenance of neighboring *Lgr5*$^{+}$ ISCs, a cell-type that is important for epithelial renewal and quick turnover. Therefore, altered PC function might impact epithelial stemness. Mitochondrial function also regulates intestinal epithelial proliferation and stemness, indicating the involvement of mitochondria in the intestinal epithelial homeostasis. Activated UPR and impaired mitochondrial function, including defects in mitochondrial respiration and metabolism, have been observed in IBD. Based on the critical role of the intestinal epithelium in IBD, we characterized the association between mitochondrial dysfunction in the ISC niche and inflammation. The use of tissue samples from inflamed CD patients, and CD-like TNF$^{\Delta ARE}$ mice helped us to characterize the link between inflammation and ISC niche function. Tissue samples from a mouse model for mitochondrial dysfunction (Hsp60$^{\Delta/\Delta ISC}$) made it possible to identify the impact of imbalances in mitochondrial proteostasis on ISC niche. Since altered mitochondrial metabolism and energy-deficiency is one feature of IBD [90], the use of intestinal organoid culture helped us to understand the impact of altered mitochondrial metabolism or a metabolic shift towards mitochondrial respiration on the ISC niche.

3. Materials and Methods

3.1 Animal experiments

3.1.1 Ethics statement

All animal experiments were approved by the Committee of the Upper Bavaria for Animal Health Care and Use (Regierung von Oberbayern; TVA 55.2-1-54-2532-214-2013, TVA 55.2-1-54-2532-12-12, TVA 55.2-1-54-2532-217-2014 and TVA 55.2-1-54-2532-104-2017 and they were performed in strict agreement with the EEC recommendations for the care and use of Lab. Anim. (European Communities Council Directive of 24 November 1986 (86/609/EEC)). The use of surgically resected CD patient samples was approved by AFFSAPS (IDRCB: 2009-A00205-52), the French Ethic Committee- Hôpital Saint-Louis (CPP 2009/17) and declared to clinicaltrials.gov (NCT03458195). All patients provided an informed written consent. For generation of the human organoids, surgically resected human tissue samples were approved by the Ethics Committee of the Medical Faculty of TUM and obtained after prior informed written consent.

3.1.2 Mouse models

Mice with *Hsp60* deletion in the intestinal epithelial cells and/or in the intestinal stem cells serve as models for mitochondrial dysfunction. *Hsp60*$^{flox/flox}$ mice were crossed with several Cre transgenic mice to generate cell-specific knockout mouse models as described previously [62]. Briefly, the stem cell-specific *Hsp60* knockout (*Hsp60*$^{\Delta/\Delta ISC}$) mouse model was generated by crossing of *Hsp60*$^{flox/flox}$ mice with Cre transgenic *Lgr5*CreER^{T2}; IRES-*Egfp*^{Tg} mice (C57Bl/6J). *Lgr5*CreER^{T2}; IRES-*Egfp*^{Tg} mice (C57Bl/6J) were purchased from Jackson lab (Bar Harbor, ME). To generate intestinal epithelial cell-specific *Hsp60* knockout mice (*Hsp60*$^{\Delta/\Delta IEC}$), *Hsp60*$^{flox/flox}$ mice were bred with Cre transgenic *Villin*CreER$^{T2\text{-}Tg}$ mice (C57Bl/6N). *Villin*CreER$^{T2\text{-}Tg}$ mice (C57Bl/6N) were provided by Klaus-Peter Janssen (Klinikum Rechts der Isar, TU München). Additionally, entire body C/EBP homologous protein knockout (*Chop*$^{-/-}$) mice were purchased from Jackson lab (Bar Harbor, ME). All mice were kept in SPF conditions and were bred for several generations in our animal facility to harmonize the intestinal microbiota. TNF$^{\Delta ARE}$ mice served as a model for CD-like ileitis. TNF$^{\Delta ARE}$ mice and their WT control littermates were provided by Case Western University in Cleveland and were housed under SPF condition (12h light/ dark cycles, 24-26˚C). They were bred for several generations in our animal facility to harmonize the intestinal microbiota and were sacrificed at the age of 18 weeks. All mice received an ad libitum standard diet (autoclaved V1124-300; Ssniff, Soest, Germany) and autoclaved water and were sacrificed by CO_2.

3.1.3 Generation of the ClpP mouse model

Similar to IEC or ISC specific Hsp60 deficient mice, mice with *ClpP* deletion in IECs serve as a model for mitochondrial dysfunction. Generation of conditional *ClpP* knockout mice was performed by Taconic-Artemis in close consultation with our laboratory. The basic targeting vector was recloned from mouse fragments of the genomic *ClpP* locus, which were subcloned using the RPCIB-731 BAC library via ET recombination, by insertion of the the FRT (Neomycin resistance cassette; NeoR) and F3 (Puromycin resistance cassette; PuroR) into the intron 2 and 5 respectively. A thymidine kinase (TK) cassette was placed downstream of the 3' UTR. Exons 3-5 were flanked by LoxP sites. The conditional knockout allele was generated after the Flp recombination and removal of the NeoR and PuroR positive selection markers from the targeted allele. Finally, tissue specific (IEC specific) knockout mice were generated by crossing of $ClpP^{flox/flox}$ mice with $VillinCre^{Tg}$ mice ($ClpP^{IEC-/-}$) that resulted in the deletion of exons 3-5. This deletion led to a loss of function of the ClpP protein function by generating a frameshift from exon 2 to 6.

3.1.4 Induction of postnatal recombination

For conditional *Hsp60* deletion, male $Hsp60^{flox/flox}$; *Lgr5*$CreER^{T2}$ $Egfp^{Tg}$ mice, male $Hsp60^{flox/flox}$; *Villin*$CreER^{T2\text{-}Tg}$ mice and their appropriate controls were fed with phytoestrogen free pellets (Ssniff, Soest, Germany) for 4 weeks starting from the 6 weeks of age. At age of 10 weeks, they received 400 mg tamoxifen citrate (Tamoxifen) per kg chow pellets (LASvendi, Soest, Germany) and were fed *ad libitum* for 7 days. Monitoring of the body weight was performed on a weekly basis, before and after oral administration of tamoxifen. During tamoxifen treatment, the body weight was monitored on a daily basis. Body weight, general condition, behavior and intestinal symptoms were assessed using a score between 0 and 10 according to the approved application for animal experiments. Animals were sacrificed by CO_2 inhalation.

3.1.5 Dichloroacetate (DCA) treatment of mice

WT and non-inflamed $TNF^{\Delta ARE}$ mice were co-housed with segmented filamentous bacteria (SFB) mono-colonized SCID mice at the age of 4 weeks for 6 weeks to induce inflammation in the susceptible host ($TNF^{\Delta ARE}$). Concomitantly, mice were treated with DCA (300mg/l) in the drinking water. Control mice from the same genotype received normal drinking water.

3.1.6 Complement 3 (C3) ELISA

C3 levels were measured by mouse C3 ELISA kit (BIOZOL, Eching, Germany) in feces of the $TNF^{\Delta ARE}$ and WT mice at week 3, 4, 5 and 6 during DCA treatment according to the manufacturer's instructions. Briefly, feces were weighed and dissolved in PBS. After centrifugation (5min; 500xg), the supernatant was collected and dissolved in 1x dilution buffer (1:25). Enzyme antibody diluted in 1x wash buffer (1:100) and added to the samples/ standards. The mixture incubated for 20 min. in dark. After incubation

with substrate solution, the reaction was stopped and the C3 concentration was measured at 450nm using a Thermo labsystem multiscan spectrometer.

3.1.7 Analysis of plasma amino-acid concentrations using LC-MS/MS

Concentration of citrulline was quantitatively measured using targeted LC-MS/MS by Pieter Giesbertz based on the method described by Harder *et al*. [138]. Briefly, 10µl plasma samples were dissolved in 500µl ice-cold methanol containing d2-citrulline as part of the ChromSystems 57004 internal standard mixture (ChromSystems, Gräfelfing, Germany). 400µL of supernatant was collected and dried after 10 min centrifugation (10°C, 3600xg). Amino acids were derivatized to their butyl esters as described by Gucciardi *et al*. [139]. Briefly, a mixture of 95% n-butanol and 5% acetylchloride (v/v) was added to the dried samples. Subsequently, the samples were incubated at 60°C for 15 minutes at 600 rpm (Eppendorf Thermomixer Comfort; Eppendorf, Hamburg, Germany). The samples were dried and reconstituted in a 300µl mixture of methanol/water/formic acid (70/30/0.1% v/v).

The analysis was performed on a triple quadrupole QTRAP 5500 LC-MS/MS system operating in positive ESI mode (AB Sciex, Framingham, MA) equipped with a 1200 series binary pump (Agilent, Santa Clara, CA) and coupled to an HTC pal autosampler (CTC Analytics, Zwingen, Switzerland). Chromatographic separation was achieved using a Zorbax Eclipse XDB-C18 column (length 150 mm, internal diameter 3.0 mm, particle size 3.5 µm; Agilent). The measurement was performed in scheduled multiple reaction monitoring (MRM). For absolute quantification, a 10-point calibration of concentrations between 1 µM and 500 µM was generated. Data analysis was done using Analyst 1.7® software (AB Sciex).

3.1.8 Transmission electron microscopy (TEM)

For TEM analysis, 0.5cm cross sections of freshly dissected ileal samples were fixed in 2.5% electron microscopy grade glutaraldehyde in 0.1 M sodium cacodylate buffer pH 7.4 (Science Services, Munich, Germany). Afterwards, they were fixed in 2% aqueous osmium tetraoxide (Dalton, 1955), dehydrated in gradual 30–100% ethanol and propylene oxide and embedded in Epon (Merck, Darmstadt, Germany). Samples were kept for 24 hours at 60°C. Tissues were cut in semi-thin sections and stained with toluidine blue. Ultrathin sections of 50 nm were mounted on 200 mesh copper grids, contrasted with uranyl acetate and lead citrate before examination by transmission electron microscopy (Zeiss Libra 120 Plus, Carl Zeiss NTS GmbH, Oberkochen, Germany). Pictures were acquired at 1260-12500x magnification, using a Slow Scan CCD-camera and iTEM software (Olympus Soft Imaging Solutions, Münster, Germany). TEM was performed by Andreas Blutke.

3.2 Histological methods

3.2.1 Mouse Tissue processing

Small intestinal and Colonic tissues were removed immediately after killing of mice. The adjacent fat tissue was trimmed. Each part of the intestine was cut open longitudinally, the stool was cleaned away and the tissue was prepared as a 'Swiss role'. To obtain cross sections, 5mm of the desired segment of the intestine was cut. For histological purposes, formalin-fixed paraffin embedded (FFPE) tissues were prepared. Briefly, tissues were fixed in 4% PBS buffered formaldehyde, dehydrated (Leica TP1020; **Table 1**) and embedded in paraffin (FFPE; VWR, Ismaning, Germany; Leica EG1150C).

Table 1 Dehydration procedure for paraffin embedding of the formalin-fixed tissue sections

Step	Reagent	Time	Step	Reagent	Time
1	70% Ethanol	60 min.	**7**	100% Ethanol	60 min.
2	70% Ethanol	60 min.	**8**	100% Ethanol	60 min.
3	80% Ethanol	60 min.	**9**	Xylene	60 min.
4	96% Ethanol	60 min.	**10**	Xylene	60 min.
5	96% Ethanol	60 min.	**11**	Paraffin	90 min.
6	100% Ethanol	60 min.	**12**	Paraffin	90 min.

3.2.2 Tissue samples from CD-patients

Ileal tissue samples from CD patients were collected from a prospective multicenter study performed by the REMIND group [116]. The recruitment period was from September 2010 to December 2016. Patients of the age >18 years, having signs of ileal or ileocolonic CD and at risk for CD-related intestinal surgery (ileocolonic resection) were included in the study.

Table *2* illustrates the patient's characteristics at the time of surgery. From this cohort, FFPE samples from ileal margins of 70 patients were selected for histological analysis and further Paneth cells/ ISC characterization [140, 141]. For histopathological assessments, 3µm thick FFPE ileal tissue sections were cut and stained with hematein eosin saffron (HES). Each section was analyzed by two pathologists in a blinded manner to the baseline detailed clinical data and to the postoperative outcomes of the patients. Ileal margins with mucosal erosion, ulceration or cryptic abscess/cryptitis were categorized as inflamed. For PC and ISC characterization, lysozyme staining and LGR5 in situ hybridization was performed.

Information related to the smoking status and the genetic background of patients were collected at time of surgery (baseline). Endoscopy was performed 6 months after surgery and the tissue pathology for each patient was evaluated according to Rutgeerts score. Endoscopic recurrence was defined as a Rutgeerts score ≥ i2, whereas margins with Rutgeerts score of i0 and i1 were considered as non-inflamed. Ileal tissue samples from patients and the information about their genetic background and the smoking status were provided by Matthieu Allez (Saint Louis Hospital, Paris, France).

Table 2 Characteristics of patients at the time of surgery

Total number of patients included	n=70
Men	28 (40%)
Median age (y, IQR)	31.7 (26.4-44.0)
Age at Crohn's Disease diagnosis (Montreal classification)	
≤16 years (A1)	5 (7%)
17 - 40 years (A2)	56 (80%)
>40 years (A3)	9 (13%)
Median disease duration (y, IQR)	6.7 (1.8-12.5)
Median time between resection and colonoscopy (mo, IQR)	6.7 (6.1-8.4)
Smoking	
Active smoker	23 (33%)
Smoking cessation at surgery	6 (9%)
Non-smoker	41 (58%)
Previous intestinal resection	13 (19%)
Number of previous resection(s)	
0	57 (82%)
1	7 (10%)
2	3 (4%)
3	3 (4%)
Surgical indication	
Stricturing complication	47 (67%)
Penetrating complication	22 (31%)
Failure of drug therapy	1 (2%)
Anoperineal lesion	13 (19%)
Extra-digestive symptoms	
Joint manifestations	18 (26%)
Skin manifestations	6 (9%)
Eye manifestations	2 (3%)
Previous exposure to anti-TNF therapy	42 (60%)
Anti-TNF therapy within 3 months before surgery	29 (41%)
Previous exposure to thiopurines	53 (76%)
Thiopurines within 3 months before surgery	20 (29%)
Ileal resection margin inflamed	20 (29%)

3.2.3 Histology and tissue staining

3.2.3.1 H&E staining

For H&E staining, FFPE sections were cut (2.5µm; Leica RM2255) and deparaffinized (**Table 3**). H&E staining was performed using hematoxylin Mayer (Medite, Burgdorf, Germany), bluing reagent (Fisher, Dreieich, Germany) and 0.2% eosin (Medite, Burgdorf, Germany) in an automated staining machine (Leica ST5020, Soest, Germany).

Table 3 Deparaffinization and H&E staining

Deparaffinization		
Step	**Reagent**	**Time**
1	Xylene	5 min.
2	Xylene	5 min.
3	100% Ethanol	5 min.
4	100% Ethanol	5 min.
5	96% Ethanol	2 min.
6	96% Ethanol	2 min.
7	70% Ethanol	2 min.
8	70% Ethanol	2 min.
9	dH_2O	1 min.
H&E staining		
1	Hematoxylin	2 min.
2	TH_2O	15 sec.
3	Bluing reagent	30 sec.
4	dH_2O	30sec.
5	96% Ethanol	30 sec.
6	Eosin	2 min.
7	96% Ethanol	30 sec.
8	96% Ethanol	30sec.
9	100% Ethanol	30 sec.
10	100% Ethanol	30sec.
11	Xylene	1.5 min.
12	Xylene	1.5 min.

3.2.3.2 Histopathological analysis

For histopathological evaluation, the ileal tissue sections were cut (2.5µm; Leica RM2255) and H&E staining was performed. Sections were blindly scored (by Sigrid Kisling and Silvia Pitariu) by assessing immune cell infiltration in the LP, GC depletion, crypt hyperplasia, villi shortening, thickening of the muscle layer and the ulcer formation resulting in a score from 0 (not inflamed) to 12 (highly inflamed) as described previously [142].

3.2.3.3 Immunohistochemical staining

Immunohistochemistry (IHC) and Immunofluorescence (IF) stainings were performed on 1.5-4µm FFPE tissue sections. The sections were deparaffinized, followed by antigen-retrieval using 10mM citrate buffer (pH=6; 23 min.; 900 watt), tris-EDTA buffer (pH=9; 20 min.; 900 watt) or proteinase K in TE buffer (20µg/ml; pH=8; 16 min at 37˚C) (**Table 4**). In the case of ClpP staining, antigen-retrieval was performed using tris-EDTA buffer. For detection of apoptosis, proteinase K antigen-retrieval was used. All other stainings were performed using aforementioned citrate buffer. The adjustment of pH for antigen retrieval was performed using HCl 6M (Diagonal, Münster, Germany).

Table 4 Buffers and solutions, used for IF / IHC stainings

Buffers & Solutions	Preparation
10mM Citrate buffer	2.94g sodium citrate tribasic dehydrate (Sigma- Aldrich, Taufkirchen, Germany) dH2O up to 1L pH=6
Tris EDTA buffer	1.21g Tris Base (Sigma- Aldrich, Taufkirchen, Germany) 2ml Ethylenediamine tetraaceticacid (EDTA; Fisher, Dreieich, Germany) dH2O up to 1L pH = 9
TE buffer	0.305 g Tris Base (Sigma- Aldrich, Taufkirchen, Germany) 100µl EDTA 500 mM (Fisher, Dreieich, Germany) 50 ml dH2O 250 µl Triton- X100 pH = 8
Phosphate buffered saline (10x PBS)	20 Tablets of PBS (Life Technologies, Carlsbad, CA) dH2O up to 1L
Blocking buffer	2.5ml 10xPBS 1.25ml serum of the same species as the secondary antibody 21.25ml dH2O 75µl Triton X-100 (100%) (Sigma- Aldrich, Taufkirchen, Germany)
Antibody dilution buffer	4ml 10xPBS 36ml dH2O 0.4g BSA 120µl Triton X-100 (100%)(Sigma- Aldrich, Taufkirchen, Germany)

For IHC staining, endogenous peroxides were blocked for 10 min with 3% H_2O_2 (Sigma- Aldrich, Taufkirchen, Germany). Sections were blocked (1h; Room temperature) with the appropriate blocking buffer (**Table 4**) according to the species from which the secondary antibody was derived, and were incubated overnight with the primary antibody. Antibodies and concentrations used are given in **Table 5**. Subsequently, sections were washed with phosphate buffered saline (1x PBS) (**Table 4**) and were incubated with the secondary antibody (1h; Room temperature) (**Table 5**). In the case of IF staining, Dapi (Sigma- Aldrich, Taufkirchen, Germany) was used for nuclei staining, and was added to the

secondary antibody solution. Sections were mounted with Aquatex (water based mounting medium; Merck KGaA, Darmstadt, Germany) and signal visualization was performed via a Fluoview FV10i microscope (Olympus, Shinjuku, Japan).

Table 5 Primary and secondary antibodies, used for IF / IHC stainings

Primary antibodies	**Species**	**Company**	**Dilution**
Anti-CC3	Rabbit	Cell signaling Technology, Danvers, MA	1:100
Anti-Chromogranin A	Rabbit	Abcam, Cambridge, UK	1:100
Anti-Chromogranin A	Goat	Santa Cruz Biotechnology, Santa Cruz, CA	1:100
Anti ClpP	Mouse	Santa Cruz Biotechnology, Santa Cruz, CA	1:200
Anti-Dclk1	Rabbit	Biomol, Hamburg, Germany	1:100
Anti-Defensin 4	Rabbit	Abcam, Cambridge, UK	1:100
Anti-E-cadherin	Mouse	Abcam, Cambridge, UK	1:300
Anti-GFP (XP)	Rabbit	Cell signaling Technology, Danvers, MA	1:200
Anti-Hsp60	Goat	Santa Cruz Biotechnology, Santa Cruz, CA	1:200
Anti-Ki67	Rabbit	Cell signaling Technology, Danvers, MA	1:400
Anti-Lysozyme	Rabbit	Dako, Agilent, Santa Clara	1:1000
Anti-MAP LC3α/ß	Goat	Santa Cruz Biotechnology, Santa Cruz, CA	1:200
Anti MMP7	Rabbit	Cell signaling Technology, Danvers, MA	1:100
Anti-Muc2	Rabbit	Bio-Techne GmbH, Novus, Wiesbaden, Germany	1:100
Anti-Pkr (M-515)	Rabbit	Santa Cruz Biotechnology, Santa Cruz, CA	1:100
Secondary antibodies		**Company**	**Dilution**
HRP conjugated mouse anti goat IgG		Dianova, Hamburg, Germany	1:300
HRP conjugated donkey anti rabbit IgG		Dianova, Hamburg, Germany	1:300
Alexa Fluor donkey anti goat 488		Life Technologies, Carlsbad, CA	1:200
Alexa Fluor donkey anti rabbit 546		Life Technologies, Carlsbad, CA	1:200
Alexa Fluor donkey anti mouse 647		Life Technologies, Carlsbad, CA	1:200
Dapi		Sigma- Aldrich, Taufkirchen, Germany	1:1000
UEA1 Rhodamin		Vector laboratories, Burlingame, CA	1:1000

In the case of IHC staining, antigen detection was performed by DAB/metal concentrate (10x) (Fisher, Dreieich, Germany) with 1:10 dilution in stable peroxide substrate buffer (1x) (Fisher, Dreieich, Germany). Nuclei were counterstained with hematoxylin. The tissue sections were dehydrated and mounted with DPX new (xylene based mounting medium; Merck KGaA, Darmstadt, Germany). Slides were scanned and further analyzed via a PreciPoint M8 microscope (Precipoint, Freising, Germany). For both IF and IHC stainings, antibodies were dissolved in antibody dilution buffer (**Table 4**).

For IHC co-staining, sections were incubated for 20 min with 3% H_2O_2 (Sigma- Aldrich, Taufkirchen, Germany), before counterstaining with hematoxylin, to inactivate antibody-bound HRPs. Subsequently, sections were blocked and were stained with the second primary antibody. The standard protocol was further used for the rest of the staining procedure. Finally, the second antigen detection was performed with the HRP green solution set (42 Life sciences GmbH, Bremerhaven, Germany). Sections were counterstained with hematoxylin and mounted with xylene based mounting medium. Slides were scanned and further analyzed with a PreciPoint M8 microscope (Precipoint, Freising, Germany).

3.2.3.4 Detection of apoptosis

For detection of apoptosis via TUNEL assay (terminal deoxynucleotidyl transferase-mediated dUTP nick end labeling), Apo-BrdU *in situ* fragmentation kit (BioVision, Milpitas, CA) was used according to the manufacturer's instructions. Briefly, FFPE tissue sections were cut into 4µm thickness, were deparaffinized and rehydrated. After incubation in Natrium chloride (NaCl 0.85%; 5min), they were washed and fixed with 4% formaldehyde for 15 min. Antigen-retrieval was performed using 20µg/ml proteinase K (5min; Roth, Karlsruhe, Germany) in TE buffer (**Table 4**). The sections were incubated with DNA labeling solution for 60 min at 37°C (BioVision, Milpitas, CA). Subsequently, antibody solution (BioVision, Milpitas, CA) was added to the sections and they were incubated for 30 min at room temperature. After washing, DNA staining was followed by an IF staining as described in section 3.2.3.3. Positive controls were treated with 1:10 rDNaseI (Macherey-Nagel, Düren, Germany) and incubated at 37°C for 15 min. Dapi (Sigma- Aldrich, Taufkirchen, Germany) was used to stain the nuclei and signal visualization was performed via a Fluoview FV10i microscope (Olympus, Shinjuku, Japan).

3.2.3.5 Alcian blue / Periodicacid-Schiff (AB/PAS) staining

AB-PAS staining was performed to visualize the presence of acidic and the neutral mucus in goblet cells. FFPE tissue sections were deparaffinized, rehydrated and stained with alcian blue (Fisher, Dreieich, Germany) for detection of acidic mucus (1% v/v in 3% acetic acid, 5min, pH=2.5). Sections were treated with periodic acid (1% v/v, 10min) and were co-stained with Schiff's reagent (Sigma-Aldrich, Taufkirchen, Germany) for monitoring neutral mucus (15min; In dark). Nuclei were counterstained with hematoxylin, and tissue sections were dehydrated and mounted with DPX new (Merck KGaA, Darmstadt, Germany). Slides were scanned and further analyzed using a PreciPoint M8 microscope (Precipoint, Freising, Germany).

3.2.4 *In situ* hybridization

In situ hybridization for murine *Lgr5*, *Olfm4* and *HopX* as well as human *LGR5*, were performed using the RNAscope-2.5 HD *in situ* assay Kit-Brown (ACD, Bio-Techne GmbH, Wiesbaden, Germany) based on the manufacturer's instructions. Briefly, 5µm thick FFPE sections were cut., the endogenous peroxides were blocked with H_2O_2 for 10 min and antigen-retrieval was performed using the provided retrieval buffer 1:10 in dH_2O. Sections were treated with Protease plus for 30 min at 40°C, washed and

incubated with desired probes (RNAscope Probe-Mm-*Lgr5*; RNAscope Probe-Mm-*Olfm4*; RNAscope Probe-Mm-*Hopx*; RNAscope Probe-Hs-*LGR5*) for 2h at 40°C. Tissue specimens were washed and signal amplifications was achieved by 6 amplification steps. Signal detection was performed using DAB solution for 10 min. Sections were counterstained with hematoxylin, dipped in ammonium hydroxide solution (0.02% v/v) and were mounted with xylene based mounting medium. Slides were scanned and further analyzed via a PreciPoint M8 microscope.

In the case of IHC co-staining, samples were incubated with 3% H_2O_2 (Sigma- Aldrich, Taufkirchen, Germany) for 20min after completing the *in situ* hybridization protocol. Slides were washed, followed by IHC staining as described in section 3.2.3.3. Finally, detection of IHC-related antigens was performed using the HRP green solution set (42 Life sciences GmbH, Bremerhaven, Germany). Sections were counterstained with hematoxylin and were mounted with xylene based mounting medium. Slides were scanned and further analyzed with a PreciPoint M8 microscope (Precipoint, Freising, Germany).

3.3 Molecular methods

3.3.1 Genotyping

To determine the presence of the *ClpP* knockout allele in the murine intestine, DNA was extracted using the NucleoSpin RNAII kit (Macherey-Nagel, Düren, Germany) from small intestinal tissue samples of constitutive ClpP knockout mice as well as organaoids at different time-points after induction of the knockout according to the manufacturer's instructions. For DNA PCR, 100ng DNA was dissolved in 10µL ddH_2O. 1µL DNA was mixed with 10µl 2x Onetaq DNA polymerase (NEB) and the necessary quantity and combination of primers, designed for detection of the WT and the knockout allele (**Table 6**). The final volume was adjusted to 20 µl with PCR water. The PCR program is defined in **Table 6**.

Table 6 Primer combinations and the PCR program settings for genotyping

Primer (nM)	**Sequence**	**Product size [bp]**	**Program**	**Temp. (°C)/ Time (Sec)**
2139 (200)	tccatcgtcctgccatagc	WT: 337 KO: 250	Initial Denaturation	94/60
			Denaturation	94/20
2140 (200)	ccctgggtttaagcactgc		Annealing	60/20
			Extension	68/30
2142 (200)	tgtcattctctagcccagtcg		Final extension	68/60
			Cooling	10/stop

3.3.2 Isolation of intestinal epithelial cells (IECs)

Primary IECs were purified as described previously [62]. Briefly, approximately 6 cm of the small intestine (jejunum/ ileum) was cut, inverted and transferred to 20 mL Dulbecco's modified Eagle's medium (DMEM; Gibbco, Cincinnati, OH) containing 10% fetal calf serum (FCS superior, Biochrom, Berlin), 1.0% Glutamine and 0.8% antibiotics/antimycotics (all Sigma- Aldrich, Taufkirchen, Germany). 1µM dithiothreitol (DTT; Roth, Karlsruhe, Germany) was added and the tissue was vortexed vigorously before incubation for 15 min at 37 °C, while shaking at maximum speed in a thermos shaker. Afterwards, the tissue was transferred into a falcon tube containing 20ml PBS (Sigma- Aldrich, Taufkirchen, Germany) and 1.5 mM EDTA (Fisher, Dreieich, Germany) and was incubated for 10 min at 37 °C. Cell suspensions from DMEM and PBS were centrifuged for 7 min, 300xg at 4°C. Finally, primary IECs were isolated by centrifugation through a 20% and 40% percoll gradient (GE Healthcare, Uppsala, Sweden) at 600xg for 30 min. Cells were obtained from the interface between the two percoll layers and were washed with cold PBS. Isolated IECs were lysed in 350-500µl RA1 buffer (Macherey-Nagel, Düren, Germany) and were further processed for RNA isolation.

3.3.3 Isolation of primary crypts

Small intestinal primary crypt isolates were obtained from mouse (jejunum and ileum) as described previously [62]. Briefly, approximately 6 cm of the small intestine was cut, inverted and incubated in 2mM EDTA (Fisher, Dreieich, Germany) for 30 min at 4°C. After four steps of shaking and fractioning in cold PBS (Sigma- Aldrich, Taufkirchen, Germany), the tissue debris was removed. The first fraction, considered as villus fraction, was centrifuged, the pellet was washed in cold PBS and was kept for further analysis. Second and third fractions were pooled and passed through a 70µm cell strainer for separation of crypts. The filtrated crypt fraction was centrifuged for 5 min at 300xg. The pellet was washed in cold PBS and was either used for organoid culture or dissolved in RA1 buffer (Macherey-Nagel, Düren, Germany) for subsequent RNA isolation.

3.3.4 Gene expression analysis

RNA of a total tissue (jejunum/ ileum/ colon), IECs, primary crypts/ villi and small intestinal organoids was isolated according to the manufacturer's instructions (NucleoSpin RNAII kit, Macherey-Nagel, Düren, Germany). Finally, RNA was eluted in 60µl (in the case of tissue, IECs and primary crypts) and 40µl (in the case of organoids) RNase free water (Macherey-Nagel, Düren, Germany). The concentration of isolated RNA was measured with a Nanodrop ND-1000 spectrophotometer. In the case of low RNA concentration, it was concentrated according to the manufactures instruction using the RNeasy MinElute Cleanup Kit (Qiagen, Hilden, Germany).

A total amount of 250ng RNA (for tissue, IEC and primary crypts), 200ng RNA (for organoids) and MMLV reverse transcriptase with point mutation (Promega, Mannheim, Germany) were used for reverse transcription. Quantitative Real-time PCR (qRT-PCR) was performed using the Universal Probe

Library System (Roche, Mannheim, Germany) and 1µl cDNA according to the manufacturer's instructions in a light-cycler 480 (Roche). Relative changes of mRNA expression for genes of interest were calculated based on Ct values, given by the light cycler 480 software. Expression was normalized to the expression of *Hprt* as housekeeper gene. In the case of human samples, *GAPDH* was used as a housekeeper. Data were calculated as a fold change over controls.

Table 7 Primer sequences, used for qRT-PCR analysis

Murine Target Gene	Forward Primer (L)	Reverse Primer (R)	Probe
Abcb10	cactgtggtcggggagaa	gctctggctattgcaatcct	29
Alpi	catctccaacatggacattga	ggttccagactggttactgtca	109
Ang4	ccccagttggaggaaagc	cgtaggaatttttcgtacctttca	106
Asns	actcaaggaggcccaagttc	gctcgcttccaatataatt	55
Atf4	atgatggcttggccagtg	ccattttctccaacatccaatc	88
Atf5	tttttatgaagaggaataagatgaggt	ggaggctgcaccaacaat	16
Atg12	cattgacttcatcaaaaagttcctt	ggcaaaggactgattcacataa	49
Bmi1	acgctaatggacattgcctac	caagttggccgaactctgtat	80
Cat	ccttcaagttggttaatgcaga	caagtttttgatgccctggt	34
ChgA	ggaggctgtggctacacaca	ccatccactgcctgagagtc	89
Chop	cgacagagccagaataacagc	aagggttagacggagccagt	91
Ckmt1	ggctggagctgggtctct	ttgtgctttcggaggtctg	17
CoxI	cagaccgcaacctaaacaca	Ttctgggtgcccaaagaat	25
CoxIV	tcactgcgctcgttctgat	cgatcgaaagtatgagggatg	7
Defa5	ttttgggacctgcagaaatc	tggttgttgaccatccttgtt	84
Dll4	aggtgccacttcggttacac	gggagagcaaatggctgata	106
Drp1	ctggatcacgggacaagg	gttgcctgttgttggttcct	77
Gapdh	gccaaaagggtcatcatctc	cacacccatcacaaacatgg	29
Grp78	ctgaggcgtatttgggaaag	tcatgacattcagtccagcaa	105
Hif1α	gcactagacaaagttcacctgaga	cgctatccacatcaaagcaa	95
Hopx	cttcaacaaggtcaacaagcac	aggcgctgcttaaaccatt	98
Hprt	tcctcctcagaccgctttt	cctggttcatcatcgctaatc	95
Hsp10	ggcccgagttcagagtcc	tgtcaaagagcggaagaaactt	77
Hsp60	tcttcaggttgtggcagtca	cccctcttctccaaacactg	1
HtrA2	tgatgctgaccctgactcc	gtgccaatttctccccaat	9
Ki67	gctgtcctcaagacaatcatca	ggcgttatcccaggagact	80
Map1lc3α	gaccagcaccccagtaagat	tgggaccagaaacttggtct	27
Ldha	gagcagtggaaggaggttca	aatggcccaggatgtgtaac	77
Lgr5	cttcactcggtgcagtgct	cagccagctaccaaataggtg	60
Lrig1	tgggcacattgaaagcaa	tgcctgcatgtagtgctatga	103
Lon	tggcgtcttcctaaagagagat	tcccgtatggtagatttcatcc	22
Lyz1	ggcaaaaccccaagatctaa	tctctcaccaccctctttgc	46
Mfn2	cgaggctctggattcacttc	caaccagccagctttattcc	21
Mmp7	taattggcttcgcaaggaga	aaggcatgacctagagtgttcc	94
mt-DNA seq (ChrM4)	caaatttacccgctactcaactc	gctataatttttcgtatttgtgtttgg	101
Muc2	ggcagtacaagaaccggagt	ggtctggcagtcctcgaa	66
Nix	tctcatgtgctggccttg	ggcttttcgtctccctcag	29
Nuclear DNA seq (Chr8)	tttacaggatctccaagattcaga	gatcaccccatgtgaacaaa	26

Pcna	ctagccatgggcgtgaac	gaatactagtgctaaggtgtctgcat	4
Prom1	cagcggcagaagcagaat	tggttagccacaaagccata	69
Olfm4	gaaattcgagagagagttttctaagg	gacctctactcggaccgtca	92
Otc	gctgtcatggtatccctgct	tttccttttgacaggcatca	99
Pgc1a	gagcgaaccttaagtgtggaa	tcttggttggctttatgagga	52
Prkaa2	cagagcaaagcgtgtgacat	ttcttcttactcgaagatggtatgc	41
Slc25a15	ccgtaaagtggttggattgg	agcagctgcattctgaaggt	40
Sod2	gacccattgcaaggaacaa	gtagtaagcgtgctcccacac	3
Tomm20	tccgaccattagtcagagaattg	ttggtatctggctcattccac	41
Trb3	gtcgctttgtcttcagcaact	tcatctgatccagtcatcacg	67
Human Target Gene	**Forward Primer (L)**	**Reverse Primer (R)**	**Probe**
CHOP	Cagagctggaacctgaggag	tgtttatggctgctttggtg	9
DLL1	gtggggagaaagtgtgcaa	tcacaaaatccatgctgctc	20
HIF1a	gaacctgatgctttaactttgct	tgctggtcatcagtttctgtg	28
HPRT1	tgatagatccattcctatgactgtaga	caagacattcttccagttaaagt	22
LGR5	accagactatgcctttggaaac	tcccagggagtggattctatt	78
LYZ	ccgctactggtgtaatgatgg	catcagcgatgttatcttgcag	68
OLFM4	gatcaaaacacccctgtcgt	gttcaccacaccaccatgac	52
PLA2G2A	aaatttctgagctacaagtttagcaac	ttatcacactcacacagttgacttct	32
PRKAA1	ctgatattttcatggtgatggaat	gacgccgactttctttttca	63

3.4 Organoid Experiments

3.4.1 Small intestinal organoid culture

Intestinal organoids were generated from mouse (jejunum and ileum) and human (ileum) small intestinal tissues as described previously [62, 143].

Table 8 Components and the concentrations of the crypt-culture medium

	Ingredient	Concentration	Company
Basic culture medium (BCM)	Advanced DMEM/ F12	97%	Gibco life technologies, Grand Island
	GlutaMax (2mM)	1%	Sigma- Aldrich, Taufkirchen, Germany
	Hepes (10mM)	1%	Sigma- Aldrich, Taufkirchen, Germany
	Antibiotics & Antimycotics (penicillin, streptomycin and amphotericin)	1%	Sigma- Aldrich, Taufkirchen, Germany
Crypt culture medium (CCM)	N2 Supplement	1x	Gibco life technologies, Grand Island
	B27 Supplement	1x	Gibco life technologies, Grand Island
	N-Acetylcystein	1mM	Sigma- Aldrich, Taufkirchen, Germany
	Recombinant murine EGF dissolved in 0.1% BSA/ PBS	50ng/ml	ImmunoTools GmbH, Friesoythe, Germany
	Murine Noggin dissolved in 0.1% BSA/PBS	100ng/ml	PeproTec, Rocky Hill, New Jersey
	Recombinant human R-spondin 1 dissolved in 0.1% BSA/PBS	0.5 µg/ml	PeproTec, Rocky Hill, New Jersey

Isolated primary crypts were (section 3.3.3) dissolved in matrigel (BD Biosciences, Franklin Lakes, NJ) and 25µl matrigel-organoid suspension was plated in a pre-warmed 48 well plate.

Organoids from WT, TNF$^{\Delta ARE}$, *Hsp60*$^{\Delta/\Delta ISC}$, *Hsp60*$^{\Delta/\Delta IEC}$ and *Hsp60*$^{flox/flox}$, *ClpP*$^{IEC-/-}$ (constitutive ClpP deficient organoids), *ClpP*$^{\Delta/\Delta IEC}$ (tamoxifen induced ClpP deficient organoids) and *Ctrl, Chop*$^{-/-}$ and *Ctrl* mice were cultivated and kept in crypt-culture medium (CCM) (**Table 8**). Organoids were passaged every 8-9 days and were embedded in fresh Matrigel. During experimental procedures, organoids were passaged 2 days prior to the start of the experiments. Human organoids were kindly provided by Tamara Zietek, cultivated in Human Intesticult medium (STEMCELL Technologies, Grenoble, France), and were transferred to CCM two days prior to the start of the experiment. *Ex vivo* inhibition of the

respiratory chain complex V and the complex I was performed with oligxomycin (Stock concentration: 2.5mM in DMSO; Final concentration: 2.5µM; Sigma- Aldrich, Taufkirchen, Germany) and Rotenone (Stock concentration: 1.26mM in DMSO; Final concentration: 1.5µM; Sigma- Aldrich, Taufkirchen, Germany), respectively. The final volume of each substance from the prepared stock was dissolved in CCM. 300µl CCM containing the final concentration of the substance was applied to each well of a 48 well plate. Organoids were sampled after 1h, 6h and 24h. Dichloroacetate (DCA; Stock concentration: 600mM in sterile water; Final concentration: 15mM; Sigma- Aldrich, Taufkirchen, Germany) was used to force the ATP generation via oxidative phosphorylation. The appropriate volume of DCA was dissolved in 300µl CCM to reach a 15mM concentration and was applied to the organoids for 24h and for 14 days. In the case of long-term treatment, DCA-containing media (15mM) was changed every 3 days. *Ex vivo* induction of *Hsp60* and *ClpP* knockout was achieved by adding 1.5µl of 100µM (Z)-4-hydroxytamoxifen (4-OHT; LKT, St Paul, MN) solution to the 300µl culture medium per well for 24h in darkness. Growth measurements were performed using an Olympus CK X 41 microscope and Olympus cellSens Entry software.

3.4.2 Measurement of living cells in organoids

Life-/ dead- cell protease activity was measured using the MultiTox-Fluor Cytotoxicity Assay (Promega, Mannheim, Germany) according to the manufacturer's instructions in 48 well plates. Fluorescent intensity (live- cell fluorescence 400_{EX}/ 500_{EM}; dead- cell fluorescence 485_{EX}/ 520_{EM}) was measured via a Tecan infinite M200 (Tecan Group Ltd., Männedorf, Switzerland) and the i-control™ Microplate Reader software (Tecan, Grödig, Austria).

3.4.3 Staining of organoids

Organoids were sampled by dissolving matrigel in cold PBS (Sigma- Aldrich, Taufkirchen, Germany) and centrifuged for 5 min at 300xg. PBS was removed, the pellet was dissolved gently in 4% formaldehyde, transferred onto a glass slide and was incubated for 15 min at room temperature. After washing with PBS, organoids were incubated with blocking buffer and stained according to the standard staining protocol described in section 3.2.3.3.

3.4.4 Measurement of ATP content in organoids

After measuring living cells, ATP content was measured using the CellTiter-Glo Luminescent Cell Viability Assay (Promega, Mannheim, Germany) according to the manufacturer's instructions in a 48 well plate. The CellTiter-Glo reagent was added to the organoid media at a 1:1 ratio and the plate was incubated for 30 min at room temperature. Luminescence was measured using a luminoscan Tecan infinite M200 (Tecan Group Ltd., Männedorf, Switzerland) and an integration time of 100 -1000ms and the i-control™ Microplate Reader software (Tecan, Grödig, Austria). Finally, ATP content was

calculated based on the number of living cells assessed by life cell protease activity and relative to non-treated controls.

3.4.5 ROS measurement of organoids

ROS (H_2O_2) levels were measured using the ROS-Glo-H_2O_2 Assay (Promega, Mannheim, Germany) according to the manufacturer's instructions in a 48 well plate. Briefly, 25µM H_2O_2 substrate was added to the organoid media. Plates were incubated for 6h at 37°C. Afterwards, ROS-Glo detection reagent was added to the organoid media at a 1:1 ratio and the plate was incubated for 20 min at room temperature. Luminescence was measured using a luminoscan Tecan infinite M200 (Tecan Group Ltd., Männedorf, Switzerland) and an integration time of 500ms and the i-control™ Microplate Reader software (Tecan, Grödig, Austria). Finally, the ROS levels were calculated based on the number of living cells assessed by life cell protease activity and relative to non-treated controls.

3.4.6 Measuring of apoptosis in organoids

Apoptosis was measured via the Apo-ONE Caspase 3/7 Assay (Promega, Mannheim, Germany) according to the manufacturer's instructions in a 48 well plate. Briefly, Organoids were seeded, grown and induced with 4-OHT. At the desired time-points after the end of tamoxifen treatment, Apo-ONE reagent was added to the organoid media at a 1:1 ratio and the plate was incubated for 6h at room temperature (in dark). Fluorescent intensity (499_{EX}/ 521_{EM}) was measured via a Tecan infinite M200 (Tecan Group Ltd., Männedorf, Switzerland) and the i-control™ Microplate Reader software (Tecan, Grödig, Austria).

3.5 Quantifications

All quantifications were performed in a blinded manner to histological scoring and genotypes.

3.5.1 Quantification of PCs

Total numbers of the LYZ^+/ Lyz^+ cells were quantified based on the IF lysozyme staining in small intestinal tissue sections. Analysis of PCs was performed in a minimum of 80 and 50 well-oriented small intestinal crypts in CD patients and mice, respectively. To assess numbers of LYZ^+/ Lyz^+ granules, a minimum of 150 PCs (ranges between 150 and 334 PCs) were quantified in patient biopsies. Cells containing ≥ 2 granules were considered as highly granular PCs. For mouse tissues, granularity was quantified in all PCs present in 50 well oriented crypts. To assess the number of LYZ^+ cells in upper crypts, signals arising from cells above the +7 position were quantified. All signals from cells in the ≤ +7 position were considered as crypt base signals. In organoids, the quantification of PCs and their granules were performed in 50 buds of 25 organoids.

3.5.2 Quantification of *LGR5*$^{+}$/ *Lgr5*$^{+}$ ISCs

LGR5^{+}/ *Lgr5*$^{+}$ transcripts were quantified based on *Lgr5/ LGR5 in situ* hybridization staining of small intestinal tissue sections. To determine *Lgr5*$^{+}$/ *LGR5*$^{+}$ crypts, the total number of crypt-based dots were quantified in 80 (for CD-patients) and 50 (for mice) well oriented small intestinal crypts. Each dot represents one transcript. Crypts with ≥ 15 *LGR5* transcripts (in CD patients) and ≥ 10 *Lgr5* transcripts (in mice) were considered as highly *LGR5/ Lgr5* expressing crypts. To assess *LGR5* expression in upper crypts, the total number of crypts with *LGR5* transcripts above +7 position were quantified. To determine the number of *Lgr5*$^{+}$cells in crypt bases, *Lgr5 in situ* hybridization and IHC co-staining for E-cadherin was performed to visualize the cell borders. For quantification of *Lgr5*$^{+}$ crypts, crypts with *Lgr5* expression were considered as positive crypts.

3.5.3 Quantification of Hsp60 and Pkr expression

The Volocity 2D-3D imaging software was used for the quantification of Hsp60 and Pkr proteins. For this purpose, 600x pictures were taken via a Fluoview FV10i microscope (Olympus, Shinjuku, Japan). A minimum of 30 well oriented intestinal crypts were quantified in inflamed and non-inflamed mouse tissues. For both cases, crypt base areas (up to the +7 cell position) were selected, and positive signals were quantified based on the best fitting threshold. The same threshold levels of signal intensity were used for quantification of all sections.

3.5.4 Quantification of *Olfm4*$^{+}$ ISCs and *Olfm4* / *HopX* expression

Determination of *Olfm4*$^{+}$ ISCs in TNF$^{\Delta ARE}$ mice was performed in 50 well oriented intestinal crypts in inflamed and non-inflamed mouse tissues. Cells above the +7 cell position were excluded from the quantification. For Hsp60$^{\Delta/\Delta ISC}$ mice, 100x images of *Olfm4* and *HopX in situ* hybridization were analyzed using the ImageJ software. In both cases, 30 well oriented intestinal crypts were selected. Due to the patchy pattern of *Olfm4* expression, the distance of the highest signal to the crypt base was measured. To avoid a bias due to differences in crypt length, distances were normalized to the total crypt length. In the case of *HopX*, the positive area was quantified within the total selected IEC area (up to the crypt-villus junction), based on the best-fitting threshold. Briefly, the intensity threshold that covered the entire positive signal in the selected crypt area was identified. The selected threshold remained unchanged for all samples over the entire quantification.

3.5.5 Quantification of Ki67 positive cells

To quantify the proliferation, IHC staining was performed for the proliferation marker Ki67. The number of positive cells were counted in a minimum of 25 small intestinal crypts (up to the crypt-villus junction) in TNF$^{\Delta ARE}$ mice.

3.5.6 Quantification of ChgA and PAS-AB positive cells

Numbers of EECs and GCs were counted based on IHC stainings for ChgA and Alcian blue/ Periodicacid-Schiff (AB/PAS), respectively. Quantification of $ChgA^+$ cells in the small intestine was performed in a minimum of 101 crypts and 57 villi in the entire Swiss-role. For PAS-AB quantification, the number of mucus-containing positive cells was quantified in a minimum of 100 crypts in small intestine.

3.5.7 Seeding efficiency, size and *de novo* crypt formation (budding) of organoids

Total numbers of $TNF^{\Delta ARE}$ and WT organoids (ranging between 80-140) were quantified at Day 1 (D1) after seeding in a minimum of 3biological replicates. At desired time-points (D3, D5, D8 and D14), numbers of living organoids were quantified in the same wells. In each case, the percentage of living organoids were calculated based on D1.

For *de novo* crypt formation, numbers of buds (0, 1, 2, 3, >4) were counted in all organoids in each well at the desired time-point in a minimum of 3 replicates. A minimum of 80 organoids (ranging between 80-140) was included in the analyses. Finally, percentages were calculated based on the total number of organoids in each well. The Area of organoids were measured using the ImageJ software.

3.6 Statistical analysis

Statistical analyses were performed using the GraphPad Prism software (GraphPad, La Jolla, CA) and applying unpaired t-tests or One-Way analysis of variances followed by Tukey tests. To determine differences in *de novo* crypt formation between experimental groups, a Mann-Whitney rank sum test was performed. Correlation analysis were performed by Pearson tests (a negative correlation coefficient (r) indicates inverse correlation). The Fisher-Exact test and the Chi-Square test was performed for determination of differences in the probability of recurrence of CD patients in remission. P-values bellow 0.05 were considered as statistically significant ($p<0.05$: *; $p<0.001$: **; $P<0.0001$: ***).

4. Results

4.1 CD-like inflammation correlates with reduced Paneth cell function and *Lgr5* expression in mice

4.1.1 Inflammation in TNF$^{\Delta ARE}$ mice correlates with reduced PC function

TNF$^{\Delta ARE}$ mice develop a gradual inflammation in the ileum and inflammation in these mice is associated with reduced Paneth cell (PC) function, which is assessed by lysozyme expression [12]. Lysozyme is an antimicrobial peptide and the pattern of lysozyme expression in PC granules indicates PC abnormalities [28]. To characterize the PC phenotype at different stages of inflammation, we used TNF$^{\Delta ARE}$ mice and characterized PCs in tissue sections, depicting a broad range of histopathology. The histopathological score (HS) was further assessed for tissue pathology. Ileal tissue sections from WT and TNF$^{\Delta ARE}$ mice with no (HS=0), mild (HS<4), and severe (HS≥4) inflammation were stained for lysozyme, as a marker for PCs (**Figure 6A**). Minor crypt loss was observed in the presence of inflammation in these mice (**Figure 6B**). PCs in TNF$^{\Delta ARE}$ mice were subcategorized into highly granular (≥2 Lyz$^+$ cytoplasmic granules) and lowly granular (<2 Lyz$^+$ cytoplasmic granules or diffuse cytoplasmic Lyz staining) cell types based on the immunofluorescent staining for lysozyme. The total number of Lyz$^+$ cells per crypt and the percentage of highly granular PCs were determined, which inversely correlated with tissue pathology, indicating PC dysfunction in response to inflammation (**Figure 6C,D**). Additionally, gene expression analysis in intestinal epithelial cells (IECs) showed reduced *Lyz1* expression in inflamed TNF$^{\Delta ARE}$ mice (**Figure 6E**).

Comparing ileal tissues from non-inflamed TNF$^{\Delta ARE}$ mice and their WT littermates, we observed no differences in total crypt numbers (**Figure 6F**). Although no changes were observed in total numbers of Lyz$^+$ cells, the percentage of highly granular PCs (≥2 Lyz$^+$ cytoplasmic granules) was mildly reduced in non-inflamed TNF$^{\Delta ARE}$ mice (**Figure 6G**). Jejunal tissue characterization depicted a minor crypt loss in inflamed TNF$^{\Delta ARE}$ mice, indicating that ileal inflammation can influence the epithelial architecture of the intestine even in non-inflamed segments (**Figure 6H**). We observed no differences in total numbers of Lyz$^+$ cells and highly granular PCs in jejunum between WT and inflamed TNF$^{\Delta ARE}$ mice (**Figure 6I,J**).

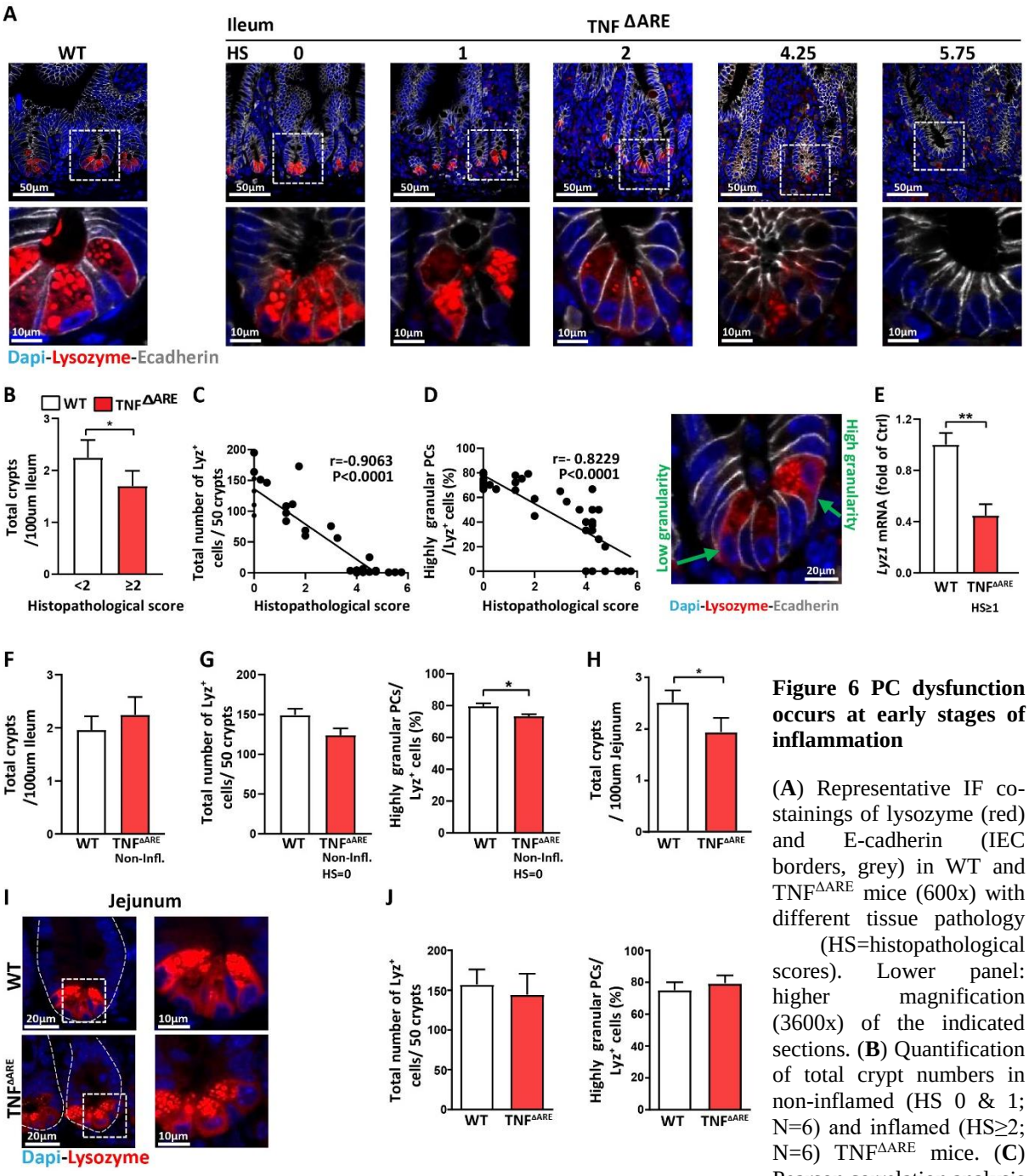

Figure 6 PC dysfunction occurs at early stages of inflammation

(**A**) Representative IF co-stainings of lysozyme (red) and E-cadherin (IEC borders, grey) in WT and TNF$^{\Delta ARE}$ mice (600x) with different tissue pathology (HS=histopathological scores). Lower panel: higher magnification (3600x) of the indicated sections. (**B**) Quantification of total crypt numbers in non-inflamed (HS 0 & 1; N=6) and inflamed (HS≥2; N=6) TNF$^{\Delta ARE}$ mice. (**C**) Pearson correlation analysis of the number of lysozyme positive (Lyz^{+}) cells with HS. (**D**) Correlation analysis (Pearson) of the proportions of highly granular Lyz^{+} cells (granules≥2) with HS. Right: representative Lyz staining showing Lyz^{+} cells with low and high granularity, respectively. (**E**) qRT-PCR analysis of IECs for *Lyz1* (N=5). (**F**) Quantification of total crypt numbers between WT (N=8) and non-inflamed (HS 0 & 1; N=6) TNF$^{\Delta ARE}$ mice. (**G**) Quantification of Lyz^{+} cells and highly granular Lyz^{+} cells in WT and non-inflamed TNF$^{\Delta ARE}$ mice. (**H**) Quantification of total crypt numbers in jejunal tissue sections from WT (N=3) and TNF$^{\Delta ARE}$ mice (N=11). (**I**) Representative immunofluorescent staining for lysozyme. (**J**) Quantification of total numbers of Lyz^{+} cells (left graph) and the percentage of highly granular PCs (right graph) on tissue sections from jejunum of WT and TNF$^{\Delta ARE}$ mice. In all cases, Dapi stained the nuclei in blue. Statistics were performed by unpaired t-tests. Asterisks indicate significant differences *P<0.05, **P<0.01, ***P<0.001.

To confirm the reduced PC function, transcriptional levels of PC-derived antimicrobial peptides (AMPs) were measured. We observed a significant reduction in defensin 5 (*Defa5*), Angiogenin 4 (*Ang4*), and

stem cell niche supporting *Dll4* expression in the ileum of TNF$^{\Delta ARE}$ mice compared to their WT littermates (**Figure 7A**). Immunofluorescent staining for matrix metalloproteinase 7 (MMP7) and Ulex Europaeus Agglutinin I (UEA1) confirmed reduced AMP activity in ileal crypt base of inflamed TNF$^{\Delta ARE}$ mice. Matrix metalloproteinases (MMPs) are enzymes that degrade and activate PC-derived inactive α-defensins [27]. Therefore, reduced MMP7 expression points to reduced AMP activation. UEA1 serves as a broader marker for PCs by binding to glycoproteins that are secreted by PCs [144]. Increased numbers of MMP7^{+} and UEA1^{+} cells were detectable above the crypt base (**Figure 7B,C**). In contrast to MMP7^{+} cells, dysfunctional PCs in inflamed TNF$^{\Delta ARE}$ mice remained UEA1^{+} (**Figure 7C**).

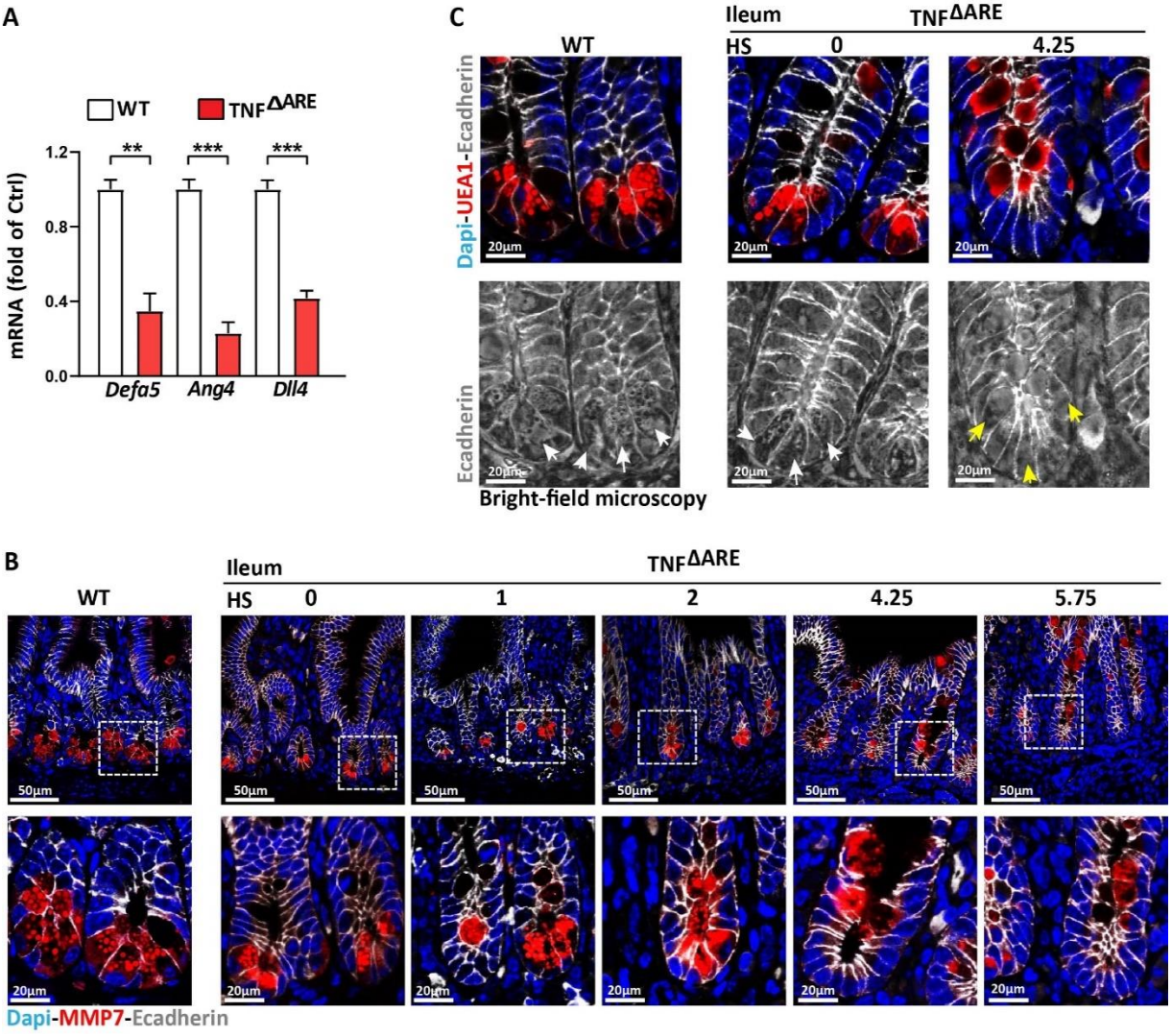

Figure 7 Inflamed TNF$^{\Delta ARE}$ mice show reduced antimicrobial peptide expression

(A) qRT-PCR analysis of ileal IECs from WT and TNF$^{\Delta ARE}$ mice for genes involved in PC function (N=5). (**B**) Representative IF co-staining of MMP7 (red) and E-cadherin (IEC borders, grey) in WT and TNF$^{\Delta ARE}$ mice (600x) with different tissue pathology (HS=histopathological scores). lower panel: higher magnification (2400x) of the indicated sections. (**D**) Representative IF co-staining of UEA1 (red) and E-cadherin (IEC borders, grey) in WT and TNF$^{\Delta ARE}$ mice histopathological scores of 0 and 4.25. lower panel shows images of bright-field microscopy. White and yellow arrows show the granular and non-granular PCs respectively. Statistics were performed by unpaired t-tests. Asterisks indicate significant differences *P<0.05, **P<0.01, ***P<0.001.

4.1.2 Inflammation in TNF$^{\Delta ARE}$ mice is associated with reduced stemness

In addition to antimicrobial peptide production and secretion, PCs support *Lgr5*$^{+}$ ISC maintenance [59]. To depict the impact of ileitis-associated reduced PC function on *Lgr5*$^{+}$ stem cells, we performed *in situ* hybridization for *Lgr5*. Numbers of dots, representing *Lgr5* transcripts, were counted in the crypt base of TNF$^{\Delta ARE}$ mice. Crypts with ≥10 *Lgr5* transcripts and <10 *Lgr5* transcripts were classified as high *Lgr5* and low *Lgr5* expressing crypts, respectively.

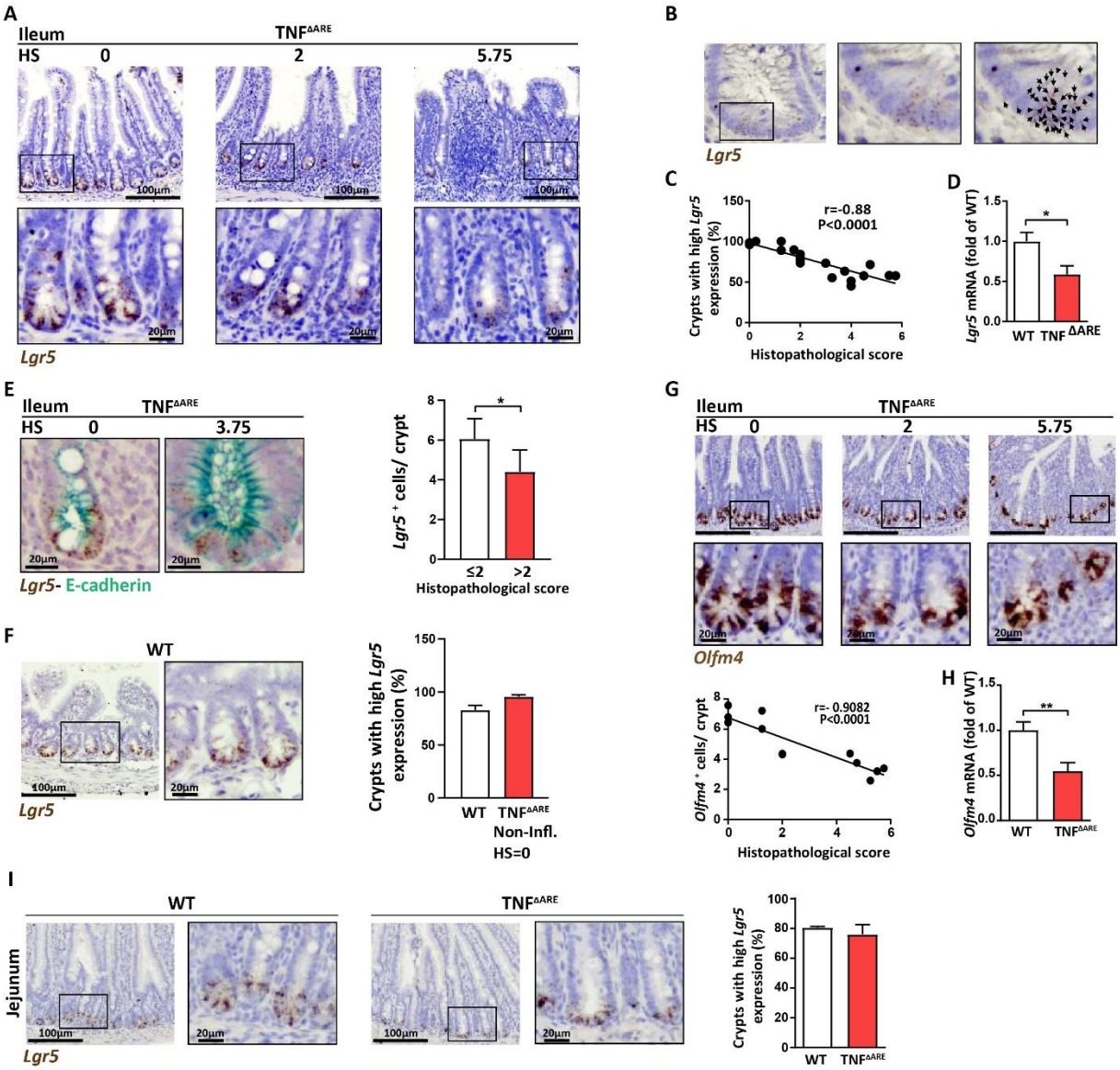

Figure 8 Inflammation in TNF$^{\Delta ARE}$ mice is associated with reduced stemness

(A) Representative pictures of *Lgr5 in situ* hybridization in ileal tissue sections from TNF$^{\Delta ARE}$ mice (400x) with different tissue pathology (HS=histopathological scores). Lower panel: higher magnification (1200x). (**B**) Illustration of the *Lgr5* quantification. Each dot represents one *Lgr5* transcript. (**C**) Pearson correlation analysis of the crypts with high *Lgr5* transcripts (≥10) with HS. (**D**) qRT-PCR analysis of ileal IECs for *Lgr5* (N=5). (**E**) Representative pictures of *Lgr5* in situ hybridization (brown) and IHC co-staining with E-cadherin (green) in TNF$^{\Delta ARE}$ mice (2400x) with different HS; Quantification of *Lgr5*$^{+}$ cells in the ileum of moderately (≤2) and highly (>2) inflamed TNF$^{\Delta ARE}$ mice. (**F**) Representative images of *Lgr5* in situ hybridization in the ileum of WT mice (400x) including magnification (1200x); Quantification of crypts with high *Lgr5* transcripts (≥10) in WT and non-

inflamed TNF$^{\Delta ARE}$ mice. (**G**) Representative pictures of *Olfm4 in situ* hybridization in the ileum of TNF$^{\Delta ARE}$ mice (400x) with different HS. Scale bars show 100µm. Lower panel: higher magnification (1200x); Correlation analysis (Pearson) of the *Olfm4*$^{+}$ cells with HS. (**H**) qRT-PCR analysis of ileal IECs for *Olfm4* (N=5). (**I**) Representative pictures of *Lgr5* in situ hybridization in jejunum of TNF$^{\Delta ARE}$ and WT mice (400x) with different tissue pathology (HS=histopathological scores). lower panel: higher magnification (1200x); Quantification of the crypts with high *Lgr5* transcripts (≥10). Statistics were performed by unpaired t-tests. Asterisks indicate significant differences *P<0.05, **P<0.01, ***P<0.001.

In line with reduced PC function, we observed reduced *Lgr5* expression in TNF$^{\Delta ARE}$ mice, which inversely correlated with tissue pathology (**Figure 8A-C**). Reduced stemness in inflamed TNF$^{\Delta ARE}$ mice was further confirmed by qPCR analysis of *Lgr5* (**Figure 8D**). To detect *Lgr5*$^{+}$ ISCs more precisely, E-cadherin co-staining was performed. E-cadherin stains the IEC borders and enables the quantification of intestinal epithelial cells. Immunohistochemical co-staining of E-cadherin with *Lgr5 in situ* hybridization showed diminished numbers of *Lgr5*$^{+}$ ISCs under inflammatory conditions (**Figure 8E**). No differences were observed in *Lgr5* expression between non-inflamed TNF$^{\Delta ARE}$ and WT mice (**Figure 8F**).

Consistent with reduced *Lgr5* expression in the ileum, *in situ* hybridization for *Olfm4*, a broader marker for CBC ISCs, confirmed reduced stemness in the crypt base of inflamed TNF$^{\Delta ARE}$ mice, which again negatively correlated with the degree of histopathology (**Figure 8G,H**). Contrarily, jejunal tissue sections of TNF$^{\Delta ARE}$ mice showed unaltered numbers of crypts with high *Lgr5* expression. Additionally, unchanged *Lgr5* and *Olfm4* expression between TNF$^{\Delta ARE}$ and WT mice, further confirmed an unaltered stemness between these two genotypes in non-inflamed intestinal segments (**Figure 8I**). Under inflammation, PCs with diffuse lysozyme staining were shown to gain proliferative capacity and by de-differentiating to *Lgr5*$^{+}$ ISCs support these cells [54]. Therefore, we stained the ileal tissue section from TNF$^{\Delta ARE}$ mice for the proliferation marker Ki67. The staining for Ki67 revealed a minor increase in numbers of Ki67^{+} cells in crypts of inflamed TNF$^{\Delta ARE}$ mice, indicating increased proliferation under inflammatory conditions (**Figure 9A**). However, in contrast to previously published studies [54], dysfunctional PCs remained Ki67 negative and non-proliferative (**Figure 9B**). The absence of proliferation in PCs supports the hypothesis that dysfunctional PCs are not de-differentiating to *Lgr5*$^{+}$ ISC.

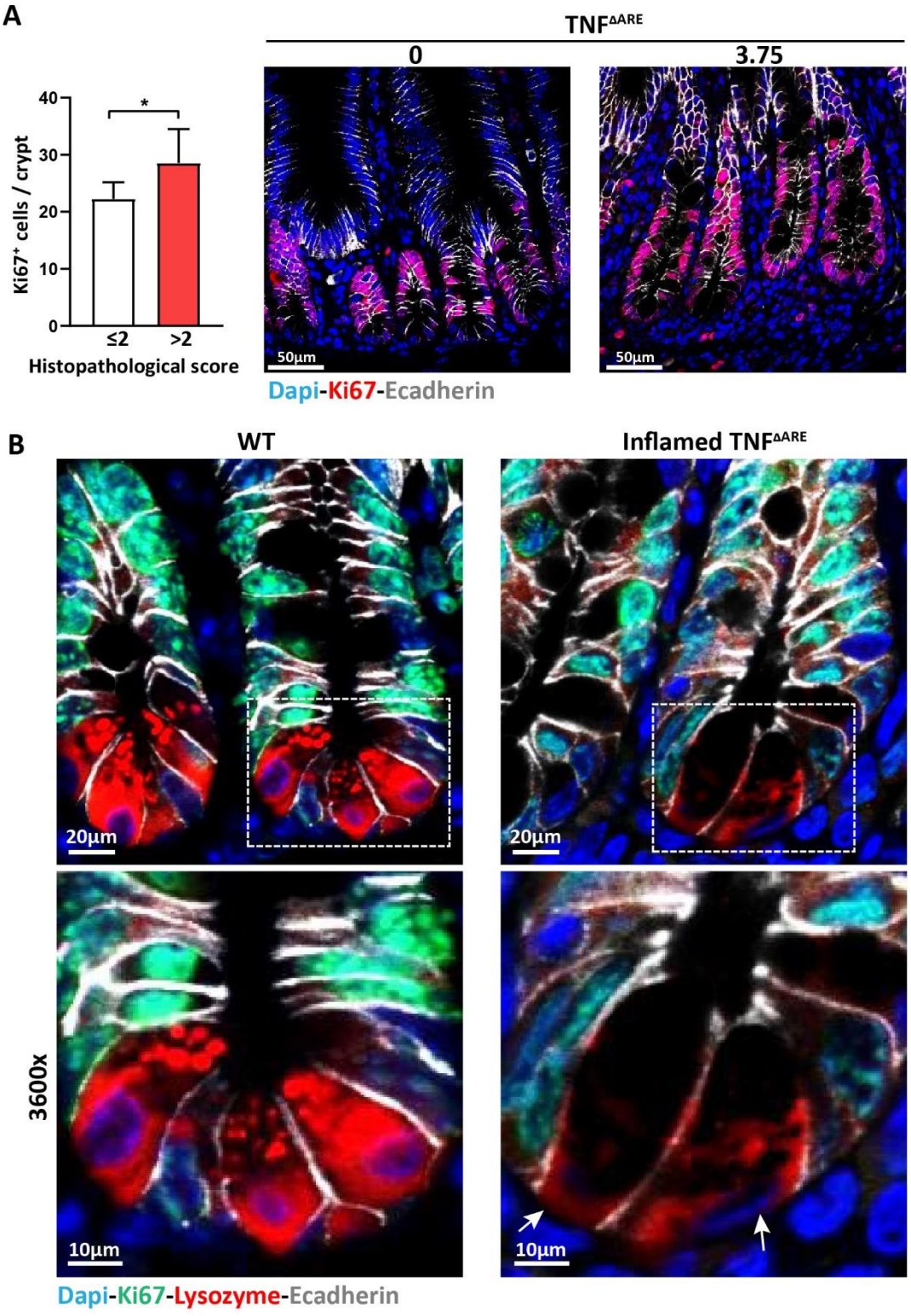

Figure 9 Dysfunctional PCs in TNF$^{\Delta ARE}$ mice are not proliferative

(A) Quantification of Ki67^{+} cells in ileal crypts of TNF$^{\Delta ARE}$ mice with moderate (HS≤2; N=5) and high (HS>2; N=9) histopathological scores; Representative IF co-staining of Ki67 (red) and E-cadherin (IEC borders, gray) (600x) in TNF$^{\Delta ARE}$ mice. (**B**) Representative IF co-staining of Ki67 (green), E-cadherin (IEC borders, gray) and lysozyme (red) (2400x) including magnification (3600x). Screening was performed on N=3-4 sections and an average of 50 crypts per section. Arrows show the dysfunctional PCs. In all cases, Dapi stained the nuclei in blue. Statistics were performed by unpaired t-tests. Asterisks indicate significant differences *P<0.05, **P<0.01, ***P<0.001.

4.2 Active CD patients show irregular PC phenotype and *LGR5* expression

To verify the findings of PC dysfunction and reduced stemness under conditions of inflammation in TNF$^{\Delta ARE}$ mice, we performed a similar analysis on ileal tissue samples from CD patients.

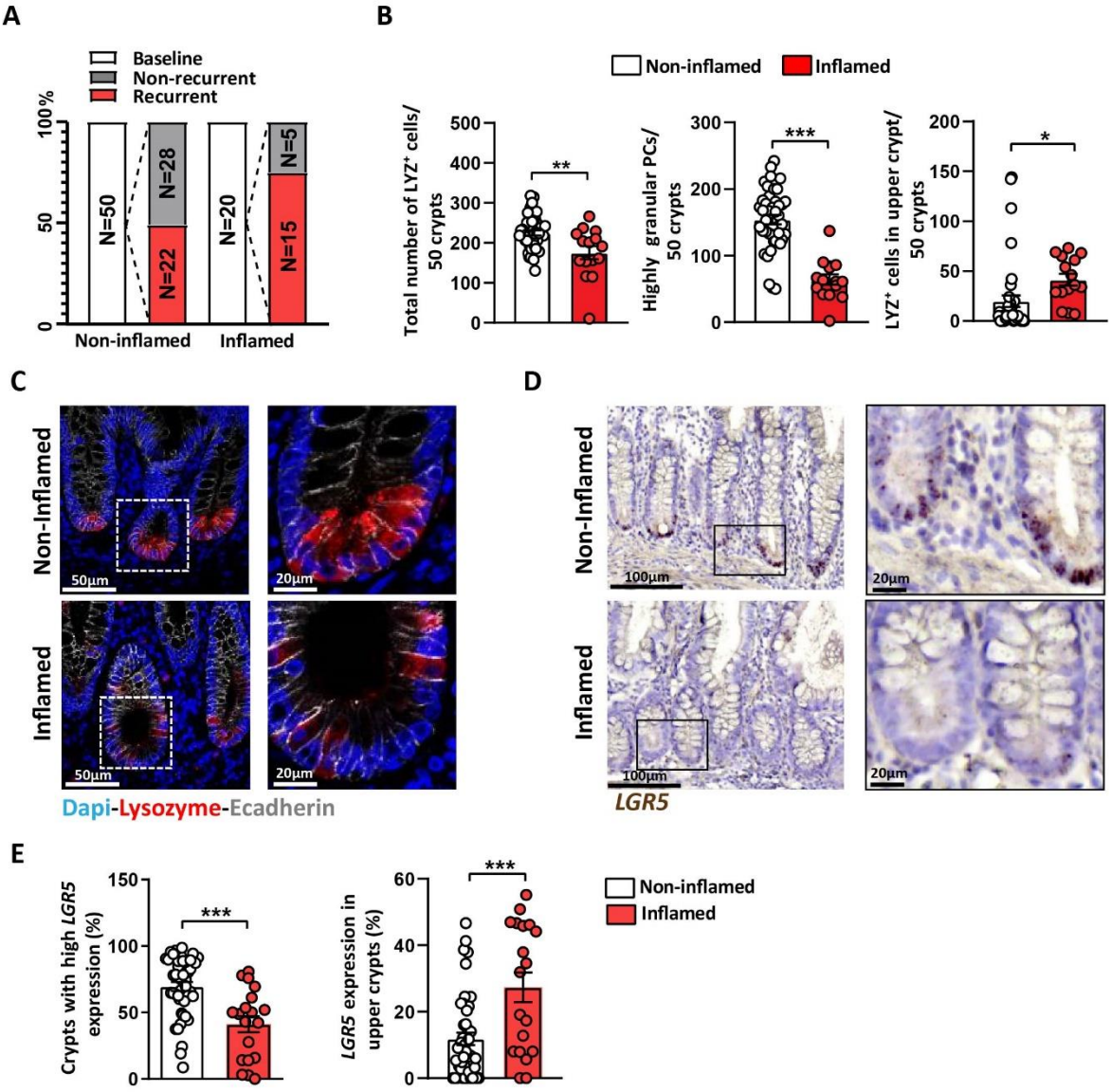

Figure 10 Aberrant PC phenotype and *LGR5* expression in CD patients with active disease

(A) Overview of CD patients at baseline and their endoscopic status (recurrent/ non-recurrent). (**B**) Quantification of the total number of LYZ$^+$ cells, granular PCs (≥2 granules) and LYZ$^+$ cells in upper crypts in ileal tissue sections of 43 non-inflamed and 15 inflamed CD patients. (**C**) Representative IF co-staining of lysozyme (red) and E-cadherin (IEC borders, grey) (600x) including magnifications (1800x). (**D**) Representative pictures of *LGR5 in situ* hybridization in ileal samples from CD patients (400x). Right panel: higher magnification (1200x). (**E**) Quantification of the crypts with high *LGR5* transcripts (≥15 transcripts; left) and *LGR5* expression in upper crypts (cell position ≥+7; right) in 45 non-inflamed and 19 inflamed CD patients. Statistics were performed by unpaired t-tests. Asterisks indicate significant differences *P<0.05, **P<0.01, ***P<0.001.

Samples were obtained from 50 non-inflamed and 20 inflamed CD patients that underwent a resection surgery from a previously published prospective study [116]. Endoscopic recurrence was assessed based on a postoperative endoscopy that was performed 6-12 months after surgery and was defined as a Rutgeerts score. Patients with a Rutgeerts score of <2 (<i2) were categorized as non-recurrent, whereas Rutgeerts score of ≥2 (≥i2) indicated clinical recurrence. Numbers of CD patients with recurrent and non-recurrent disease phenotype are illustrated in **Figure 10A**. Patients were classified based on the resected tissue samples at baseline and according to the presence or absence of inflammation. 44% of non-inflamed and 75% of inflamed patients experienced endoscopic recurrence 6-12 months after surgery (**Figure 10A**). Inflamed and non-inflamed margins of CD patients were stained for lysozyme. Similar to findings in the CD-like ileitis model, total numbers of LYZ^+ cells, as well as highly granular PCs (≥2 Lyz^+ cytoplasmic granules), were significantly reduced in inflamed margins of CD patients (**Figure 10B,C**). Increased numbers of LYZ^+ cells in 'upper crypts' (at a position higher than +7 from the crypt base) were indicative of aberrant stem cell niche function and architecture under inflammatory conditions (**Figure 10B,C**). Consistent with $TNF^{\Delta ARE}$ mice, we observed a reduced proportion of crypts with high *LGR5* expression (≥15 transcripts) in inflamed CD patients (**Figure 10D,E**). However, the percentage of crypts with *LGR5* expression in upper crypts significantly increased (**Figure 10E**).

4.3 Aberrant PCs and *LGR5* expression predict disease recurrence in non-inflamed CD patients

Inflammation in resected ileal tissue at baseline predicts endoscopic recurrence [116], yet 44% of the analyzed patients with non-active CD at baseline developed recurrent disease 6-12 months after surgery (**Figure 10A**). Abnormal PCs were shown to correlate with disease recurrence after resection surgery in CD patients [124]. Therefore, we expanded our observations to stem cells and tested if the ISC niche phenotype and *LGR5* expression predict disease recurrence in non-active CD patients. Although no changes were observed in total numbers of LYZ^+ cells between recurrent and non-recurrent patients (**Figure 11A,B**), recurrent patients showed significantly reduced granular PCs (≥2 Lyz^+ cytoplasmic granules), which was predicting disease recurrence (**Figure 11C,D**). In addition to reduced PC granularity, we observed an aberrant PC localization in recurrent patients with significantly induced numbers of LYZ^+ cells in upper crypts (≥ +7 position). The presence of LYZ^+ cells in upper crypts further predicted disease recurrence in CD patients (**Figure 11E,F**).

Along with the altered PC phenotype, we observed diminished numbers of crypts with high *LGR5* expression (≥15 transcripts) in patients that experienced recurrence 6-12 months after surgery.

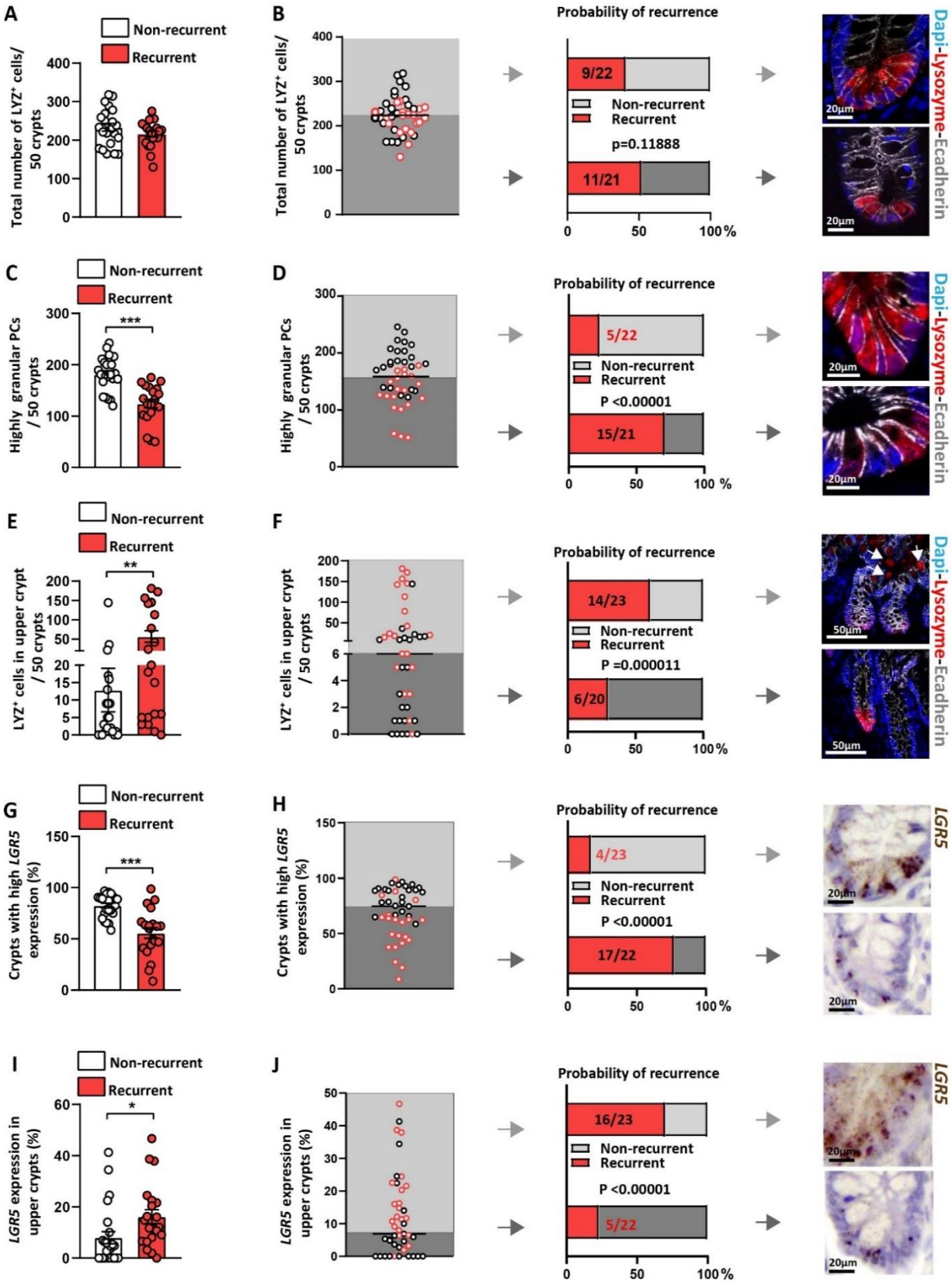

Figure 11 ISC niche phenotype predict disease recurrence in non-inflamed margins of CD patients

Ileal tissue sections from non-inflamed CD patients were analyzed for PC phenotype and *LGR5* expression. **(A,C,E)** Overall comparison of recurrent vs non-recurrent patient for the respective pattern of LYZ expression. (**B,D,F**) Left: Distribution of non-inflamed recurrent (red) and non-recurrent (gray) patients for the respective PC

pattern. The line indicates the median. Middle: Probability of patients who underwent recurrence or stayed non-recurrent above (upper bar) and below (lower bar) median for respective PC pattern. Right: Representative IF co-staining of LYZ (red) and E-cadherin (gray). Dapi stained the nuclei in blue. **(A,B**) Quantification of the total number of LYZ$^+$ cells. **(C,D**) Quantification of the granular PCs (≥2 granules). **(E,F**) Quantification of the LYZ$^+$ cells above the crypt base in 43 non-inflamed CD patients. **(G,I**) Overall comparison of recurrent vs non-recurrent patient for the respective stem cells pattern of expression. (**H,I**) Left: Distribution of non-inflamed recurrent (red) and non-recurrent (gray) patients for the *LGR5* expression. The line indicates the median. Middle: Probability of patients who underwent recurrence or stayed non-recurrent above (upper bar) and below (lower bar) median for respective *LGR5* expression pattern. Right: Representative images of *LGR5 in situ* hybridization. **(G,H**) Quantification of the crypts with high *LGR5* expression (≥15 transcripts). **(I,J**) Quantification of the crypts with *LGR5* expression above the crypt base position (≥+7) in 45 non-inflamed CD patients. Statistics were performed by unpaired t-tests in recurrent vs non-recurrent patients. Probability of recurrence was measured via Chi-Square test. Asterisks indicate significant differences *P<0.05, **P<0.01, ***P<0.001.

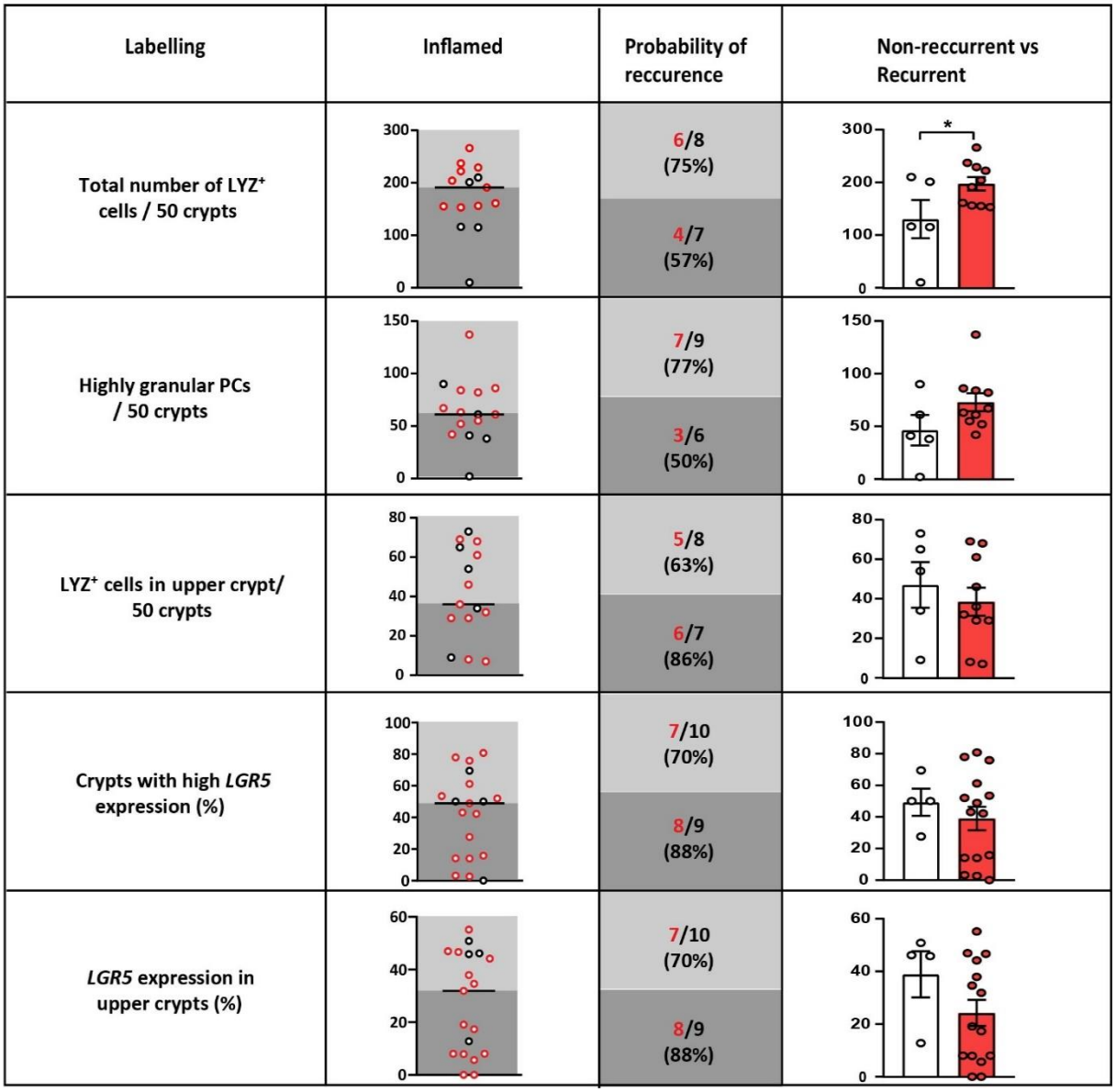

Figure 12 ISC niche factors do not predict endoscopic recurrence in inflamed CD patients

Ileal tissue sections of inflamed CD patients undergoing surgical resection were analyzed at baseline. Tissue sections were stained for LYZ by IF and for *LGR5* by *in situ* hybridization, respectively, and expression patterns were quantified. From top to bottom: total numbers of lysozyme positive (LYZ$^+$) cells, numbers of highly granular

LYZ$^+$ cells (≥2 granules), numbers of LYZ$^+$ cells in upper crypts (in 15 inflamed patients), proportion of crypts with high *LGR5* expression (≥15 *LGR5* transcripts), and proportion of crypts with *LGR5* expression in upper crypts (in 19 inflamed patients) were determined. CD patients with endoscopic recurrence (Rutgeerts score ≥i2) 6-12 months after surgery were compared to CD patients not experiencing recurrence. From left to right: distribution of the respective marker among recurrent and non-recurrent CD patients with median indicated; probability of CD patients to experience recurrence if above or below the median for the respective marker; overall comparison of recurrent versus non-recurrent patients for the respective marker. Statistics were performed by unpaired *t*-tests. Asterisks indicates significant differences *P<0.05.

Additionally, the number of crypts with *LGR5* expression in upper crypts was elevated in these patients (**Figure 11G,I**). Interestingly, reduced *LGR5* expression in the crypt-base and an induced *LGR5* expression in upper crypts predicted disease recurrence in non-inflamed margins of CD patients (**Figure 11H,J**). We also demonstrated that the presence of each factor, defined as dysfunctional PCs, low *LGR5* expression, and aberrant LYZ and *LGR5* localization, was significantly associated with an increased risk of endoscopic recurrence (**Figure 13A**).

In contrast to non-active CD patients, altered PC phenotype, reduced stemness, and aberrant LYZ and *LGR5* expression could not predict endoscopic recurrence in patients categorized as inflamed at baseline (**Figure 12**)

4.4 Smoking and genetic risk factors have no additional impact on the ISC niche and disease recurrence

Previously, smoking was identified as a risk factor for disease recurrence in this cohort [116]. To assess the additional impact of smoking on the ISC niche, patients were stratified according to their smoking status. 38% of non-active CD patients (19 patients) were identified as smokers at baseline among them, 63.2% (12 patients) experienced postoperative endoscopic recurrence (**Figure 13B**). In non-active patients, smoking was associated with reduced PC granularity, enhanced numbers of LYZ$^+$ cells in upper crypts, and a low proportion of crypts with high *LGR5* expression. No impact on total numbers of LYZ$^+$ cells and *LGR5* expression was observed in upper crypts (**Figure 13C,D**). However, within non-active CD patients experiencing recurrence, smoking had no additional impact on PC phenotype and *LGR5* expression (**Figure 13E,F**). Similarly, we observed no impact of smoking on the ISC niche function in patients that remained non-recurrent (**Figure 13G,H**).

From inflamed CD patients that were identified as smokers at baseline, 90% experienced disease recurrence. Despite the overall impact of smoking on disease recurrence, smoking also showed no additional impact on PC phenotype and stemness within inflamed patients and patients that experienced endoscopic recurrence later on (Data not shown).

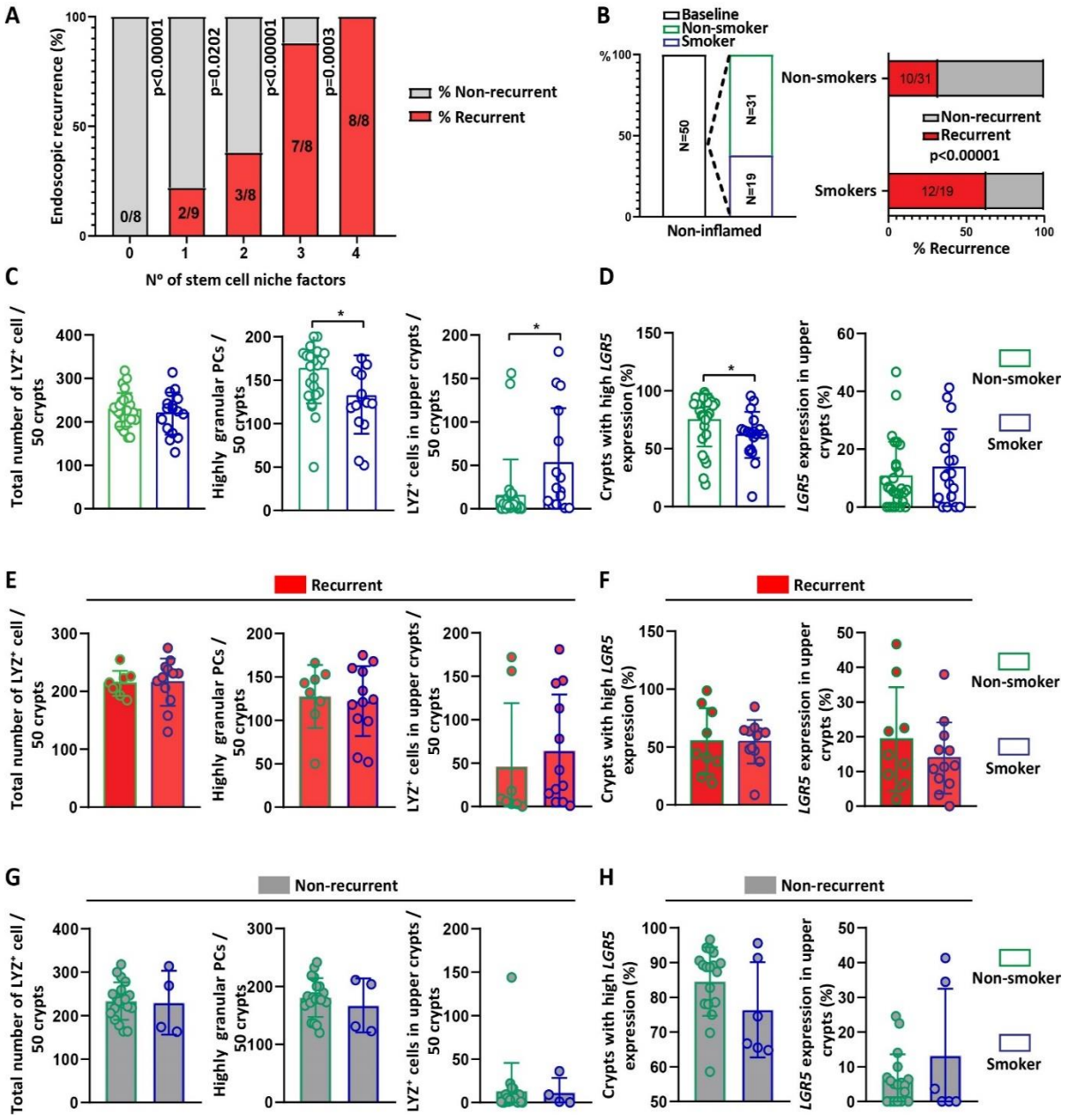

Figure 13 Smoking has no impact on ISC niche phenotype in non-inflamed margins of CD patients

(**A**) Probability of CD patients experiencing recurrence possessing the indicated numbers of stem cell niche factors. Statistical analyses were performed via Chi-square test. (**B**) Left: Overview of smoker and non-smoker CD patients with non-active disease course; Right: The percentage of endoscopic recurrence based on smoking status of non-active patients. (**C,D**) Total numbers of LYZ^+ cells, numbers of highly granular LYZ^+ cells (≥2 granules), numbers of LYZ^+ cells in upper crypts (in 16 smokers and 26 non-smokers), percentage of crypts with high *LGR5* expression (≥15 *LGR5* transcripts), and percentage of crypts with *LGR5* expression in upper crypts (in 18 smokers and 27 non-smokers) are depicted for all patients based on smoking status, regardless of endoscopic recurrence. (**E,F**) The same readouts as in (**C**) and (**D**) are given for patients experiencing endoscopic recurrence (PC readouts: N=12 smokers and N=8 non-smokers; SC readouts: N=12 smokers and N=9 non-smokers). (**G,H**) The same readouts as in (**C**) and (**D**) are depicted for non-recurrent patients and according to the smoking status (PC readouts: N=4 smokers and N=18 non-smokers; SC readouts: N=6 smokers and N=18 non-smokers). Statistics were performed by unpaired *t*-tests. Asterisks indicates significant differences *P<0.05.

In addition to smoking, genes, including *NOD2*, have been identified as risk factors for CD recurrence [145]. CD-associated risk alleles *NOD2*, *ATG16L1*, and in particular their combination have been reported to impact PC phenotype [124]. The presence of genetic risk factors in non-active CD patients experiencing postoperative endoscopic recurrence are schematically illustrated in **Figure 14A,B**. The presence of single nucleotide polymorphisms in *ATG16L1* (rs6752107), *NOD2* (rs2066845/ rs2066844), and a combination of all three risk alleles showed no impact on PC phenotype and *LGR5* expression between recurrent and non-recurrent patients (**Figure 14C,D**). Therefore, in our cohort, we could not find evidence for the influence of genetic risk factors on the ISC niche.

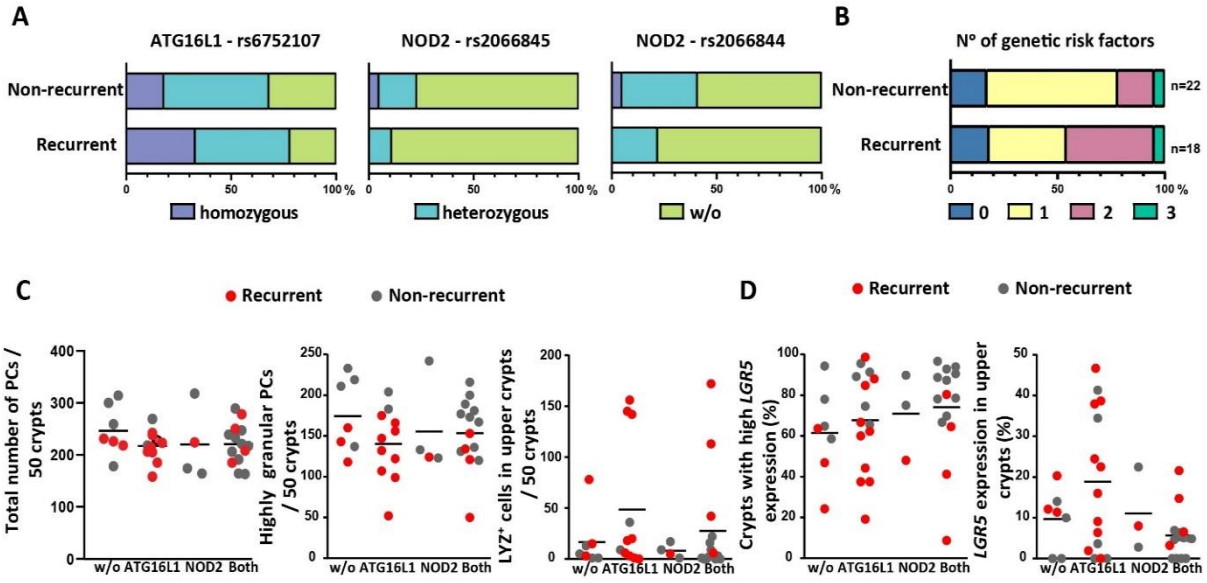

Figure 14 The presence of genetic risk factors have no impact on ISC niche appearance

(**A**) Overview of the percentage of non-active recurrent and non-recurrent CD patient based on homozygosity, heterozygosity and absence of mentioned genetic risk factor (N=40). (**B**) Probability of CD patients experiencing recurrence or not, carrying with indicated numbers of genetic risk factors. Genetic risk factors included *ATG16L1* (rs6752107), *NOD2* (rs2066845) and *NOD2* (rs2066844). (**C**) Quantification of the total number of LYZ^+ cells, numbers of highly granular LYZ^+ cells (≥2 granules) and numbers of LYZ^+ cells in upper crypts according to the genetic background of patients (No risk: N=7; *ATG16L1*: N=11; *NOD2*: N=4; Both: N=14). (**D**) Quantification of the percentage of crypts with high *LGR5* expression (≥15 *LGR5* transcripts), and percentage of crypts with *LGR5* expression in upper crypts (No risk: N=7; *ATG16L1*: N=15; *NOD2*: N=3; Both: N=14) are depicted for patients based on their genetic backgrounds, given in the graph. Statistical analyses were performed by One-way analysis of variance (ANOVA) followed by Tukey test. Information on the genetic background of patients was provided by Matthieu Allez. Execution of the experiment and data quantification was performed by Sevana Khaloian. Data integration and the generation of graphs were performed by Eva Rath.

4.5 Inflammation is associated with impaired mitochondrial function

Mitochondrial stress and elevated HSP60 expression have been reported in the intestinal epithelium of IBD patients [66]. HSP60 is a mitochondrial chaperone and a target gene of mt-UPR signaling. Therefore, its elevated levels serve as a marker for mitochondrial stress and mt-UPR activation [62, 66] Dysfunctional PCs were shown to have reduced mitochondrial integrity and elevated numbers of degenerating mitochondria [28]. Since TNF$^{\Delta ARE}$ mice showed increased numbers of dysfunctional PCs, we investigated the impact of CD-like inflammation on mitochondrial function. Inflammation in TNF$^{\Delta ARE}$ mice was associated with reduced cellular adenosine triphosphate (ATP) levels in ileal crypt isolates (**Figure 15A**). Along with reduced ATP levels, mt-UPR marker proteins Hsp60 and Pkr (double-stranded-RNA-activated protein kinase) were significantly induced in crypt bases under inflammatory conditions (**Figure 15B-D**). Pkr is a mitochondrial function-associated protein, and its elevated expression was observed in IBD patients [66]. Concomitantly, we observed an upregulation of transcription of mt-UPR target genes (*Trb3*, *Atf5*, and *Chop*), oxidative-stress response (*Hif1α*), and cellular energy response (*Prkaa2*/ encoding AMPK) in ileal crypt isolates of TNF$^{\Delta ARE}$ mice (**Figure 15E,F**). Although mitochondrial respiratory chain complex IV (cytochrome C oxidase) subunit I (mt-*CoxI*) expression was reduced in TNF$^{\Delta ARE}$ mice, transcriptional levels of *CoxIV* (mitochondrial complex IV subunit IV) remained unaltered (**Figure 15G**). *CoxIV* is encoded by nuclear DNA, whereas *CoxI* is encoded by the mitochondrial genome. Therefore, reduced *CoxI* expression indicates a reduced mitochondrial function. Citrulline is one of the major metabolites that is partly processed in the mitochondrial matrix. The synthesis of citrulline from ornithine is facilitated by ornithine transcarbamylase (OTC) [85]. Significantly reduced ornithine transcarbamylase (*Otc*) expression and plasma citrulline concentrations, as well as unchanged transcriptional levels of ornithine-citrulline carrier *Slc25a15*, were indicative of a disrupted mitochondrial function under inflammatory conditions (**Figure 15H,I**). These data were consistent with our previous observations [62]. In contrast to mt-UPR target genes, expression of *Grp78*, a surrogate marker of ER stress, remained unaltered (**Figure 15J**).
Transmission electron microscopy (TEM) showed significantly reduced PC numbers with normal morphological features in the crypt base of TNF$^{\Delta ARE}$ mice. Additionally, we observed PC-like cells with broadened halos and intracytoplasmic vacuolations. These cells displayed mitochondrial swelling with dissolution and disruption of cristae, loss of matrix density, and occasionally formation of intramitochondrial electron-dense inclusions (**Figure 16**), which indicated an altered mitochondrial function in PCs upon inflammation.

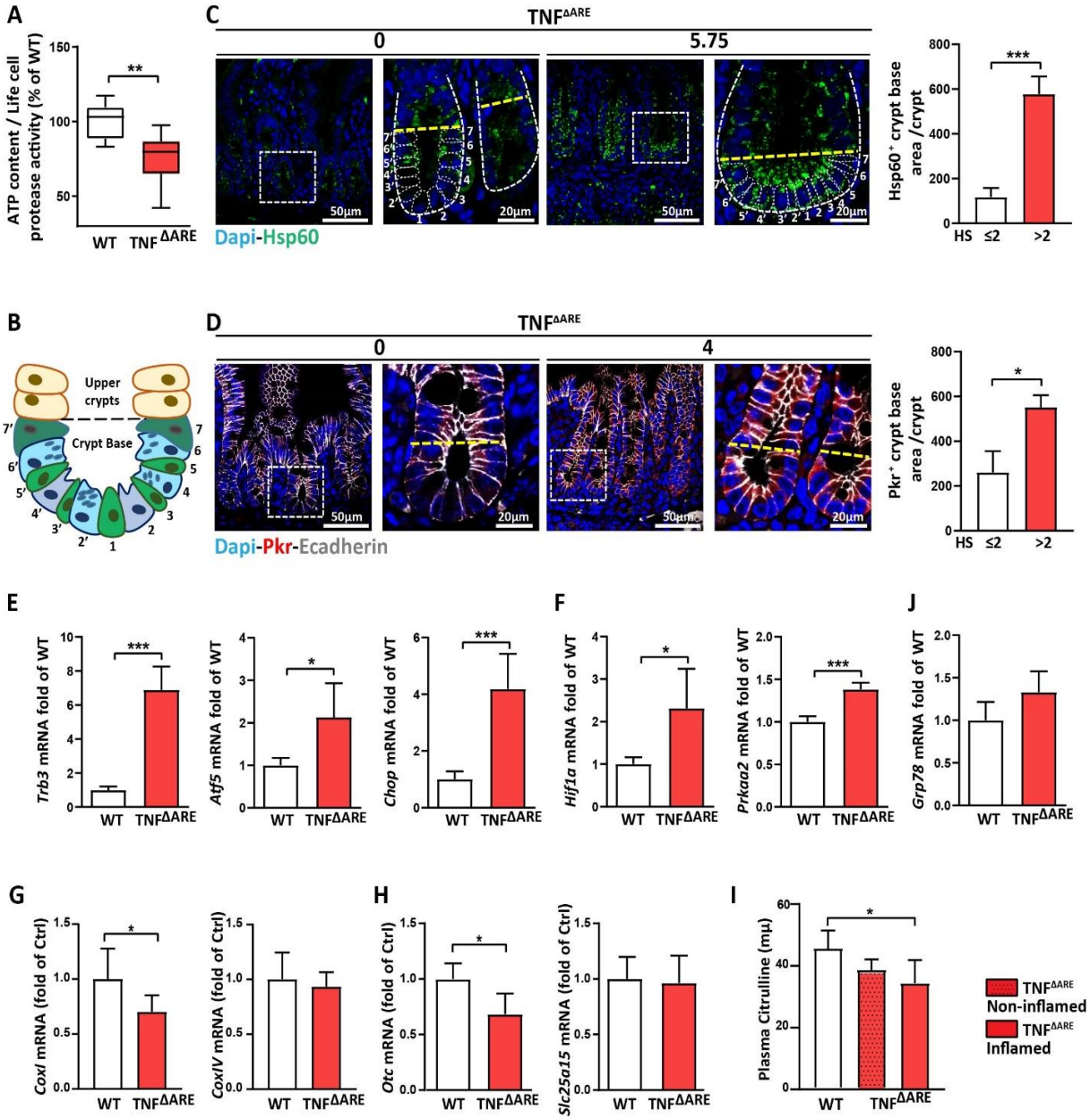

Figure 15 Crypts of inflamed TNF$^{\Delta ARE}$ mice show signs of mitochondrial dysfunction

(**A**) Measurement of the ATP content relative to life-cell protease activity in primary crypt isolates of TNF$^{\Delta ARE}$ mice (N=10; biological replicates) and WT controls (N=7; biological replicates); Execution of the experiment and the analysis in **A** was performed by Elisabeth Gleisinger. (**B**) Overview of crypt structure and illustration of the crypt base area used for protein quantification. (**C**) Representative IF images of Hsp60 (green) counterstained with Dapi (nuclei, blue; 600x), including magnifications (2400x). Numbers above the pictures indicate the histopathological score (HS) of the respective tissue section. Right: Quantification of the Hsp60 signal in ileal crypt bases of moderately inflamed (HS≤2; N=8) and highly inflamed (HS>2; N=6) TNF$^{\Delta ARE}$ mice. (**D**) IF co-staining of Pkr (red) and E-cadherin (IEC borders, grey) counterstained with Dapi (nuclei, blue), including magnifications. Numbers above the pictures indicate the histopathological score (HS) of the respective tissue section. Right: Quantification of the Pkr signal in ileal crypt bases of moderately inflamed (HS≤2; N=3) and highly inflamed (HS>2; N=6) TNF$^{\Delta ARE}$ mice. (**E,F,J**) qRT-PCR analysis of primary ileal crypt isolates for genes involved in mitochondrial mt-UPR, mitochondrial signaling and (**J**) ER stress (N=6). (**G,H**) qRT-PCR analysis of IEC isolates for genes involved in mitochondrial respiration and metabolic signaling (N=5). (**I**) Plasma Citrulline concentrations in WT (N=5), non-inflamed (N=3) and inflamed (N=5) TNF$^{\Delta ARE}$ mice. Statistics were performed by unpaired *t*-tests. Statistics in I was performed by one-way ANOVA. Asterisks indicate significant differences **P*<0.05, ***P*<0.01, ****P*<0.001.

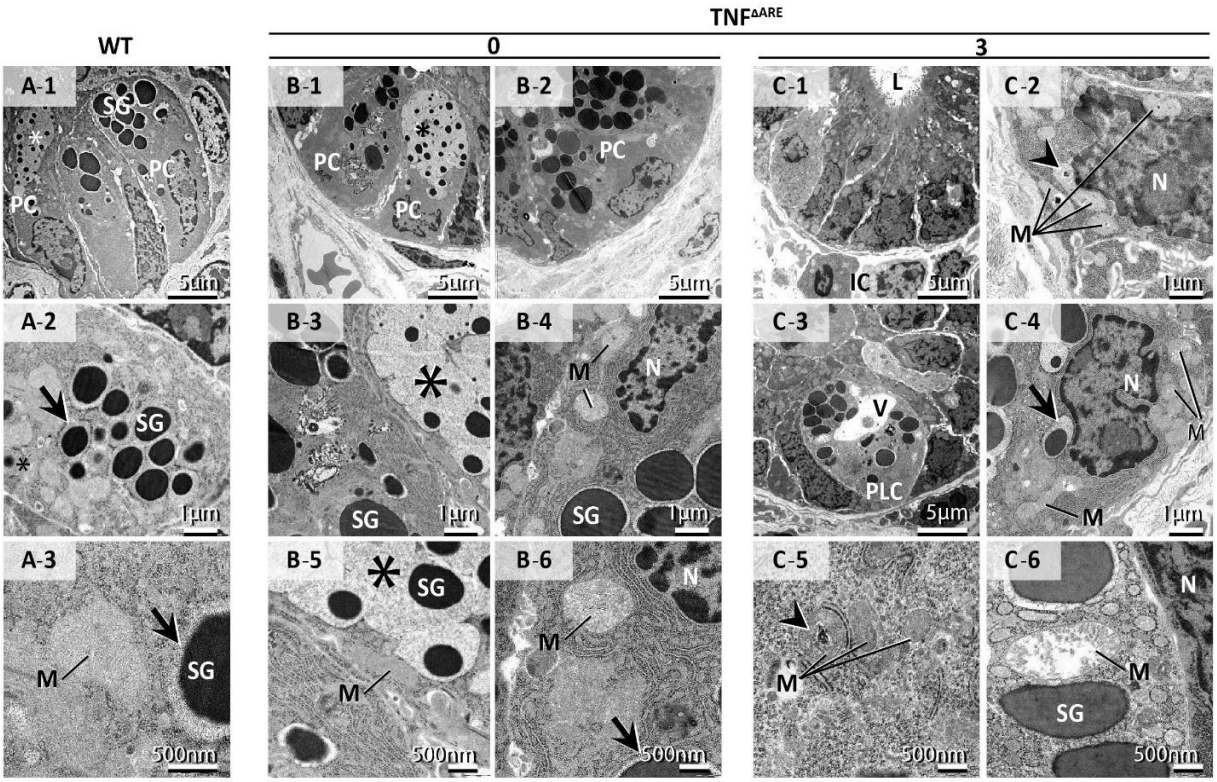

Figure 16 Inflammation in TNF$^{\Delta ARE}$ mice is associated with altered mitochondrial morphology in PCs

Transmission electron microscopy (TEM) of ileal crypt bases from WT and non-inflamed/ inflamed TNF$^{\Delta ARE}$ mice. Panel **A:** WT; **A1-2:** Paneth cells (PC) display abundant, apical, electron-dense secretory granules (SG) with narrow halos (arrow). Asterisks mark secretory granules with small electron dense cores and wide rims of flocculent material of low electron-density. **A-3**. Unaltered appearance of mitochondria (M) in a WT-PC. **B:** non-inflamed TNF$^{\Delta ARE}$ mice; **B-1-6:** PC ultrastructure essentially resembles WT mice. N: nucleus. **C:** inflamed TNF$^{\Delta ARE}$ mice. **C-1-2:** Crypt base of inflamed TNF$^{\Delta ARE}$ mice, showing Paneth-Like-Cell (PLC). Mitochondria of crypt epithelial cells often display electron-dense inclusions (arrowheads). L: crypt lumen. IC: infiltrating inflammatory cell. **C-3-4:** Few remaining cells with PLC-typical location and morphology often show vacuolation (V) and broadened halos of secretory granules. **C-4-6:** Mitochondrial lesions in PLC include intramitochondrial inclusions (**C-4**, **C-5**), mitochondrial swelling with dissolution and disruption of cristae, and loss of matrix density (**C-6**). TEM was performed by Andreas Blutke [141].

4.6 Hsp60^{-} - *Lgr5*$^{+}$ stem cells give rise to dysfunctional Paneth cells

4.6.1 Mitochondrial impairment is associated with reduced stemness and increased PC abnormalities in mice

We observed altered PC functionality and reduced *Lgr5*$^{+}$ stem cells, together with impaired mitochondrial function in inflamed TNF$^{\Delta ARE}$ mice. Mitochondrial function was shown to control intestinal epithelial stemness [146]. Based on these findings, we characterized the role of mitochondrial dysfunction on the stem cell niche function in mouse models of mitochondrial stress. Mice with an inducible *Hsp60* deletion in *Lgr5*$^{+}$ stem cells (Hsp60$^{\Delta/\Delta ISC}$) serve as models for mitochondrial dysfunction. Hsp60 was deleted by the administration of tamoxifen to mice for one week at the age of 10 weeks. Mice were sampled at days 0, 2, 4, and 6 after completion of the tamoxifen treatment (**Figure 17A**). *Hsp60* expression was transiently reduced in Hsp60$^{\Delta/\Delta IS}$ mice after finishing tamoxifen treatment (**Figure 17B**). Confirming mt-UPR activation upon Hsp60 loss, transcriptional levels of *Hsp10* were increased. Hsp10 is a mitochondrial chaperone binding protein, has a shared promoter with Hsp60, and is a surrogate marker of mt-UPR activation. Additionally, we observed an induced expression of mt-UPR target genes (*Trb3* and *Chop*), oxidative stress- (*Hif1a*), and low ATP signaling- (*Prkaa2*) related genes shortly after induction of Hsp60 loss (**Figure 17C**).

Characterizing *Lgr5* expression in the ileum of Hsp60$^{\Delta/\Delta ISC}$ mice, we observed a transient reduction in the proportion of crypts with high *Lgr5* expression at day 2. Similar effects were observed in jejunal tissue sections from Hsp60$^{\Delta/\Delta ISC}$ mice (**Figure 17D,E**).

Altered mitochondrial function has been observed in dysfunctional PCs [106]. Therefore, we characterized PCs in Hsp60$^{\Delta/\Delta ISC}$ mice using immunofluorescent staining for the PC marker lysozyme. Although total numbers of lysozyme-positive cells remained unaltered upon mitochondrial impairment in both ileum and jejunum (**Figure 18A,B**), Hsp60 loss caused PC dysfunction. The proportion of highly granular PCs decreased from day 0 after *Hsp60* deletion, reaching the lowest numbers at day 4 (**Figure 18C**).

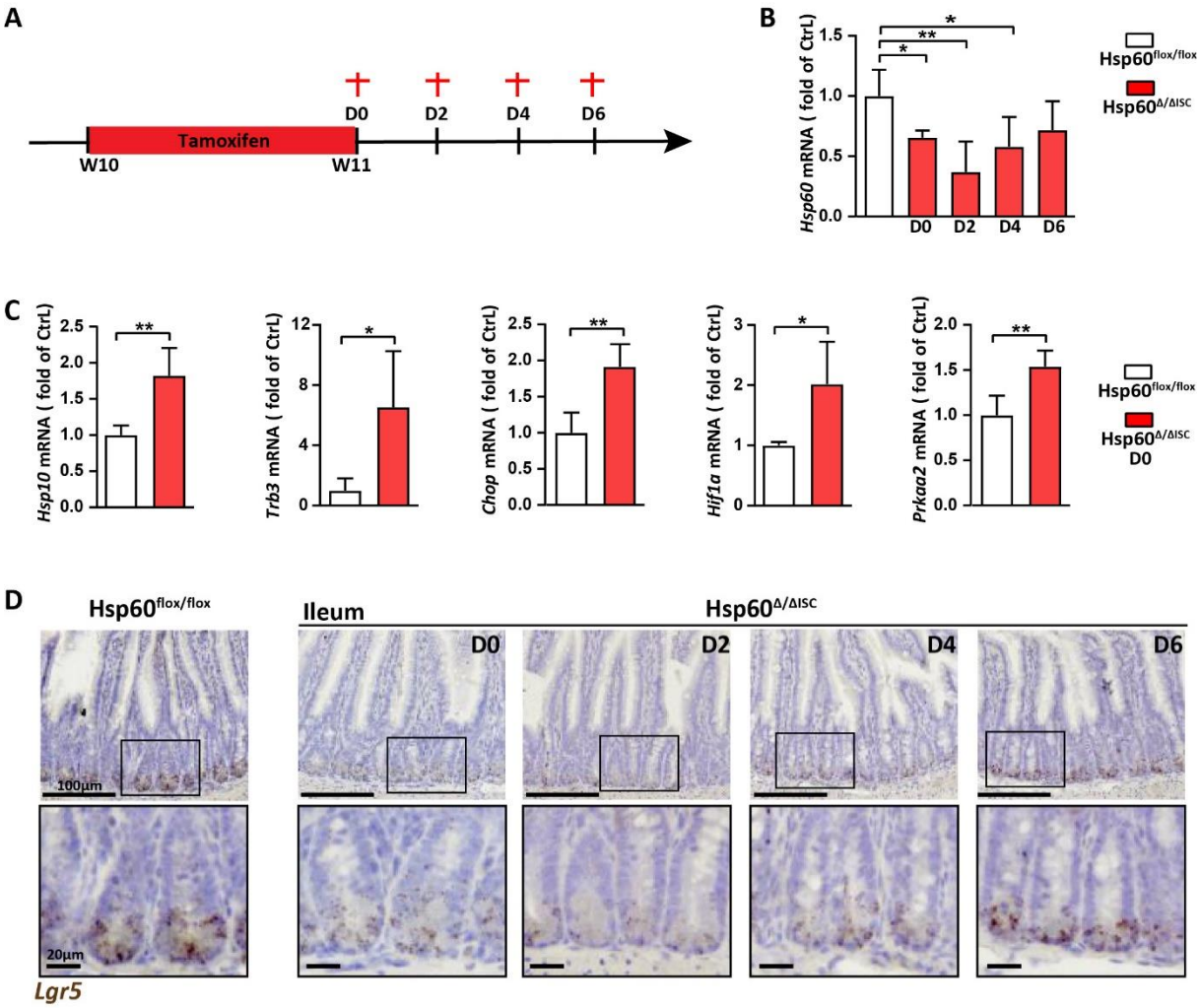

Figure 17 Hsp60 deletion in *Lgr5*$^{+}$ stem cells is associated with reduced stemness

(**A**) Experimental scheme for induction of Hsp60 knockout in Hsp60$^{\Delta/\Delta ISC}$ mice. (**B**) qRT-PCR analysis for *Hsp60* on ileal IECs from Hsp60$^{fox/flox}$ and Hsp60$^{\Delta/\Delta ISC}$ mice (each case N=4) at different time points after induction of Hsp60 knockout. (**C**) qRT-PCR analysis for genes involved in mt-UPR and mitochondrial signaling on ileal IECs from Hsp60$^{fox/flox}$ and Hsp60$^{\Delta/\Delta ISC}$ mice (each case N=4) at D0 after induction of Hsp60 knockout. (**D**) Representative pictures of *Lgr5* in situ hybridization in ileal tissues (400x) including magnification (1200x). (**E**) Quantification of the crypts with high *Lgr5* transcripts (≥10 transcripts) in Hsp60$^{fox/flox}$ and Hsp60$^{\Delta/\Delta ISC}$ mice (each case N=4) at different time-points after induction of the knockout. Statistics were performed by unpaired t-tests for two groups and one-way ANOVA for multiple comparisions. Asterisks indicate significant differences *P<0.05, **P<0.01, ***P<0.001.

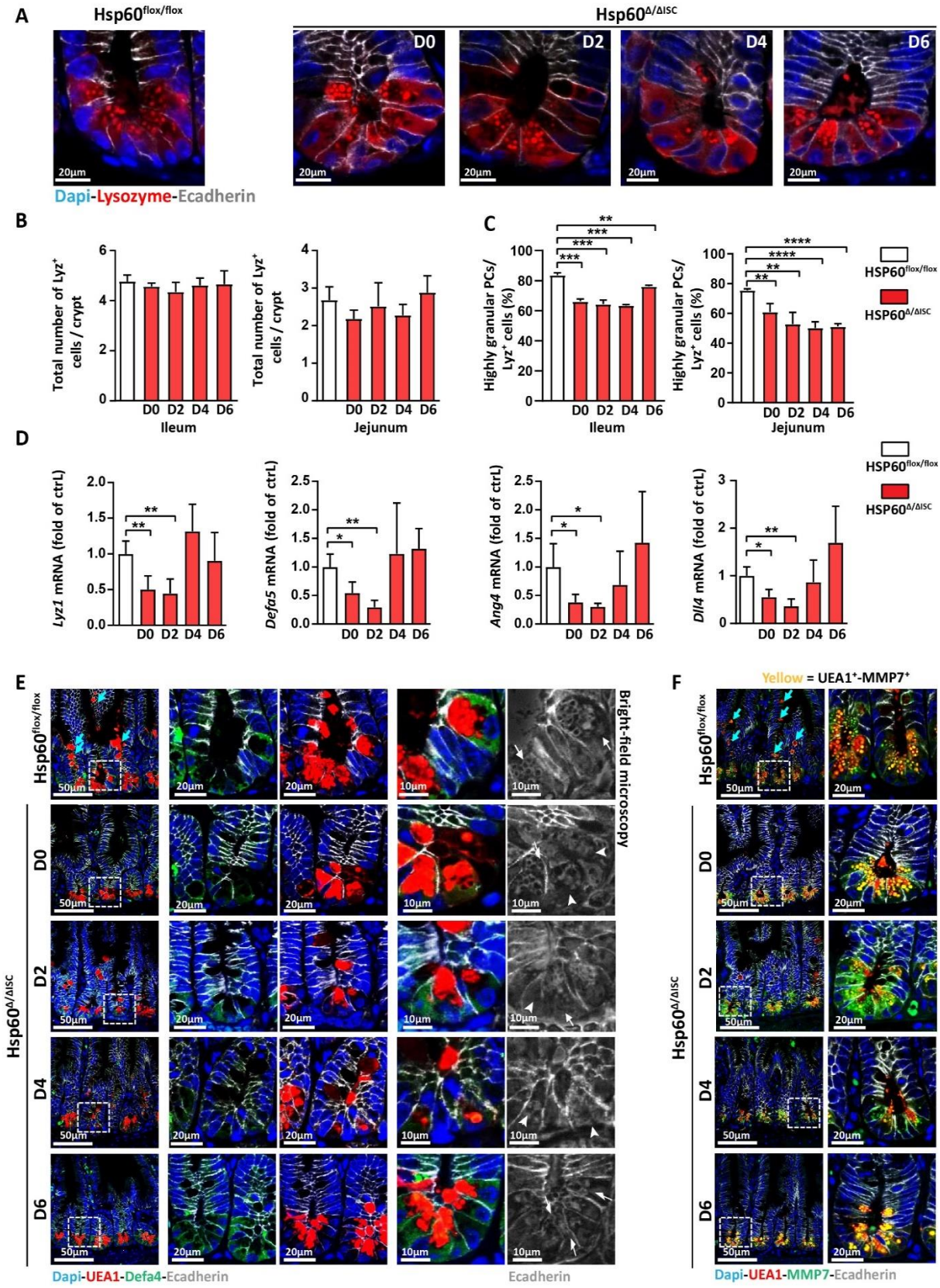

Figure 18 Mitochondrial impairment is associated with the occurrence of dysfunctional PCs

(**A**) Representative IF co-staining of lysozyme (red) and E-cadherin (IEC borders, gray) counterstained with Dapi (nuclei, blue; 2400x). (**B**) Quantification of total Lyz^+ cells at different time-points after induction of the Hsp60 knockout in the ileum (left) and the jejunum (right) of $Hsp60^{fox/flox}$ and $Hsp60^{\Delta/\Delta ISC}$ mice (each case N=4). (**C**)

Quantification of highly granular PCs (granules ≥2) in the ileum (left) and the jejunum (right) of Hsp60$^{fox/flox}$ and Hsp60$^{\Delta/\Delta ISC}$ mice (N=4). (**D**) qRT-PCR analysis of IECs from the ileum of Hsp60$^{fox/flox}$ and Hsp60$^{\Delta/\Delta ISC}$ mice for PC-derived AMPs and Notch ligand *Dll4*. (**E**) Representative images of IF co-staining for Defa4 (green), UEA1 (red) and E-cadherin (IEC borders, gray), counterstained with Dapi (nuclei, blue) including magnifications. Turquoise arrows indicate UEA1 positive cells above the crypt base and in villi. Right panel shows the bright-field microscopy. White arrows indicate granular PCs. White arrowheads indicate PCs with low granularity. (**F**) Representative pictures of IF co-stainings for MMP7 (green), UEA1 (red) and E-cadherin (IEC borders, gray), counterstained with Dapi (nuclei, blue) including magnifications (1800x). Turquoise arrows indicate UEA1 positive cells above the crypt base and in villi. Screening was performed on N=3 sections and an average of 30 crypts per section. Statistical analyses were performed by One-way analysis of variance (ANOVA) followed by Tukey test. Asterisks indicate significant differences **P*<0.05, ***P*<0.01, ****P*<0.001.

Along with transiently reduced *Lgr5* expression and diminished PC granularity in Hsp60$^{\Delta/\Delta ISC}$ mice, PC-derived antimicrobial peptides *Lyz1*, *Defa5*, *Ang4*, and Notch ligand *Dll4* were significantly reduced at day 0 and day 2. Yet, the expression was regained at day 4 and day 6, indicating that dysfunctional PCs might be replaced by mature and functional PCs (**Figure 18D**). Furthermore, representative immunofluorescent stainings for Defensin4 (Defa4), UEA1, and MMP7 showed decreased Defa4^{+} cells starting from day 0 and diminished numbers of UEA1^{+} and MMP7^{+} cells, starting from day 2 in the crypt base of Hsp60$^{\Delta/\Delta ISC}$ mice (**Figure 18E,F**), confirming reduced PC function. Since Defa4 and lysozyme antibodies arise from the same species, co-staining of Defa4 and lysozyme was not possible. However, UEA1 staining was performed to detect PCs in the crypt base. UEA1 binds to fucosylated glycoproteins that are secreted by different cells, including PCs, serving as a broader marker for PCs [144]. Representative images showed a decline in numbers of UEA1^{+} cells in upper crypts of Hsp60$^{\Delta/\Delta ISC}$ mice compared to Hsp60$^{fox/flox}$ controls, indicating that in addition to stem cell niche, mitochondrial dysfunction might target cells with fucosylated glycoproteins (**Figure 18E,F**). Unexpectedly, Defa4 staining failed to stain the PC granules. Therefore, we used bright-field microscopy to further characterize Defa4 expression in PCs with granularity. Cells with diminished Defa4 or UEA1 expression were confirmed to be dysfunctional PCs based on the bright-field microscopy (**Figure 18E**) Defa4, UEA1, and MMP7 signals re-appeared at day 6 in highly granular PCs (**Figure 18E,F**)**.**

Lgr5^{+} ISCs and PC granularity were reduced at D2 after the end of tamoxifen treatment in Hsp60$^{\Delta/\Delta ISC}$ mice (**Figure 17A** and **Figure 18**). Mitochondrial dysfunction was shown to be associated with increased apoptosis or necrosis of the epithelium [106]. Therefore, TUNEL staining was performed to determine if the transient reduction of *Lgr5*$^{+}$ ISCs and loss of PC granularity is due to apoptosis in these cells, which could be mediated by mitochondrial dysfunction in Hsp60$^{\Delta/\Delta ISC}$ mice. Using the *Hsp60*$^{flox/flox}$; *Lgr5*CreER^{T2}; IRES-*Egfp*^{Tg} mice, in which the expression of green fluorescent protein (eGFP) is driven from the *Lgr5* locus, enables us to follow the alterations in *Lgr5*$^{+}$ stem cells upon mitochondrial dysfunction [62]. Screening of TUNEL double staining with eGFP or lysozyme on 3-4 sections per genotype and an average of 150 crypts at day 0 and day 2 revealed the absence of apoptotic cell death in *Lgr5*$^{+}$ stem cells and PCs, respectively. These are the time-point when the most pronounced loss of *Lgr5*$^{+}$ expression was detected (**Figure 19A,B**). The absence of cleaved caspase 3 (CC3) staining, as an additional apoptosis marker, at day 0 and day 2 further confirmed the absence of enhanced

apoptosis at early time-points after the end of tamoxifen treatment. However, apoptosis was increased in crypt bases at day 4 and day 6, indicating that dysfunctional PCs might be removed from epithelium through apoptosis-mediated mechanisms (**Figure 19C**).

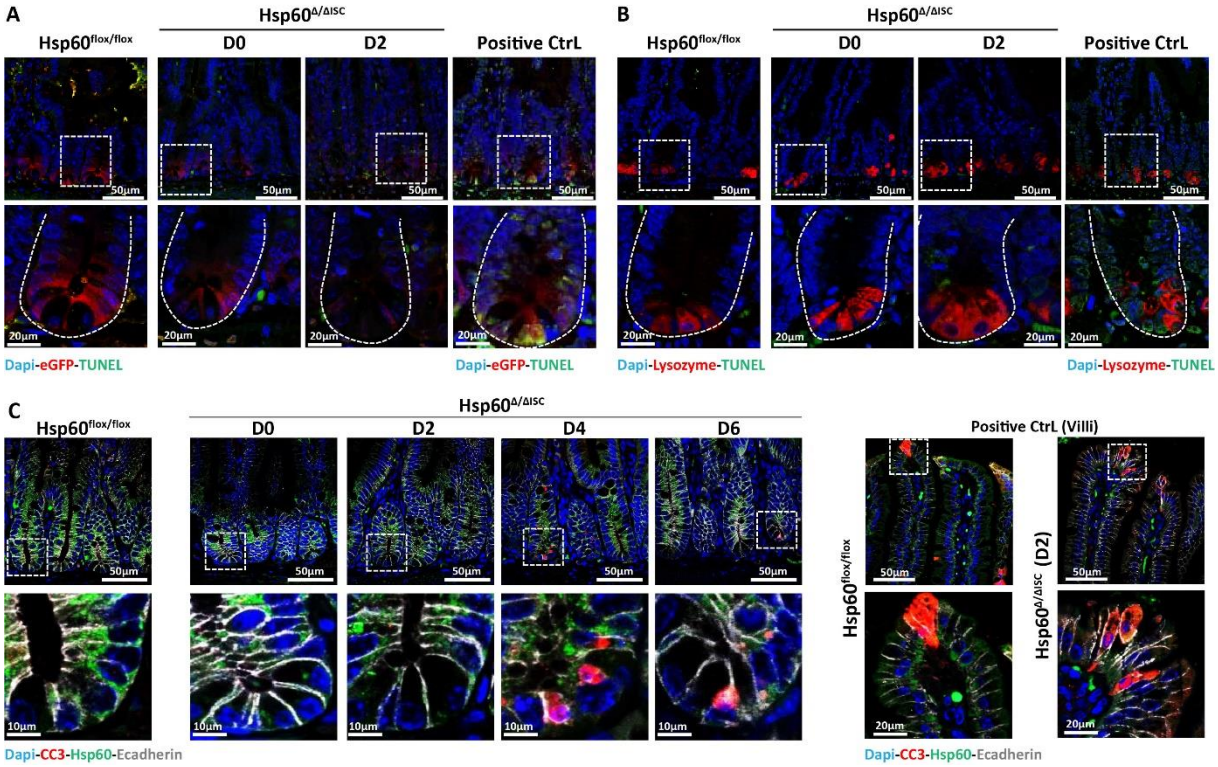

Figure 19 Enhanced apoptosis in crypt bases is only detectable subsequent to reduced stemness and the occurrence of dysfunctional PCs

(**A, B**) IF co-staining of TUNEL (green) and eGFP (**A**; red) / lysozyme (**B**; red) counterstained with Dapi (nuclei, blue) in ileal tissue sections of the Hsp60$^{fox/flox}$ and Hsp60$^{\Delta/\Delta ISC}$ mice (600x) at indicated time-points after induction of the Hsp60 knockout. Lower panel shows magnifications; Dotted lines indicate crypt; rDNaseI treated sections served as a positive control for the TUNEL assay. Yellow staining indicates the overlap of eGFP and TUNEL staining. (**C**) Representative IF images for co-staining of Hsp60 (green), cleaved caspase 3 (CC3; red) and E-cadherin (IEC borders, gray) counterstained with Dapi (nuclei, blue) in ileal tissue sections of the Hsp60$^{fox/flox}$ and Hsp60$^{\Delta/\Delta ISC}$ mice (600x) at indicated time-points after induction of the Hsp60 knockout, including magnifications (3600x); Lower panel shows the positive CC3 staining in villi, serving as a positive control. Screening was performed on N=3-4 sections and an average of 50 crypts per section.

4.6.2 *Hsp60* deletion leads to reduced proliferation in the crypt base without affecting the proliferative zone

Determining the impact of ISC-specific Hsp60 deficiency on the epithelial proliferative status, ileal tissue sections were co-stained for Hsp60 and the proliferation marker Ki67. We observed complete loss of proliferation in the crypt base of Hsp60$^{\Delta/\Delta ISC}$ mice at day 0 and day 2 (**Figure 20A**).

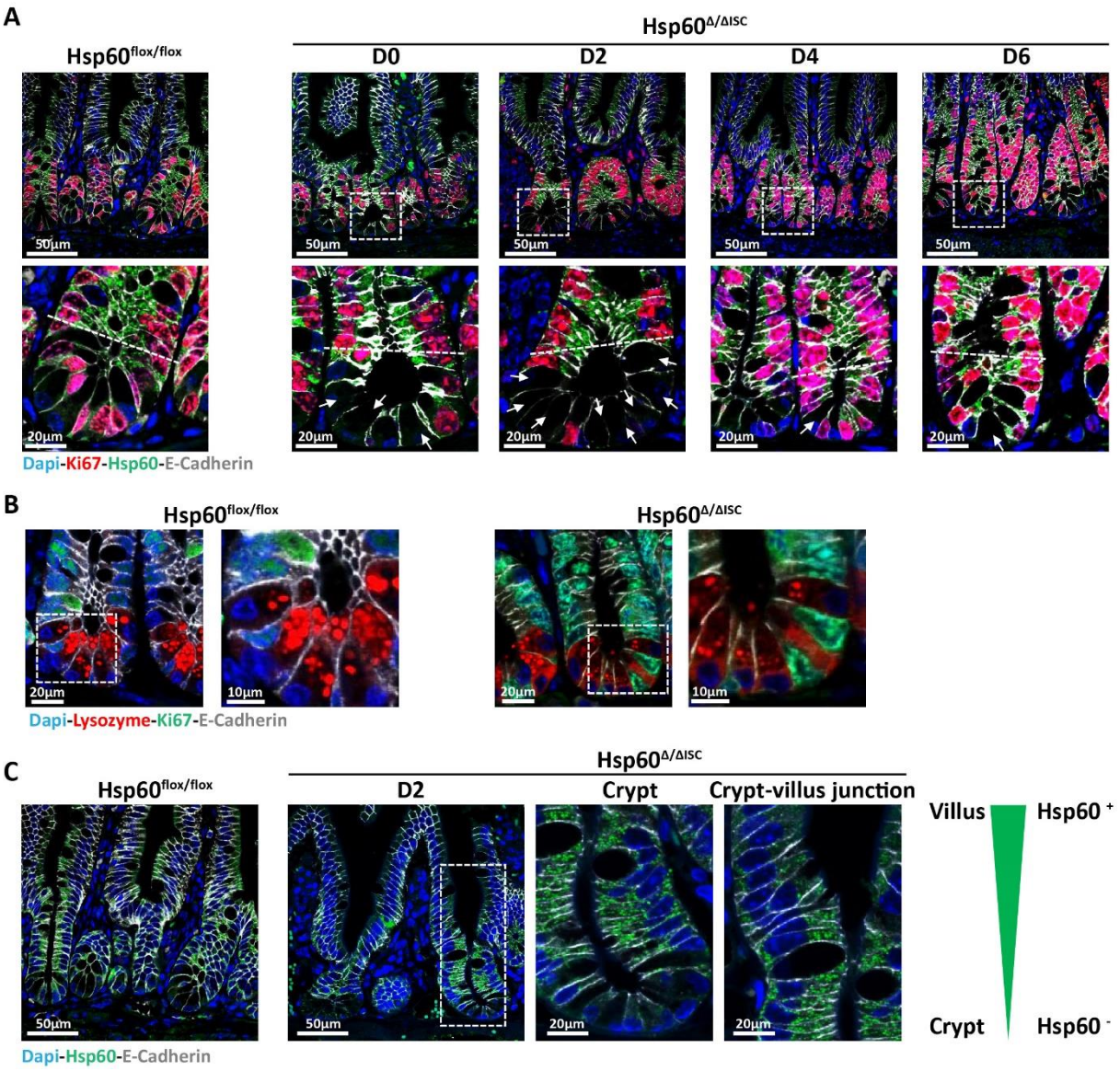

Figure 20 Hsp60 negative cells are Ki67 negative

(**A**) IF co-staining of Hsp60 (green), Ki67 (red) and E-cadherin (IEC borders, gray) counterstained with Dapi (nuclei, blue) in ileal tissue sections of the Hsp60$^{fox/flox}$ and Hsp60$^{\Delta/\Delta ISC}$ mice (600x) at indicated time-points after induction of the Hsp60 knockout. Lower panel shows the magnifications (2400x); Dashed line illustrates the crypt base area: Arrows indicate the Hsp60 negative – Ki67 negative (non-proliferative) cells. (**B**) Representative IF co-staining of Ki67 (green), E-cadherin (IEC borders, gray) and lysozyme (red) (2400x) including magnification (3600x). Arrows show the dysfunctional PCs. In all cases, Dapi stained the nuclei in blue. (**C**) Representative IF co-staining of Hsp60 (green) counterstained with Dapi (nuclei, blue; 600x), including magnifications (2400x). Screening was performed on N=3-4 sections and an average of 50 crypts per section.

Similar to TNF$^{\Delta ARE}$ mice (**Figure 9B**), dysfunctional PCs showed no ki67 staining, indicating that these cells do not de-differentiate to *Lgr5*$^{+}$ stem cells (**Figure 20B**). Despite the loss of Hsp60 and Ki67 signal in the crypt base, the transit-amplifying zone remained completely Hsp60 and Ki67 positive (**Figure 20A**). Additionally, Hsp60 expression was not lost in the upper crypts and villi (**Figure 20C**). Hsp60 positive crypt base localized cells at day 4 and day 6 regained the Ki67 expression. Together, these data suggest that apoptotic cell death might extrude Hsp60 negative, non-proliferative dysfunctional cells from the crypt base (**Figure 20A**).

Despite the presence of highly proliferative and Hsp60 positive transit-amplifying zone, dysfunctional PCs that were differentiated from the transit-amplifying zone were stained negative for Hsp60. However, Hsp60 co-staining with Mucin 2 (Muc2; a marker for goblet cells), Chromogranin A (ChgA; a general marker for enteroendocrine cells), and Doublecortin-like kinase 1 (Dclk1; a marker for tuft cells) indicated the presence of Hsp60 in these secretory cell-types at day 0 and day 2 after *Hsp60* deletion. This indicates that *Lgr5*$^{+}$ stem cells that suffered from mitochondrial dysfunction acquired only lysozyme expression, while other cell-types remained non-affected from the impact of mitochondrial dysfunction (**Figure 21A,B,C**).

4.6.3 Mitochondrial impairment in *Lgr5*$^{+}$ stem cells drives a transition towards dysfunctional Paneth cells

Parallel efforts to characterize the PC and stem cell phenotypes demonstrated an increased abundance of *Lgr5*$^{+}$- Lyz^{+} double-positive cells in Hsp60$^{\Delta/\Delta ISC}$ mice (**Figure 22A**). In line with reduced *Lgr5*$^{-}$- Lyz^{+} cells, the proportion of *Lgr5*$^{+}$- Lyz^{+} double-positive cells increased in both ileum and jejunum, reaching the highest numbers at day 2 and day 4 (**Figure 22B-E**). The number of *Lgr5*$^{+}$- Lyz^{+} double-positive cells dropped at day 6, which could be an indicator for the replacement of these cell-types, de-differentiation, or apoptotic cell death (**Figure 22B,C**). Representative eGFP co-stainings with lysozyme demonstrated the presence of eGFP^{+}- Lyz^{+} double-positive cells in Hsp60$^{\Delta/\Delta ISC}$ mice. Together, these data indicate that dysfunctional PCs might originate from *Lgr5*$^{+}$ stem cells (**Figure 22E**). Following *Hsp60* deletion specifically in *Lgr5*$^{+}$ ISCs, the majority of cells in the crypt base were Hsp60 negative at day 0 and day 2. Confirming that dysfunctional PCs arise from mitochondrial function-impaired *Lgr5*$^{+}$ stem cells. Co-staining of lysozyme and Hsp60 revealed an increased proportion of Lyz^{+} cells with a lack of Hsp60 signal (Lyz^{+}- Hsp60^{-} cells) at day 0 and day 2 (**Figure 22F,G**). Subsequently, the proportion of Lyz^{+}- Hsp60^{-} cells decreased at day 4 and day 6, reaching control levels in jejunum at day 6 (**Figure 22F**). Mainly dysfunctional PCs with reduced granularity and diffuse cytoplasmic lysozyme staining seemed to be Hsp60 negative, indicating that *Lgr5*$^{+}$ stem cells that suffer from mitochondrial dysfunction directly differentiate to Hsp60 negative PCs (**Figure 22H**).

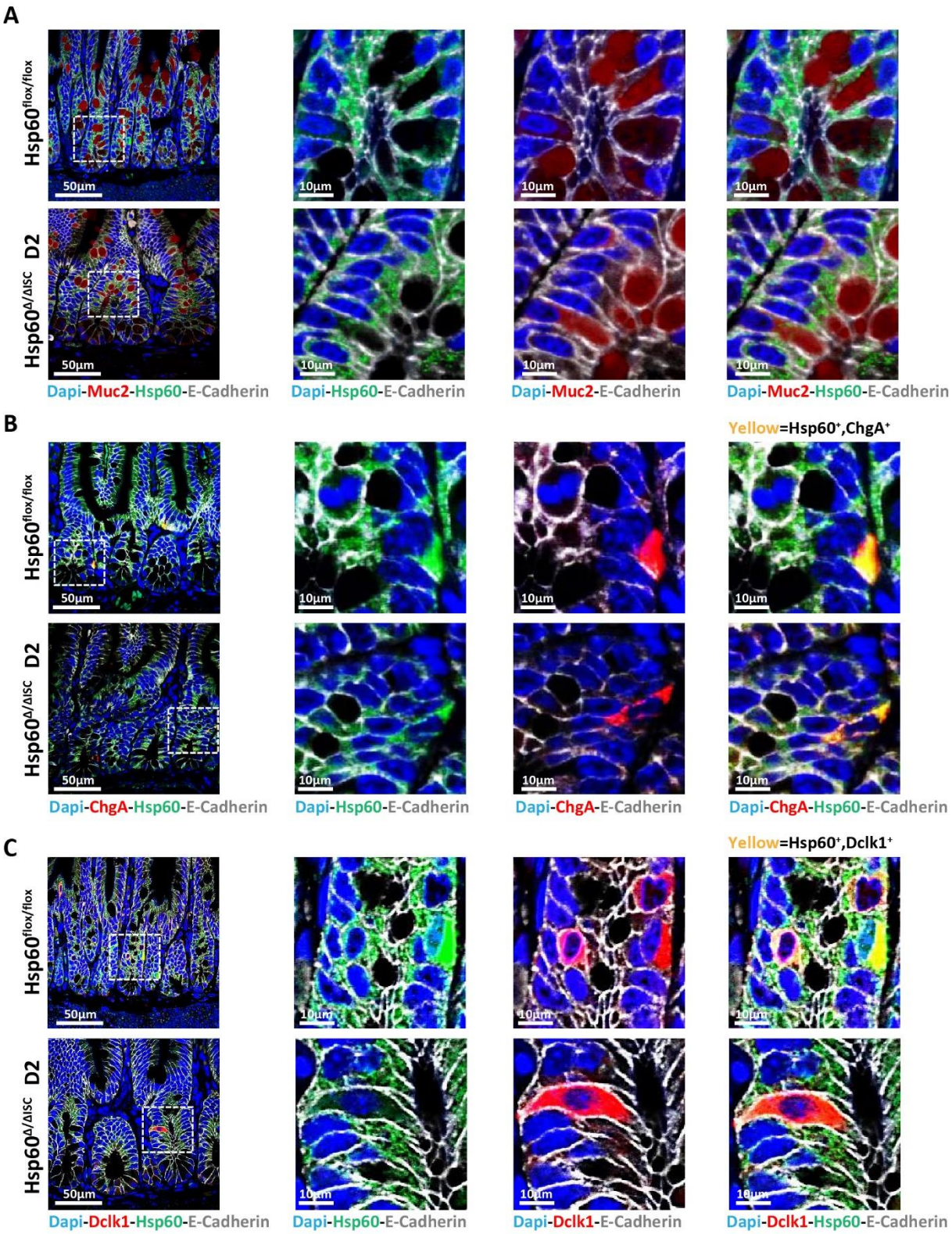

Figure 21 Apart from PCs, additional IEC-belonging secretory lineages remain Hsp60 positive

(**A, B, C**) IF co-staining of Hsp60 (green), Muc2 (**A**; goblet cells; red)/ ChgA (**B**; enteroendocrine cells; red)/ Dclk1 (**C**; tuft cells; red) and E-cadherin (IEC borders, gray) counterstained with Dapi (nuclei, blue) in ileal tissue sections of the $Hsp60^{fox/flox}$ and $Hsp60^{\Delta/\Delta ISC}$ mice (600x) at indicated time-points after induction of the Hsp60 knockout including magnifications (3600x). Muc2, ChgA and Dclk1 positive cell remain Hsp60 positive throughout the experiment.

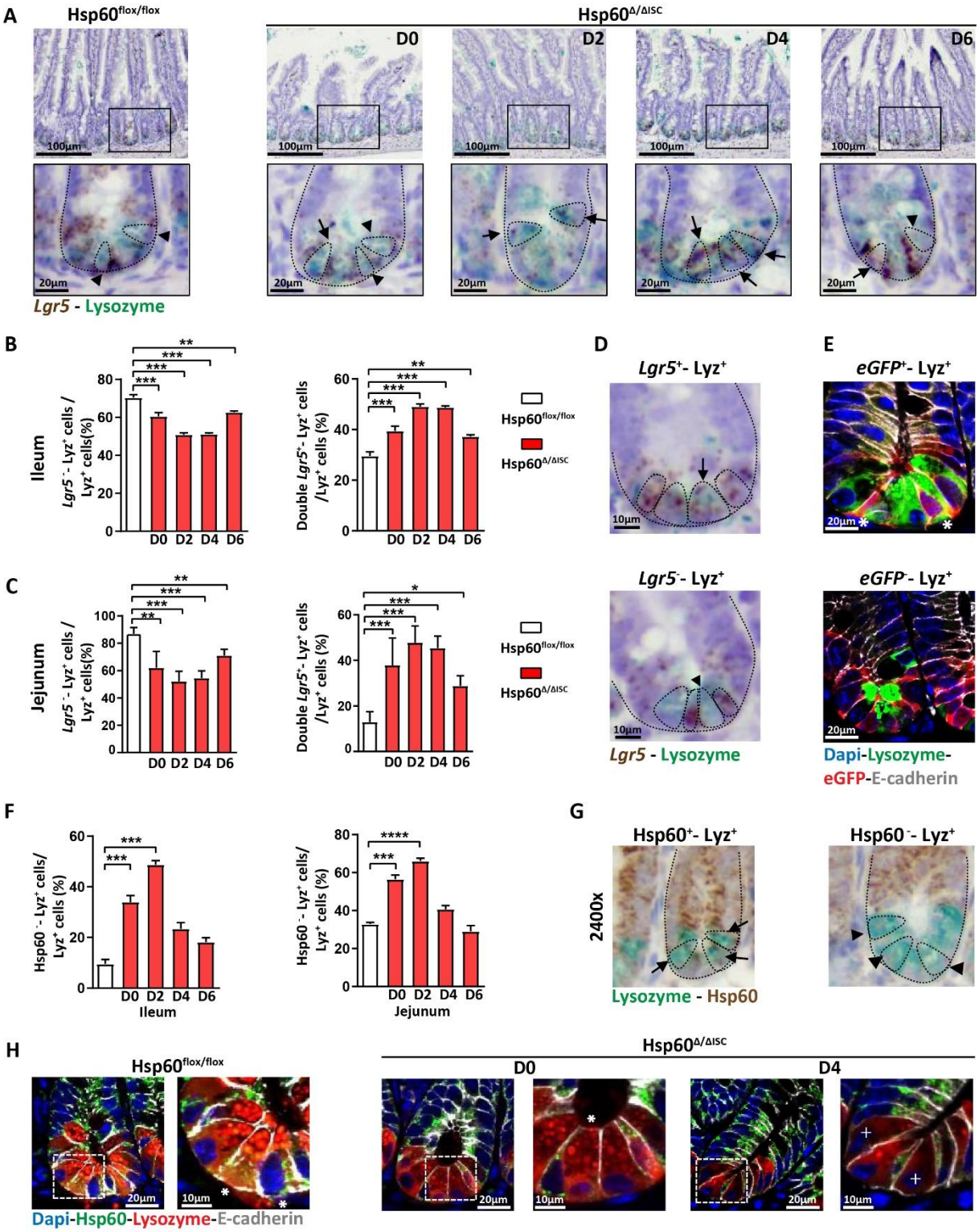

Figure 22 Dysfunctional PCs originate from *Lgr5*$^{+}$ stem cells suffering from impaired mitochondrial function

(**A**) *Lgr5 in situ* hybridization (brown) and IHC co-staining for lysozyme (turquoise) in the ileum of Hsp60$^{fox/flox}$ and Hsp60$^{\Delta/\Delta ISC}$ mice (400x), lower panel shows the magnifications (2400x); Dotted lines indicate crypt and cell borders, arrow-heads indicate single Lyz^{+} cells, arrows indicate *Lgr5*$^{+}$ – Lyz^{+} double-positive cells. (**B**) Quantification of the proportion of *Lgr5* negative, Lyz single-positive cells and the proportion of *Lgr5*$^{+}$ – Lyz^{+} double-positive cells over time in ileal tissues. (**C**) Represents the same quantifications as in (**B**) but in the jejunum. (**D**) Representative pictures of *Lgr5*$^{+}$ – Lyz^{+} double-positive cells, and *Lgr5* negative, Lyz single-positive cells;

Dotted lines indicate crypt and cell borders, arrows indicate *Lgr5*$^{+}$ – Lyz^{+} double-positive cells, arrow-heads indicate *Lgr5* negative, Lyz single-positive cells. (**E**) IF co-staining of eGFP (red), lysozyme (green) and E-cadherin (IEC borders, grey) counterstained with Dapi (nuclei, blue). Asterisk indicate the *eGFP*$^{+}$ – Lyz^{+} cells in yellow. (**F**) Quantification of Hsp60 negative-Lyz single-positive cells in the ileum (left) and jejunum (right) of Hsp60$^{fox/flox}$ and Hsp60$^{\Delta/\Delta ISC}$ mice (N=4). (**G**) Representative images of IHC co-staining for Hsp60 (brown) and lysozyme (turquoise) used for quantification; dotted lines indicate crypt and cell borders, arrow indicate Hsp60^{+}–Lyz^{+} double-positive cells, arrow-heads indicate Hsp60^{-}-Lyz^{+} cells. (**H**) IF co-staining of Hsp60 (green), lysozyme (red), and E-cadherin (IEC borders, grey) counterstained with Dapi (nuclei, blue; 1800x), including magnifications (3600x). Asterisks indicate Hsp60^{+}–Lyz^{+} double-positive granular Paneth cells, crosses indicate Hsp60^{-}-Lyz^{+} cells with a diffuse Lyz staining. Statistical analyses were performed by One-way analysis of variance (ANOVA) followed by Tukey test. Asterisks indicate significant differences **P*<0.05, ***P*<0.01, ****P*<0.001.

4.6.4 Reserve stem cells expand in response to loss of *Lgr5*$^{+}$ cells

Reserve stem cells are compensatory cell-types that contribute to the repopulation of crypts upon *Lgr5*$^{+}$ stem cell loss [147]. Therefore, we performed *in situ* hybridization for *Olfm4* and *HopX*, markers for reserve stem cells, including label-retaining cells, on small intestinal tissue sections from Hsp60$^{\Delta/\Delta ISC}$ mice. Since both markers entirely covered the crypt base area and the cell borders were not distinguishable, we quantified the distance of the highest *Olfm4* positive signal to the crypt base and the *HopX* positive area. The expression of *Olfm4* and *HopX* were transiently enhanced at day 2, the time-point with the most pronounced *Lgr5*$^{+}$ stem cell loss. This indicates that upon mitochondrial impairment, both populations of uninfluenced active stem cells (*Olfm4* positive cells) and reserve stem cells (*HopX* positive cells) may compensate for the loss of *Lgr5*$^{+}$ stem cells (**Figure 23A,B**).

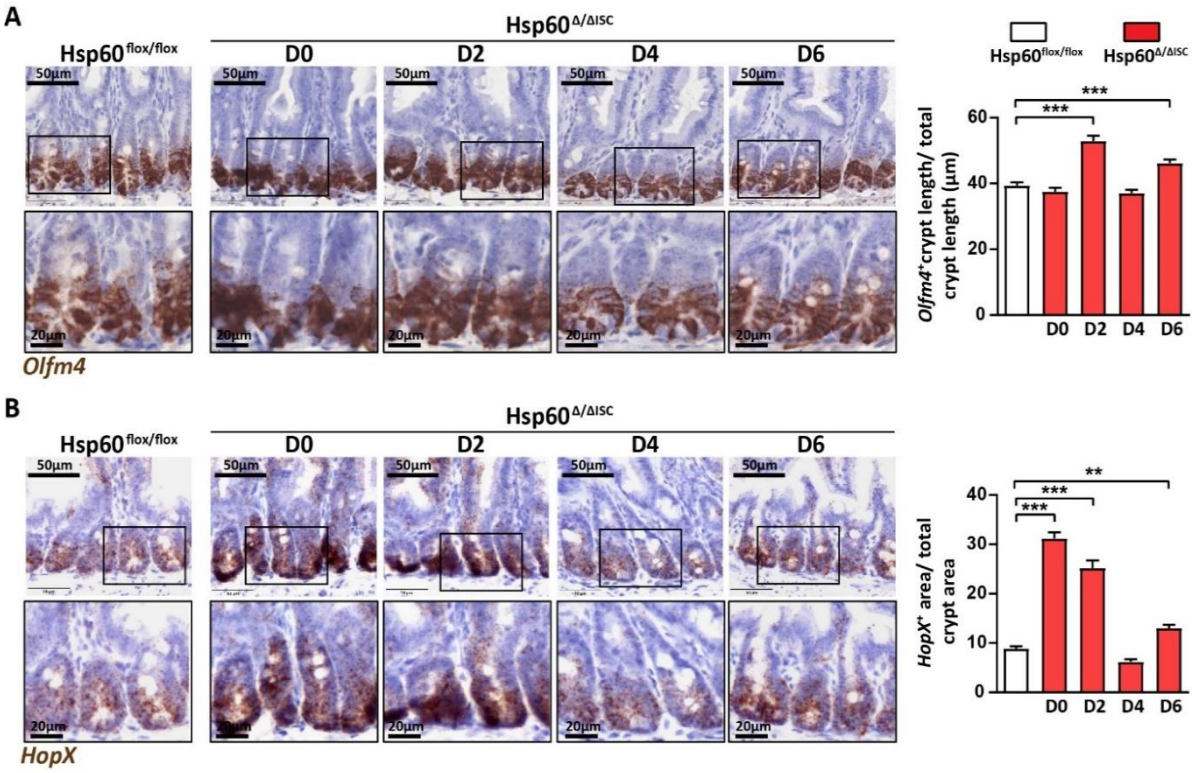

Figure 23 *HopX* and *Olfm4* positive cells expand in response to loss of *Lgr5*$^{+}$ ISCs

Small intestinal tissue sections from Hsp60$^{\Delta/\Delta ISC}$ mice and Hsp60$^{flox/flox}$ controls were analyzed at different time points after the end of tamoxifen treatment. (**A**) Left: Representative images of *Olfm4 in situ* hybridization (600x) including magnifications; Right: Quantification of the distance of the most upper *Olfm4* positive cell to the crypt

ground normalized to crypt length (N=3). (**B**) Left: Representative images of *HopX in situ* hybridization (600x) including magnifications; Right: quantification of the area positive for *Hopx* normalized to crypt area (N=3). Statistical analyses were performed via One-way analysis of variance (ANOVA) followed by Tukey test. Asterisks indicate significant differences *P<0.05, **P<0.01, ***P<0.001.

4.6.5 Autophagy is induced in the crypt base upon mitochondrial dysfunction and inflammation

Autophagy is a process that contributes to the recruitment of cellular energy sources and the removal of the dysfunctional organelle. Alterations in autophagy-related genes have been linked to changes in mitochondrial integrity and loss of PC granules [28]. Parallel to morphologic alteration in stem cell niche, light chain 3 (LC3) staining and transcriptional analysis of *Map1lc3α* showed induction of autophagy in the crypt base of Hsp60$^{\Delta/\Delta ISC}$ mice at day 2 and day 4, time-points with a low proportion of highly granular PCs (**Figure 24A,B**). Similarly, inflamed TNF$^{\Delta ARE}$ mice depicted induced autophagy in the crypt base (**Figure 24C,D**). This indicates that the induced autophagy in the crypt base could be a possible approach to maintain the survival of dysfunctional cell-types that appeared due to impaired mitochondrial function.

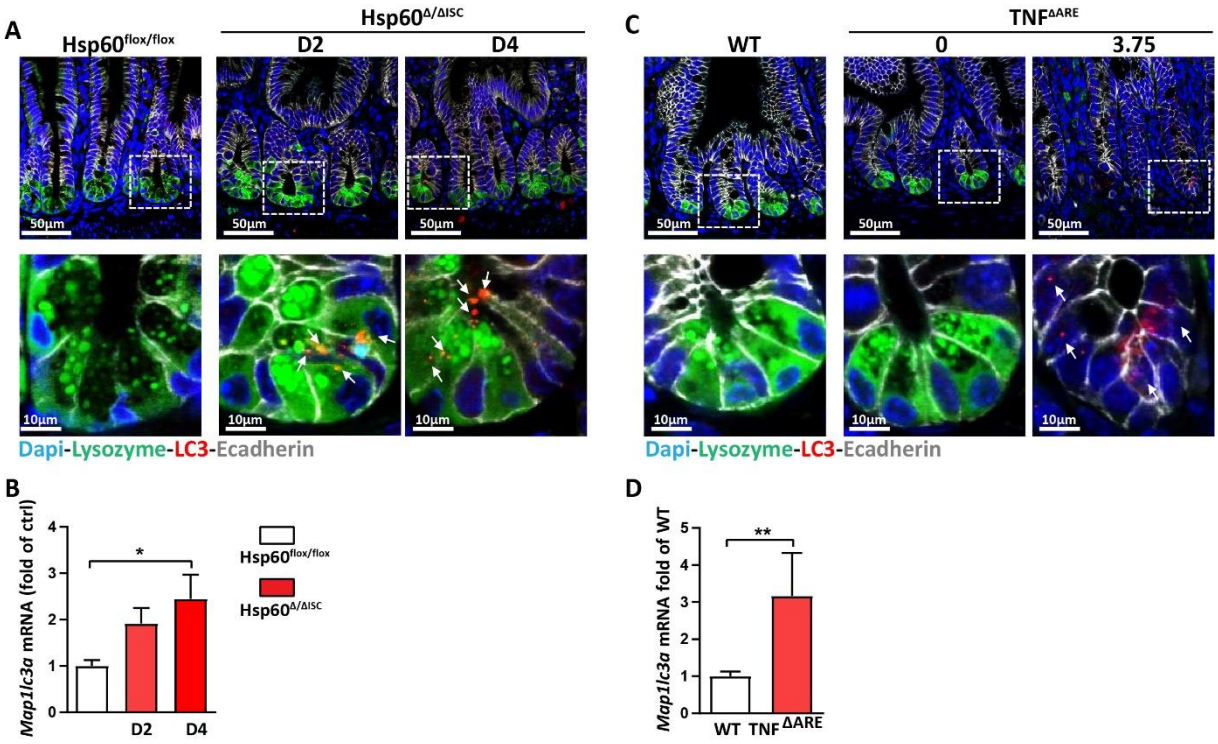

Figure 24 Autophagy is induced in the crypt base of mouse models for mitochondrial dysfunction and inflammation

(**A,C**) Representative IF co-staining of lysozyme (green), LC3 (red) and E-cadherin (IEC borders, gray) counterstained with Dapi (nuclei, blue) in ileal tissue sections of Hsp60$^{fox/flox}$ and Hsp60$^{\Delta/\Delta ISC}$ mice (600x) at indicated time-points after induction of the Hsp60 knockout (**A**) and in WT and TNF$^{\Delta ARE}$ mice (**C**). The lower panel shows the magnifications; Arrows indicate LC3 positive signal. (**B**) qRT-PCR analysis of the *Map1lc3a* gene in IEC isolates derived from Hsp60$^{fox/flox}$ and Hsp60$^{\Delta/\Delta ISC}$ mice (each case N=4) at day 2 and day 4 with indicated histopathological scores. (**D**) qRT-PCR analysis of the *Map1lc3a* gene in primary ileal crypt isolates derived from TNF$^{\Delta ARE}$ mice (N=5). Statistical analyses were performed by unpaired t-tests. Asterisks indicate significant differences *P<0.05, **P<0.01.

4.6.6 Intestinal epithelial cell-specific *Hsp60* deletion causes more profound alterations in the stem cell niche phenotype

Berger *et al.* previously showed the association between intestinal epithelial cell (IEC)-specific *Hsp60* deletion ($Hsp60^{\Delta/\Delta IEC}$) with mitochondrial dysfunction and reduced stemness. In contrast to knockout crypts, hyper-proliferative nodules in this mouse model were shown to be entirely *Olfm4* positive [62]. Since *Hsp60* in these mice is deleted in all epithelial cells, including PCs, we characterized the ISC niche function, and more specifically, the PC phenotype in $Hsp60^{\Delta/\Delta IEC}$ mice. Hsp60 loss in IECs was associated with reduced crypt numbers in these mice (**Figure 25A**). Low numbers of $Lgr5^{+}$ dots, representing *Lgr5* transcripts, were detectable in crypts of $Hsp60^{\Delta/\Delta IEC}$ mice. Therefore, instead of classifying crypts to crypts with high (>10 *Lgr5* transcripts) or low (<10 *Lgr5* transcripts) *Lgr5* expression, crypts were categorized as positive or negative for *Lgr5* expression. Characterizing the role of *Hsp60* deletion in IECs on stem cell niche regulation, we observed significantly reduced numbers of crypts with *Lgr5* expression in the crypt base of $Hsp60^{\Delta/\Delta IEC}$ mice. Furthermore, the number of *Lgr5* negative crypts increased. The majority of Hsp60 knockout (KO) crypts were *Lgr5* negative, whereas the nodules remained *Lgr5* positive (**Figure 25A-C**). Parallel efforts to characterize the PC phenotype showed an increased proportion of $Lgr5^{+}$- Lyz^{+} double-positive cells in KO crypts (**Figure 25B**). Additionally, Hsp60 deficiency in IECs was associated with reduced numbers of Lyz^{+} cells in both KO crypts and Hsp60 positive nodules (**Figure 25D-F**). Along with reduced stem cells and PCs, the proportion of highly granular PCs significantly dropped at D2 after finishing tamoxifen treatment. However, loss of PC granularity was more pronounced in KO crypts (50%) compared to nodules (20%) (**Figure 25E,G**). Interestingly, we observed a more profound reduction in PC granularity of $Hsp60^{\Delta/\Delta IEC}$ compared to $Hsp60^{\Delta/\Delta ISC}$ mice (**Figure 25F**), indicating that mitochondrial dysfunction in PCs causes PC dysfunction in mature PCs. Lysozyme staining confirmed the presence of non-granular PCs in KO crypts, whereas PCs in nodules remained mainly granular (**Figure 25D**).

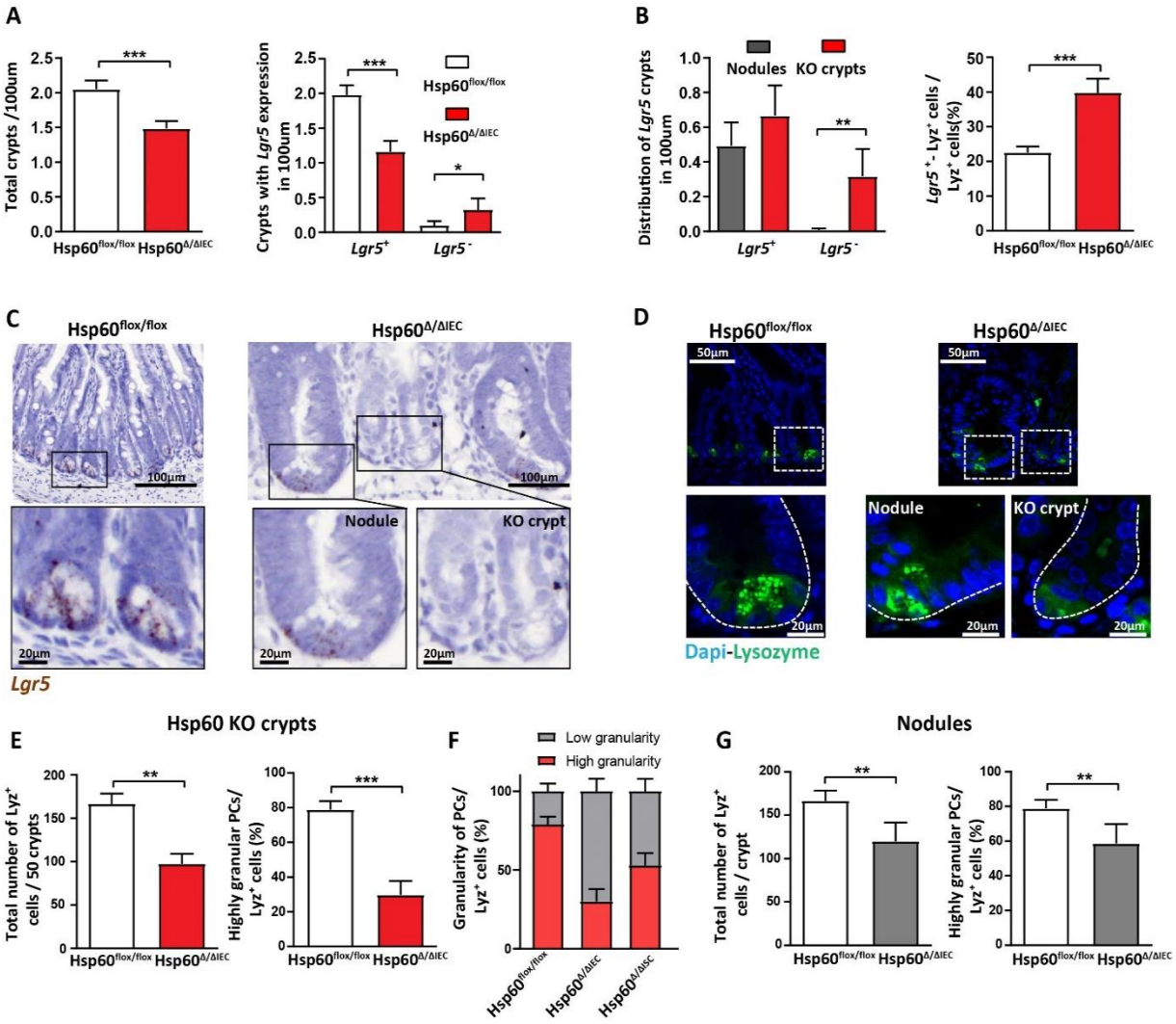

Figure 25 IEC-specific *Hsp60* deletion causes a more profound PC dysfunction compared to Hsp60$^{\Delta/\Delta ISC}$

(**A**) Quantification of the total numbers of crypts and the number of *Lgr5*$^{+}$ and *Lgr5*$^{-}$ crypts in 100µm small intestine of the Hsp60$^{fox/flox}$ and Hsp60$^{\Delta/\Delta IEC}$ mice. (**B**) Quantification of distribution of the *Lgr5*$^{+}$ and *Lgr5*$^{-}$ nodules and KO crypts in 100µm small intestine of the Hsp60$^{\Delta/\Delta IEC}$ mice (left; N=5); Quantification of the proportion of *Lgr5*$^{+}$ – Lyz^{+} double-positive cells in small intestine of the Hsp60$^{fox/flox}$ and Hsp60$^{\Delta/\Delta IEC}$ mice at D2 after induction of the knockout (right; N=5). (**C**) *Lgr5 in situ* hybridization (brown) in small intestine of the Hsp60$^{fox/flox}$ and Hsp60$^{\Delta/\Delta IEC}$ mice including magnifications. (**D**) Representative IF images of lysozyme staining (green) counterstained with Dapi (nuclei, blue) including magnifications, showing the granular and non-granular PCs in nodules and KO crypts; Dotted line indicate the crypt structure. (**E**) Quantification of the total numbers of Lyz^{+} cells and the proportion of highly granular PCs in small intestinal Hsp60 deficient crypts (KO crypts) (N=5) of the Hsp60$^{fox/flox}$ and Hsp60$^{\Delta/\Delta IEC}$ mice at D2 after induction of the knockout. (**F**) Direct comparison of PC granularity between IEC- and ISC-specific Hsp60 deleted mice. Data shown for Hsp60$^{\Delta/\Delta IEC}$ are presented in (**E**) and for Hsp60$^{\Delta/\Delta ISC}$ are presented in **figure 18C** Ileum (D2). These data are depicted for convenient comparison. (**G**) Same quantifications as in (**E**) but in Hsp60 positive nodules (N=5). (Statistical analyses were performed by unpaired t-tests. Asterisks indicate significant differences **P*<0.05, ***P*<0.01, ****P*<0.001.

4.7 Inflamed crypts derived from TNF$^{\Delta ARE}$ mice fail to generate organoids

Small intestinal *ex vivo* organoid culture is an important model for investigating growth, tissue renewal, and epithelial homeostasis. Additionally, it offers an opportunity to characterize signals that are important for the maintenance of the stem cell niche function [148]. To identify the role of already established inflammation on the growth of organoids, primary ileal crypts were isolated from inflamed and non-inflamed TNF$^{\Delta ARE}$ mice. Staining of ileal tissue sections from inflamed mice showed reduced numbers of lysozyme positive PCs (**Figure 26A**). Additionally, inflammation was associated with reduced expression of stem cell markers *Lgr5* and *Olfm4*, as well as diminished *Lyz* expression in isolated crypts from inflamed mice (**Figure 26B**). Investigating the impact of reduced stemness and PC dysfunction on the establishment of organoid culture, we seeded the isolated crypts in matrigel and medium containing EGF, noggin, and R-spondin (CCM). It was previously shown that this medium supports the growth of all epithelial sub-types in organoid culture [149]. Interestingly, crypts derived from inflamed TNF$^{\Delta ARE}$ mice successfully formed spheres at day 1 and day 2 after seeding, similar to WT or non-inflamed TNF$^{\Delta ARE}$ mice-derived crypts. However, the proportion of living organoids significantly dropped starting from day 3, indicating that inflamed TNF$^{\Delta ARE}$ mice-derived organoids failed to grow and proliferate. These organoids failed to grow at day 5 and they were completely degraded at day 7 (**Figure 26C**). Comparing inflamed and non-inflamed TNF$^{\Delta ARE}$ mice, ileal organoids derived from inflamed TNF$^{\Delta ARE}$ mice completely failed to grow at day 5. The remaining crypts displayed ~50% circular appearance, and the majority of remaining crypts showed reduced budding (1-2 buds), suggesting that inflammation negatively affects the *de novo* crypt formation (**Figure 26D**). Confirming *in vivo* observations with reduced crypt numbers in the jejunum of the inflamed TNF$^{\Delta ARE}$ mice (Error! R eference source not found.**D**), jejunal crypts derived from these mice showed reduced ability to form organoids and grow. However, no defect was observed in *de novo* crypt formation. Together, these data indicate that the presence of stem cells and mature PCs have a positive impact on *de novo* crypt formation (**Figure 26E**). Ileal organoids derived from non-inflamed TNF$^{\Delta ARE}$ and WT mice showed no significant differences in the proportion of living organoids and *de novo* crypt formation at day 5 after seeding. These data suggest that inflammation and not genotype impairs the growth (**Figure 26F**).

Wnt factors arising from PCs or mesenchyme are essential for the maintenance of *Lgr5*$^{+}$ stem cells. Inflammation is associated with PC loss. To test if Wnt-conditioned media can compensate for PC-derived Wnt factors, we applied this media to TNF$^{\Delta ARE}$ organoids directly after crypt isolation. Despite the presence of Wnt factors, we were unable to rescue the growth of inflamed TNF$^{\Delta ARE}$ organoids after 5 days of seeding (**Figure 26G**). These data could suggest that altered stem cell niche function, including reduced *Lgr5*$^{+}$ stem cells and PCs, contribute to the inflammation-mediated growth defects.

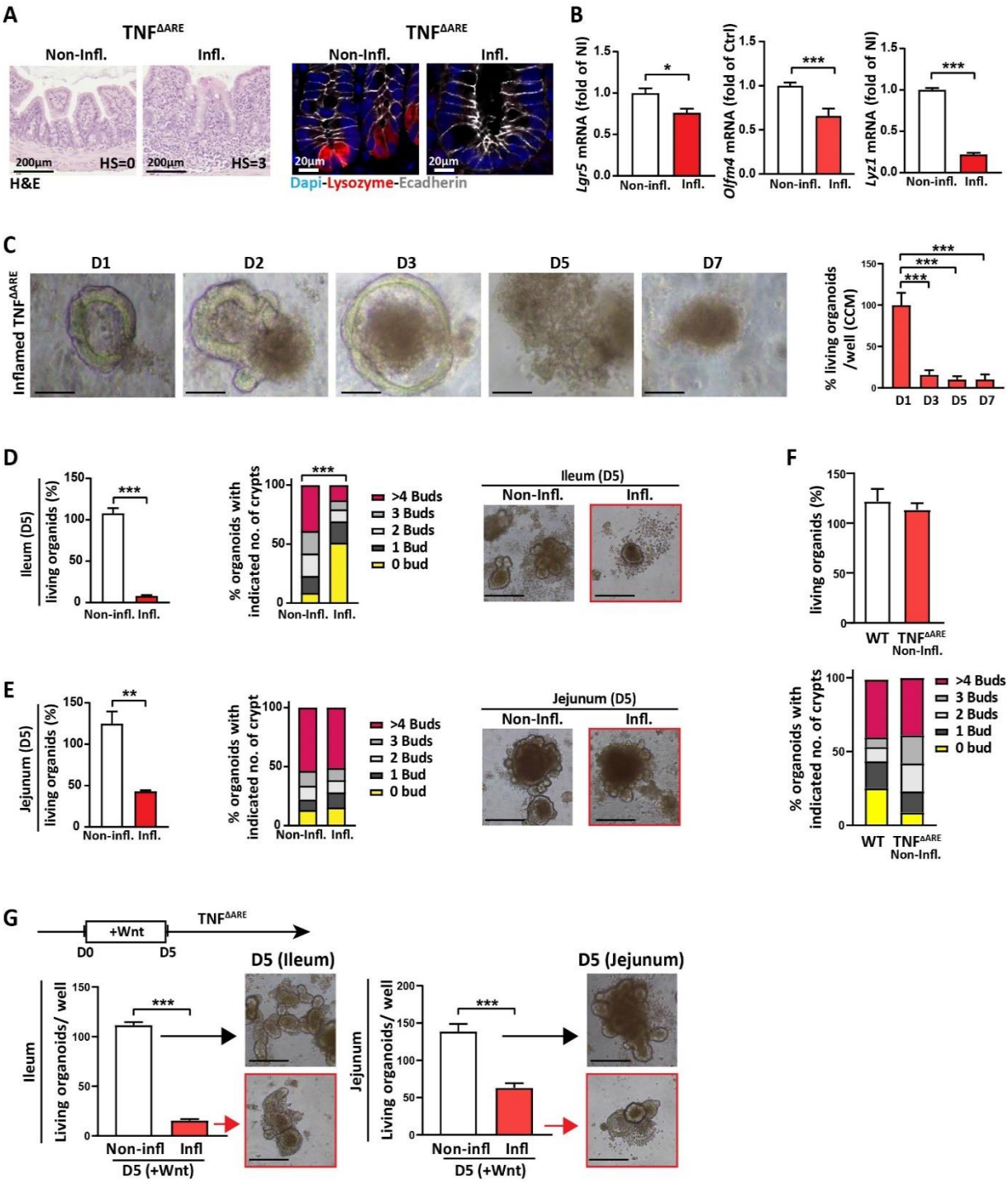

Figure 26 Inflamed TNF$^{\Delta ARE}$ mice-derived organoids show growth defects

(**A**) Representative pictures of ileal sections; Left: H&E staining with histopathological score indicated; Right: IF co-staining of lysozyme (red), and E-cadherin (grey) counterstained with Dapi (nuclei, blue), showing absence of PCs in inflamed tissue. (**B**) qRT-PCR analysis of primary ileal crypts for *Lgr5* and *Lyz1* (N=6). (**C**) Monitoring the growth of ileal organoids derived from inflamed TNF$^{\Delta ARE}$ mice at mentioned time-points (N=4) on CCM; Proportion of living organoids adjusted to the numbers observed at day 1. (**D,E**) Characterization of intestinal organoids derived from ileal (**D**) and jejunal (**E**) crypts at day 5 of *ex vivo* culture (infl.: N=10 and non-infl.: N=4). Left: Proportion of living organoids; middle: quantification of *de novo* crypt formation (budding); right: representative bright field pictures. (**F**) Characterization of intestinal organoids derived from ileal crypts of WT and non-inflamed TNF$^{\Delta ARE}$ mice at day 5 of *ex vivo* culture. Upper graph: proportion of living organoids; Lower graph: quantification of *de novo* crypt formation (budding) (WT: N=3, non-infl.: N=4). (**G**) Ileal (left) and jejunal (right) crypts derived from non-inflamed and inflamed TNF$^{\Delta ARE}$ mice were cultured in commercially available

medium containing Wnt factors (Intesticult) for 5 days. Proportion of living organoids and representative bright field pictures are shown. Scale bars show 200µm. Statistical analyses were performed via unpaired t-tests. For multiple comparisons, One-way analysis of variance (ANOVA) followed by Tukey test was performed. For de novo crypt formation, a Kruskal–Wallis test on ranks followed by Dunns test was performed. Asterisks indicate significant differences *P<0.05, **P<0.01, ***P<0.001.

4.8 Mitochondrial dysfunction in Hsp60$^{\Delta/ISC}$ organoids is associated with altered stem cell niche function

In line with *in vivo* experiments, organoids-derived from Hsp60$^{\Delta/\Delta IEC}$ mice showed growth defects, impaired mitochondrial function as well as reduced stemness. *Hsp60* deletion in IECs of Hsp60$^{\Delta/\Delta IEC}$ mice was associated with increased oxidative stress [62]. Therefore, we investigated the impact of mitochondrial dysfunction that was induced specifically in *Lgr5*$^{+}$ ISCs, on the growth of Hsp60$^{\Delta/\Delta ISC}$ organoids as well as on stem cell niche function. The induction of *Hsp60* knockout *ex vivo* was performed using 4-hydroxy tamoxifen (4-OHT). Two days after passaging, Hsp60$^{\Delta/\Delta ISC}$ small intestinal organoids were treated with 4-OHT for 24h and were sampled at day 2 and day 6 (**Figure 27A**). *Hsp60* expression was measured to confirm the successful gene deletion (**Figure 27B**). In contrast to inflamed TNF$^{\Delta ARE}$ organoids, Hsp60$^{\Delta/\Delta ISC}$ organoids displayed no difference in the growth at day 2 after *Hsp60* deletion. Despite unaltered bud numbers and *de novo* crypt formation at day 2 and day 6, Hsp60$^{\Delta/\Delta ISC}$ organoids depicted a markedly larger area at day 6, which confirmed the enhanced growth of these organoids (**Figure 27C,D**). Transcriptional analyses were performed to verify altered mitochondrial functions after Hsp60 loss in *Lgr5*$^{+}$ stem cells. Upregulation of mt-UPR target genes (*Trb3*, *Atf5*, and *Chop*) and genes involved in mitochondrial oxidative response (*Hif1α*), biogenesis (*Pgc1α*), and fusion (*Mfn2*) confirmed the mitochondrial stress (**Figure 27E**).

Since oxidative stress was induced at day 2, we measured levels of reactive oxygen species (ROS) at this time point. The proportion of living organoids and ROS levels remained unaltered between Hsp60$^{flox/flox}$ and Hsp60$^{\Delta/\Delta ISC}$ organoids. The cleavage of caspase-3 represents the apoptotic responses [150]. Although Caspase 3/7 was not activated at day 2, it was induced at day 3 after *Hsp60* deletion, which indicates induced apoptosis or cell shedding in these organoids. (**Figure 27F**).

To validate the *in vivo* observation of reduced stemness and an elevated proportion of dysfunctional PCs upon mitochondrial impairment, we characterized the stem cell niche in Hsp60$^{\Delta/\Delta ISC}$ organoids. The transcriptional analysis demonstrated reduced *Lgr5* expression at day 2. Additionally, diminished *Olfm4* expression was observed at day 2, the time-point with detectable *Hsp60* downregulation. However, in line with the regain of *Hsp60* expression at day 6, *Olfm4* expression was recovered (**Figure 27G**).

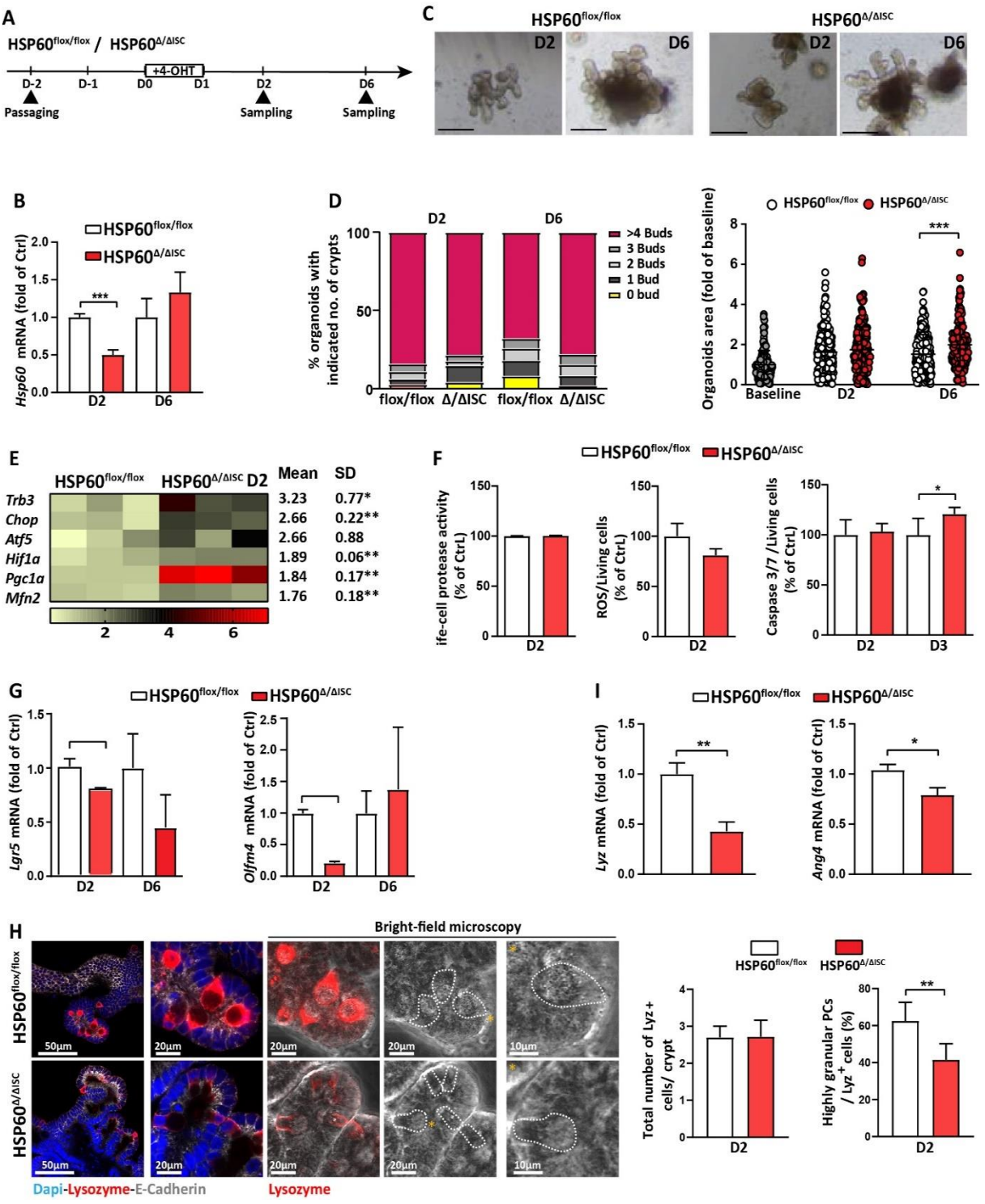

Figure 27 ISC-specific *Hsp60* deletion leads to reduced stemness and PC dysfunction

(**A**) Experimental scheme showing the process of tamoxifen treatment. Organoids derived from Hsp60$^{flox/flox}$ mice were treated with tamoxifen to induce ISC-specific Hsp60 loss and sampled at day 2 and day 6. Tamoxifen treated Cre negative organoids served as a control. (**B**) qRT-PCR analysis of *Hsp60* at D2 and D6 (N=3). (**C**) Representative bright field pictures for Hsp60$^{flox/flox}$ and Hsp60$^{\Delta/\Delta ISC}$ organoids at indicated time-points. Scale bar indicates 200µm. (**D**) Left: quantification of *de novo* crypt formation (budding); Right: measurement of the area of organoids. (**E**) qRT-PCR analysis of mitochondrial function related genes at D2 (N=3). (**F**) Measurement of the life-cell protease activity; ROS content relative to life-cell protease activity; Caspase 3/7 (apoptosis marker) relative to life-cell protease activity in Hsp60$^{flox/flox}$ and Hsp60$^{\Delta/\Delta ISC}$ organoids (N=5). (**G**) qRT-PCR analysis of

Hsp60$^{flox/flox}$ and Hsp60$^{\Delta/\Delta ISC}$ organoids for stem cell markers *Lgr5* and *Olfm4* at indicated time-points (N=6). (**H**) Representative pictures of IF co-staining for lysozyme (red) and E-cadherin (IEC borders, grey) counterstained with Dapi (nuclei, blue), including magnifications and bright field pictures in small intestinal organoids from Hsp60$^{flox/flox}$ and Hsp60$^{\Delta/\Delta ISC}$ mice. Dotted lines indicate cell borders of lysozyme positive (Lyz$^+$) cells; asterisks indicate the magnified Lyz$^+$ cells in the right- side pictures; Right: Lyz$^+$ cell numbers per crypt (left graph) and the proportion of highly granular (≥2 granules) Lyz$^+$ cells (right graph) (N≥5 biological replicates; 50 buds). (**I**) qRT-PCR analysis of Hsp60$^{flox/flox}$ and Hsp60$^{\Delta/\Delta ISC}$ organoids for PC markers *Lyz1* and *Ang4* at day 2 after induction of the knockout (N=6). Statistical analyses were performed via unpaired t-tests between two groups at specific time-point. For de novo crypt formation, a Kruskal–Wallis test on ranks followed by Dunnś test was performed. Asterisks indicate significant differences *P<0.05, **P<0.01, ***P<0.001.

The presence and the phenotype of PCs in Hsp60$^{\Delta/\Delta ISC}$ organoids were further characterized by lysozyme staining. In line with the *in vivo* experiment, the total number of PCs remained unaltered. However, mitochondrial dysfunction in *Lgr5*$^+$ stem cells was associated with reduced PC-granularity (≥2 Lyz$^+$ cytoplasmic granules) and cytoplasmic lysozyme expression in Hsp60$^{\Delta/\Delta ISC}$ compared to Hsp60$^{flox/flox}$ organoids (**Figure 27H**). Additionally, transcriptional analysis of lysozyme (*Lyz1*) and Angiogenin 4 (*Ang4*) confirmed diminished PC function under mitochondrial dysfunction in Hsp60$^{\Delta/\Delta ISC}$ organoids (**Figure 27I**). These data indicate that similar to the crypts derived from the inflammatory environment, impaired mitochondrial function in Hsp60$^{\Delta/\Delta ISC}$ organoids resulted in PC dysfunction.

4.9 Inhibition of mitochondrial respiration impairs stem cell niche functions

In addition to glycolysis, mitochondrial oxidative phosphorylation (OXPHOS) provides the ATP for different IEC sub-types [63]. *Ex vivo*, organoids-derived from Hsp60$^{\Delta/\Delta IEC}$ mice showed reduced ATP content and reduced respiratory capacity [62]. *Hsp60* deletion causes mitochondrial dysfunction at a broad level. To be more specific and to gain insight into the role of mitochondrial dysfunction, resulting from impaired mitochondrial respiration, on the stem cell niche, we treated small intestinal organoids-derived from WT mice with sub-lethal doses of oligomycin (2.5µM), an inhibitor of ATP synthase (complex V).

Characterizing early events, 1h treatment with oligomycin, upregulated the mt-UPR target gene *Chop* and reduced the cellular ATP content. However, transcriptional levels of stem cell niche (*Lgr5*, *Olfm4*, and *Lyz*) and oxidative response-associated gene (*Hif1a*) remained unchanged, indicating that the 1h treatment was not sufficient to alter stem cell niche function (**Figure 28A,B**).

Subsequently, organoids were treated for 6h with the same dose of oligomycin. 6h treatment elevated transcriptional levels of *Chop*, oxidative stress response-related gene (*Hif1a*), and cellular energy response (*Prkaa2*), which indicated an induced mitochondrial stress. Although the expression of *Olfm4* and PC function-related genes (*Lyz* and *Ang4*) were reduced after 6h treatment, transcriptional levels of *Lgr5* remained unchanged (**Figure 28C**). This suggests that the 6h time-point was sufficient to impair mitochondrial signaling and alter the stem cell niche function but was not adequate to affect *Lgr5*$^{+}$ stem cells.

To investigate the long-term impact of OXPHOS inhibition, organoids were treated for 24h. Pictures of bright-field microscopy displayed normal growth of the treated organoids (**Figure 28D; left**). Life-cell protease activity confirmed non-toxic treatment conditions for the organoids (**Figure 28G**). Lysozyme staining of oligomycin-treated WT organoids depicted lower numbers of Lyz^{+} cells and displayed markedly reduced PC granularity (≥2 Lyz^{+} cytoplasmic granules) (**Figure 28D**). Similarly, we observed activation of mitochondrial stress signaling (*Chop*, *Hif1a*, and *Prkaa2*) after 24h treatment. In contrast to the 6h treatment, 24h was sufficient to significantly reduce *Lgr5* and *Olfm4* expression. Confirming our observations from immunofluorescent staining, transcriptional levels of *Lyz* and *Ang4* significantly reduced, which verifies the presence of dysfunctional PCs concurrent to impaired mitochondrial respiration (**Figure 28E**).

Remarkably, these results were mirrored by human organoids, where 24h oligomycin treatment induced the mt-UPR activation (*Chop*), oxidative stress response (*Hif1a*), and reduced stemness (*Lgr5* and *Olfm4*) and PC function (*LYZ* and *PLA2G2A*) (**Figure 28F**). Slightly reduced life-cell protease activity in human organoids paralleled with reduced dead cells. Therefore, the ratio of live/ dead cells remained elevated (data not shown) (**Figure 28H**).

Together, these data indicate that *ex vivo* altered mitochondrial respiration, caused by inhibition of the ATP synthase, reduces stemness and leads to PC dysfunction.

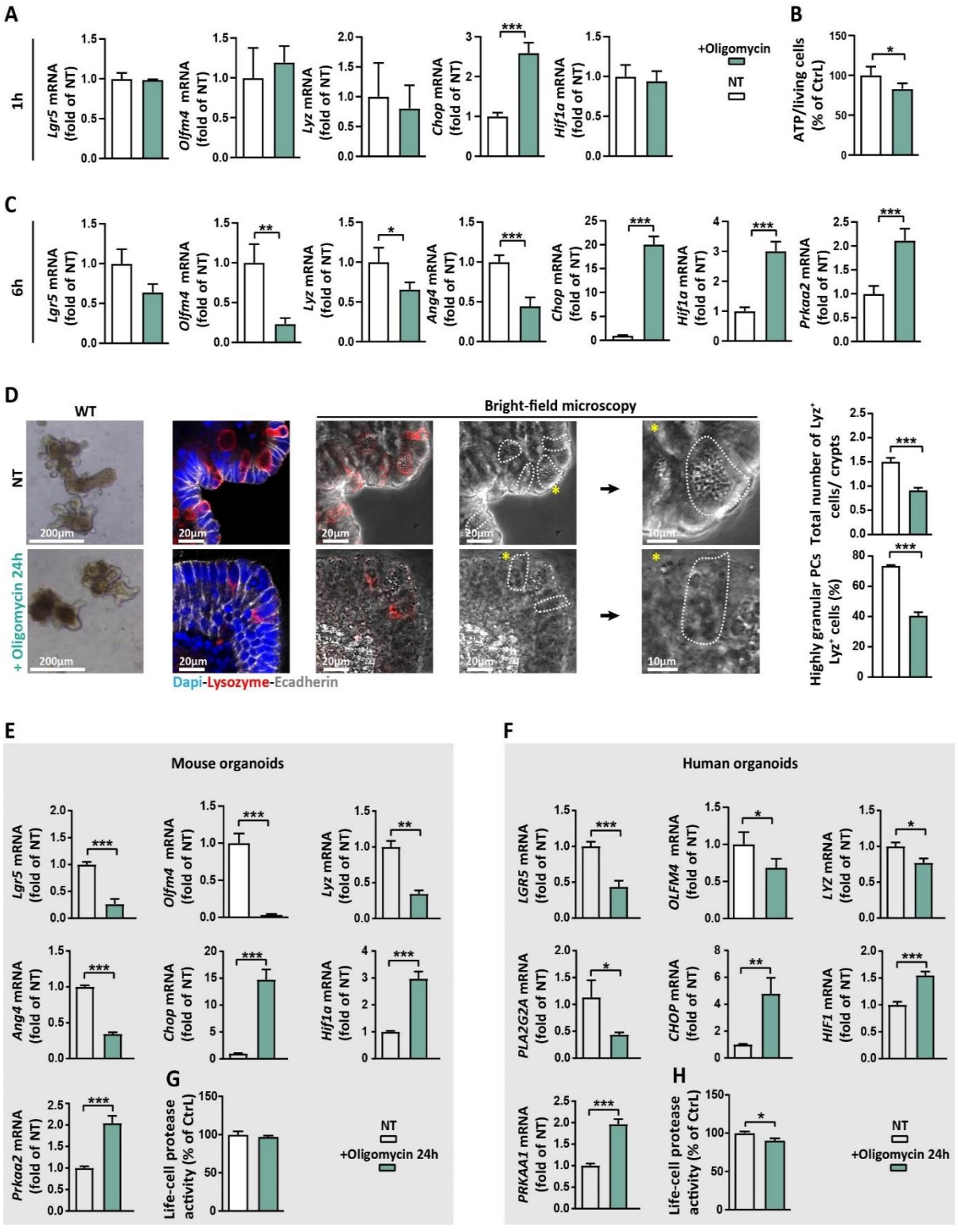

Figure 28 Oligomycin treatment reduces stemness and PC granularity

Small intestinal organoids derived from WT mice were treated for 1h, 6h and 24h with 2.5µM Oligomycin. (**A**) qRT-PCR analysis of WT organoids for stem cell markers (*Lgr5* and *Olfm4*), Paneth cell marker (*Lyz*) and for genes associated with mitochondrial signaling after 1h treatment (N=3). (**B**) Measurement of the ATP content relative to life-cell protease activity (N=4). (**C**) qRT-PCR analysis of WT organoids for stem cell markers (*Lgr5* and *Olfm4*), Paneth cell function related genes (*Lyz* and *Ang4*) and for genes associated with mitochondrial signaling (*Chop*, *Hif1a* and *Prkaa2*) after 6h treatment (N=3). (**D**) Left: bright field and IF co-staining of lysozyme (red) and E-cadherin (IEC borders, grey) counterstained with Dapi (nuclei, blue). Dotted lines indicate cell borders

of Lyz positive (Lyz^+) cells; asterisks indicate Lyz^+ cells magnified in the pictures on the right side. Right: quantification of the total numbers of Lyz^+ cells per crypt (upper graph) and the proportion of highly granular (≥2 granules) PCs (lower graph) (N=6 biological replicates; 50 buds; 25 different organoids). (**E**) qRT-PCR analysis of small intestinal organoids for stem cell markers (*Lgr5* and *Olfm4*), Paneth cell function-associated genes and for genes associated with mitochondrial signaling (N=6). (**F**) Same analysis as in (**E**) for human organoids derived from the small intestine and treated with oligomycin for 24h (N≥6). (**G,H**) Measurement of the life-cell protease activity (**G**: in mouse organoids and **H**: in human organoids) (N=6). Statistical analyses were performed via unpaired t-tests. Asterisks indicate significant differences *P<0.05, **P<0.01, ***P<0.001.

In contrast to oligomycin, which inhibits ATP synthesis (complex V) and reduces the ATP generation, Rotenone inhibits the nicotinamide adenine dinucleotide (NADH) processing by complex I. Characterizing the impact of complex I inhibition on the stem cell niche, sub-lethal doses of Rotenone (1.5µM) were applied to WT mice-derived small intestinal organoids for 6h and 24h. We observed no mt-UPR activation, oxidative stress- and cellular energy- response upon 6h Rotenone treatment. Yet, 6h time-point was sufficient to reduce transcriptional levels of stem cell markers (*Lgr5* and *Olfm4*) and PC function-related genes (*Lyz* and *Ang4*) (**Figure 29A**). Contrasting oligomycin treatment, 1h Rotenone treatment had no influence on cellular ATP levels in mouse organoids (**Figure 29B**), indicating that ATP levels might not be the mediator of *Lgr5* downregulation.

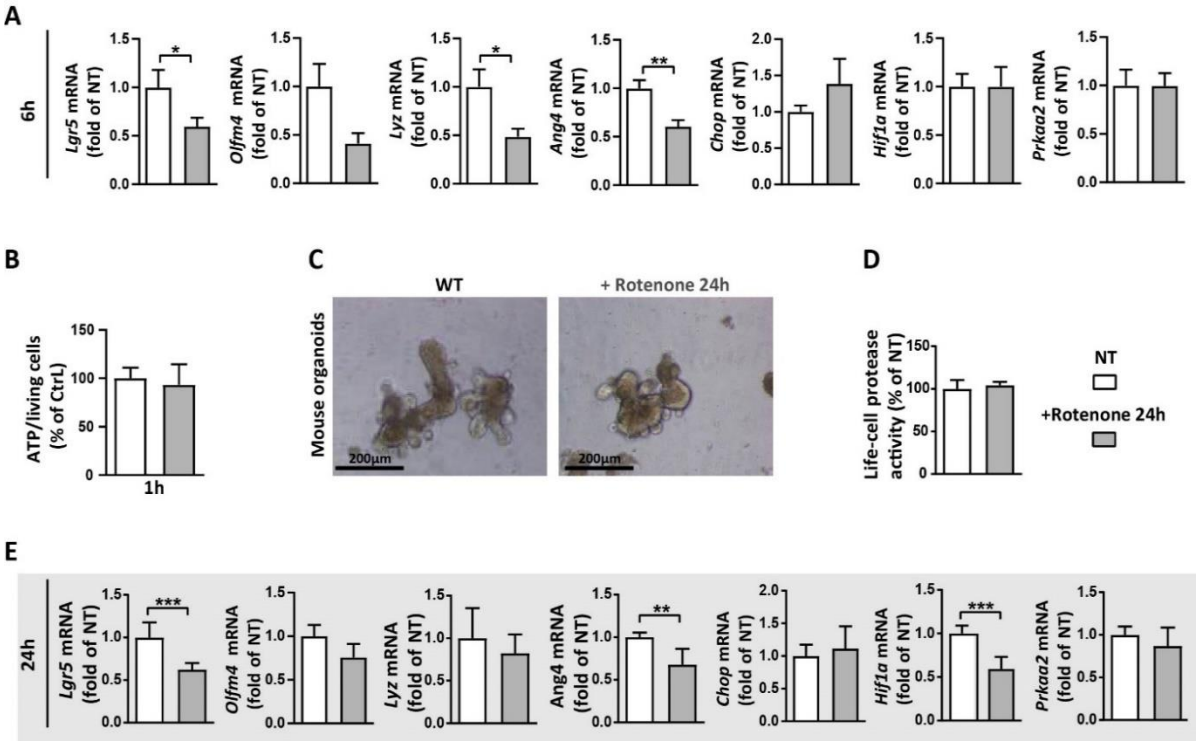

Figure 29 Complex I inhibition has a slight impact on ISC niche

Small intestinal organoids derived from WT mice were treated for 6h and 24h with 1.5µM Rotenone. (**A**) qRT-PCR analysis of WT organoids for stem cell markers (*Lgr5* and *Olfm4*), Paneth cell function related genes (*Lyz* and *Ang4*) and for genes associated with mitochondrial signaling (*Chop*, *Hif1a* and *Prkaa2*) after 6h treatment (N=3). (**B**) Measurement of ATP content relative to life-cell protease activity (N=4). (**C**) Representative bright-field microscopy pictures of Rotenone treated and non-treated mouse small intestinal organoids (**D**) Measurement of life-cell protease activity (N=6). (**E**) qRT-PCR analysis of small intestinal organoids for stem cell markers (*Lgr5* and *Olfm4*), Paneth cell function-associated genes (*Lyz* and *Ang4*), and for genes associated with mitochondrial signaling (*Chop*, *Hif1a* and *Prkaa2*) (N=6). Statistical analyses were performed via unpaired t-tests. Asterisks indicate significant differences *P<0.05, **P<0.01, ***P<0.001.

The long-term (24h) influence of complex I inhibition was additionally investigated in WT organoids. Bright-field microscopy depicted a normal growth of organoids after Rotenone treatment (**Figure 29C**). Additionally, life-cell protease activity confirmed the non-toxicity of treatment conditions (**Figure 29D**). Similar to the 6h treatment, no changes were observed in *Chop* and *Prkaa2* expression. Yet, transcription of *Hif1a* was reduced, indicating reduced ROS levels due to an elevated mitochondrial membrane potential or the accumulation of metabolic substrates [151]. We additionally observed a decline in *Lgr5* expression. However, *Olfm4* expression remained unaltered between treated and non-treated groups. Although *Lyz* levels remained unchanged, a drop in *Ang4* expression indicated PC dysfunction upon Rotenone treatment (**Figure 29E**). Since Rotenone inhibits the function of complex I, other complexes of the respiratory chain can compensate for the reduced function of complex I. That might be a potential explanation for unaltered transcription of mitochondrial function-related genes upon complex I inhibition.

4.9.1 Impact of oligomycin on the stem cell niche function is Chop independent

Inhibition of the respiratory chain complex V with oligomycin was associated with an elevated *Chop* expression (**Figure 28**). Chop is a transcription factor and mt-UPR target gene involved in cell-cycle progression, cellular proliferation, and respiration [152, 153]. The activation of mt-UPR signaling in IEC-specific Hsp60 knockout mice was shown to be independent of Chop-mediated signaling [62]. Therefore, we used $Chop^{-/-}$ small intestinal organoids and treated them with the same dose and duration of oligomycin to investigate whether the impact of OXPHOS inhibition in inducing mitochondrial dysfunction is chop dependent. Transcriptional analysis of $Chop^{-/-}$ organoids depicted that oligomycin treatment was associated with reduced stemness (*Lgr5*) and PC dysfunction *(Lyz* and *Ang4*) (**Figure 30A**). Similar impacts were previously observed in WT organoids in **Figure 28E**. Although we observed no significant changes in *Prkaa2* expression in $Chop^{-/-}$ organoids upon oligomycin treatment, *Hif1a* was significantly upregulated (**Figure 30A**). The life-cell protease activity showed a mild reduction in the percentage of living cells after oligomycin treatment (**Figure 30B**). Yet, a reduced proportion of dead cells resulted in a consistent ratio of living/ dead cells between the treated group and non-treated controls (Data not shown). Additionally, bright-field microscopy showed the normal growth of $Chop^{-/-}$ organoids, indicating that the duration and dose of treatment were not lethal for these organoids (**Figure 30C**).

In order to verify *Chop* deletion, we analyzed transcriptional levels of chop target genes between WT and $Chop^{-/-}$ organoids. Despite the downregulation of tribble 3 (*Trb3*) and interleukin1 receptor antagonist (*Il1rn*) in $Chop^{-/-}$ organoids, activating transcription factor 4 (*Atf4*) expression remained consistent between the two genotypes. Contrarily we observed an upregulation in aspargine synthase (*Asns*) expression in $Chop^{-/-}$ organoids (**Figure 30D**). 24h oligomycin treatment of $Chop^{-/-}$ organoids depicted a slightly lower impact on the expression of Chop target genes (*Asns*, *Trb3*, and *Il1rn*) compared to WT (**Figure 30E,F**).

Although Chop deficiency in organoids might impact the expression of target genes, the altered expression had no impact on ISC niche function. Therefore, we could conclude that the impact of OXPHOS inhibition on the stem cell niche is Chop independent.

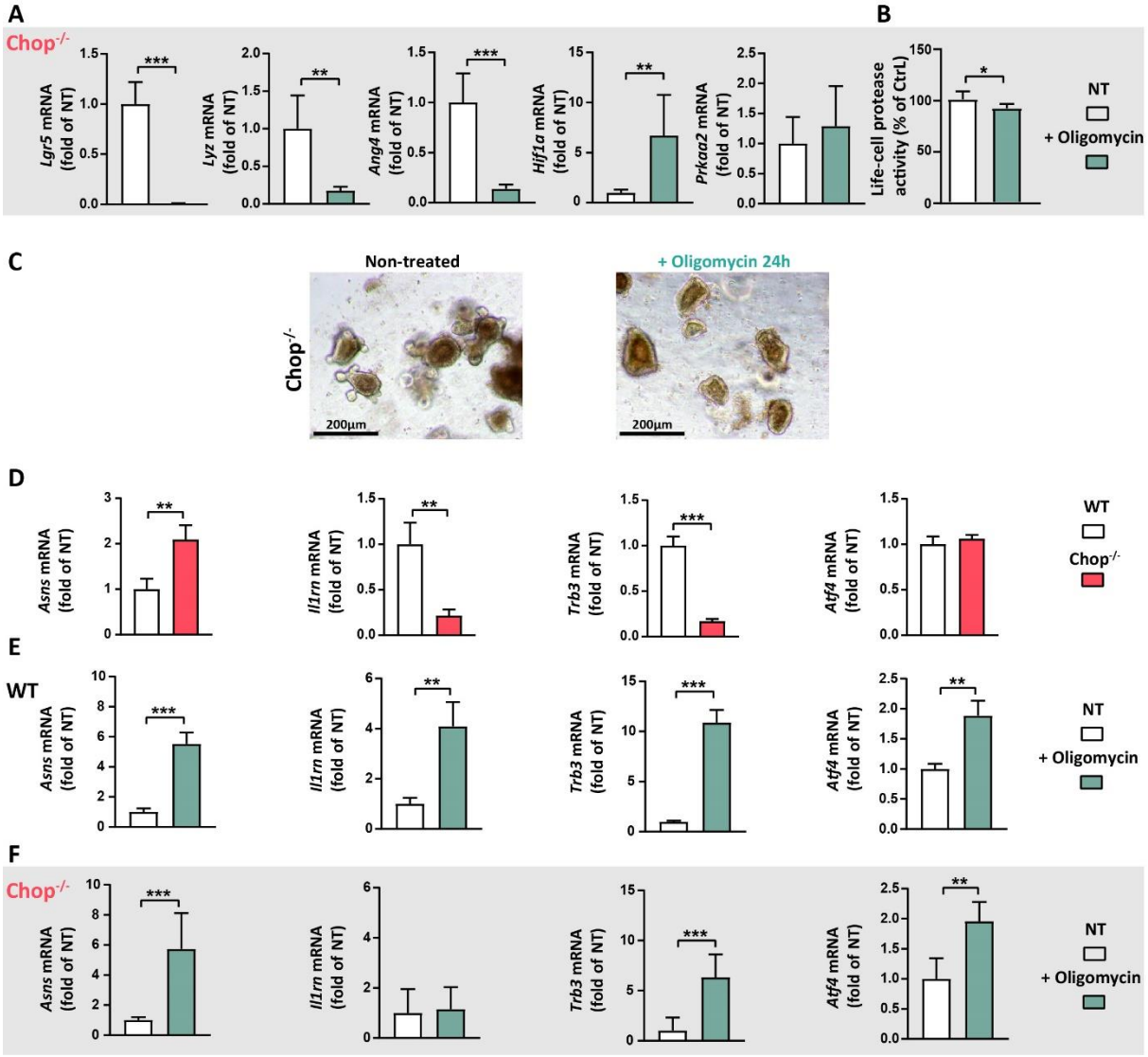

Figure 30 Impact of OXPHOS inhibition on small intestinal organoids is Chop independent

Small intestinal organoids derived from Chop$^{-/-}$ mice were treated for 24h with 2.5µM oligomycin. (**A**) qRT-PCR analysis of Chop$^{-/-}$ organoids for stem cell marker (*Lgr5*), Paneth cell function related genes (*Lyz* and *Ang4*) and for genes associated with mitochondrial signaling (*Hif1a* and *Prkaa2*) after 24h treatment (N=5). (**B**) Measurement of the life-cell protease activity (N=6). (**C**) Representative bright-field pictures of Chop$^{-/-}$ organoids comparing oligomycin treated organoids to non-treated controls. (**D**) qRT-PCR analysis of small intestinal organoids derived from WT and Chop$^{-/-}$ mice for Chop target genes (N=3). (**E**) qRT-PCR analysis of the Chop target genes in WT organoids after oligomycin treatment (N=5). (**F**) qRT-PCR analysis of the Chop target genes in Chop$^{-/-}$ organoids after oligomycin treatment (N=5). Statistical analyses were performed via unpaired t-tests between two groups and by One-way analysis of variance (ANOVA) followed by Tukey test for multiple comparisons. Asterisks indicate significant differences *P<0.05, **P<0.01, ***P<0.001.

4.10 Metabolic shift towards mitochondrial OXPHOS restores inflammation-mediated dysfunction of the stem cell niche

4.10.1 Dichloroacetate (DCA)-mediated shift in metabolism induces stemness

Inhibiting OXPHOS by oligomycin leads to reduced PC granularity and *Lgr5* expression in WT organoids (**Figure 28**). In order to characterize the impact of altered metabolism on stem cell niche function, we treated WT mice-derived small intestinal organoids with dichloroacetate (DCA; 15mM) for 24h. DCA inhibits pyruvate dehydrogenase kinase, shifting ATP generation to OXPHOS [154]. The non-toxicity of the DCA treatment was confirmed by bright-field microscopy and life-cell protease activity measurement (**Figure 31A,B**). Characterizing the PC phenotype, we observed no changes in total numbers of Lyz^+ cells between DCA-treated and non-treated organoids. However, lysozyme staining revealed slightly reduced numbers of highly granular PCs ($\geq$2 Lyz^+ cytoplasmic granules) after DCA treatment (**Figure 31C,D**). Additionally, reduced *Lyz* expression and unaltered transcription of *Ang4* highlighted the minimal effect of DCA on PC function (**Figure 31E**). Induced mitochondrial signaling after DCA treatment (*Chop* and *Prkaa2*) was paralleling with transcriptional upregulation of *Lgr5* in mouse organoids (**Figure 31E**), indicating that DCA-associated shift in mitochondrial metabolism induces stemness.

DCA treatment of human small intestinal organoids led to a minor reduction in life-cell protease activity (**Figure 31B**). However, the ratio of Live/ dead cells remained elevated compared to the non-treated controls (data not shown). Transcriptional analysis of human organoids showed no alteration in mitochondrial signaling (*CHOP*, *HIF1*, and *PRKAA1*) after DCA treatment. PC characterization depicted a slight reduction in *LYZ* and *PLA2G2A* expression, which were indicative of minor changes in PC function. The DCA-mediated shift in metabolism was associated with elevated *LGR5* expression. Yet, increased stemness remained non-significant in human organoids (**Figure 31F**), which could indicate species-dependent differences in response to treatment.

Together, these data indicate the minimal impact of DCA treatment on healthy organoids with only a minor shift in observed epithelial cell populations, specifically in stem cells and PCs.

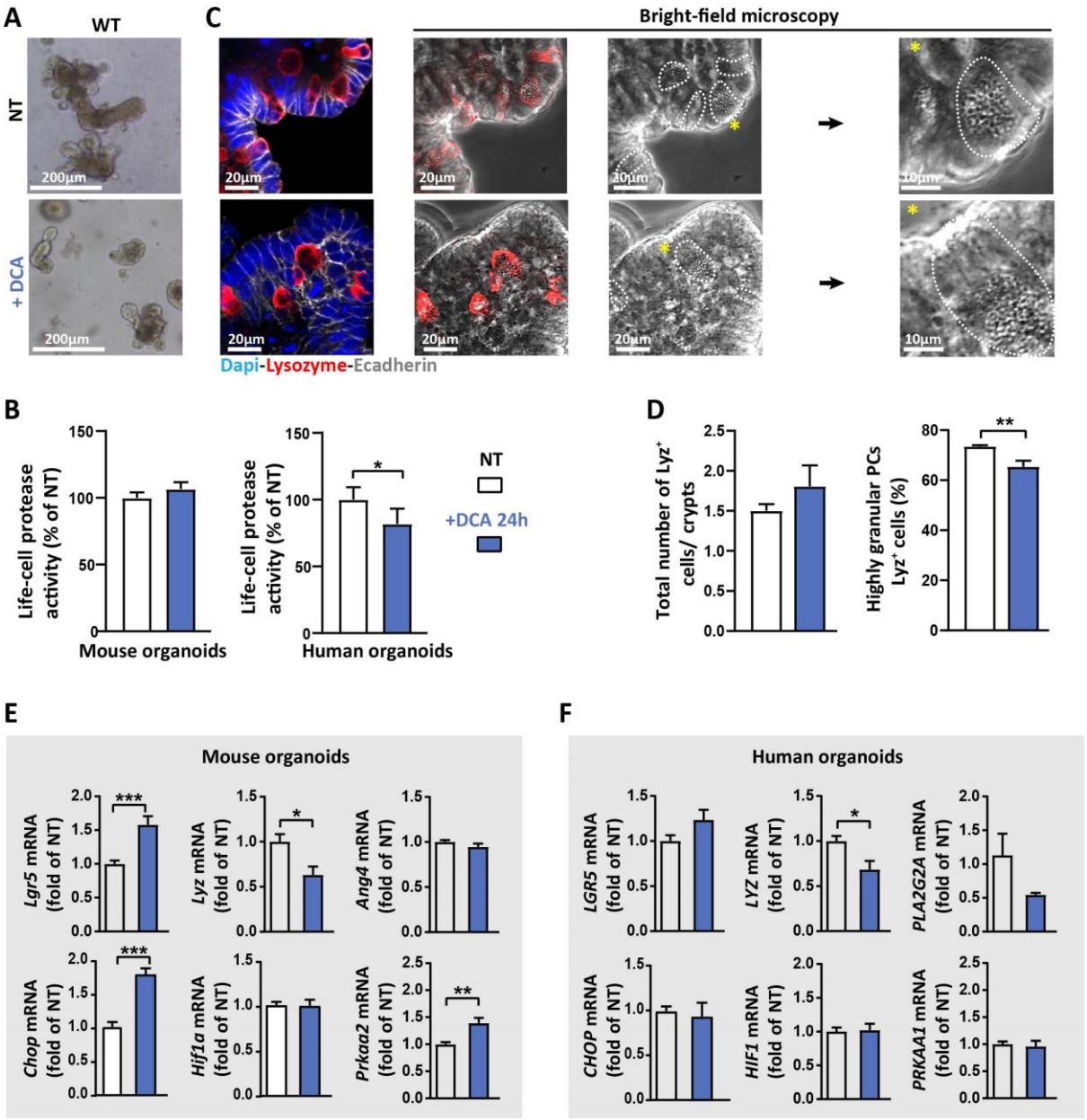

Figure 31 DCA treatment has a minimal impact on WT organoids

Small intestinal organoids derived from WT mice and humans were treated for 24h with 15mM dichloroacetate (DCA). (**A**) Bright field pictures comparing DCA-treated and non-treated controls. (**B**) Measurement of the life-cell protease activity (N=6). (**C**) IF co-staining of lysozyme (red) and E-cadherin (IEC borders, grey) counterstained with Dapi (nuclei, blue). Dotted lines indicate cell borders of Lyz positive (Lyz^+) cells; asterisks indicate Lyz^+ cells magnified in the pictures on the right side. (**D**) Right: quantification of the total numbers of Lyz^+ cells per crypt; Left: proportion of the highly granular (≥2 granules) PCs (N=6 biological replicates; 50 buds; 25 different organoids). (**E**) qRT-PCR analysis of small intestinal organoids for stem cell marker (*Lgr5*), Paneth cell function-associated genes and for genes associated with mitochondrial signaling (N=6). (**F**) Same analysis as in (**E**) for human organoids derived from the small intestine and treated with DCA for 24h (N=4). Statistical analyses were performed via unpaired t-tests. Asterisks indicate significant differences *P<0.05, **P<0.01, ***P<0.001.

4.10.2 DCA treatment improves the survival of inflamed TNF$^{\Delta ARE}$ organoids

DCA has been used as a therapeutic agent for patients with mitochondria-related disorders [155]. To test if DCA treatment might reverse growth defects of inflamed TNF$^{\Delta ARE}$ organoids and rescue the inflammation-mediated mitochondrial and metabolic alterations, we treated inflamed TNF$^{\Delta ARE}$ mice-derived ileal organoids immediately after seeding for 8 days with DCA (**Figure 32A**). Although we observed a drop in the proportion of living organoids in both non-treated and DCA-treated groups at day 3 and day 8, the percentage of living organoids were significantly higher in the DCA-treated group compared to non-treated controls. In terms of *de novo* crypt formation, no significant changes were detectable between the two groups at day 3. However, the number of organoids with more than 4 buds was significantly increased in DCA-treated organoids at day 8, indicating that DCA treatment might prevent growth defects and increase proliferation and differentiation in inflamed TNF$^{\Delta ARE}$ organoids. In contrast to DCA-treated organoids, non-treated organoids showed growth defects, and they appeared circular (**Figure 32B,E**).

To study the long-term effect of DCA, we passaged organoids at day 8 and cultured them on DCA-containing or DCA-free medium for additional 6 days (day 14) (**Figure 32C**). Interestingly, withdrawal of DCA subsequent to passaging at day 8 showed no negative impact on the growth of organoids compared to those remaining on DCA. Unchanged *De novo* crypt formation in both groups at day 14 could indicate that a single exposure to DCA is sufficient to restore the inflammation-mediated metabolic dysfunction of the stem cell niche (**Figure 32D,E**).

Comparing the impact of DCA treatment on stemness between WT and inflamed TNF$^{\Delta ARE}$ organoids, we observed an elevated expression of *Lgr5* at day 14 in inflamed TNF$^{\Delta ARE}$ organoids. Yet, transcriptional analyses showed no alteration in PC function-related genes between the two groups (**Figure 32F**).

These data suggest that rearrangement of the inflammation-mediated metabolic alterations in stem cell niche can serve as a target for therapeutic interventions.

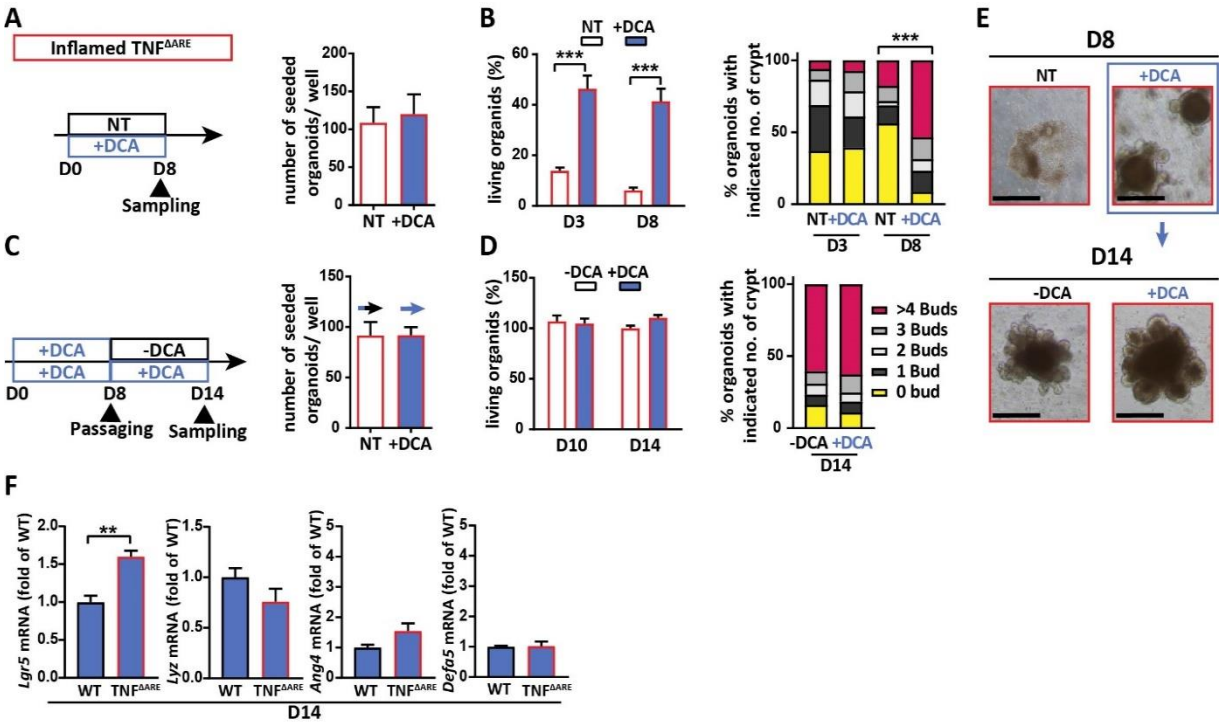

Figure 32 DCA-mediated shift in metabolism improves the growth and survival of TNF$^{\Delta ARE}$ organoids

Ileal organoids derived from inflamed TNF$^{\Delta ARE}$ mice were analyzed. (**A**) Experimental scheme of DCA treatment. Non-treated and 15mM DCA-treated organoids were compared for 8 days. D0 is the seeding and starting of the culture; Number of seeded organoids for the experiment in each well. (**B**) The proportion of living organoids at day 3 and day 8 of culture (left) compared to day 1; Quantification of *de novo* crypt formation at day 3 and day 8 (right). (**C**) Experimental scheme. DCA treated organoids were passaged at day 8 and were cultured on DCA-containing (blue)/ DCA-free (black) media; Number of seeded organoids after passaging in each well. Blue-Black arrow shows withdrawal of DCA from the media after passaging. (**D**) Similar readouts as in (**B**) but for D10 and D14 meaning 2 days and 6 days after passaging respectively. (**E**) Representative bright field pictures of organoids at day 8 (before passaging) and at day 14 of culture. Scale bar is 200µm (**F**) WT and inflamed TNF$^{\Delta ARE}$ mice-derived ileal organoids were treated with DCA for 14 days. qRT-PCR analysis for *Lgr5* and Paneth cell function-associated genes. Statistical analyses were performed via unpaired t-tests. Statistics for budding analyses were performed by Kruskal–Wallis test on ranks. Asterisks indicate significant differences *P<0.05, **P<0.01, ***P<0.001.

4.10.3 DCA treatment maintained PC granularity in TNF$^{\Delta ARE}$ mice

DCA treatment rescued the growth of inflamed TNF$^{\Delta ARE}$ organoids (**Figure 32**). We investigated whether DCA treatment *in vivo* might protect mice from inflammation, restore the ISC niche function, and have therapeutic effects. Hence, we colonized TNF$^{\Delta ARE}$ and WT mice with segmented filamentous bacteria (SFB) to have consistent inflammation and treated them at the age of 4 weeks for 6 weeks with DCA (in drinking water). Mice that received drinking water without DCA served as control groups for the same genotype, whereas WT mice served as genotype controls. H&E staining of the ileal tissue sections from WT mice showed comparable crypt-villus structure and tissue pathology in these mice between two treatment groups. In contrast to WT mice, TNF$^{\Delta ARE}$ mice showed signs of inflammation. The preliminary *in vivo* DCA treatment depicted consistent inflammation between water- and DCA-treated TNF$^{\Delta ARE}$ mice (**Figure 33A**). To verify the presence of inflammation, fecal complement 3 (C3) concentration was measured at different time-points. C3 is an inflammation-associated protein. Although C3 levels were increased in both treatment groups of TNF$^{\Delta ARE}$ mice compared to the WT controls at week 6, we observed no significant differences between water- and DCA-treated TNF$^{\Delta ARE}$ mice. Additionally, water-treated TNF$^{\Delta ARE}$ mice showed significantly increased C3 concentration at week 6 compared to other time-points (**Figure 33B**).

Characterizing the stem cell niche, we stained ileal tissue sections of water- and DCA-treated groups of WT and TNF$^{\Delta ARE}$ mice with lysozyme. No changes were detectable in total numbers of Lyz^{+} cells between water- and DCA-treated groups of the same genotype (**Figure 33C**). Unaltered *Lyz* expression was further confirmed by transcriptional analysis (**Figure 33D**). Yet, the number of Lyz^{+} cells significantly dropped in TNF$^{\Delta ARE}$ mice compared to WT controls (**Figure 33C**). Numbers of highly granular PCs (≥2 Lyz^{+} cytoplasmic granules) remained unchanged between two treatment groups of WT mice. However, DCA treatment significantly increased the number of highly granular PCs in TNF$^{\Delta ARE}$ mice. Comparing two genotypes, it is important to mention that the number of highly granular PCs remained low in TNF$^{\Delta ARE}$ mice compared to WT controls. This indicates that DCA treatment might have an impact on PC granularity independent of tissue pathology (**Figure 33C**). *In situ* hybridization for *Lgr5* and *Lgr5* transcriptional analysis depicted no changes in *Lgr5* expression between water- and DCA-treated groups of each genotype (**Figure 33E,F**). However, DCA treatment non-significantly increased *Lgr5* expression in TNF$^{\Delta ARE}$ mice, showing that DCA treatment might impact stemness.

Together, these data indicate that DCA treatment, independent of tissue pathology, might have an effect on the ISC niche function. Yet, due to low animal numbers and due to low numbers of PCs/ highly granular PCs this study remains inconclusive. Further experiments will be necessary to understand the preventive or therapeutic *in vivo* effects of DCA more clearly.

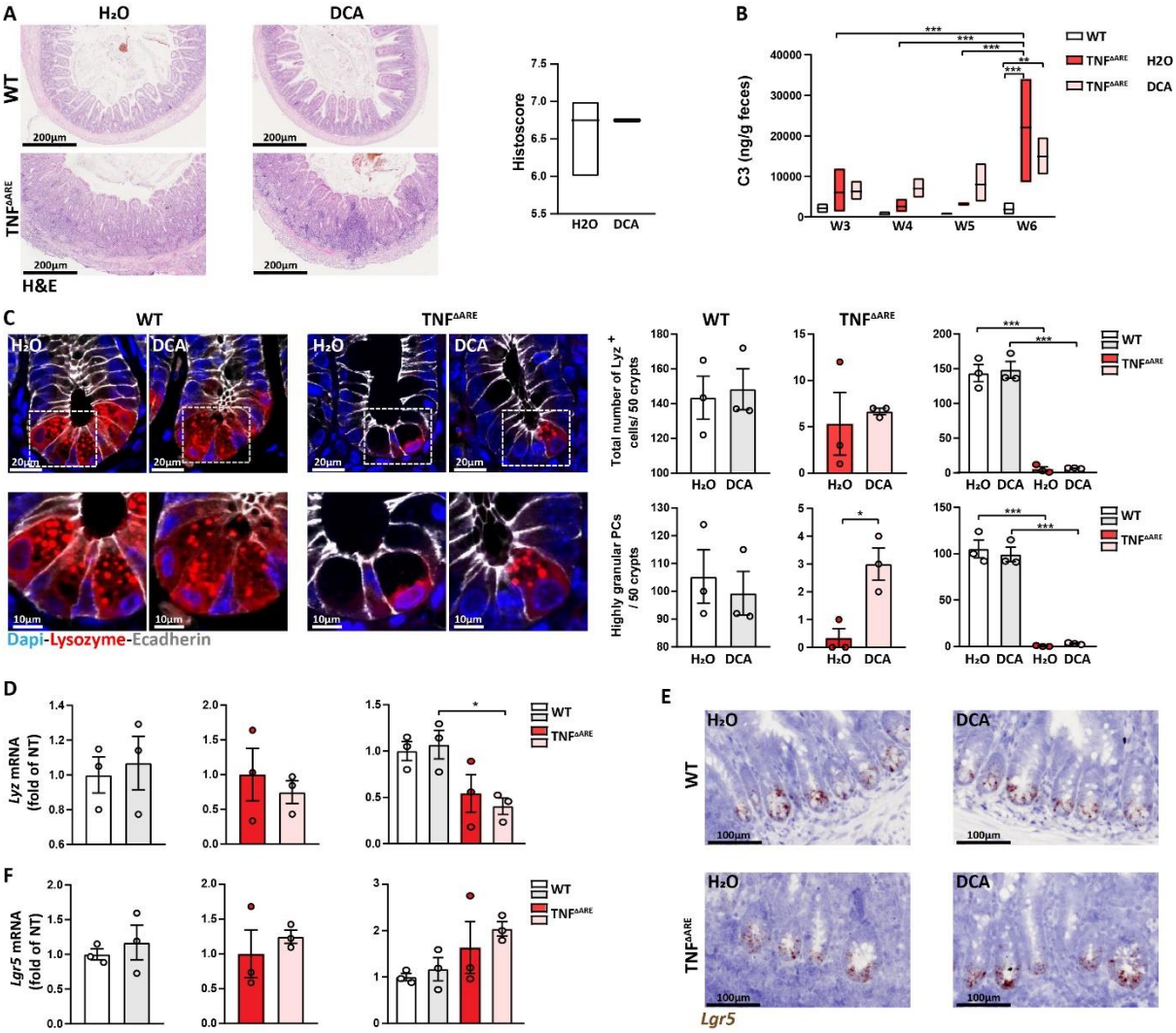

Figure 33 In vivo DCA treatment maintained PC granularity in TNF$^{\Delta ARE}$ mice

WT and TNF$^{\Delta ARE}$ mice were treated with DCA (300mg/l in drinking water) or remained non-treated (water control). Ileal tissue section were analyzed. (**A**) Representative H&E staining; Histological scoring of the water- and DCA-treated TNF$^{\Delta ARE}$ mice (N=3). (**B**) C3 concentrations in the feces of WT and water- and DCA-treated TNF$^{\Delta ARE}$ mice (N=3). (**C**) Representative IF pictures of lysozyme (red) and E-cadherin (IEC borders, gray) counterstained with Dapi (nuclei, blue) including magnifications; Lower panel: quantification of the total number of Lyz^{+} cells and highly granular PCs (≥2 granules). (**D**) qRT-PCR analysis of *Lyz* on primary ileal crypt isolates (N=3). (**E**) Representative images of *Lgr5 in situ* hybridization on ileal tissue sections (N=3). (**F**) qRT-PCR analysis of *Lgr5* on primary ileal crypt isolates (N=3). Statistical analyses were performed via unpaired t-tests between two groups, by One-way analysis of variance (ANOVA) followed by Tukey test for multiple groups and by Two-way analysis of variance (ANOVA) for multiple comparisons in C3 case. Asterisks indicate significant differences *P<0.05, **P<0.01, ***P<0.001.

4.11 IEC-specific ClpP deficient mice as model for disturbed mitochondrial proteostasis

Previously, constitutive *Hsp60* deletion in mice, as the major chaperone of the mitochondrial matrix, was shown to cause embryonic lethality [62]. We tested whether ClpP loss, as a matrix localized protease, will also impact the growth of mice. Conditional ClpP knockout mice were generated by removal of neomycin and puromycin resistance cassettes from the targeting vector, where LoxP sites flanked exons 3-5, resulting in a frameshift from exon 2-6. To generate an intestinal epithelial cell (IEC)-specific ClpP deficiency, the ClpP$^{flox/flox}$ mice were crossed with VillinCre^{Tg} mice (**Figure 34A**).

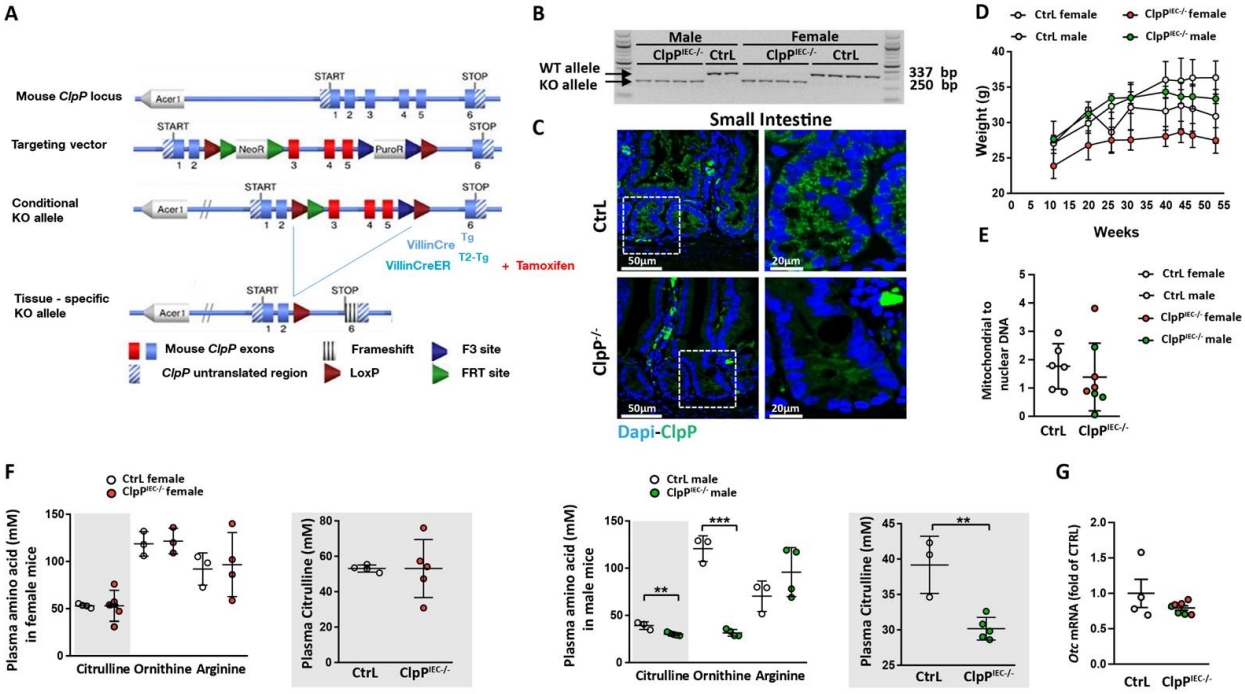

Figure 34 Constitutive ClpP deficiency is associated with metabolic alterations in male mice

(**A**) Schematic illustration of the ClpP conditional- and tissue specific-knockout generation. (**B**) Mutation-specific PCR showing the WT and ClpP knockout (KO) allele in DNA extracted from the small intestinal tissues of a male and female control and constitutive ClpP deficient (ClpP$^{IEC-/-}$) mice. (**C**) Representative IF pictures of ClpP (green) counterstained with Dapi (nuclei, blue) including magnifications. (**D**) Weight development curves until age of 53 weeks. (**E**) The ratio of mitochondrial to nuclear DNA in small intestinal IECs (CtrL: N=6, ClpP$^{-/-}$: N=8) (**F**) Left: plasma amino acid concentrations, including citrulline concentrations in the female of control (N=3) and ClpP$^{IEC-/-}$ mice (N=5); Right: shows the same readouts as left graphs, but for male control (N=3) and ClpP$^{IEC-/-}$ mice (N>4). (**G**) qRT-PCR analysis of *Otc* (N=4 control and N=7 ClpP$^{IEC-/-}$ mice). Statistical analyses were performed via unpaired t-tests. Asterisks indicate significant differences **P<0.01, ***P<0.001.

Constitutive ClpP deficient mice (ClpP$^{IEC-/-}$) were sampled at the age of 53 weeks. Mutation-specific PCR verified the presence of knockout allele in ClpP$^{IEC-/-}$ mice (**Figure 34B**). The loss of ClpP in IECs was further confirmed by immunofluorescent staining (**Figure 34C**). ClpP$^{IEC-/-}$ mice depicted a normal weight development until the age of 53 weeks, indicating a normal growth and development of these mice (**Figure 34D**). Additionally, ClpP$^{IEC-/-}$ mice showed no morphological changes in the small intestine and colon (**Figure 35A-E**). Measuring mitochondrial to nuclear DNA ratio between ClpP$^{flox/flox}$

and ClpP$^{IEC-/-}$ mice, we observed unaltered mitochondrial abundance upon *ClpP* deletion in both male and female mice (**Figure 34E**).

Although plasma amino acid concentrations, specifically citrulline levels, remained unchanged between female ClpP$^{IEC-/-}$ and ClpP$^{flox/flox}$ mice, male mice showed reduced plasma citrulline and ornithine concentrations, indicating reduced mitochondrial function (**Figure 34F**). Transcriptional analysis depicted an unaltered expression for the enzyme ornithine transcarbamylase (*Otc*), which converts ornithine to citrulline (**Figure 34G**). These data indicate slight metabolic alterations in male ClpP$^{IEC-/-}$ mice. Reduced citrulline levels in these mice might be due to reduced substrate flow through OTC and might not be reflected by altered mitochondrial genes or enzymatic function.

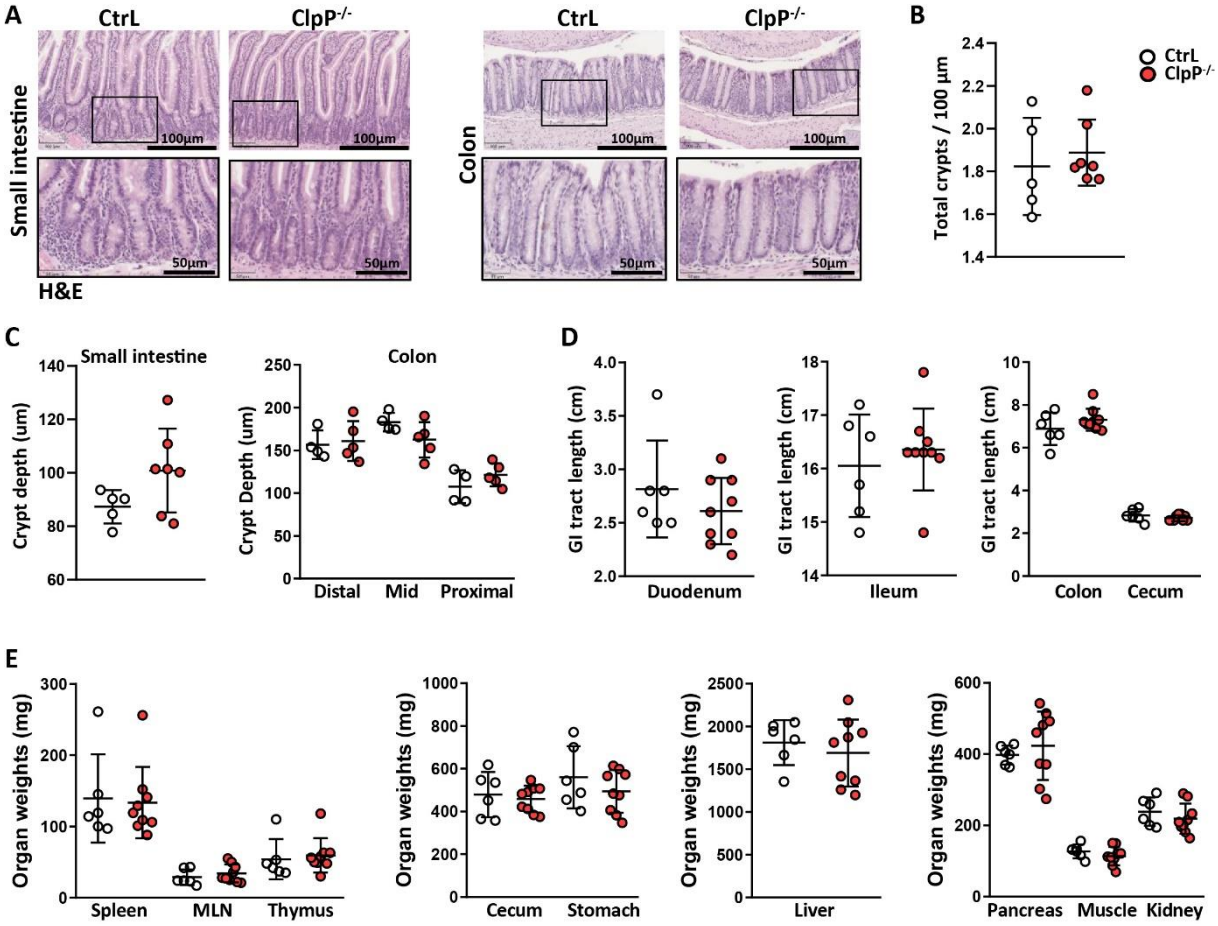

Figure 35 Morphological appearance of the GI tract and organ characteristics in ClpP$^{IEC-/-}$ mice

(**A**) Representative H&E staining of the small intestine and colon. (**B**) Quantification of the total crypt numbers in 100µm small intestine of the floxed control (N=5) and ClpP$^{IEC-/-}$ mice (N=7) at age of 53 weeks. (**C**) Crypt depth in small intestine (CtrL: N=5, ClpP$^{IEC-/-}$: N=7) and different colonic parts (CtrL: N=4, ClpP$^{IEC-/-}$: N=5). (**D**) GI tract length and different organ weights in 53 weeks of control (N=6) and ClpP$^{IEC-/-}$ mice (N=9). Statistical analyses were performed via unpaired t-tests.

Transcriptional analysis showed no *ClpP* expression in IECs of 53 weeks old ClpP$^{IEC-/-}$ mice, confirming the lack of ClpP in these mice. However, the expression of additional mitochondrial proteases *Lon* and *HtrA2* remained unaltered, showing no compensation. Mt-UPR marker-gene expression revealed no sign of mt-UPR activation. Yet, a slight downregulation in mitochondrial creatine kinase (*CKmt1*) levels could indicate reduced mitochondrial energy shuttling. Additionally, the unaltered expression of *Prkaa2*, which is the mitochondrial global energy sensor, might point to the activation of compensatory mechanisms (**Figure 36A**). Investigating the impact of ClpP loss on mitochondrial function, we observed no changes in the transcriptional levels of mitochondrial function (*Slc25a15*, *Tomm20*) and respiration (*CoxI* and *CoxIV*) related genes (**Figure 36B**). Similarly, no alteration was detectable in anti-oxidative response (*Hif1a*, *Sod2*, and *Catalase*) upon ClpP loss (**Figure 36C**).

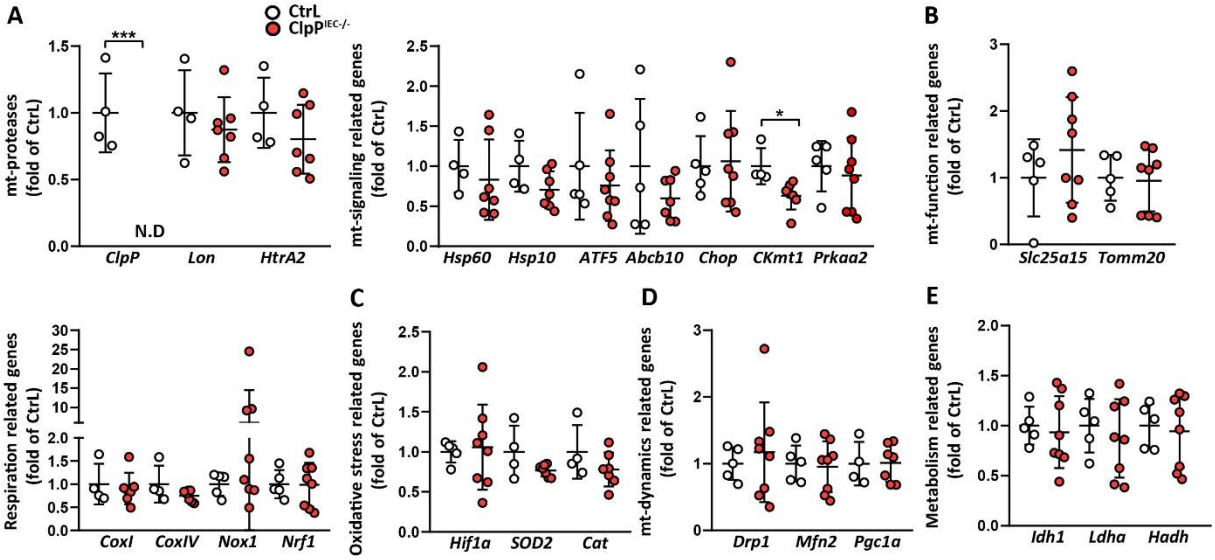

Figure 36 ClpP$^{IEC-/-}$ mice show no signs of activated mt-UPR and altered mitochondrial function

qRT-PCR analysis of (**A**) mitochondrial proteases and mitochondrial signaling-related genes, (**B**) mitochondrial function and respiration-related genes, (**C**) oxidative stress-response and (**D**) mitochondrial dynamics-related genes, (**E**) mitochondrial metabolism-related genes on small intestinal IECs derived from 53 weeks old control (N=4-5) and ClpP$^{-/-}$ mice (N=8). Statistical analyses were performed via unpaired t-tests between controls and the ClpP$^{-/-}$ mice for each gene of interest. Asterisks indicate significant differences *P<0.05, ***P<0.001.

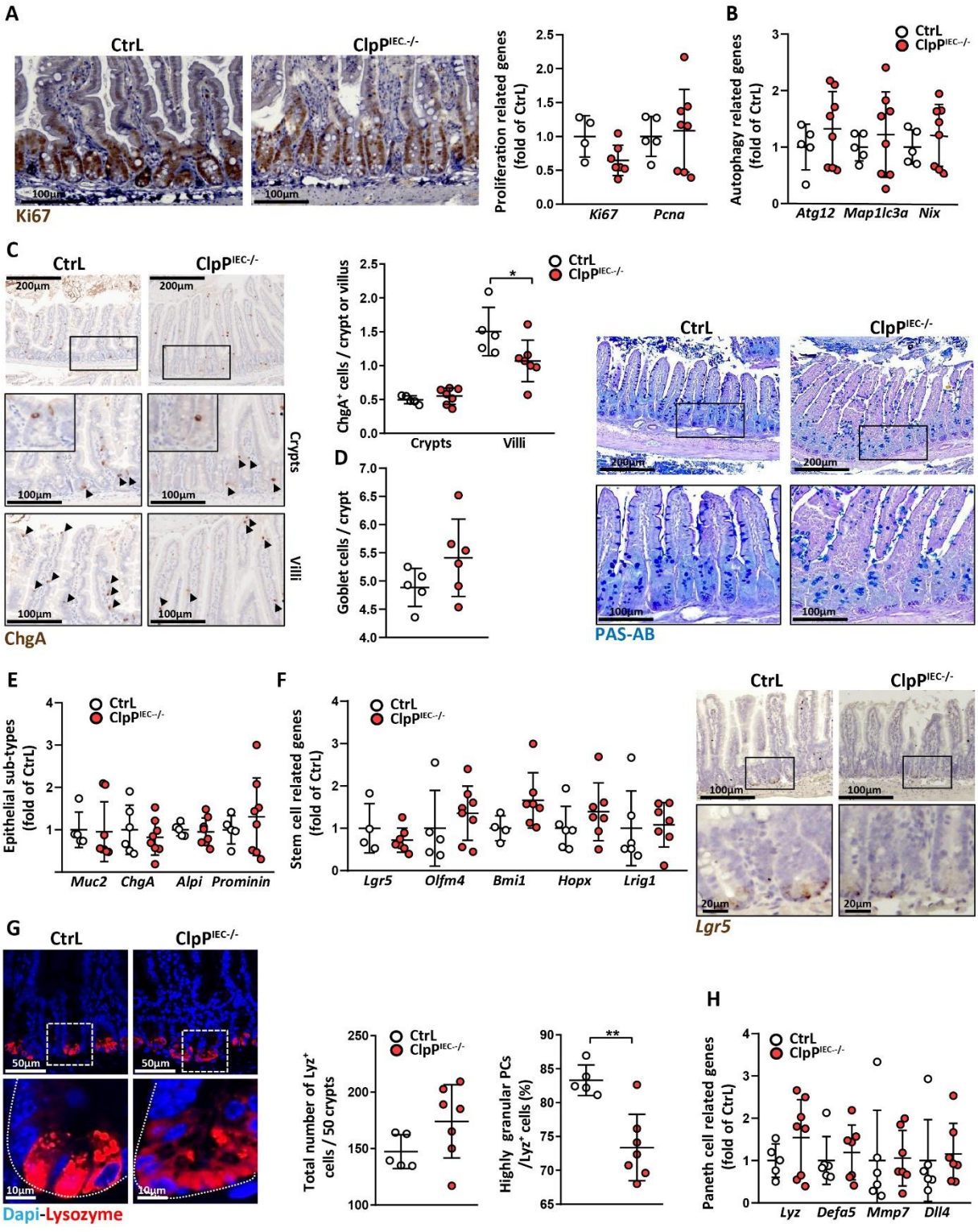

Figure 37 *ClpP* deletion does not alter epithelial proliferation and sub-types

(**A**) Representative images of IHC staining for Ki67; qRT-PCR analysis of small intestinal IECs for proliferation markers (Ctrl: N≥4; ClpP$^{-/-}$: N≥7). (**B**) qRT-PCR analysis for Autophagy-associated genes in small intestinal IECs of floxed control (N≥4) and ClpP$^{-/-}$ mice (N≥7). (**C**) Representative pictures of IHC staining for ChgA including magnifications. Arrow-heads illustrate the ChgA^{+} cells in crypts (middle picture) and in villi (lower picture); Quantification of the ChgA^{+} cells in the crypt and villi of control (N=5) and ClpP$^{IEC-/-}$ mice (N=7). (**D**) Quantification of the PAS-AB^{+} cells in the crypt of control (N=5) and ClpP$^{IEC-/-}$ mice (N=6); Representative pictures of PAS-AB staining including magnifications. (E,F) qRT-PCR analysis for genes related to epithelial sub-

types (**E**) and stem cell markers (**F**) in floxed control (N≥4) and ClpP$^{IEC-/-}$ mice (N≥7). (**F**) *Lgr5 in situ* hybridization in small intestinal tissue sections. (**G**) Representative IF pictures of lysozyme (red) counterstained with Dapi (nuclei, blue) including magnifications; Quantification of the total number of Lyz^{+} cells and highly granular (≥2 granules) PCs (Ctrl: N=5; ClpP$^{IEC-/-}$: N=7). (**H**) qRT-PCR analysis of small intestinal IECs for PC function-related genes (Ctrl: N=5; ClpP$^{IEC-/-}$: N=7). Statistical analyses were performed via unpaired t-tests between controls and the ClpP$^{IEC-/-}$ mice for each gene of interest. Asterisks indicate significant differences *P<0.05, **P<0.01.

Transcriptional levels of mitochondrial dynamic-related genes, including mitochondrial fission (*Drp1*), fusion (*Mfn2*), and biogenesis (*Pgc1a*), as well as mitochondrial metabolism-related genes also remained comparable between ClpP$^{IEC-/-}$ and control mice (**Figure 36D,E**).

Having previously shown the effect of mitochondrial dysfunction on epithelial proliferation and stemness [62], Ki67 staining in small intestinal tissue sections depicted an unaltered epithelial proliferation in ClpP deficient mice. Transcriptional analyses for proliferation markers *Ki67* and *Pcna* further confirmed unaltered proliferation (**Figure 37A**). In contrast to our mouse models of inflammation and ISC-specific *Hsp60* deletion (**Figure 24**), autophagy and mitophagy were not activated after ClpP loss (**Figure 37B**), indicating that compensation of ClpP loss might start early in development. Therefore, ClpP loss might not cause acute stress. We also detected unchanged transcription of markers for intestinal epithelial sub-populations, including *Muc2* (goblet cells), *ChgA* (enteroendocrine cells), *Alpi* (enterocytes), and *Prominin* (Transit-amplifying-cells) (**Figure 37E**). ChgA and PAS-AB stainings further confirmed the presence of comparable numbers of enteroendocrine cells and goblet cells in the crypt base of ClpP$^{IEC-/-}$ and control mice, respectively. Yet, ChgA^{+} cells were slightly reduced in villi of ClpP$^{IEC-/-}$ mice (**Figure 37C,D**).

Investigating the role of mitochondrial function on stem cell niche regulation, we characterized the PC phenotype and *Lgr5* expression in ClpP$^{IEC-/-}$ mice. Transcriptional analysis as well as *in situ* hybridization showed unaltered *Lgr5* expression in ClpP deficient mice. Additional stem cell markers remained unchanged in tissue sections from ClpP$^{IEC-/-}$ mice compared to controls, indicating that ClpP deficiency had no impact on epithelial stemness (**Figure 37F**). Characterizing the PC phenotype, we observed no alteration in numbers of Lyz^{+} cells in the small intestine of 53 weeks old ClpP$^{IEC-/-}$ mice. However, the proportion of highly granular PCs was reduced (**Figure 37G**). Transcriptional analysis for PC function-associated genes showed consistent expression between control and ClpP$^{IEC-/-}$ mice (**Figure 37H**).

Germline deletion of *ClpP* was further analyzed in 4 weeks old ClpP$^{IEC-/-}$ mice. IEC-specific ClpP loss was associated with unchanged mitochondrial signaling. Increased transcription of *Nix* and *Drp1* was pointing to an altered mitochondrial dynamic (mitophagy and fission) in the small intestine after 4 weeks of ClpP loss. Despite reduced *Lyz* expression, epithelial stemness remained unaltered in these mice (**Figure 38**).

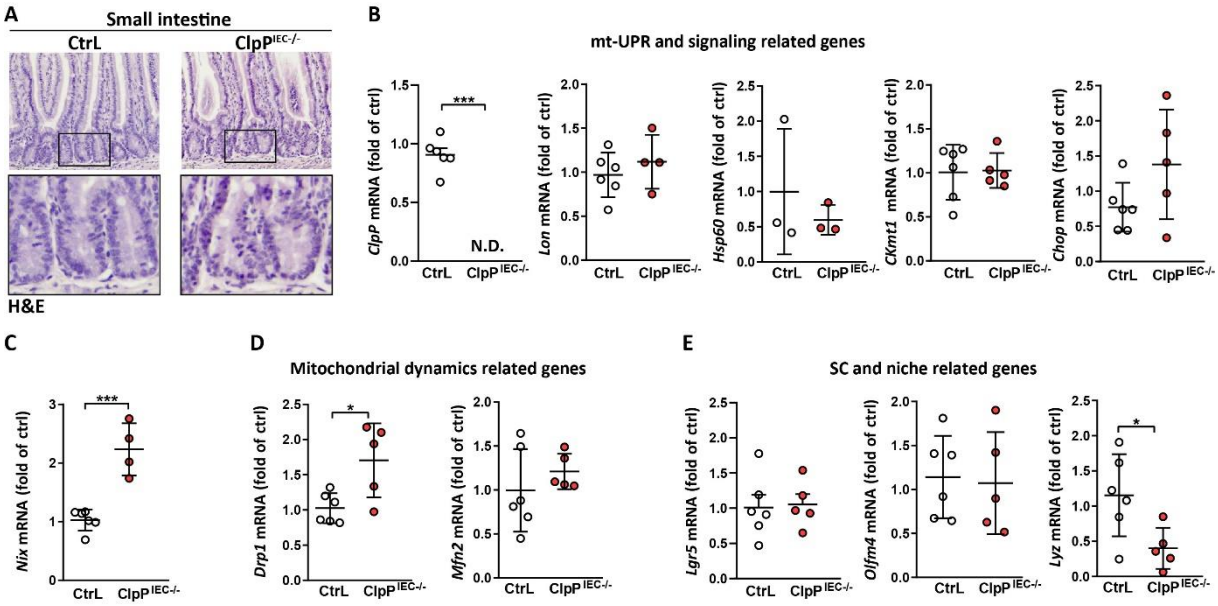

Figure 38 Adaptation of mice to ClpP loss leads to unaltered mitochondrial signaling and function

(**A**) Representative small intestinal H&E staining of 4 weeks old floxed control and ClpP$^{IEC-/-}$ mice. (**B-E**) qRT-PCR analysis of small intestinal tissues for mt-UPR and mitochondrial signaling-associated genes (Ctrl: N≥3; ClpP$^{IEC-/-}$: N≥3) (**B**); mitophagy-related gene *Nix* control (Ctrl: N=6; ClpP$^{IEC-/-}$: N=4) (**C**); mitochondrial dynamics (**D**) and stem cell niche (**E**) -related gene in control (N=6) and ClpP$^{IEC-/-}$ mice (N=5). Statistical analyses were performed via unpaired t-tests. Asterisks indicate significant differences *P<0.05, **P<0.01.

In conclusion, in contrast to constitutive Hsp60 knockout mice [62], ClpP$^{IEC-/-}$ mice are not embryonically lethal. These mice do not show mt-UPR activation, altered epithelial proliferation and stemness. Yet, constitutive *ClpP* deletion is associated with PC dysfunction, and altered mitochondrial metabolism.

4.12 Characterization of ClpP deficient organoids as models of mitochondrial dysfunction

4.12.1 Induced ClpP loss show increased apoptosis and circular growth in organoids

Although no enhanced proliferation was observed in response to ClpP loss *in vivo*, constitutive ClpP$^{IEC-/-}$ small intestinal organoids showed larger area at day 8 after passaging (**Figure 39A**). This might indicate an increased proliferation and differentiation in these organoids.

Hsp60$^{\Delta/\Delta IEC}$ mice-derived organoids previously showed growth defects, altered mitochondrial metabolism, and activated mt-UPR. Additionally, stemness was reduced upon *Hsp60* deletion [62]. Therefore, we investigated the impact of *ClpP* deletion in small intestinal organoids-derived from tamoxifen-inducible ClpP$^{\Delta/\Delta IEC}$ mice. To induce the *ClpP* deletion, organoids were treated for 24h with 4-hydroxy tamoxifen (4-OHT) and sampled at day 2 and day 6. Reduced size and bud numbers of ClpP$^{\Delta/\Delta IEC}$ organoids were indicative of growth defect starting from day 2. At day 6, the majority of ClpP deficient organoids depicted a circular phenotype. The spherical appearance of organoids and reduced differentiation were previously observed upon the presence of Wnt factors in the medium of organoids [59]. The area of ClpP$^{\Delta/\Delta IEC}$ organoids was significantly reduced at both time-points after induction of the knockout (**Figure 39B**). For measurement of the seeding efficiency, organoids were passaged and kept in culture for additional 6 days. Despite the circular appearance, ClpP$^{\Delta/\Delta IEC}$ organoids could expand and grow (**Figure 39C**).

Transcriptional analysis for *ClpP* confirmed a successful gene deletion after tamoxifen treatment at day 2 and day 6. Moreover, Mutation-specific PCR verified the presence of knockout allele at day 6 (**Figure 39D**). Life-cell protease activity showed no differences in the proportion of living cells at day 2 between ClpP$^{\Delta/\Delta IEC}$ organoids and controls, which ensured the equal cell numbers in these organoids. Caspase 3/7 activity indicated elevated apoptosis at day 2. Interestingly, the apoptosis rate was further induced at day 3, which could possibly influence the circular appearance of these organoids. Since genes of anti-oxidative stress response were induced in Hsp60$^{\Delta/\Delta IEC}$ mice [62], we measured ROS levels in ClpP$^{\Delta/\Delta IEC}$ organoids. ROS measurements depicted a minor but significant reduction in ROS levels in ClpP $^{\Delta/\Delta IEC}$ organoids at day 2, which could be a sign of altered mitochondrial function (**Figure 39E**).

In line with our *in vivo* observations, unaltered expression of proliferation markers (*Ki67* and *Pcna*) and autophagy-related genes (*Nix* and *Atg12*) *ex vivo* in organoids culture were indicating that the proliferation and autophagy are not activated upon *ClpP* deletion (**Figure 39F**).

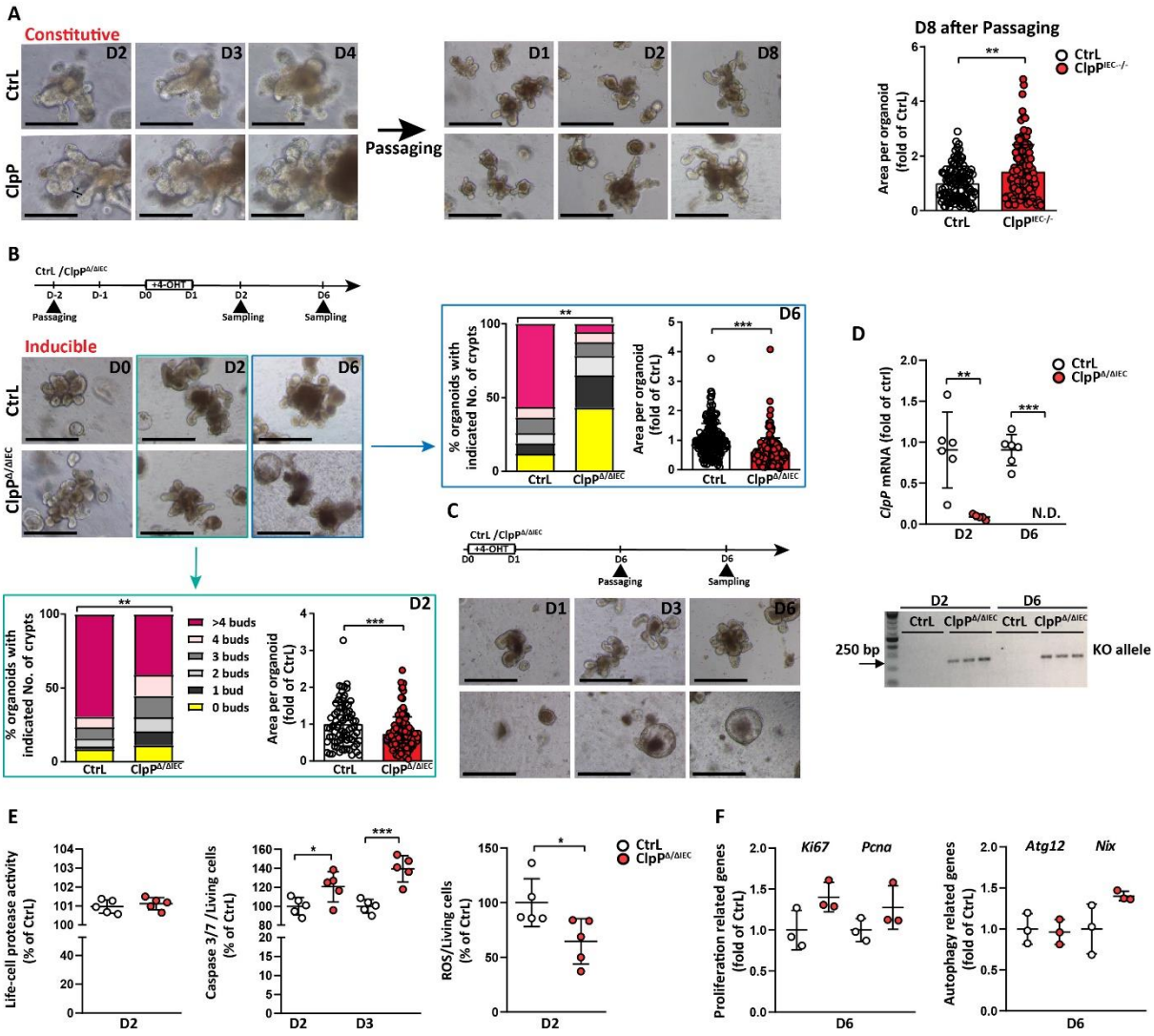

Figure 39 Inducible ClpP$^{\Delta/\Delta IEC}$ organoids have growth defects

(**A**) Representative bright field pictures for constitutive ClpP$^{IEC-/-}$ organoids and floxed controls at indicated time-points; Right: measurement of the size of organoids. (**B**) Experimental scheme showing the process of tamoxifen treatment. Organoids derived from ClpP$^{\Delta/\Delta IEC}$ mice were treated with tamoxifen to induce IEC-specific ClpP loss and sampled at day 2 and day 6. Tamoxifen treated Cre negative organoids served as a control; Quantification of the *de novo* crypt formation (budding) and the size of organoids at day 2 (green box) and at day 6 (blue box) after tamoxifen treatment; (**C**) Experimental scheme showing the long term monitoring of ClpP$^{\Delta/\Delta IEC}$ organoids after passaging. (**D**) qRT-PCR analysis of *ClpP* at D2 and D6 after treatment (N=6); Mutation-specific PCR showing the ClpP knockout (KO) allele in DNA extracted from the ClpP$^{\Delta/\Delta IEC}$ and control organoids (N=3). (**E**) Measurement of the life-cell protease activity; Caspase 3/7 (apoptosis marker) relative to life-cell protease activity after 6h and 24h; ROS content relative to life-cell protease activity (6h) at day 2 after tamoxifen treatment in ClpP$^{\Delta/\Delta IEC}$ organoids and controls (N=5). (**F**) qRT-PCR analysis of the proliferation markers and Autophagy-associated genes. Scale bar indicates 200µm. Statistical analyses were performed via unpaired t-tests between two groups at specific time-point. For de novo crypt formation, a Kruskal–Wallis test on ranks followed by Dunnś test was performed. Asterisks indicate significant differences *P<0.05, **P<0.01, ***P<0.001.

4.12.2 Induced ClpP loss impairs mitochondrial function and activates mt-UPR in organoids

Characterizing mitochondrial signaling in ClpP$^{\Delta/\Delta IEC}$ organoids, we observed an increased expression of mitochondrial intermembrane-localized protease *HtrA2* at day 6. This could indicate a compensatory mechanism in response to ClpP loss. Although no differences were observed in *Hsp60* expression, *Atf5* and *Chop* transcriptions were elevated at day 6 and day 2, respectively, indicating that mt-UPR signaling pathways are activated upon *ClpP* deletion. Consistent with *in vivo* experiments, we observed a downregulation in *CKmt1* expression in ClpP$^{\Delta/\Delta IEC}$ organoids (**Figure 40A**), which could suggest reduced mitochondrial energy shuttling.

Since ROS levels were reduced in ClpP$^{\Delta/\Delta IEC}$ organoids (**Figure 39E**), we investigated genes involved in mitochondrial oxidative response and respiration. Elevated expression of transcription factor *Hif1a* at day 2 and induced expression of the enzyme *HO1* at day 6 suggested an activated anti-oxidative response in ClpP$^{\Delta/\Delta IEC}$ organoids. Yet, the transcriptional levels of enzymes *Sod2* and *Catalase* remained unaltered at both time-points (**Figure 40B**). Also, respiration-related genes (*CoxI* and *CoxIV*) were not altered in expression at day 6 in ClpP$^{\Delta/\Delta IEC}$ organoids compared to controls, showing that the OXPHOS was not affected by *ClpP* deletion (**Figure 40D**).

Elevated Drp1 was previously observed in cells in response to ClpP knockdown [156]. Similarly, the expression of mitochondrial fission-related gene *Drp1* was significantly upregulated at day 6. In contrast to *Drp1, Pgc1a* expression was induced at the early time-point (day 2). Together, these data indicate that elevated mitochondrial dynamics and biogenesis might help cells to overcome ClpP loss (**Figure 40C**). In line with mt-UPR activation, the transcriptional analysis showed a mild but significant elevation in the expression of the ER-chaperone *Grp78* (**Figure 40E**).

These data indicate that mice with ClpP loss in IECs serve as models for mild mitochondrial dysfunction.

4.12.3 Loss of ClpP is associated with reduced PC granularity

Berger *et al*. previously showed the association between the loss of Hsp60 in organoids and reduced stemness [62]. In this thesis, we also observed reduced stemness and PC dysfunction upon inflammation and mitochondrial dysfunction *in vivo*. Therefore, we investigated intestinal epithelial sub-populations, specifically the ISC niche function, in ClpP$^{\Delta/\Delta IEC}$ organoids. Characterizing epithelial sub-populations, we observed that expression of *Muc2, Dclk1* and *ChgA*, markers for secretory IEC sub-types (goblet cells, tuft cells and enteroendocrine cells), and expression of *Alpi*, a marker for enterocytes, significantly increased at day 6 in ClpP$^{\Delta/\Delta IEC}$ organoids (**Figure 41A**). Additionally, ClpP$^{\Delta/\Delta IEC}$ organoids showed reduced transcription of stem cell markers *Lgr5* and *Olfm4* (**Figure 41B**). In line with reduced stemness, we observed significant downregulation in the PC marker *Lyz* at day 2. At day 6 after tamoxifen treatment, organoids regained *Lyz* expression (**Figure 41B**). To test if reduced *Lyz* expression is due to reduced numbers of Lyz$^+$ cells or an altered PC function, we performed lysozyme staining in ClpP$^{\Delta/\Delta IEC}$ organoids at day 2. Total numbers of Lyz$^+$ cells remained unchanged after *ClpP* deletion. However, the

proportion of highly granular PCs was reduced in ClpP$^{\Delta/\Delta IEC}$ organoids (**Figure 41E**), indicating that the ISC niche function is affected by *ClpP* deletion.

Together, these data indicate the adaption of cells to the lack of ClpP *in vivo*. Yet, in organoids, cells need to adapt to the actual loss of ClpP. This might be the reason for induced epithelial secretory cell-types to compensate for ClpP loss.

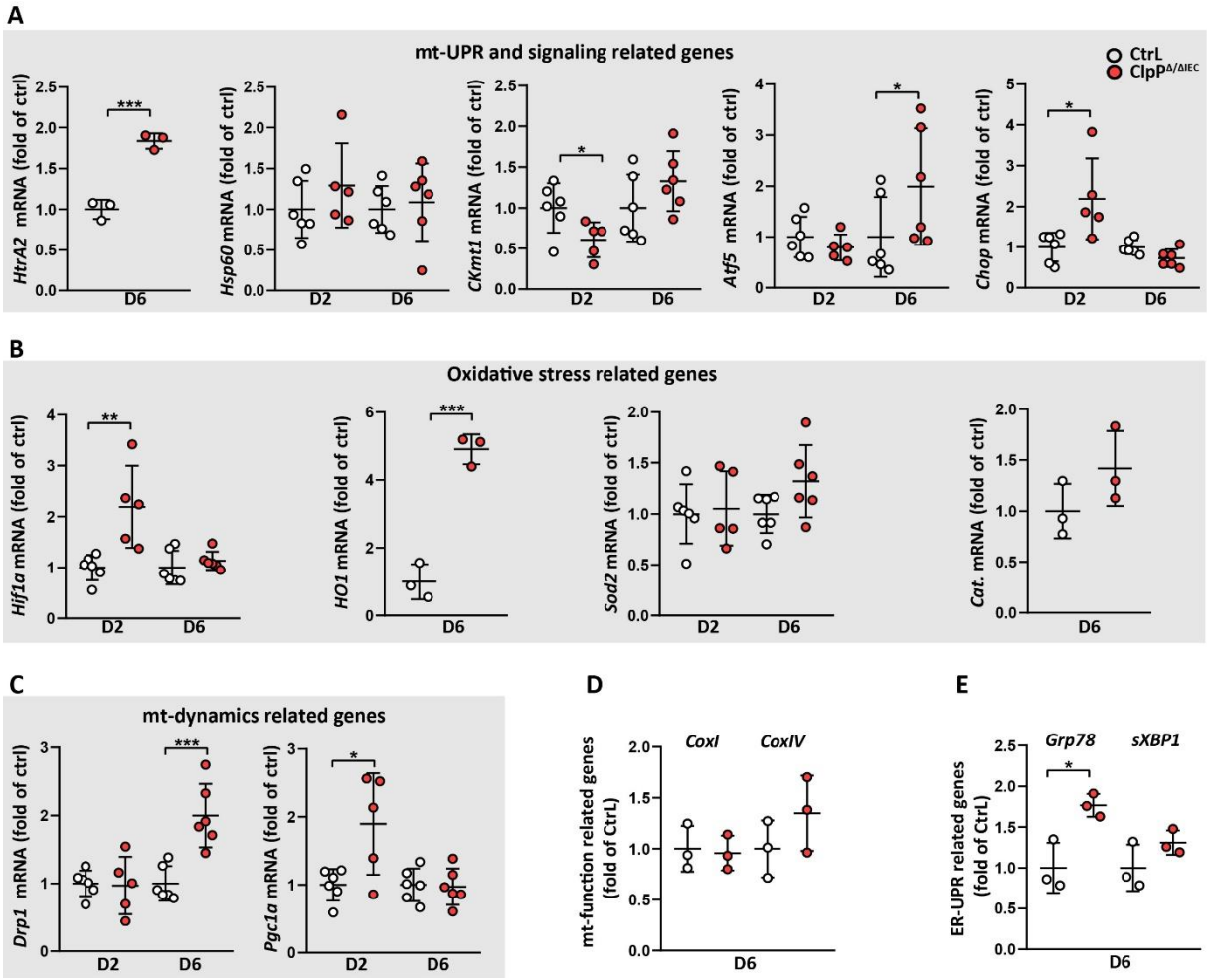

Figure 40 Characterization of mitochondrial function, mt-UPR activation and oxidative stress in tamoxifen induced ClpP$^{\Delta/\Delta IEC}$ organoids

Transcriptional analysis of the small intestinal Organoids derived from ClpP$^{\Delta/\Delta IEC}$ mice and controls were analyzed at day 2 and day 6 after tamoxifen treatment. qRT-PCR analysis of the mt-UPR and mitochondrial signaling-related genes (**A**); Oxidative stress-associated genes (**B**); mitochondrial dynamics-related genes (**C**); mitochondrial respiration- related genes (**D**); ER-UPR-associated genes (**E**) in ClpP$^{\Delta/\Delta IEC}$ and control organoids (N≥3). Statistical analyses were performed via unpaired t-tests between two groups at specific time-point. Asterisks indicate significant differences *P<0.05, **P<0.01, ***P<0.001.

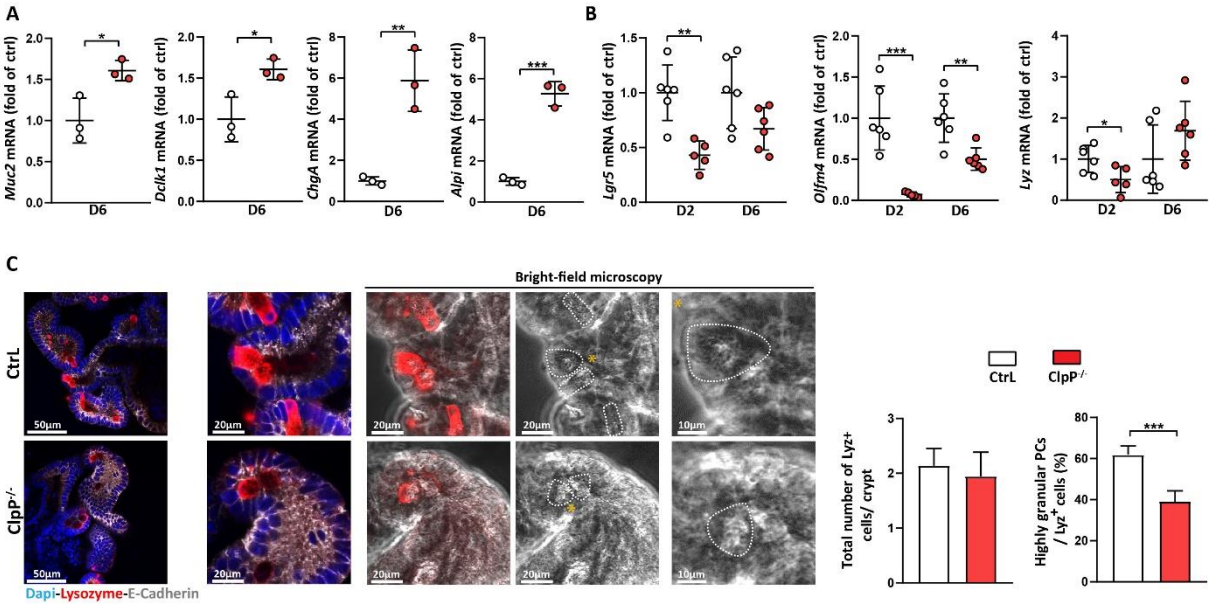

Figure 41 The ISC niche function is altered upon *ClpP* deletion in ClpP$^{\Delta/\Delta IEC}$ organoids

Transcriptional levels of different genes were analyzed in the small intestinal Organoids derived from ClpP$^{\Delta/\Delta IEC}$ and control mice. (**A**) qRT-PCR analyses of intestinal epithelial sub-population-related genes at day 6 in ClpP$^{\Delta/\Delta IEC}$ and control organoids (N=3). (**B**) qRT-PCR analyses of the Stem cell markers (*Lgr5* and *Olfm4*) and PC marker (*ysozyme*) in ClpP$^{\Delta/\Delta IEC}$ and control organoids (N=6). (**C**) Representative picture of IF co-staining for lysozyme (red) and E-cadherin (IEC borders, grey) counterstained with Dapi (nuclei, blue). Dotted lines indicate cell borders of Lyz positive (Lyz$^+$) cells; asterisks indicate Lyz$^+$ cells magnified in the pictures on the right side; Quantification of the total numbers of Lyz$^+$ cells per crypt (upper graph) and the proportion of highly granular (≥2 granules) PCs (lower graph) (N=6 biological replicates; 50 buds; 25 different organoids). Statistical analyses were performed via unpaired t-tests between two groups at specific time-point. Asterisks indicate significant differences *P<0.05, **P<0.01, ***P<0.001.

5. Discussion

IBD, including Crohn's disease and ulcerative colitis, constitute a global health problem [157]. The heterogeneity of IBD is a major challenge in the treatment of disease [158]. A great number of CD-relevant genes and diverse environmental triggers contribute to CD pathogenesis, causing different phenotypes in CD [28, 117]. Although several therapies have been used for CD, the majority of patients with severe disease course need surgery [115]. In the present study, we investigated the role of mitochondrial dysfunction in the ISC niche, including PCs, and characterized its association with inflammation. In mouse modes of inflammation and mitochondrial dysfunction, ileal margins of CD patients, as well as *ex vivo* organoid culture, we observed reduced stemness and PC dysfunction. Mitochondrial impairment further caused the differentiation of *Lgr5*$^{+}$ stem cells into dysfunctional PCs. Based on the ISC niche phenotype in ileal tissue sections from non-active CD patients we could predict postoperative endoscopic recurrence. We suggest that the DCA-mediated shift towards mitochondrial respiration restores dysfunction of the ISC niche, caused by inflammation. Our data suggest that changing the ISC niche through mitochondrial function-dependent processes might serve as a novel drug target in CD pathogenesis.

5.1 Inflammation is associated with altered ISC niche function

PCs produce and secrete antimicrobial peptides (AMPs), which are important for the establishment of the mucosal barrier [159, 160] and the regulation of the gut microbiome [161]. Wehkamp *et al*. have shown the association between reduced AMP production and barrier disruption, compromised mucosal defense and increased risk of CD [162]. Reduced PC function in the context of AMP production and alterations of the intestinal microbiota have been studied extensively [24, 25, 126]. Similarly, we found reduced PC numbers and PC dysfunction in patients with CD and in inflamed TNF$^{\Delta ARE}$ mice. Reduced PC numbers were confirming the observations from Schaubeck *et al.*, in which bacterial dysbiosis, concomitant with reduced PC numbers, occurred subsequent to inflammation [12]. PCs differentiate directly above the crypt base and migrate into the crypt base [4]. By residing between *Lgr5*$^{+}$ stem cells and having close contact with *Lgr5*$^{+}$ stem cells, PCs provide essential signals, including Wnt factors and metabolites that are necessary for the maintenance of *Lgr5*$^{+}$ stem cells [59, 148, 163]. Therefore, abnormalities in PCs can lead to alterations in ISCs. Consequently, we found an inflammation-mediated gradual reduction in *Lgr5*$^{+}$ ISCs in the crypt base of TNF$^{\Delta ARE}$ mice, which was reflecting the inflammation-mediated gradual loss of PCs and PC function. Similarly, inflamed CD patients showed reduced *LGR5* expression and PC numbers, which confirmed the association between inflammation and reduced stemness as well as ISC niche alterations. In line with reduced stemness and PC dysfunction, we observed a distorted pattern of *LGR5* and LYZ expression in inflamed margins of CD patients, which

indicates an irregular ISC niche architecture under inflammation. So far, reduced stemness has been observed in response to acute epithelial injury [54] and γ-irradiation [164-166]. However, the impact of chronic intestinal inflammation, including CD, on *LGR5*$^{+}$ stem cells remains unclear. Schmitt *et al*. have previously suggested that the rapid restoration of *Lgr5*$^{+}$ stem cells following their depletion in response to DSS-induced inflammation is due to the activation of regenerative responses in the crypt base [54]. It has also been reported that upon depletion of *Lgr5*$^{+}$ stem cells, PCs with proliferative capacity (Ki67) and cytoplasmic lysozyme expression acquire stem-like properties, de-differentiate to *Lgr5*$^{+}$ ISCs and support the repair and the regeneration of the damaged epithelium [54]. In our study, reduced stemness was associated with increased proliferation in crypts of TNF$^{\Delta ARE}$ mice. However, PCs showed no proliferation (ki67), suggesting that dysfunctional PCs in TNF$^{\Delta ARE}$ mice might not de-differentiate to *Lgr5*$^{+}$ ISCs. Increased proliferation might point to elevated cellular differentiation and reduced stem cell self-renewal in these mice. In addition to PC de-differentiation that supports the reconstitution of *Lgr5*$^{+}$ ISCs, quiescent stem cells or de-differentiation of transit-amplifying cells have been shown to restore depleted stem cells [164-166]. Suzuki *et al.* have shown an association between elevated numbers of small intestinal crypt epithelial cells in organoids derived from active CD patients with increased *OLFM4* expression in crypts [167]. This suggests a modification of stem cell properties upon inflammation. Yet, crypt elongation and increased epithelial cell proliferation in our mouse model of CD-like ileitis were paralleling reduced *Olfm4* expression. *Olfm4* is a target gene of Notch signaling and reduced expression of *Olfm4* might be associated with reduced Notch activity [168]. Carulli *et al*. have shown an association between *Notch1* deletion and reduced stemness [168]. Notch inhibition leads to the differentiation of intestinal crypts towards secretory cell-types [43-45]. In this context, we found an induced MMP7 expression in upper crypts of inflamed TNF$^{\Delta ARE}$ mice, which was similar to distorted LYZ expression in upper crypts of CD patients with active disease. MMP7 is a Wnt target gene [169] and the elevated expression could indicate altered epithelial differentiation. Furthermore, Rubio *et al*. have shown an association between gastric intestinal metaplasia and intermediate goblet-Paneth cells in the epithelium [170]. The presence of intermediate cell-types in the intestinal epithelium indicates disturbed epithelial differentiation. Intermediate cells are not found under homeostatic conditions in the small intestine. Nevertheless, it has been reported that epithelial injury and infection stimulate these cell-types, which leads to the expansion of secretory cells in crypts and the improvement of epithelial repair [171, 172]. Moreover, similar to MMP7 expression in the upper crypt position of TNF$^{\Delta ARE}$ mice, the presence of LYZ^{+} cells above the crypt base in CD patients could indicate the activation of intermediate cell-types. Therefore, it will be crucial to investigate whether aberrant PCs have an intermediate goblet-Paneth cell feature.

Irradiation and DSS-induced inflammation cause acute mucosal injury, which is not entirely reflecting the chronic inflammation that is observed in CD pathology. Despite reduced *Lgr5* expression upon DSS-induced inflammation, crypts-derived from these mice had enhanced capacity to form organoids [54]. This is contrasting our observation, in which crypts-derived from inflamed TNF$^{\Delta ARE}$ mice failed to give

rise to organoids. The failure of inflamed TNF$^{\Delta ARE}$ mice-derived organoids to propagate and form full-size budding organoids goes in line with reduced crypt numbers *in vivo* in inflamed TNF$^{\Delta ARE}$ mice. The degradation of inflamed TNF$^{\Delta ARE}$ organoids might be due to reduced *Lgr5*$^{+}$ stem cells or the presence of dysfunctional PCs in these organoids, similar to the phenotype observed *in vivo* in inflamed TNF$^{\Delta ARE}$ mice. Dysfunctional PCs that are generated upon inflammation might not be able to provide essential factors to support *Lgr5*$^{+}$ stem cell maintenance. Hence, impaired ISC niche function might lead to total epithelial destruction in inflamed TNF$^{\Delta ARE}$ organoids. Growth factors (Wnt factors, EGF, TGFα) and Notch ligands, including Dll4, arise from Paneth cells and positively influence organoid formation [148]. Wnt factors arising from PCs support the maintenance of *Lgr5*$^{+}$ stem cells. Therefore, the addition of Wnt ligands and growth factors to the organoid medium partially substitutes PC function by providing Wnt factors and supports the maintenance of *Lgr5*$^{+}$ stem cells [59]. Dysfunctional PCs in inflamed TNF$^{\Delta ARE}$ organoids might not be able to provide necessary Wnt signals to *Lgr5*$^{+}$ stem cells, which might lead to growth defects and failure in the propagation of these organoids. Contradicting the findings from Rodriguez *et al*., in which Wnt factors were beneficial for the growth of organoids [59], the addition of the Wnt-conditioned medium in our study had no impact on the survival of inflamed TNF$^{\Delta ARE}$ organoids. Wnt factors arise from both the mesenchyme and PCs. The Wnt-containing medium that was used in our experiments is commercially available. If Wnt components that are present in this medium are mainly arising from the mesenchyme, they are unable to substitute PC function and rescue the inflammation-altered ISC niche function. In this commercially available medium, lack of information about the cell-type from which Wnt signals originate might be a limiting factor in our study. Hence, phenotypic changes of the ISC niche under inflammation in TNF$^{\Delta ARE}$ mice is not associated with restoration of stemness and healing of the epithelium but rather indicate disturbed stem compartment, which is a feature of CD pathology.

5.2 The role of mitochondrial signaling in ISC niche regulation

Several studies have shown the involvement of organelle stress in the pathogenesis of IBD [66, 107, 126]. Yet, it is not clear whether the activation of organelle stress is a cause or consequence of inflammation. Previously, Rath *et al*. showed PKR activation in IBD patients and mouse models of experimental colitis, linking mitochondrial stress to inflammation [66]. This goes in line with our findings of elevated Pkr expression in response to inflammation in TNF$^{\Delta ARE}$ mice. Additionally, *Pkr* deficiency protected mice from epithelial injury [66]. We suggest that the crypt-base epithelium under inflammation suffers from mitochondrial dysfunction, and the induced mitochondrial signaling might not protect the epithelium from genetically-driven ileal inflammation. Investigating the link between inflammation, mitochondrial function and the function of the ISC niche, Theiss *et al*. have shown the association between mitochondrial dysfunction in PCs and intestinal inflammation [173]. Similarly, we found an impaired mitochondrial function in the intestinal stem cell niche, including dysfunctional PCs that were generated in the early stages of inflammation. Altered Hsp60 expression in crypts of TNF$^{\Delta ARE}$

mice was indicative of mt-UPR activation upon inflammation. This was confirming an elevated HSP60 expression in intestinal epithelial cells of IBD patients [66]. Hsp60 is not only a mitochondrial chaperone but also a mt-UPR target gene. Mouse models with disturbed proteostasis, which are generated by *Hsp60* deletion in IECs ($Hsp60^{\Delta/\Delta IEC}$) or ISCs ($Hsp60^{\Delta/\Delta ISC}$), have been considered as models for activated UPR and mitochondrial dysfunction [62]. The experimental disturbance of mitochondrial function in intestinal stem cells was associated with reduced stemness and PC dysfunction. This goes in line with findings from Berger *et al*., which suggest that mitochondrial function regulates intestinal epithelial stemness, and proliferation to maintain the epithelial homeostasis [62]. Berger *et al*. have previously shown reduced stemness both *in vivo* and *ex vivo* upon mitochondrial dysfunction in intestinal epithelial cells [62]. Dying stem cells have been shown to activate Wnt signaling and support tissue maintenance [174]. A similar phenomenon was observed in $Hsp60^{\Delta/\Delta IEC}$ mice, where paracrine Wnt signals from Hsp60 deficient crypts might support escaper stem cells and improve tissue regeneration [62]. Therefore, dying stem cells in the present study might support the epithelium to regenerate. Imbalances in intestinal epithelial cell homeostasis and epithelial cell death have been characterized as potential pathological mechanisms, driving CD [175]. Caspase-mediated apoptosis in IECs plays a role in the pathogenesis of CD. Several studies have shown the association between enhanced apoptosis in the crypt compartment and reduced differentiation, as well as the dysregulation of antimicrobial function [130, 175, 176]. The activation of necroptosis, in the absence of apoptosis, leads to a severe intestinal phenotype [130]. Increased cell death in the murine crypt base activates necroptosis in PCs. Similarly, PCs show an elevated necroptosis upon ileal inflammation in humans. Therefore, necroptosis plays a crucial role in the pathogenesis of CD [130, 175]. In addition to apoptosis and necroptosis, the activation of autophagy is important for the maintenance of the cellular energy homeostasis and leads to cell survival [125]. Cadwell *et al*. have previously shown that disturbed autophagy in PCs is associated with the impairment of mitochondria [28]. Moreover, Bel *et al*. have depicted the association between organelle stress, induced by a bacterial infection, and increased lysozyme secretion by PCs through secretory autophagy [177], which is an alternative way of energy generation. In our study, we demonstrated that the stem cell loss associated with mitochondrial dysfunction is not due to apoptotic cell death in the crypt base. In contrast to apoptosis, the induction of autophagy in dysfunctional PCs at the time-point with the highest number of dysfunctional PCs could be a possible mechanism to maintain the survival of these cell-types. Dysfunctional PCs express low levels of antimicrobial peptides (AMPs), including lysozyme, which might provide low-grade AMPs to the epithelium to overcome the mitochondrial dysfunction-induced epithelial complications. On one hand, following the repopulation of $Lgr5^{+}$ stem cells, apoptotic cell death might lead to the clearance of dysfunctional cell-types that are localized in the crypt base from the epithelium. On the other hand, Hsp60 negative cells might no longer be able to survive and will shed from the epithelium. This process might prevent activation of necroptosis in the intestinal epithelium as well as inducing intestinal inflammation in $Hsp60^{\Delta/\Delta ISC}$ mice. In the future, it is necessary to investigate

the activation of Wnt signaling as well as necroptosis in stem cell niche, including PCs, in our model and to observe if Wnt activation in the stem compartment might be a driving force in regeneration.

Several studies have shown the compensation of reduced CBCs by quiescent stem cells [178-180]. Similarly, in our study, we demonstrated an expansion of the quiescent stem compartment (*HopX*$^{+}$) and label-retaining cells (*Olfm4*$^{+}$), indicating that reserve stem cells might compensate for CBC ISC loss. Induced ER stress in IECs and uncontrolled UPR in PCs has been shown to cause PC abnormalities and spontaneous ileal pathologies [107, 126]. Similarly, the induction of mitochondrial stress in IECs caused PC dysfunction, indicating that impaired mitochondrial function in mature PCs might cause PC abnormalities. Upon mitochondrial stress, dysfunctional PCs do not express the proliferation marker (ki67). Therefore, they might not de-differentiate to *Lgr5*$^{+}$ stem cells. A similar phenotype was observed in our inflammatory model (TNF$^{\Delta ARE}$ mice). On the other hand, mitochondrial impairment in ISCs of Hsp60$^{\Delta/\Delta ISC}$ mice only affects the crypt compartment without affecting the transit-amplifying zone. Since Hsp60 knockout cells cannot propagate, all differentiated cells from the transit-amplifying zone, except PCs, remained protected from mitochondrial dysfunction. In this thesis, we demonstrate that PCs with dysfunctional appearance do not express Hsp60. Therefore, stem cells suffering from mitochondrial impairment directly differentiate to dysfunctional PCs (**Figure 42**). Together, these data indicate that mitochondrial dysfunction in stem cells disturbs the balance between self-renewal and differentiation. The inability of the epithelium to tolerate the impaired mitochondrial function subsequently interferes with differentiation processes, including PC maturation.

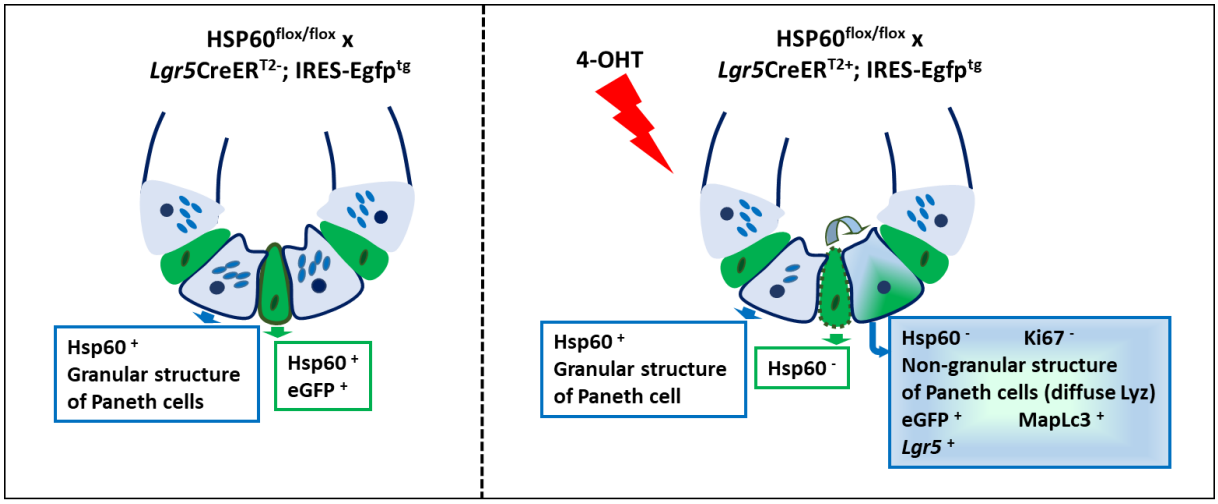

Figure 42 *Hsp60* deletion in stem cells lead to the transition of *Lgr5*$^{+}$ ISCs to dysfunctional PCs

The figure illustrates the impact of *Hsp60* deletion in ISCs and the dysfunctional PCs that are originating from *Lgr5*$^{+}$ ISCs. 4-OHT:4-hydroxy tamoxifen; Hsp60: Heat shock protein 60; *Lgr5* (Leucine rich repeat containing G protein-coupled receptor 5) and eGFP (Green fluorescent protein) are stem cell markers in this mouse model; Ki67, MapLc3 (Microtubule Associated Protein Light Chain 3) and Lyz (lysozyme) are markers for proliferation, autophagy and Paneth cells, respectively.

5.3 The role of mitochondrial metabolism in inflammation

Mitochondrial stress and disturbed mitochondrial signaling have been observed in IBD patients [66] and in TNF$^{\Delta ARE}$ mice. Different metabolic pathways take place in mitochondria. Citrulline, as one of the metabolites in the mitochondrial matrix, has been identified as a potential marker for bowel function [85]. Reduced plasma citrulline levels have been previously observed in short bowel syndrome [85]. Moreover, altered citrulline levels might indicate an altered mitochondrial function [85, 86]. Berger *et al*. have shown reduced plasma citrulline concentrations upon impairment of mitochondrial function in IECs of mice [62]. In our study, reduced plasma citrulline levels further confirmed the presence of mitochondrial dysfunction and altered mitochondrial metabolism in inflamed TNF$^{\Delta ARE}$ mice. In line with reduced expression of *Otc*, an enzyme that converts ornithine to citrulline in the mitochondrial matrix, plasma citrulline levels were decreased. Yet, the expression of ornithine-citrulline carrier remained unaltered, indicating that impaired mitochondrial metabolism in the CD-like ileitis model is caused by altered mitochondrial function rather than reduced mitochondrial numbers.

Previously, it has been suggested that impaired function of mitochondrial respiratory complexes results in reduced energy (ATP) generation in the colonic epithelium under inflammatory conditions [90]. Therefore, UC has been suggested as an energy-deficiency syndrome [90]. Reduced complex I activity in the rectum [181] and decreased complex II, III and IV activities in the colonic mucosa of UC patients were indicative of an altered mitochondrial function in response to inflammation [91, 92]. Similarly, as ATP levels were reduced in crypts of TNF$^{\Delta ARE}$ mice, we suggested that cells of the crypt compartment in the CD-like ileitis model are energy deficient upon inflammation. Oxygen deficiency in the intestinal epithelium, leading to hypoxia, has been previously observed upon active inflammation [182]. Responses to oxygen deprivation are mainly mediated through hypoxia-inducible factor (HIF) complexes [183]. The transcriptional activation of *Hif1α* in both TNF$^{\Delta ARE}$ and Hsp60$^{\Delta/\Delta ISC}$ mice as well as in Hsp60$^{\Delta/\Delta ISC}$ organoids could indicate a link between inflammation, mitochondrial metabolic impairment, and altered mitochondrial ROS levels. This could promote either tissue injury or tissue regeneration. The activation of hypoxia and the organelle stress in IBD patients was shown to mediate epithelial responses, including the activation of quiescent stem cells, to switch injury-repair cycles and to reinforce regeneration of the colonic epithelium [53]. Additionally, hypoxia regulates epithelial barrier function in experimental colitis [184], reduces the expression of pro-inflammatory cytokines (*Tnfa* and *Il6*) and promotes autophagy activation, which ameliorates intestinal inflammation [182]. However, mitochondrial dysfunction in our inflammatory model was rather promoting epithelial injury than regeneration.

Mitochondria have been shown to regulate metabolic processes during the differentiation of intestinal epithelial cells and play a pivotal role in ISC fate [63]. Mitochondrial oxidative phosphorylation (OXPHOS), together with glycolysis, provides the energy (ATP) that is needed for different IEC sub-types [63]. Therefore, the inhibition of either pathway can influence the cellular energy levels and cause

mitochondrial impairment. In *Lgr5*$^{+}$ stem cells isolated from the mouse small intestine, OXPHOS highly contributes to cellular bioenergetics and plays a crucial role in the initiation of de-novo crypt formation in intestinal organoids [59]. In our study, reduced ATP content in crypt isolates from inflamed TNF$^{\Delta ARE}$ mice was associated with growth defects and failure in the propagation of these organoids. This goes in line with reduced ATP production and reduced respiratory capacity in Hsp60$^{\Delta/\Delta IEC}$ mice-derived organoids, which is associated with defects in their propagation [62]. Additionally, the inhibition of the activity of respiratory chain complexes was previously shown to reduce ATP generation and disturb cellular energy metabolism [94]. Rodriguez *et al.* showed a reduced crypt formation in organoids after OXPHOS inhibition using Rotenone and oligomycin, which blocks the electron transport chain complex I and the ATP synthase, respectively [59]. Contrasting these findings, both oligomycin and Rotenone treatments had no significant impact on crypt formation of WT organoids, which confirmed the selection of a non-toxic dose and timing of the substances for treatment. *Ex vivo* inhibition of the ATP synthase in both murine and human organoids was associated with reduced stemness and PC dysfunction. Additionally, complex V inhibition led to transcriptional activation of the mt-UPR signaling-related genes (*Chop* and *Hif1α*) and the cellular energy response gene *Prkaa2*. All these genes link mitochondrial homeostasis to mt-UPR, ROS signaling, and energy-sensing mechanisms, which are commonly observed in IBD patients [63, 152, 185, 186]. *Prkaa2* (encoding AMP-kinase (AMPK) alpha2) expression depends on cellular energy levels, and reduced cellular ATP levels lead to the upregulation of *Prkaa2*, meaning activation of AMPK [187]. Therefore, inhibition of the ATP synthase in organoids, sensing cellular ATP/ADP levels, might reduce cellular ATP contents. Low cellular energy levels in organoids might lead to an induced *Prkaa2* expression. On the other hand, activation of AMPK is important for the restoration of cellular and physiological energy levels upon metabolic stress [188]. Additionally, we provide experimental evidence that reduced stemness and altered ISC niche function, which is mediated by mitochondrial impairment, is Chop independent. Ishikawa *et al*. have shown a role for Chop in regulating mitochondrial respiration-related genes [153]. *Chop* deletion in organoids was associated with reduced pseudokinase Tribble 3 (*Trb3*) and elevated Aspargine synthase (*Asns*) expression. This is in line with findings from Su *et al.*, in which amino acid deprivation and ER stress were associated with an induction of *Chop* expression, which suppressed transcriptional levels of *Asns* and induced *Trb3* expression [189]. Similarly, elevated *Chop* and *Trb3* levels were observed in response to mitochondrial dysfunction in Hsp60$^{\Delta/\Delta IEC}$ mice. However, *Chop* deletion in these mice had no impact on *Trb3* expression [62]. Together, these data suggest that oligomycin treatment influences the ISC niche function through a Chop-independent pathway.

In contrast to the inhibition of the ATP-synthase, complex I inhibition had no impact on ATP concentration. Yet, it was associated with reduced *Lgr5* expression and PC dysfunction. The function of complex I can be compensated by other respiratory chain complexes. Complex I consists of 45 subunits, and the N-module of this complex, which is the active part, is facing towards the mitochondrial matrix [190, 191]. Therefore, the N-module of complex I is in direct contact with mitochondrial

chaperones and proteases. In line with this, the ClpXP complex controls complex I, by regularly replacing the N-module components [191]. The regular turnover of the N-module of complex I via ClpXP preserves the function of this complex and maintains mitochondrial respiratory function [191]. Hence, it might be interesting to investigate the activity of the ClpXP complex in organoids after rotenone treatment. In contrast to oligomycin treatment, the inhibition of complex I was associated with the downregulation of *Hif1a* expression. A similar impact was previously observed in different cell lines, indicating that functional mitochondria and a respiratory chain are needed for the activation of hypoxic responses and the reaction to reduced oxygen levels [192, 193]. Induction of *Hif1α* was shown to be important for the neutralization of the toxic effects of Rotenone [194]. Rotenone treatment had no impact on the proportion of the living cells in our study, which could indicate the non-toxic effect of this treatment and no *Hif1α* upregulation. Mitochondrial complex I is the main contributor to the mitochondrial ROS production [195] and hypoxia-induced ROS levels, independent of *Hif1α*, control *Chop* expression [196]. Therefore, Rotenone treatment in our study did not downregulate *Chop* expression in mouse organoids. Since complex I activity can be compensated by other respiratory chain complexes, Rotenone treatment showed no impact on cellular ATP content and did not induce *Prkaa2* expression. Inflammation-associated reduced ATP levels in $TNF^{\Delta ARE}$ mice were paralleled by reduced stemness. Moreover, the expression of *Lgr5* was not associated with ATP levels upon inhibition of the ATP synthase. Unchanged ATP levels in response to the complex I inhibition were as well associated with reduced *Lgr5* expression. Together, these data indicate that cellular ATP levels might not be the mediator of *Lgr5* downregulation. However, excessive OXPHOS might lead to reduced stemness upon inflammation in this study. Induced ROS signaling has been shown to cause a toxic accumulation of α-ketoglutarate and influence stemness properties [197, 198]. Furthermore, the enhanced activity of pyruvate dehydrogenase, over-activation of the TCA cycle, and loss of mitochondrial membrane potential lead to the accumulation of toxic metabolites in mitochondria [197, 199]. Therefore, it might be necessary to characterize if induced ROS levels or further metabolic processes might mediate the *Lgr5* loss upon inhibition of respiration.

Reduced stemness and PC dysfunction in crypts-derived from inflamed $TNF^{\Delta ARE}$ mice might be the reason for the failure of these crypts to give rise to organoids. Furthermore, energy deficiency (indicated by reduced ATP and induced *Prkaa2*) in inflamed crypts, a reduced respiratory function (decreased *CoxI* expression) and an activated oxidative stress response (*Hif1a*) might point towards a reduced activity of OXPHOS in these mice. Increased *Hif1a* expression has been shown to activate the pyruvate dehydrogenase kinase (PDK) [200]. This enzyme inhibits the function of pyruvate dehydrogenase (PDH) and prevents ATP generation via OXPHOS. Instead, PDK induces lactate production [200]. Inhibition of PDK via dichloroacetate (DCA) has been identified as a possible approach to improve mitochondrial respiration (OXPHOS) [155] (**Figure 43**). This ability of DCA has been used for the treatment of solid tumors to reverse the 'Warbung' effect in cancer cells, as well as for patients with mitochondria-related disorders [154, 201-203]. Here we provide evidence that metabolic alteration,

mediated by DCA, rescues stemness and the inflammation-mediated growth defects in TNF$^{\Delta ARE}$ organoids. Previously, it has been reported that actively cycling *Lgr5*$^{+}$ stem cells highly depend on oxidative metabolism [59]. In this study, DCA treatment restored *Lgr5* expression, which was reduced by inflammation.

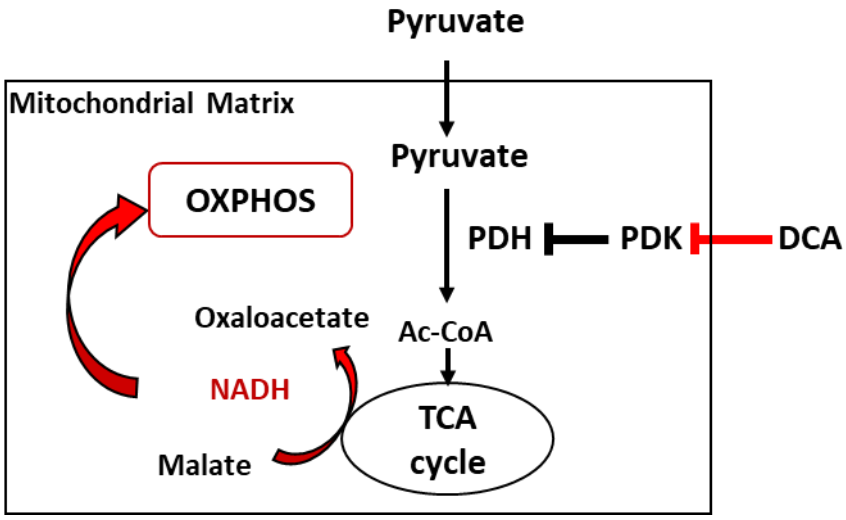

Figure 43 DCA shifts metabolism towards OXPHOS

Dichloroacetate (DCA)-mediated metabolic shift towards oxidative phosphorylation. PDK: Pyruvate dehydrogenase kinase; PDH: Pyruvate dehydrogenase. Ac-CoA: Acetyl CoA; TCA; Tricarboxylic acid cycle; NADH: Nicotinamide adenine dinucleotide; OXPHOS: Oxidative phosphorylation.

Preliminary *in vivo* experiments in DCA-treated TNF$^{\Delta ARE}$ mice suggested the protective impact of DCA on maintaining PC granularity. However, DCA showed no impact on the inflammation status of mice and could not rescue PC loss. This could be due to the wrong dosage, the inappropriate timing and the application techniques. Future experiments will be necessary to identify target metabolites that alter the ISC niche homeostasis. Additional research could help us identifying the therapeutic role of DCA on CD-like ileal pathology.

5.4 The ISC niche predicts endoscopic recurrence in CD patients

The heterogeneity of IBD is a major challenge in the treatment of disease [158]. Therefore, the therapeutic purpose of IBD is to maintain remission in patients [110]. In addition to anti-TNF therapies for the treatment of CD [204], combination therapies with immunomodulators [113], IL12/ IL23 inhibitors [205], and stem cell therapies [114] have been suggested to be effective approaches in reducing the disease burden in patients with severe disease course. Gisbert *et al.* have shown that two-third of CD patients need to undergo surgery and intestinal resection despite the existence of different approaches to maintain remission and to delay relapse in IBD patients [206]. In addition to different physiological complications, CD is associated with an altered PC function [28, 124, 207]. Organelle stress [107] and the cumulative number of *NOD2* and *ATG16L1* risk alleles [124] have been shown to

be associated with an aberrant granule structure in PCs and diffuse LYZ distribution. This links multiple CD-associated genetic risk loci to an altered PC phenotype. Transcriptional activation of cytokine stimulation in mice with hypomorphic expression of Atg16l1 [28] and an activated immune response gene signature in CD patients have further been linked to the dysfunctional PC phenotype [124]. In line with gross alterations in tissue pathology, we found PC dysfunction in inflamed $TNF^{\Delta ARE}$ mice and in inflamed CD patients. Normal PC function in non-inflamed $TNF^{\Delta ARE}$ mice and in non-inflamed jejunal tissue sections in $TNF^{\Delta ARE}$ mice were confirming the association of PC dysfunction with inflammation in our study. Disease relapses in CD patients are triggered by unknown factors. Although the prediction of primary responses to biological therapies might be challenging due to the complexity of the disease in CD patients [206], VanDussen *et al*. have shown an approach to predict the postoperative recurrence based on dysfunctional PCs [124]. Our findings on PC granularity confirm these findings in an independent cohort of CD patients. In our cohort, PC dysfunction in resected tissue margins predicts endocopic recurrence 6-12 months after surgery. Moreover, our findings expand the predictive markers to *LGR5* expression and the aberrant LYZ as well as *LGR5* localization. Yet, the ISC niche phenotype does not predict postoperative endoscopic recurrence in active CD patients. This phenomenon might be due to the already established inflammation and altered epithelial architecture. Here we show that abnormalities in the ISC niche are detected before the onset of severe tissue pathology and in non-active CD patients. Therefore, the altered ISC niche function might represent an early molecular marker for inflammation.

In contrast to the findings from VanDussen *et al*. in which *NOD2* and *ATG16L1* risk alleles were associated with PC abnormalities [124], the presence of genetic risk alleles of *NOD2* or *ATG16L1* and their combination had no impact on the ISC niche phenotype in the present study. The low sample size of patients possessing *NOD2* and/or *ATG16L1* risk alleles might be the reason for this observation. In addition to genetic risk factors, smoking has previously been identified as an environmental factor, which has a contradictory impact on IBD patients [116, 118]. A meta-analysis concluded that smokers might be less likely to develop UC [208]. However, smoking was shown to have a detrimental impact on the severity of the disease course in CD patients [208, 209]. Auzolle *et al*. as well reported the association between, the smoking status of CD patients at the time of resection surgery with an increased risk of postoperative endoscopic recurrence [116]. Despite the overall impact of smoking on the ISC niche phenotype, smoking showed no additional impact on the ISC niche appearance and architecture in patients that experienced postoperative endoscopic recurrence. These data indicate that both environmental and genetic risk factors including smoking and *NOD2*/ *ATG16L1*, respectively, most likely have an impact on disease susceptibility. Yet, the changes in the phenotype of the ISC niche might only be determined by the onset of inflammation. PC phenotype, *LGR5* expression, and the aberrant expression of LYZ and *LGR5* in upper crypts may serve as potential markers for prediction of disease recurrence in non-active CD patients.

5.5 ClpP deficient mice are models for mild mitochondrial dysfunction

Hsp60$^{\Delta/\Delta IEC}$ mice have been previously characterized as models for mt-UPR activation and mitochondrial dysfunction. Constitutive deletion of the mitochondrial matrix-localized chaperone Hsp60 in IECs of mice resulted in embryo-lethality [62]. In this study, we demonstrated that ClpP deficiency in IECs, as a mitochondrial matrix-localized protease, has no impact on the viability of mice, and ClpP deficient mice serve as mild models for mitochondrial dysfunction. ClpP null mice show infertility and growth retardation [82]. Infertility in female ClpP deficient mice was shown to be due to defects in oocyte maturation. However, other organs in these mice had no phenotypic changes [82]. In our study, we observed no changes in the intestinal tissue upon IEC-specific *ClpP* deletion, confirming that the deletion of mitochondrial protease has no impact on intestinal tissue and survival of mice. Yet, *ex vivo ClpP* deletion in organoid cultures caused reduced budding and circular appearance of organoids at day6 after tamoxifen treatment, suggesting reduced proliferation and differentiation in these organoids. In contrast to Hsp60 deficient organoids, which could not maintain and propagate [62], the circular appearance of ClpP deficient organoids had no influence on their maintenance and propagation. Previously, ClpP deficiency was shown to increase mitochondrial fragmentation, increase mitochondrial biogenesis (*Pgc1a*) and mitochondrial fission (*dynamin-related protein1* (*Drp1*); *Optic Atrophy 1* (*OPA1*) in muscle cells to maintain the mitochondrial quality [156, 210]. In our study, mitochondrial biogenesis was not altered upon constitutive *ClpP* deletion *in vivo*. Yet, it was induced *ex vivo* in organoid cultures shortly after induction of the knockout (day 2). Elevated mitochondrial fission after four weeks of constitutive *ClpP* deletion, as well as in ClpP deficient organoids, could point to the importance of mitochondrial dynamics in maintaining healthy mitochondria. Additionally, it could suggest a possible mechanism to overcome the cellular stress that is caused by *ClpP* deletion. Consistent with our inflammatory model (TNF$^{\Delta ARE}$ mice) in this thesis, citrulline concentrations were reduced in mice lacking ClpP. Yet, citrulline levels were only reduced in male but not female ClpP knockout mice, which were indicating an altered mitochondrial metabolism in male mice. This goes in line with findings from Didelija *et al*., in which a higher citrulline flux and an increased arginine synthesis were observed in female mice upon arginase II deficiency [211]. Our data suggest that in male mice lacking ClpP, it might be a reduced substrate flux through the mitochondrial ornithine-citrulline carrier.

Previously, *Hsp60* deletion in IECs was associated with an induced *ClpP* expression, indicating that in the absence of the chaperone, mitochondrial proteases might be activated to degrade misfolded proteins [62]. Contrarily, *ClpP* deletion depicted no influence on *Hsp60* expression. These data were consistent with an unaltered *Hsp60* expression upon loss of HtrA2, as a mitochondrial intermembrane-space-localized protease [212]. Although HtrA2-deficiency was associated with no changes in *ClpP* expression [212], *ex vivo ClpP* deletion in this study was associated with an enhanced *HtrA2* expression. This suggests the activation of additional mitochondrial proteases to compensate for the protein folding capacity of the organelle and to maintain the mitochondrial quality in response to *ClpP* deletion. Loss

of mitochondrial proteases was shown to cause respiratory defects and oxidative damage [212, 213]. Yet, long-term ClpP deficiency *in vivo* showed no alteration in oxidative stress-responses and mitochondrial respiration-related genes. In contrast to *in vivo* experiments, the induced oxidative stress response was observed *ex vivo* in organoids. This is in line with observations from Berger *et al*. for Hsp60 deficient organoids [62] and indicates an association of mitochondrial stress with oxidative damage. For investigation of altered respiration in response to ClpP loss, respiration measurements and measurement of the ATP content will be necessary in the future.

So far, several studies have shown an association between organelle stress and reduced stemness, PC dysfunction and epithelial differentiation [32, 62, 141, 173]. In line with previous observations *ex vivo* [62], *ClpP* deletion reduced epithelial stemness and PC function *ex vivo*. Yet, the mucus expression by goblet cells was increased in organoids. Wu et al. previously have shown reduced PC numbers and increased mucus production by goblet cells in response to infection, which maintains the protective function of the epithelium [214]. Therefore, following reduced PC function, which is caused by mitochondrial dysfunction, elevated secretory cell-types including goblet cells *ex vivo* might protect the epithelium from further influences of the impaired mitochondrial function. ClpP deficiency was shown to activate mTOR signaling and increase mTORC1 protein levels in ovaries [83]. mTORC1 in PCs forces stem cells into differentiation rather than self-renewal [57]. This might be the reason for unaltered epithelial sub-populations after long-term constitutive *ClpP* deletion.

Together, these data suggest that an IEC-specific ClpP knockout mouse model might serve as a model for milder mitochondrial dysfunction. In this study, the impact of *ClpP* deletion on mt-UPR activation and ISC niche function was observed *ex vivo* only immediately after induction of the knockout. Compensatory mechanisms, such as signals arising from the mesenchyme or enhancement of mitochondrial protein degradation by additional proteases might participate in preventing epithelium from damage. Therefore, further *in vivo* experiments will be necessary to characterize the role of ClpP on the ISC niche function. Being a model for mild mitochondrial dysfunction, the crossing of ClpP knockout mice with inflammatory or tumorigenic models will make it possible to investigate the involvement of mitochondria and mitochondrial metabolic processes in inflammation and tumorigenesis.

Conclusion

This work represents a novel approach, identifying the ISC niche as the target of inflammation and predictive molecular marker for postoperative endoscopic recurrence in non-active CD patients. We demonstrate a link between impaired mitochondrial function and CD-associated loss of stemness and PC-dysfunction. Since altered mitochondrial metabolism might be a driving force for CD [63, 106], by consequences of a drug-mediated shift towards mitochondrial respiration, we provide evidence for the restoration of ISC niche function before the onset of histopathology. Thereby, reinforcing mitochondrial respiration might be a novel therapeutic approach for CD.

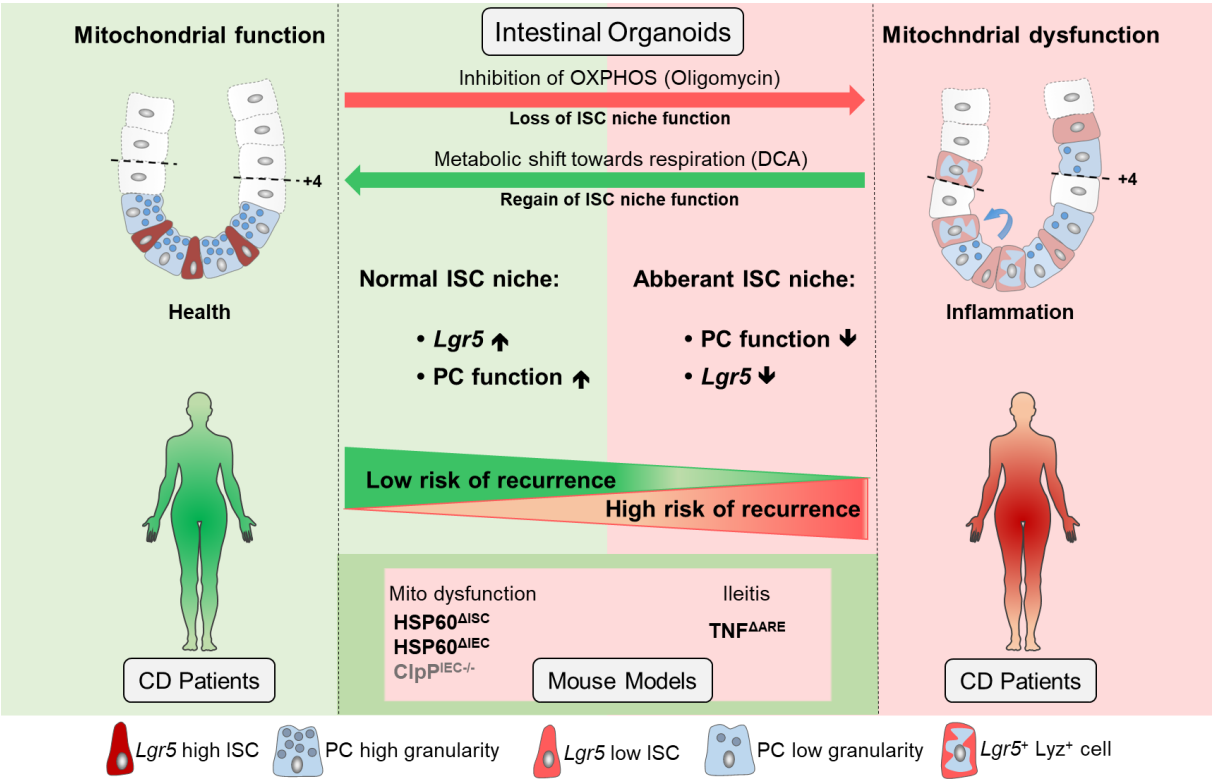

Figure 44 Mitochondrial impairment drives ISC transition towards dysfunctional PCs predicting Crohn's disease recurrence

Schematic illustration of the main findings in the present work. ISC-specific disruption of mitochondrial function leads to the transition of ISC into dysfunctional PCs, which are characterized by loss of Lyz positive granules and cytoplasmic Lyz expression. Mitochondrial impairment upon inflammation results in reduced stemness and PC dysfunction. Aberrant *LGR5* and LYZ expression in upper crypts and altered ISC niche function. These alterations predict disease recurrence in non-active CD patients. Ex. Vivo inhibition of mitochondrial respiration in organoids reflect the impact of an inflammatory condition on ISC niche. A shift towards mitochondrial respiration overrides altered ISC niche function that is mediated by inflammation. ARE: Adenosine-uracil (AU)-rich elements; TNF: Tumor necrosis factor; Hsp60: Heat shock protein 60; ClpP; Caseinolytic protease P; CD: Crohn's disease; PC; Paneth cells; DCA: Dichloroacetate; OXPHOS: Oxidative phosphorylation; Lyz: Lysozyme; *Lgr5*: Leucine rich repeat containing G protein-coupled receptor5.

List of figures

List of tables

Abbreviations

Abcb	ATP-binding cassette subfamily b
AB/ PAS	Alcian blue / Periodicacid-Schiff
AMPs	Antimicrobial peptides
Ang	Angiogenin
APC	Adenomatous polyposis coli
ARE	Adenosine-Uracil (AU)-rich regulatory element
ATF	Activating transcription factor
Atg	Autophagy related gene
Atoh	Protein atonal homolog
ATP	Adenosine triphosphate
BMP	Bone Morphogenic Protein
BMPRII	BMP receptor type II
cADPR	Cyclic ADP ribose
CBCs	Crypt base columnar cells
CCM	Crypt-culture medium
CC	Cleaved caspase
CD	Crohn's disease
C/EBP	CCAAT/enhancer-binding protein
ChgA	Chromogranin A
Chop	C/EBP homologous protein
ClpP	caseinolytic peptidase subunit P
CRC	Colorectal cancer
CtrL	Control
DCA	Dichloroacetate
Dclk1	Doublecortin-like kinase 1
Defa	Defensin
DLL	Delta-like ligand
DSS	Dextran sodium sulfate
EECs	Enteroendocrine cells
EGF	Epidermal growth factor
FFPE	Formalin-fixed paraffin embedded
ER	Endoplasmic reticulum
GI tract	Gastrointestinal tract
HopX	Homeodomain-only protein homeobox
HRP	Horseradish proxidase
Hsp	Heat shock protein
IC	Intesticult
IEC	Intestinal epithelial cell
IF	Immunofluorescent
IHC	Immunohistochemistry
Infl.	Inflamed
IRE	Inositol-requiring enzyme
ISC	Intestinal stem cell
JAG	Jagged
JNK	c-Jun N-terminal kinase
LC3	Microtubule-associated protein 1A/1B-light chain 3
Lgr5	Leucine-rich repeat-containing G-protein coupled receptor 5
Lyz	lysozyme
MMP	Matrix metalloproteinase
MPC	Mitochondrial pyruvate carrier
MT	Mitochondria
MUC	Mucine
Mure	mt-UPR element
NFκB	Nuclear factor kappa-light-chain enhancer of activated B-cells
NOD	Nucleotide-binding oligomerization domain
Non-infl.	Non-inflamed
4-OHT	4-Hydroxy-tamoxifen
Olfm4	Olfactomedin 4
OTC	Ornithine transcarbamylase
OXPHOS	Oxidative phosphorylation
PCs	Paneth cells
PKR	Double-stranded RNA-activated protein kinase
PDH	Pyruvate dehydrogenase
PDK	Pyruvate dehydrogenase kinase
ROS	Reactive oxygen species
SPF	Specific pathogen free
sPLA2s	Secretory Phospholipases A2
TA cells	Transit-amplifying cells
TCA	Tricarboxylic acid cycle
Tcf	Transcription factor T-cell factor
TIM	Translocase of the inner membrane
TNF	Tumor necrosis factor
TNFR	TNF receptor
TOM	Translocase of the outer membrane
UC	Ulcerative Colitis
UEA	Ulex Europaeus Agglutinin
UPR	Unfolded protein responses
Wnt	Wingless-related MMTV integration site
WT	Wild type
XBP1	*X-box-binding protein 1*

References

1. Mowat, A.M. and W.W. Agace, Regional specialization within the intestinal immune system. Nat Rev Immunol, 2014. 14(10): p. 667-85.
2. Helander, H.F. and L. Fandriks, Surface area of the digestive tract - revisited. Scand J Gastroenterol, 2014. 49(6): p. 681-9.
3. Hillman, E.T., et al., Microbial Ecology along the Gastrointestinal Tract. Microbes Environ, 2017. 32(4): p. 300-313.
4. Barker, N., Adult intestinal stem cells: critical drivers of epithelial homeostasis and regeneration. Nat Rev Mol Cell Biol, 2014. 15(1): p. 19-33.
5. Sekirov, I., et al., Gut microbiota in health and disease. Physiol Rev, 2010. 90(3): p. 859-904.
6. Ahmed, S., et al., Mucosa-associated bacterial diversity in relation to human terminal ileum and colonic biopsy samples. Appl Environ Microbiol, 2007. 73(22): p. 7435-42.
7. Rahayu, E.S., et al., Gut microbiota profile in healthy Indonesians. World J Gastroenterol, 2019. 25(12): p. 1478-1491.
8. David, L.A., et al., Diet rapidly and reproducibly alters the human gut microbiome. Nature, 2014. 505(7484): p. 559-63.
9. Desai, M.S., et al., A Dietary Fiber-Deprived Gut Microbiota Degrades the Colonic Mucus Barrier and Enhances Pathogen Susceptibility. Cell, 2016. 167(5): p. 1339-1353 e21.
10. Kovatcheva-Datchary, P., et al., Dietary Fiber-Induced Improvement in Glucose Metabolism Is Associated with Increased Abundance of Prevotella. Cell Metab, 2015. 22(6): p. 971-82.
11. Bhalodi, A.A., et al., Impact of antimicrobial therapy on the gut microbiome. J Antimicrob Chemother, 2019. 74(Supplement_1): p. i6-i15.
12. Schaubeck, M., et al., Dysbiotic gut microbiota causes transmissible Crohn's disease-like ileitis independent of failure in antimicrobial defence. Gut, 2016. 65(2): p. 225-37.
13. Heiss, C.N. and L.E. Olofsson, Gut Microbiota-Dependent Modulation of Energy Metabolism. J Innate Immun, 2018. 10(3): p. 163-171.
14. Backhed, F., et al., Dynamics and Stabilization of the Human Gut Microbiome during the First Year of Life. Cell Host Microbe, 2015. 17(6): p. 852.
15. Cohen, L.J., et al., Genetic Factors and the Intestinal Microbiome Guide Development of Microbe-Based Therapies for Inflammatory Bowel Diseases. Gastroenterology, 2019. 156(8): p. 2174-2189.
16. Johansson, M.E., J.M. Larsson, and G.C. Hansson, The two mucus layers of colon are organized by the MUC2 mucin, whereas the outer layer is a legislator of host-microbial interactions. Proc Natl Acad Sci U S A, 2011. 108 Suppl 1: p. 4659-65.
17. de Santa Barbara, P., G.R. van den Brink, and D.J. Roberts, Development and differentiation of the intestinal epithelium. Cell Mol Life Sci, 2003. 60(7): p. 1322-32.
18. Carulli, A.J., L.C. Samuelson, and S. Schnell, Unraveling intestinal stem cell behavior with models of crypt dynamics. Integr Biol (Camb), 2014. 6(3): p. 243-57.
19. van der Flier, L.G., et al., OLFM4 is a robust marker for stem cells in human intestine and marks a subset of colorectal cancer cells. Gastroenterology, 2009. 137(1): p. 15-7.
20. Barker, N., A. van Oudenaarden, and H. Clevers, Identifying the stem cell of the intestinal crypt: strategies and pitfalls. Cell Stem Cell, 2012. 11(4): p. 452-60.
21. Barker, N., et al., Identification of stem cells in small intestine and colon by marker gene Lgr5. Nature, 2007. 449(7165): p. 1003-7.

22. Giroux, V., et al., Mouse Intestinal Krt15+ Crypt Cells Are Radio-Resistant and Tumor Initiating. Stem Cell Reports, 2018. 10(6): p. 1947-1958.
23. Tian, H., et al., A reserve stem cell population in small intestine renders Lgr5-positive cells dispensable. Nature, 2011. 478(7368): p. 255-9.
24. Gassler, N., Paneth cells in intestinal physiology and pathophysiology. World J Gastrointest Pathophysiol, 2017. 8(4): p. 150-160.
25. Salzman, N.H., et al., Enteric defensins are essential regulators of intestinal microbial ecology. Nat Immunol, 2010. 11(1): p. 76-83.
26. Salzman, N.H., et al., Protection against enteric salmonellosis in transgenic mice expressing a human intestinal defensin. Nature, 2003. 422(6931): p. 522-6.
27. Ehmann, D., et al., Paneth cell alpha-defensins HD-5 and HD-6 display differential degradation into active antimicrobial fragments. Proc Natl Acad Sci U S A, 2019. 116(9): p. 3746-3751.
28. Cadwell, K., et al., A key role for autophagy and the autophagy gene Atg16l1 in mouse and human intestinal Paneth cells. Nature, 2008. 456(7219): p. 259-63.
29. Bhinder, G., et al., Intestinal epithelium-specific MyD88 signaling impacts host susceptibility to infectious colitis by promoting protective goblet cell and antimicrobial responses. Infect Immun, 2014. 82(9): p. 3753-63.
30. Schroeder, B.O., Fight them or feed them: how the intestinal mucus layer manages the gut microbiota. Gastroenterol Rep (Oxf), 2019. 7(1): p. 3-12.
31. Volk, J.K., et al., The Nlrp6 inflammasome is not required for baseline colonic inner mucus layer formation or function. J Exp Med, 2019.
32. Coleman, O.I., et al., Activated ATF6 Induces Intestinal Dysbiosis and Innate Immune Response to Promote Colorectal Tumorigenesis. Gastroenterology, 2018. 155(5): p. 1539-1552 e12.
33. Malin E. V. Johansson, et al., The inner of the two Muc2 mucin-dependent mucus layers in colon is devoid of bacteria. PNAS, 2008. 105 (39) 15064-15069.
34. Zietek, T. and E. Rath, Inflammation Meets Metabolic Disease: Gut Feeling Mediated by GLP-1. Front Immunol, 2016. 7: p. 154.
35. Sjolund, K., et al., Endocrine cells in human intestine: an immunocytochemical study. Gastroenterology, 1983. 85(5): p. 1120-30.
36. Banerjee, A., et al., Interpreting heterogeneity in intestinal tuft cell structure and function. J Clin Invest, 2018. 128(5): p. 1711-1719.
37. Fevr, T., et al., Wnt/beta-catenin is essential for intestinal homeostasis and maintenance of intestinal stem cells. Mol Cell Biol, 2007. 27(21): p. 7551-9.
38. Gregorieff, A. and H. Clevers, Wnt signaling in the intestinal epithelium: from endoderm to cancer. Genes Dev, 2005. 19(8): p. 877-90.
39. Yu, S., et al., Dual gene deficient models of Apc(Min/+) mouse in assessing molecular mechanisms of intestinal carcinogenesis. Biomed Pharmacother, 2018. 108: p. 600-609.
40. Fre, S., et al., Notch and Wnt signals cooperatively control cell proliferation and tumorigenesis in the intestine. Proc Natl Acad Sci U S A, 2009. 106(15): p. 6309-14.
41. van Es, J.H., et al., Wnt signalling induces maturation of Paneth cells in intestinal crypts. Nat Cell Biol, 2005. 7(4): p. 381-6.
42. Demitrack, E.S. and L.C. Samuelson, Notch regulation of gastrointestinal stem cells. J Physiol, 2016. 594(17): p. 4791-803.
43. VanDussen, K.L., et al., Notch signaling modulates proliferation and differentiation of intestinal crypt base columnar stem cells. Development, 2012. 139(3): p. 488-97.
44. Tian, H., et al., Opposing activities of Notch and Wnt signaling regulate intestinal stem cells and gut homeostasis. Cell Rep, 2015. 11(1): p. 33-42.

45. Worthington, J.J., F. Reimann, and F.M. Gribble, Enteroendocrine cells-sensory sentinels of the intestinal environment and orchestrators of mucosal immunity. Mucosal Immunol, 2018. 11(1): p. 3-20.
46. Zecchini, V., et al., Notch signaling regulates the differentiation of post-mitotic intestinal epithelial cells. Genes Dev, 2005. 19(14): p. 1686-91.
47. Yu, S., et al., Paneth Cell Multipotency Induced by Notch Activation following Injury. Cell Stem Cell, 2018. 23(1): p. 46-59 e5.
48. Beumer, J. and H. Clevers, Regulation and plasticity of intestinal stem cells during homeostasis and regeneration. Development, 2016. 143(20): p. 3639-3649.
49. Haramis, A.P., et al., De novo crypt formation and juvenile polyposis on BMP inhibition in mouse intestine. Science, 2004. 303(5664): p. 1684-6.
50. He, X.C., et al., BMP signaling inhibits intestinal stem cell self-renewal through suppression of Wnt-beta-catenin signaling. Nat Genet, 2004. 36(10): p. 1117-21.
51. Gehart, H. and H. Clevers, Tales from the crypt: new insights into intestinal stem cells. Nat Rev Gastroenterol Hepatol, 2019. 16(1): p. 19-34.
52. Yan, K.S., et al., The intestinal stem cell markers Bmi1 and Lgr5 identify two functionally distinct populations. Proc Natl Acad Sci U S A, 2012. 109(2): p. 466-71.
53. Wang, Y., et al., Long-Term Culture Captures Injury-Repair Cycles of Colonic Stem Cells. Cell, 2019. 179(5): p. 1144-1159 e15.
54. Schmitt, M., et al., Paneth Cells Respond to Inflammation and Contribute to Tissue Regeneration by Acquiring Stem-like Features through SCF/c-Kit Signaling. Cell Rep, 2018. 24(9): p. 2312-2328 e7.
55. Spit, M., B.K. Koo, and M.M. Maurice, Tales from the crypt: intestinal niche signals in tissue renewal, plasticity and cancer. Open Biol, 2018. 8(9).
56. Pentinmikko, N., et al., Notum produced by Paneth cells attenuates regeneration of aged intestinal epithelium. Nature, 2019. 571(7765): p. 398-402.
57. Yilmaz, O.H., et al., mTORC1 in the Paneth cell niche couples intestinal stem-cell function to calorie intake. Nature, 2012. 486(7404): p. 490-5.
58. Schewe, M., et al., Secreted Phospholipases A2 Are Intestinal Stem Cell Niche Factors with Distinct Roles in Homeostasis, Inflammation, and Cancer. Cell Stem Cell, 2016. 19(1): p. 38-51.
59. Rodriguez-Colman, M.J., et al., Interplay between metabolic identities in the intestinal crypt supports stem cell function. Nature, 2017. 543(7645): p. 424-427.
60. Miyoshi, H., et al., Wnt5a potentiates TGF-beta signaling to promote colonic crypt regeneration after tissue injury. Science, 2012. 338(6103): p. 108-13.
61. Beppu, H., et al., Stromal inactivation of BMPRII leads to colorectal epithelial overgrowth and polyp formation. Oncogene, 2008. 27(8): p. 1063-70.
62. Berger, E., et al., Mitochondrial function controls intestinal epithelial stemness and proliferation. Nat Commun, 2016. 7: p. 13171.
63. Rath, E., A. Moschetta, and D. Haller, Mitochondrial function - gatekeeper of intestinal epithelial cell homeostasis. Nat Rev Gastroenterol Hepatol, 2018. 15(8): p. 497-516.
64. Kuhlbrandt, W., Structure and function of mitochondrial membrane protein complexes. BMC Biol, 2015. 13: p. 89.
65. Munch, C., The different axes of the mammalian mitochondrial unfolded protein response. BMC Biol, 2018. 16(1): p. 81.
66. Rath, E., et al., Induction of dsRNA-activated protein kinase links mitochondrial unfolded protein response to the pathogenesis of intestinal inflammation. Gut, 2012. 61(9): p. 1269-1278.

67. Saito, A. and K. Imaizumi, Unfolded Protein Response-Dependent Communication and Contact among Endoplasmic Reticulum, Mitochondria, and Plasma Membrane. Int J Mol Sci, 2018. 19(10).
68. Hartl, S.A.B.a.F.U., Mitochondrial stress signaling: a pathway unfolds. Cell Biology, 2008: p. 1-4.
69. Qureshi, M.A., C.M. Haynes, and M.W. Pellegrino, The mitochondrial unfolded protein response: Signaling from the powerhouse. J Biol Chem, 2017. 292(33): p. 13500-13506.
70. Meng, Q., B.X. Li, and X. Xiao, Toward Developing Chemical Modulators of Hsp60 as Potential Therapeutics. Front Mol Biosci, 2018. 5: p. 35.
71. Fiorese, C.J., et al., The Transcription Factor ATF5 Mediates a Mammalian Mitochondrial UPR. Curr Biol, 2016. 26(15): p. 2037-2043.
72. Deshwal, S., K.U. Fiedler, and T. Langer, Mitochondrial Proteases: Multifaceted Regulators of Mitochondrial Plasticity. Annu Rev Biochem, 2020.
73. Chambers, J.W. and P.V. LoGrasso, Mitochondrial c-Jun N-terminal kinase (JNK) signaling initiates physiological changes resulting in amplification of reactive oxygen species generation. J Biol Chem, 2011. 286(18): p. 16052-62.
74. Horibe, T. and N.J. Hoogenraad, The chop gene contains an element for the positive regulation of the mitochondrial unfolded protein response. PLoS One, 2007. 2(9): p. e835.
75. Aldridge, J.E., T. Horibe, and N.J. Hoogenraad, Discovery of genes activated by the mitochondrial unfolded protein response (mtUPR) and cognate promoter elements. PLoS One, 2007. 2(9): p. e874.
76. Heijmans, J., et al., ER stress causes rapid loss of intestinal epithelial stemness through activation of the unfolded protein response. Cell Rep, 2013. 3(4): p. 1128-39.
77. Papa, L., M. Djedaini, and R. Hoffman, Mitochondrial Role in Stemness and Differentiation of Hematopoietic Stem Cells. Stem Cells Int, 2019. 2019: p. 4067162.
78. Zhang, H., K.J. Menzies, and J. Auwerx, The role of mitochondria in stem cell fate and aging. Development, 2018. 145(8).
79. Quiros, P.M., T. Langer, and C. Lopez-Otin, New roles for mitochondrial proteases in health, ageing and disease. Nat Rev Mol Cell Biol, 2015. 16(6): p. 345-59.
80. Yano, M., ABCB10 depletion reduces unfolded protein response in mitochondria. Biochem Biophys Res Commun, 2017. 486(2): p. 465-469.
81. Jenkinson, E.M., et al., Perrault syndrome is caused by recessive mutations in CLPP, encoding a mitochondrial ATP-dependent chambered protease. Am J Hum Genet, 2013. 92(4): p. 605-13.
82. Gispert, S., et al., Loss of mitochondrial peptidase Clpp leads to infertility, hearing loss plus growth retardation via accumulation of CLPX, mtDNA and inflammatory factors. Hum Mol Genet, 2013. 22(24): p. 4871-87.
83. Wang, T., et al., Mitochondrial unfolded protein response gene Clpp is required to maintain ovarian follicular reserve during aging, for oocyte competence, and development of pre-implantation embryos. Aging Cell, 2018. 17(4): p. e12784.
84. Jovaisaite, V., L. Mouchiroud, and J. Auwerx, The mitochondrial unfolded protein response, a conserved stress response pathway with implications in health and disease. J Exp Biol, 2014. 217(Pt 1): p. 137-43.
85. Curis, E., et al., Almost all about citrulline in mammals. Amino Acids, 2005. 29(3): p. 177-205.
86. Bertolo, R.F. and D.G. Burrin, Comparative aspects of tissue glutamine and proline metabolism. J Nutr, 2008. 138(10): p. 2032S-2039S.

87. Shekhawat, P.S., et al., Spontaneous development of intestinal and colonic atrophy and inflammation in the carnitine-deficient jvs (OCTN2(-/-)) mice. Mol Genet Metab, 2007. 92(4): p. 315-24.
88. Yetkin-Arik, B., et al., The role of glycolysis and mitochondrial respiration in the formation and functioning of endothelial tip cells during angiogenesis. Sci Rep, 2019. 9(1): p. 12608.
89. Vacanti, N.M., et al., Regulation of substrate utilization by the mitochondrial pyruvate carrier. Mol Cell, 2014. 56(3): p. 425-35.
90. Heller, S., et al., Reduced mitochondrial activity in colonocytes facilitates AMPKalpha2-dependent inflammation. FASEB J, 2017. 31(5): p. 2013-2025.
91. Santhanam, S., et al., Mitochondrial electron transport chain complex dysfunction in the colonic mucosa in ulcerative colitis. Inflamm Bowel Dis, 2012. 18(11): p. 2158-68.
92. Sifroni, K.G., et al., Mitochondrial respiratory chain in the colonic mucosal of patients with ulcerative colitis. Mol Cell Biochem, 2010. 342(1-2): p. 111-5.
93. Lemarie, A. and S. Grimm, Mitochondrial respiratory chain complexes: apoptosis sensors mutated in cancer? Oncogene, 2011. 30(38): p. 3985-4003.
94. Stock, U., et al., Measuring interference of drug-like molecules with the respiratory chain: toward the early identification of mitochondrial uncouplers in lead finding. Assay Drug Dev Technol, 2013. 11(7): p. 408-22.
95. Dodiya, H.B., et al., Chronic stress-induced gut dysfunction exacerbates Parkinson's disease phenotype and pathology in a rotenone-induced mouse model of Parkinson's disease. Neurobiol Dis, 2020. 135: p. 104352.
96. Li, N., et al., Mitochondrial complex I inhibitor rotenone induces apoptosis through enhancing mitochondrial reactive oxygen species production. J Biol Chem, 2003. 278(10): p. 8516-25.
97. Formentini, L., et al., Mitochondrial ROS Production Protects the Intestine from Inflammation through Functional M2 Macrophage Polarization. Cell Rep, 2017. 19(6): p. 1202-1213.
98. Xu, R.H., et al., Inhibition of glycolysis in cancer cells: a novel strategy to overcome drug resistance associated with mitochondrial respiratory defect and hypoxia. Cancer Res, 2005. 65(2): p. 613-21.
99. Zhang, J., et al., Metabolic regulation in pluripotent stem cells during reprogramming and self-renewal. Cell Stem Cell, 2012. 11(5): p. 589-95.
100. Xu, X., et al., Mitochondrial regulation in pluripotent stem cells. Cell Metab, 2013. 18(3): p. 325-32.
101. Stringari, C., et al., Metabolic trajectory of cellular differentiation in small intestine by Phasor Fluorescence Lifetime Microscopy of NADH. Sci Rep, 2012. 2: p. 568.
102. Cali, T., D. Ottolini, and M. Brini, Mitochondria, calcium, and endoplasmic reticulum stress in Parkinson's disease. Biofactors, 2011. 37(3): p. 228-40.
103. Salminen, A., et al., ER stress in Alzheimer's disease: a novel neuronal trigger for inflammation and Alzheimer's pathology. J Neuroinflammation, 2009. 6: p. 41.
104. Beck, J.S., E.J. Mufson, and S.E. Counts, Evidence for Mitochondrial UPR Gene Activation in Familial and Sporadic Alzheimer's Disease. Curr Alzheimer Res, 2016. 13(6): p. 610-4.
105. Deuring, J.J., et al., Absence of ABCG2-mediated mucosal detoxification in patients with active inflammatory bowel disease is due to impeded protein folding. Biochem J, 2012. 441(1): p. 87-93.
106. Jackson, D.N., et al., Mitochondrial dysfunction during loss of prohibitin 1 triggers Paneth cell defects and ileitis. Gut, 2020.
107. Kaser, A., et al., XBP1 links ER stress to intestinal inflammation and confers genetic risk for human inflammatory bowel disease. Cell, 2008. 134(5): p. 743-56.

108. Kaser, A., T.E. Adolph, and R.S. Blumberg, The unfolded protein response and gastrointestinal disease. Semin Immunopathol, 2013. 35(3): p. 307-19.
109. Yamamoto-Furusho, J.K., et al., Incidence and prevalence of inflammatory bowel disease in Mexico from a nationwide cohort study in a period of 15 years (2000-2017). Medicine (Baltimore), 2019. 98(27): p. e16291.
110. Wilkins, T., K. Jarvis, and J. Patel, Diagnosis and management of Crohn's disease. Am Fam Physician, 2011. 84(12): p. 1365-75.
111. Collaborators, G.B.D.I.B.D., The global, regional, and national burden of inflammatory bowel disease in 195 countries and territories, 1990-2017: a systematic analysis for the Global Burden of Disease Study 2017. Lancet Gastroenterol Hepatol, 2020. 5(1): p. 17-30.
112. Elisa Liverani, et al., How to predict clinical relapse in inflammatory bowel disease patients. World J Gastroenterol, 2016. 22(3): p. 1017–1033.
113. Ananthakrishnan, A.N., et al., The benefit of combination therapy depends on disease phenotype and duration in Crohn's disease. Aliment Pharmacol Ther, 2017. 46(2): p. 162-168.
114. Hazel, K. and A. O'Connor, Emerging treatments for inflammatory bowel disease. Ther Adv Chronic Dis, 2020. 11: p. 2040622319899297.
115. Chongthammakun, V., et al., Correlation of the Rutgeerts score and recurrence of Crohn's disease in patients with end ileostomy. Gastroenterol Rep (Oxf), 2017. 5(4): p. 271-276.
116. Auzolle, C., et al., Male gender, active smoking and previous intestinal resection are risk factors for post-operative endoscopic recurrence in Crohn's disease: results from a prospective cohort study. Aliment Pharmacol Ther, 2018. 48(9): p. 924-932.
117. Virgin, H.W. and J.A. Todd, Metagenomics and personalized medicine. Cell, 2011. 147(1): p. 44-56.
118. Molodecky, N.A. and G.G. Kaplan, Environmental risk factors for inflammatory bowel disease. Gastroenterol Hepatol (N Y), 2010. 6(5): p. 339-46.
119. Park, S.C. and Y.T. Jeen, Genetic Studies of Inflammatory Bowel Disease-Focusing on Asian Patients. Cells, 2019. 8(5).
120. Momozawa, Y., et al., IBD risk loci are enriched in multigenic regulatory modules encompassing putative causative genes. Nat Commun, 2018. 9(1): p. 2427.
121. Stappenbeck, T.S., et al., Crohn disease: a current perspective on genetics, autophagy and immunity. Autophagy, 2011. 7(4): p. 355-74.
122. Wehkamp, J., et al., NOD2 (CARD15) mutations in Crohn's disease are associated with diminished mucosal alpha-defensin expression. Gut, 2004. 53(11): p. 1658-64.
123. Coretti, L., et al., The Interplay between Defensins and Microbiota in Crohn's Disease. Mediators Inflamm, 2017. 2017: p. 8392523.
124. VanDussen, K.L., et al., Genetic variants synthesize to produce paneth cell phenotypes that define subtypes of Crohn's disease. Gastroenterology, 2014. 146(1): p. 200-9.
125. Levine, B., N. Mizushima, and H.W. Virgin, Autophagy in immunity and inflammation. Nature, 2011. 469(7330): p. 323-35.
126. Adolph, T.E., et al., Paneth cells as a site of origin for intestinal inflammation. Nature, 2013. 503(7475): p. 272-6.
127. Jiminez, J.A., et al., Animal models to study acute and chronic intestinal inflammation in mammals. Gut Pathog, 2015. 7: p. 29.
128. Bleich, A., et al., Refined histopathologic scoring system improves power to detect colitis QTL in mice. Mamm Genome, 2004. 15(11): p. 865-71.
129. Yabal. M., et al., Characterisation of Paneth cell dysfunction in XIAP-deficient mice Journal of Crohn's and Colitis, 2018. 12(supplement_1): p. S020–S021.

130. Gunther, C., et al., Caspase-8 regulates TNF-alpha-induced epithelial necroptosis and terminal ileitis. Nature, 2011. 477(7364): p. 335-9.
131. Tschurtschenthaler, M., et al., Defective ATG16L1-mediated removal of IRE1alpha drives Crohn's disease-like ileitis. J Exp Med, 2017. 214(2): p. 401-422.
132. Pizarro, T.T., et al., SAMP1/YitFc mouse strain: a spontaneous model of Crohn's disease-like ileitis. Inflamm Bowel Dis, 2011. 17(12): p. 2566-84.
133. Bamias, G., et al., Intestinal-specific TNFalpha overexpression induces Crohn's-like ileitis in mice. PLoS One, 2013. 8(8): p. e72594.
134. Adegbola, S.O., et al., Anti-TNF Therapy in Crohn's Disease. Int J Mol Sci, 2018. 19(8).
135. Ruder, B., R. Atreya, and C. Becker, Tumour Necrosis Factor Alpha in Intestinal Homeostasis and Gut Related Diseases. Int J Mol Sci, 2019. 20(8).
136. Kontoyiannis, D., et al., Impaired on/off regulation of TNF biosynthesis in mice lacking TNF AU-rich elements: implications for joint and gut-associated immunopathologies. Immunity, 1999. 10(3): p. 387-98.
137. Roulis, M., et al., Intestinal epithelial cells as producers but not targets of chronic TNF suffice to cause murine Crohn-like pathology. Proc Natl Acad Sci U S A, 2011. 108(13): p. 5396-401.
138. Harder, U., B. Koletzko, and W. Peissner, Quantification of 22 plasma amino acids combining derivatization and ion-pair LC-MS/MS. J Chromatogr B Analyt Technol Biomed Life Sci, 2011. 879(7-8): p. 495-504.
139. Gucciardi, A., et al., A rapid UPLC-MS/MS method for simultaneous separation of 48 acylcarnitines in dried blood spots and plasma useful as a second-tier test for expanded newborn screening. Anal Bioanal Chem, 2012. 404(3): p. 741-51.
140. Hammoudi, N., et al., Association Between Microscopic Lesions at Ileal Resection Margin and Recurrence After Surgery in Patients With Crohn's Disease. Clin Gastroenterol Hepatol, 2019.
141. Khaloian, S., et al., Mitochondrial impairment drives intestinal stem cell transition into dysfunctional Paneth cells predicting Crohn's disease recurrence. Gut, 2020.
142. Erben, U., et al., A guide to histomorphological evaluation of intestinal inflammation in mouse models. Int J Clin Exp Pathol, 2014. 7(8): p. 4557-76.
143. Zietek, T. and E. Rath, Chapter 3 - Intestinal organoids: Mini-guts grown in the laboratory, in Organs and Organoids, J.A. Davies and M.L. Lawrence, Editors. 2018, Academic Press. p. 43-71.
144. Liu, S.M. and C.Y. Li, Immunohistochemical study of Ulex europaeus agglutinin 1 (UEA-1) binding of megakaryocytes in bone marrow biopsy specimens: demonstration of heterogeneity in staining pattern reflecting the stages of differentiation. Hematopathol Mol Hematol, 1996. 10(1-2): p. 99-109.
145. Alvarez-Lobos, M., et al., Crohn's disease patients carrying Nod2/CARD15 gene variants have an increased and early need for first surgery due to stricturing disease and higher rate of surgical recurrence. Ann Surg, 2005. 242(5): p. 693-700.
146. Zhao, Q., et al., A mitochondrial specific stress response in mammalian cells. EMBO J, 2002. 21(17): p. 4411-9.
147. Takeda, N., et al., Interconversion between intestinal stem cell populations in distinct niches. Science, 2011. 334(6061): p. 1420-4.
148. Sato, T., et al., Paneth cells constitute the niche for Lgr5 stem cells in intestinal crypts. Nature, 2011. 469(7330): p. 415-8.
149. Li, Y., et al., A growth factor-free culture system underscores the coordination between Wnt and BMP signaling in Lgr5(+) intestinal stem cell maintenance. Cell Discov, 2018. 4: p. 49.
150. Hua, G., et al., Crypt base columnar stem cells in small intestines of mice are radioresistant. Gastroenterology, 2012. 143(5): p. 1266-1276.

151. Larosa, V. and C. Remacle, Insights into the respiratory chain and oxidative stress. Biosci Rep, 2018. 38(5).
152. Waldschmitt, N., et al., C/EBP homologous protein inhibits tissue repair in response to gut injury and is inversely regulated with chronic inflammation. Mucosal Immunol, 2014. 7(6): p. 1452-66.
153. Ishikawa, F., et al., Gene expression profiling identifies a role for CHOP during inhibition of the mitochondrial respiratory chain. J Biochem, 2009. 146(1): p. 123-32.
154. Kankotia, S. and P.W. Stacpoole, Dichloroacetate and cancer: new home for an orphan drug? Biochim Biophys Acta, 2014. 1846(2): p. 617-29.
155. Rai, P.K., et al., Potential compounds for the treatment of mitochondrial disease. Br Med Bull, 2015. 116: p. 5-18.
156. Deepa, S.S., et al., Down-regulation of the mitochondrial matrix peptidase ClpP in muscle cells causes mitochondrial dysfunction and decreases cell proliferation. Free Radic Biol Med, 2016. 91: p. 281-92.
157. Ng, S.C., et al., Worldwide incidence and prevalence of inflammatory bowel disease in the 21st century: a systematic review of population-based studies. Lancet, 2018. 390(10114): p. 2769-2778.
158. Danese, S., New therapies for inflammatory bowel disease: from the bench to the bedside. Gut, 2012. 61(6): p. 918-32.
159. Yokoi, Y., et al., Paneth cell granule dynamics on secretory responses to bacterial stimuli in enteroids. Sci Rep, 2019. 9(1): p. 2710.
160. Lueschow, S.R., et al., Loss of murine Paneth cell function alters the immature intestinal microbiome and mimics changes seen in neonatal necrotizing enterocolitis. PLoS One, 2018. 13(10): p. e0204967.
161. Farin, H.F., et al., Paneth cell extrusion and release of antimicrobial products is directly controlled by immune cell-derived IFN-gamma. J Exp Med, 2014. 211(7): p. 1393-405.
162. Wehkamp, J., et al., Reduced Paneth cell alpha-defensins in ileal Crohn's disease. Proc Natl Acad Sci U S A, 2005. 102(50): p. 18129-34.
163. Dayton, T.L. and H. Clevers, Beyond growth signaling: Paneth cells metabolically support ISCs. Cell Res, 2017. 27(7): p. 851-852.
164. Otsuka, K. and T. Iwasaki, Effects of dose rates on radiation-induced replenishment of intestinal stem cells determined by Lgr5 lineage tracing. J Radiat Res, 2015. 56(4): p. 615-22.
165. Metcalfe, C., et al., Lgr5+ stem cells are indispensable for radiation-induced intestinal regeneration. Cell Stem Cell, 2014. 14(2): p. 149-59.
166. Otsuka, K., et al., Cellular responses and gene expression profiles of colonic Lgr5+ stem cells after low-dose/low-dose-rate radiation exposure. J Radiat Res, 2018. 59(suppl_2): p. ii18-ii22.
167. Suzuki, K., et al., Single cell analysis of Crohn's disease patient-derived small intestinal organoids reveals disease activity-dependent modification of stem cell properties. J Gastroenterol, 2018. 53(9): p. 1035-1047.
168. Carulli, A.J., et al., Notch receptor regulation of intestinal stem cell homeostasis and crypt regeneration. Dev Biol, 2015. 402(1): p. 98-108.
169. Taketo, M.M., Wnt signaling and gastrointestinal tumorigenesis in mouse models. Oncogene, 2006. 25(57): p. 7522-30.
170. Rubio, C.A. and R. Befrits, Increased lysozyme expression in gastric biopsies with intestinal metaplasia and pseudopyloric metaplasia. Int J Clin Exp Med, 2009. 2(3): p. 248-53.
171. Kamal, M., et al., Mucosal T cells regulate Paneth and intermediate cell numbers in the small intestine of T. spiralis-infected mice. Clin Exp Immunol, 2001. 126(1): p. 117-25.

172. King, S.L., J.J. Mohiuddin, and C.M. Dekaney, Paneth cells expand from newly created and preexisting cells during repair after doxorubicin-induced damage. Am J Physiol Gastrointest Liver Physiol, 2013. 305(2): p. G151-62.
173. Jackson, D.N., et al., Mitochondrial dysfunction during loss of prohibitin 1 triggers Paneth cell defects and ileitis. Gut, 2020. 69(11): p. 1928-1938.
174. Brock, C.K., et al., Stem cell proliferation is induced by apoptotic bodies from dying cells during epithelial tissue maintenance. Nat Commun, 2019. 10(1): p. 1044.
175. Kaser, A., S. Zeissig, and R.S. Blumberg, Inflammatory bowel disease. Annu Rev Immunol, 2010. 28: p. 573-621.
176. Gunther, C., et al., Caspase-8 controls the gut response to microbial challenges by Tnf-alpha-dependent and independent pathways. Gut, 2015. 64(4): p. 601-10.
177. Bel, S., et al., Paneth cells secrete lysozyme via secretory autophagy during bacterial infection of the intestine. Science, 2017. 357(6355): p. 1047-1052.
178. Carroll, T.D., et al., Lgr5(+) intestinal stem cells reside in an unlicensed G1 phase. J Cell Biol, 2018. 217(5): p. 1667-1685.
179. Tetteh, P.W., et al., Replacement of Lost Lgr5-Positive Stem Cells through Plasticity of Their Enterocyte-Lineage Daughters. Cell Stem Cell, 2016. 18(2): p. 203-13.
180. Bankaitis, E.D., et al., Reserve Stem Cells in Intestinal Homeostasis and Injury. Gastroenterology, 2018. 155(5): p. 1348-1361.
181. Haberman, Y., et al., Ulcerative colitis mucosal transcriptomes reveal mitochondriopathy and personalized mechanisms underlying disease severity and treatment response. Nat Commun, 2019. 10(1): p. 38.
182. Cosin-Roger, J., et al., Hypoxia ameliorates intestinal inflammation through NLRP3/mTOR downregulation and autophagy activation. Nat Commun, 2017. 8(1): p. 98.
183. Schofield, C.J. and P.J. Ratcliffe, Oxygen sensing by HIF hydroxylases. Nat Rev Mol Cell Biol, 2004. 5(5): p. 343-54.
184. Karhausen, J., et al., Epithelial hypoxia-inducible factor-1 is protective in murine experimental colitis. J Clin Invest, 2004. 114(8): p. 1098-106.
185. Donohoe, D.R., et al., The microbiome and butyrate regulate energy metabolism and autophagy in the mammalian colon. Cell Metab, 2011. 13(5): p. 517-26.
186. Giatromanolaki, A., et al., Hypoxia inducible factor 1alpha and 2alpha overexpression in inflammatory bowel disease. J Clin Pathol, 2003. 56(3): p. 209-13.
187. Athea, Y., et al., AMP-activated protein kinase alpha2 deficiency affects cardiac cardiolipin homeostasis and mitochondrial function. Diabetes, 2007. 56(3): p. 786-94.
188. Garcia, D. and R.J. Shaw, AMPK: Mechanisms of Cellular Energy Sensing and Restoration of Metabolic Balance. Mol Cell, 2017. 66(6): p. 789-800.
189. Su, N. and M.S. Kilberg, C/EBP homology protein (CHOP) interacts with activating transcription factor 4 (ATF4) and negatively regulates the stress-dependent induction of the asparagine synthetase gene. J Biol Chem, 2008. 283(50): p. 35106-17.
190. Helmerhorst, E.J., et al., Characterization of the mitochondrial respiratory pathways in Candida albicans. Biochim Biophys Acta, 2002. 1556(1): p. 73-80.
191. Szczepanowska, K., et al., A salvage pathway maintains highly functional respiratory complex I. Nat Commun, 2020. 11(1): p. 1643.
192. Agani, F.H., et al., Inhibitors of mitochondrial complex I attenuate the accumulation of hypoxia-inducible factor-1 during hypoxia in Hep3B cells. Comp Biochem Physiol A Mol Integr Physiol, 2002. 132(1): p. 107-9.
193. Prior, S., et al., Mitochondrial respiratory function induces endogenous hypoxia. PLoS One, 2014. 9(2): p. e88911.

194. Ferlazzo, N., et al., Up-regulation of HIF-1alpha is associated with neuroprotective effects of agmatine against rotenone-induced toxicity in differentiated SH-SY5Y cells. Amino Acids, 2020. 52(2): p. 171-179.
195. Giachin, G., et al., Dynamics of Human Mitochondrial Complex I Assembly: Implications for Neurodegenerative Diseases. Front Mol Biosci, 2016. 3: p. 43.
196. Carriere, A., et al., Mitochondrial reactive oxygen species control the transcription factor CHOP-10/GADD153 and adipocyte differentiation: a mechanism for hypoxia-dependent effect. J Biol Chem, 2004. 279(39): p. 40462-9.
197. Singh, K., et al., Alpha-Ketoglutarate Curbs Differentiation and Induces Cell Death in Mesenchymal Stromal Precursors with Mitochondrial Dysfunction. Stem Cells, 2017. 35(7): p. 1704-1718.
198. Li, B., et al., Targeting glutaminase 1 attenuates stemness properties in hepatocellular carcinoma by increasing reactive oxygen species and suppressing Wnt/beta-catenin pathway. EBioMedicine, 2019. 39: p. 239-254.
199. Zhou, T., et al., Glutamine Metabolism Is Essential for Stemness of Bone Marrow Mesenchymal Stem Cells and Bone Homeostasis. Stem Cells Int, 2019. 2019: p. 8928934.
200. Kim, J.W., et al., HIF-1-mediated expression of pyruvate dehydrogenase kinase: a metabolic switch required for cellular adaptation to hypoxia. Cell Metab, 2006. 3(3): p. 177-85.
201. Khan, A., et al., A novel form of dichloroacetate therapy for patients with advanced cancer: a report of 3 cases. Altern Ther Health Med, 2014. 20 Suppl 2: p. 21-8.
202. Stacpoole, P.W., et al., Dichloroacetate in the treatment of lactic acidosis. Ann Intern Med, 1988. 108(1): p. 58-63.
203. Stacpoole, P.W., et al., A controlled clinical trial of dichloroacetate for treatment of lactic acidosis in adults. The Dichloroacetate-Lactic Acidosis Study Group. N Engl J Med, 1992. 327(22): p. 1564-9.
204. Allez, M., et al., The efficacy and safety of a third anti-TNF monoclonal antibody in Crohn's disease after failure of two other anti-TNF antibodies. Aliment Pharmacol Ther, 2010. 31(1): p. 92-101.
205. Khader, S.A. and S. Thirunavukkarasu, The Tale of IL-12 and IL-23: A Paradigm Shift. J Immunol, 2019. 202(3): p. 629-630.
206. Gisbert, J.P. and M. Chaparro, Predictors of primary response to biologic treatment (anti-TNF, vedolizumab and ustekinumab) in patients with inflammatory bowel disease: from basic science to clinical practice. J Crohns Colitis, 2019.
207. Liu, T.C., et al., Paneth cell defects in Crohn's disease patients promote dysbiosis. JCI Insight, 2016. 1(8): p. e86907.
208. Calkins, B.M., A meta-analysis of the role of smoking in inflammatory bowel disease. Dig Dis Sci, 1989. 34(12): p. 1841-54.
209. Karczewski, J., et al., The effect of cigarette smoking on the clinical course of inflammatory bowel disease. Prz Gastroenterol, 2014. 9(3): p. 153-9.
210. Bhaskaran, S., et al., Loss of mitochondrial protease ClpP protects mice from diet-induced obesity and insulin resistance. EMBO Rep, 2018. 19(3).
211. Didelija, I.C., M.A. Mohammad, and J.C. Marini, Ablation of Arginase II Spares Arginine and Abolishes the Arginine Requirement for Growth in Male Mice. J Nutr, 2017. 147(8): p. 1510-1516.
212. Moisoi, N., et al., Mitochondrial dysfunction triggered by loss of HtrA2 results in the activation of a brain-specific transcriptional stress response. Cell Death Differ, 2009. 16(3): p. 449-64.
213. Hu, D., et al., Alpha-synuclein suppresses mitochondrial protease ClpP to trigger mitochondrial oxidative damage and neurotoxicity. Acta Neuropathol, 2019. 137(6): p. 939-960.

214. Wu, A., et al., Transmissible gastroenteritis virus targets Paneth cells to inhibit the self-renewal and differentiation of Lgr5 intestinal stem cells via Notch signaling. Cell Death Dis, 2020. 11(1): p. 40.

Acknowledgements

First and foremost, I would like to thank Prof. Dirk Haller for granting me the opportunity to be part of the Nutrition & Immunology team. Thanks for letting me try, fall and rise, fail and succeed. To remind me that scientific work is like a sport life, there are time points to work hard but also time points to slow down and build up. Thanks for challenging me, guiding and supporting me and for reminding me that working on strengths is always easier than the weaknesses. Thanks for accepting me and the situations when I was discriminated from participation to some conferences.

My appreciation goes to Dr. Eva Rath for her scientific support. Thanks for all nice and also hard times we had together. Thanks for open discussions, all idea exchanges we had together and your feedback.

Next, I would like to thank Olivia, Brita, Helene, Katharina, Adam, Nina, Amira and Baraa for being there. For being there to talk, to share, to laugh and to cry. To be there in difficult and also happy times. Thanks for your advices. I am so proud to have colleagues, whom I can consider as real friends.

A big thanks to Nico for all the technical support. For the chips evenings and the talks. For being there during my long lasting experiments and in general for being there when I needed.

Huge thanks to Silvia, Sabine, Marlene and Sigrid for their support with the work in the animal facility. Thanks for forbidding me from doing something that could hurt me without questioning me.

Thanks to the mt-UPR team (Emanuel, Soo and Elisabeth), and all members of the Nutrition & Immunology group. I really appreciate the time we spent together as friends or colleagues. Thanks for being there and being with me throughout the roller coaster of my PhD life.

Thanks to Prof. Jan Willem van de Kuilen for providing additional support and advice during my PhD.

Thanks to my running and archery trainers who taught me to try and never to give up. Who forced me to smile even if I was in pain. I learned that success in not always reaching the gold, but the highest possible. Encouragement is necessary for motivation, but self-motivation is even more important. Finally, falling is not failing and even failing is not the end of everything.

Finally, most thanks as ever to my family, Hamlet, Evelyne, Ani and Aren. Thanks for supporting me, encouraging me, helping me and holding my hand. Thanks for believing in me and making me believe in myself. For worrying about me and getting happy and sad with me. For giving me the most correct advices and being not only a family, but also a best friend. Thanks for being so close to me even though being so far.

Even though being a sprinter, thanks to everybody who helped me to successfully pass though the finish-line of the longest marathon of my life.